A Comparison Between CFD-Based Aerodynamic Models and BEM Theory-Based Models Applied in Coupled Simulations of Floating Offshore Wind Turbines

Submitted by Rachael Smith

to the University of Exeter as a thesis for the degree of

Doctor of Philosophy in Renewable Energy

July 2022

I certify that all material in this thesis which is not my own work has been identified and that any material that has previously been submitted and approved for the award of a degree by this or any other University has been acknowledged.

Abstract

Interest in floating offshore wind as a renewable energy source is growing, as it offers the potential to access deeper waters than those suited to bottom-fixed offshore turbines. A key design challenge for floating offshore wind turbines (FOWTs) is capturing the aerodynamic behaviour using numerical models, which is significantly more complex than for bottom fixed turbines due to the motions of the floating platform that result in unsteady relative wind flow at the rotor. Many of the engineering models available for analysing wind turbine aerodynamics such as the blade element momentum (BEM) method were designed for fixed turbines and require empirical corrections to account for unsteady aerodynamic effects, and may not be suitable for analysing the more complex aerodynamics associated with FOWTs. Higher order modelling approaches including computational fluid dynamics (CFD) may offer improved accuracy as they capture more of the flow physics, however, they can have extremely high associated computational costs. In this thesis, the performance of different aerodynamic models for FOWTs is investigated by studying the motion and load response of a FOWT in a range of load cases covering operational and extreme conditions using a BEM method and two different CFD-based models.

Firstly, the BEM method used in the wind turbine engineering tool FAST is compared with an actuator line model (ALM) from the CFD wind turbine code package SOWFA for a range of load cases. Comparisons are made in load cases that have specific challenges for FOWTs and where the BEM method has known limitations, including rotor misalignment with the wind due to yaw, and varying wave conditions. The two modelling approaches are then used to study FOWT behaviour in realistic operational and extreme environmental conditions, and the model results are compared against available field data from full scale FOWT demonstration projects. The impact of using high order large eddy simulation (LES) to generate a turbulent wind field is also compared against a lower order statistical approach. Finally, a high order modelling approach is proposed that couples a geometry-resolved CFD model of a wind turbine blade with a structural model based on 3D finite element analysis (FEA) to enable two way coupled fluid structure interaction simulation. This model provides detailed information on the

loading and deformation of blades, and is compared against FAST for studying a large flexible wind turbine blade in the parked and feathered position.

This research provides improved understanding of the impact that the choice of aerodynamic and wind models have on the predicted response of a floating offshore wind turbine. ALM predictions are found to diverge from BEM predictions in increasingly large rotor yaw misalignment angles. Turbine loads and platform motions are found to be sensitive to the atmospheric stability condition, with stable conditions having a significant effect, however the use of high fidelity LES modelling of neutral conditions has little effect on turbine response (in either operational or extreme conditions) compared to using more efficient statistical modelling of turbulence using the Kaimal model.

The results of the presented comparisons in this work are used to make recommendations on the use of different models in the design process for FOWTs. It is found that FAST is suitable for the majority of load cases, and may provide improved predictions of a FOWT in extreme conditions over an ALM that may underestimate aerodynamic loading on the tower. However, an ALM may provide improved predictions for a yawed turbine. The use of a high fidelity coupled CFD-FEA approach has potential to be a useful tool for analysing the detailed response of highly flexible blades where low fidelity methods are less reliable, though further work is needed to validate the modelling.

Acknowledgements

Firstly, I would like to thank my supervisory team; Prof Lars Johanning, Dr Ajit Pillai, Prof Gavin Tabor and Prof Philipp Thies, without whom this research would not have been possible.

This research project was funded by a PhD studentship award from the College of Engineering, Mathematics and Physical Sciences at the University of Exeter. Additional research activities were funded by EPSRC grant EP/R007519/1. I would also like to acknowledge that much of this research was made possible through the use of High Performance Computing (HPC) facilities at the University of Exeter.

I am thankful to all those who helped and advised me during this project. In particular I extend my thanks to Gerasimos Chourdakis for all the time and help given to me as I battled learning to use preCICE.

I am thankful to my pastoral tutor, Dr Ian Ashton, for his advice and encouragement that was invaluable in helping me to complete this thesis.

Finally, I am immensely thankful to my friends and family for their continued support and love through all of the ups and downs of this journey.

Table of Contents

List of Figures

List of Tables

Chapter 1

Introduction

1.1 Background and Motivation

As the world faces a climate crisis caused by the burning of fossil fuels, the need for transition to clean, renewable sources of energy is becoming increasingly urgent. Of the renewable energy technologies available, wind energy is one of the most mature. Offshore wind in particular offers a high potential for energy production due to higher average wind speeds and lower turbulence levels than wind over land, and is projected to grow rapidly in the next few decades. The offshore wind capacity in the UK was approximately 14 GW either commissioned or under construction in 2021, and a target of 40 GW capacity by 2030 was set by the UK government [1]. In 2019, the Committee on Climate Change (CCC) recommended that the UK would need 75 GW of offshore wind installed capacity by 2050 in order to meet its net zero obligations [2].

Bottom fixed offshore wind turbines are typically limited to water depths of up to 50 m. The use of floating foundations means that offshore wind turbines can be installed in much deeper waters, which offers the potential for offshore wind farms further from the shore, where the wind speed is higher and more consistent than nearshore sites [3]. As shown in Figure 1.1, offshore wind farms are being installed with increasing distance from the shore [4]. In order to meet ambitious offshore wind targets, floating offshore wind will therefore play a key role. Floating offshore wind turbines (FOWTs) also have other advantages over bottom fixed offshore wind turbines, including potential avoidance of NIMBY (‘Not in my back yard’) criticism since they can be installed further from shore, and lower associated installation costs [5].

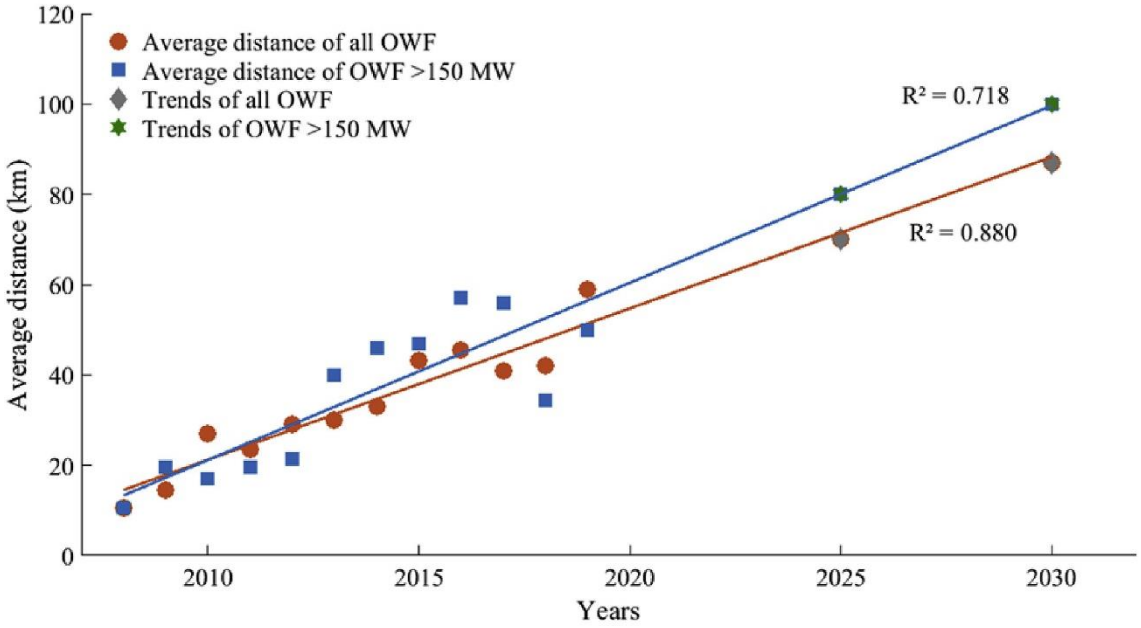

Figure 1.1: Average distance of new offshore wind farms (OWF) from the shore in Europe [4]. Values for 2025 and 2030 are predicted according to current trends.

Floating offshore wind turbines have several unique engineering challenges associated with their design, including maintaining steady power output whilst ensuring platform stability as the turbine is subjected to loading from wind, waves, current and other sources of loading in the offshore environment [6]. Deployment in deeper waters further from shore also results in floating offshore wind turbines being exposed to harsher environments [7]. The dynamic behaviour of FOWTs is fundamentally different to that of onshore or bottom fixed offshore turbines due to the added dynamics associated with the floating platform. This changes the design requirements of floating turbines compared to their bottom fixed counterparts. In order to design more cost effective FOWTs, the dynamic response of the structure must be well understood, which requires extensive physical or numerical modelling.

As Figure 1.2 shows, floating offshore wind is growing substantially but is still relatively new technology [8]. The availability of data for full scale floating offshore wind turbines is currently extremely limited. Experimental testing using physical models is expensive and often has its own challenges associated with using a scaled down version of the intended utility scale design, and so the design process for FOWTs therefore relies heavily on numerical modelling.

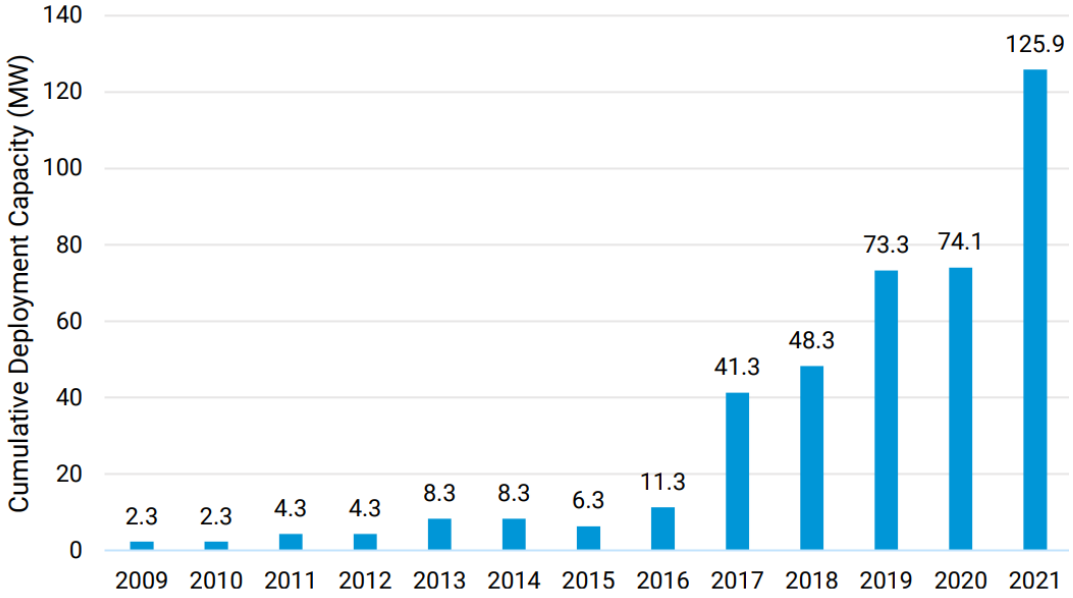

Figure 1.2: Growth in global deployed capacity of floating wind [8]

Many of the available numerical modelling tools were developed for fixed turbines, whilst the tools used for analysing platform hydrodynamics and mooring dynamics are adapted from the offshore oil and gas industry [9]. However, FOWTs are complex systems and there exist various couplings between the different dynamics which must be taken into account [10]. The fundamentally different dynamic behaviour and design requirements may therefore mean that traditional analysis tools are not always applicable for FOWTs.

1.2 Aims and Research Questions

Designs for FOWTs rely on accurate computational models that are able to predict the dynamic behaviour of the structure in response to wind and wave loading. Understanding the aerodynamics of wind turbines is crucial in order to be able to predict power output and therefore design turbines with a minimal cost of energy whilst also avoiding potential structural failure during extreme load conditions. Many of the engineering models available for analysing wind turbine aerodynamics were designed for fixed turbines, and may not take into account the fundamentally different aerodynamics of a FOWT due to the motions of the floating platform. However, more complex models that capture all of the flow physics using computational fluid dynamics (CFD) can have extremely high computational costs. It is difficult to know where low order engineering tools are

sufficient and where higher order models are necessary without validation against reliable data for full scale turbines.

The overall aim of this thesis is to provide an assessment and comparison of leading numerical models that are used to improve understanding of floating offshore wind turbine behaviour, and recommendations for the use of these models based on this assessment. The focus of this work is on aerodynamic modelling. The research questions that were identified and determined in order to achieve this aim are as follows:

- How does the widely used blade element momentum theory compare with higher fidelity CFD based actuator line modelling for simulating the aerodynamic loads of a FOWT?
- How well do numerical models perform against experimental data for FOWT behaviour in realistic operational and extreme conditions?
- To what extent does the modelling approach for the wind input impact the behaviour of numerical models of FOWTs?
- How can high fidelity fluid structure interaction modelling help to inform on FOWT behaviour compared to more commonly used low fidelity models?

1.3 Contributions of this Work

The original contributions of this thesis are summarised as follows:

- Comparative analysis of blade element momentum and actuator line models within a coupled aero-servo-hydro-elastic modelling framework applied to FOWTs.
- Improved understanding of the ability of widely used aerodynamic models to capture FOWT behaviour in a range of load cases, including operational and extreme environmental conditions, through validation against available field measurements.
- Proposal and demonstration of a high fidelity CFD and FEA based approach using open source tools for modelling the behaviour of a large flexible wind turbine blade typical of floating offshore wind turbine designs, and comparison against low order modelling.

- Recommendations for the use of aerodynamic models with different levels of complexity in the design process for FOWT rotors and blades.

1.4 Thesis outline

Chapter 2 investigates the modelling approaches for the wind and turbine aerodynamics used in the literature, and reviews progress made in validating numerical tools against experimental data for FOWTs. Chapter 3 describes the methodologies, chosen from those surveyed in Chapter 2, that are used in the numerical modelling presented in this thesis, and introduces the computational tools used to implement the models.

The implementation of the numerical models is explored in Chapters 4 to 6. Chapter 4 compares a low order blade element momentum (BEM) model with a mid-fidelity actuator line model (ALM) based CFD approach for modelling FOWT response in a range of cases involving uniform wind input and regular waves. The impacts of yaw misalignment, wind-wave misalignment, wave height and wave period on rotor and platform behaviour are studied. Chapter 5 investigates the ability of low and high order numerical models to accurately predict FOWT behaviour in realistic operational and extreme conditions by comparing model results against measurements from two floating wind turbine demonstration projects. Chapter 6 introduces a new high order model for performing fluid structure interaction simulations of a large flexible wind turbine blade using CFD and FEA.

Chapter 7 discusses the results presented in chapters 4-6. Finally, concluding remarks are presented in Chapter 8. The structure of this thesis is illustrated in Figure 1.3.

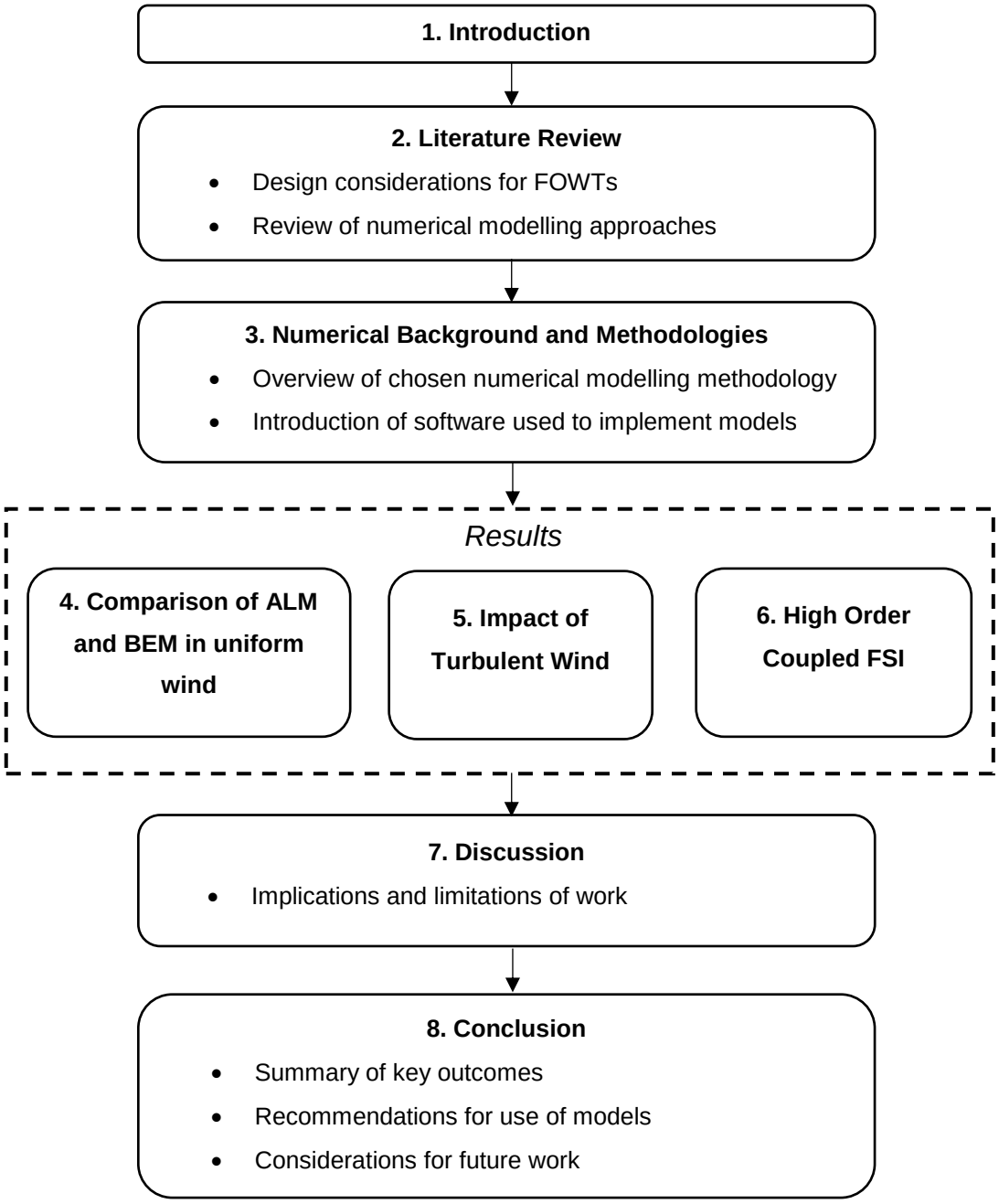

Figure 1.3: Overview of thesis structure and components

Chapter 2

Literature Review

This chapter reviews the progress made in creating reliable numerical models of floating offshore wind turbines. An overview of the unique design requirements and challenges associated with modelling FOWTs compared to their bottom fixed counterparts is first presented. A range of established numerical models for analysing the different components of FOWT dynamics are then reviewed. Some examples of different codes and numerical tools that take into account the complex coupled dynamics of floating offshore wind turbines are also reviewed.

2.1 Design Considerations for Floating Offshore Wind Turbines

Floating offshore wind turbines present a number of unique challenges that must be addressed in the design stage. The design process for wind turbines requires both numerical and physical modelling of the turbine system. Numerical models are important because they allow for a wide range of load cases to be modelled at a lower cost than physical models, which often have their own challenges associated with using a scaled down version of the intended utility scale design [11]. The purpose of modelling is to improve understanding of the structure's behaviour in order to be able to make improvements to the design that will ultimately reduce costs. The aim of design optimisation procedures for wind turbines and their components is often to reduce the levelised cost of energy (LCOE), which may involve improving annual power output, reducing component mass and therefore material costs, and reducing operation and maintenance costs among other factors [12,13]. This section examines some of the modelling requirements and challenges specific to floating offshore wind turbines, with a primary focus on challenges associated with FOWT aerodynamics.

2.1.1 Floating Platform Considerations

The key difference between a FOWT and a bottom fixed turbine by nature is the use of a non-rigid, buoyant support structure that is moored to the seabed. A fundamental design challenge for floating offshore wind turbines is designing a support structure that maintains stability whilst withstanding the overturning thrust load from the turbine [10]. Existing designs for floating wind turbines have thus far focused design efforts primarily on the floating support structures and mooring systems, and utilised existing turbine designs.

Several designs for FOWT support structures have been proposed and explored through experimental testing and demonstration projects. These can be classified into three primary designs (illustrated in Figure 2.1 [14]), which each have their unique strengths and weaknesses;

- Semi-submersible or barge type structures feature a large waterplane area which enables the structure to maintain stability by creating a stabilising moment when the structure is displaced about the rotational axis due to the large second moment of area [15]. The concept is well understood, due to its common use in offshore oil and gas projects, and is relatively simple to install [10]. However, semi-submersible platforms are also prone to experiencing large motions, particularly in storm conditions [16].
- Spar buoy concepts feature a deep draft and achieve stability through a ballast that keeps the centre of gravity of the platform below the centre of buoyancy. Spar platforms experience a smaller response to wave forcing and therefore less motion than semi-submersible designs due to their small waterplane area [17]. The requirement of a deep draft means that spar platforms can only be situated in very deep waters. This also presents a challenge for assembling and transporting the turbine, as it can only be towed through waters of a required minimum depth [18].
- Tension leg platforms (TLPs) maintain stability though the use of taut moorings and excess buoyancy in the platform. TLPs tend to undergo significantly less dynamic response than other floating platform types [19]. However, TLPs are also significantly more complex to install than spar or semi-submersible platforms, and have a higher risk of becoming unstable due to mooring line or anchor failure [15,20].

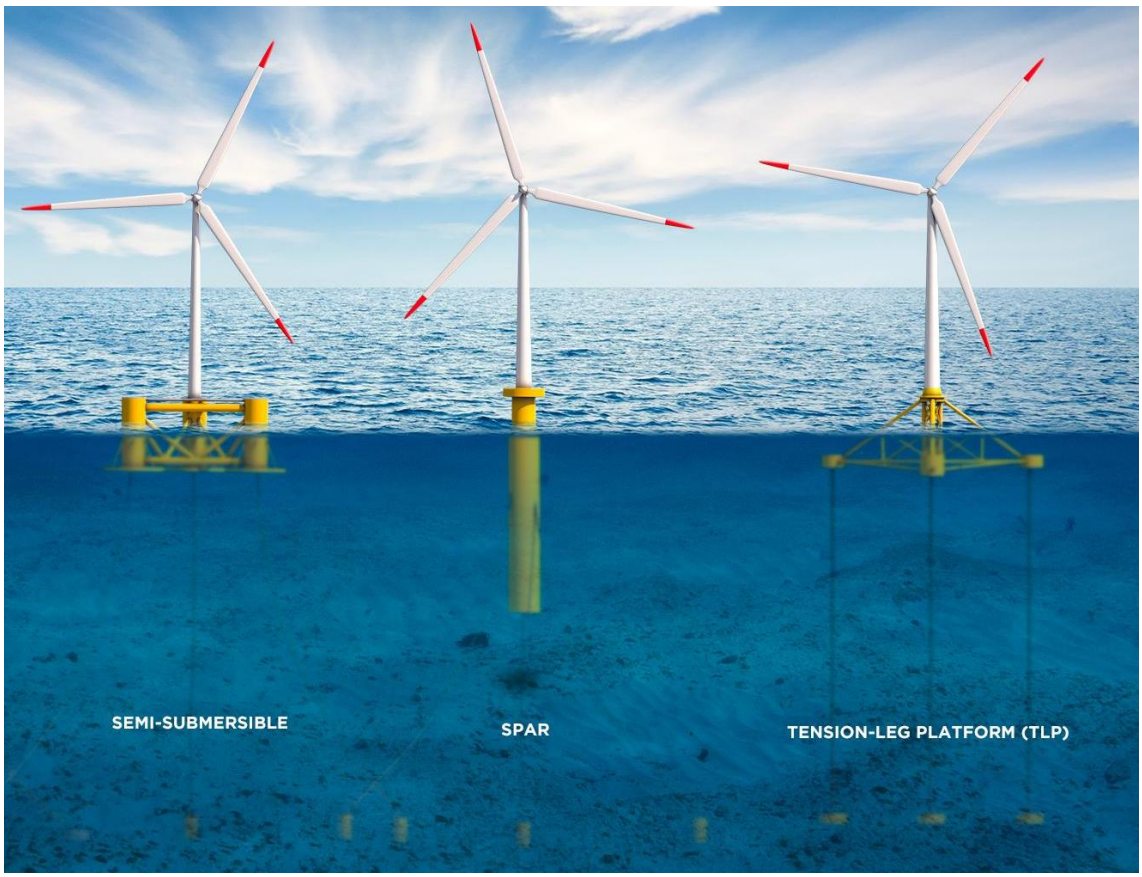

Figure 2.1: Floating offshore wind turbine platform concepts [14]

Unlike bottom fixed turbines, floating offshore wind turbines are subjected to motions due to the six degrees of freedom (6DoF) of the floating substructure, which consists of three translational modes (surge, sway and heave) and three rotational modes (roll, pitch and yaw). For floating substructures without taut moorings, the natural periods of the 6DoF floating motions are typically much larger than for other structural degrees of freedom, such as tower bending [21]. There is a risk that the platform motion natural periods may coincide with the wave periods if the floating structure and mooring system are not designed appropriately, which may cause the structure to resonate with very large motions. The platform motions may also be influenced by the turbine control system. In particular, the platform pitch mode can become unstable in above rated wind conditions due to negative damping from conventional blade pitch-to-feather control [22]. This is because the steady state rotor thrust, which contributes to tower motion damping, decreases as the wind speed increases above the rated value. This negative damping can be prevented by ensuring that the lowest pitch control natural frequency is lower than the tower natural frequencies [21].

Moorings

The mooring lines attaching the floating structure to the seabed maintain the turbine's position and orientation, and constrain the motions of the floating platform [10]. Moorings contribute to the overall stiffness of the FOWT system, and will therefore affect the natural frequencies of the platform motions, particularly surge, sway and yaw motions that are not affected by hydrostatic restoring [23]. The stiffness properties of the mooring system are therefore an important design consideration for FOWTs. For a spar or semi-submersible platform, catenary moorings are usually used, which allow for large, low frequency motions. For a mooring stabilised TLP, the lines are taut, which results in higher natural frequencies for the heave, roll and pitch modes [15].

Mooring lines are typically constructed from chains or synthetic rope, whilst the choice of anchor type depends on the seabed conditions [10]. Lines may have clump weights or buoys attached in order to adjust their stiffness characteristics. In order to calculate the forces on the FOWT system due to moorings, numerical models must take into account several effects including mooring line compliance due to elasticity or geometric flexibility, inertia due to line mass and hydrodynamic added mass, damping forces due to internal line damping and hydrodynamic drag, and interactions with the seabed [24].

2.1.2 Rotor and Blade Considerations

The design process should also take into account the effect of platform motions on the rotor loads, as various complex flow effects associated with the motions of the floating platform have been identified. For example, surge and pitch motion will introduce an additional fluctuating component to the relative wind speed and angle of inflow at the rotor, in addition to complex interaction with the rotor wake, which increases unsteady loading on the structure [25]. An aerodynamic phenomenon that presents a significant modelling challenge is vortex ring state, which has been observed where the rotor interacts with its own wake due to surge and pitch motions and acts as a propeller [9,26]. This leads to increased turbulence and may result in more frequent occurrence of dynamic stall, which increases loading on the blades. The yaw and pitch modes of the platform will also result in fluctuations in the orientation of the rotor, which may cause the turbine to be more frequently misaligned with the oncoming wind. This leads to

increased unsteady loading on blades due to the varying local angle of attack as the rotor rotates in misaligned conditions, which may also increase fatigue loading [27].

The structural response of the turbine must also be taken into account in the design process. The average turbine size in offshore wind farms has increased dramatically in the past few decades, from less than 1 MW prior to 2000 to around 6 MW in 2020, with a corresponding rotor diameter increase from less than 50 m to over 150 m, and is expected to continue to increase for the foreseeable future [28]. The growth of offshore wind turbine size is illustrated in Figure 2.2 [29]. In order to reduce material cost and weight, these increasingly long wind turbine blades are becoming more flexible. Aerodynamic loading on blades therefore leads to deflections, and they are more susceptible to aeroelastic issues such as flutter that can damage the structure [30].

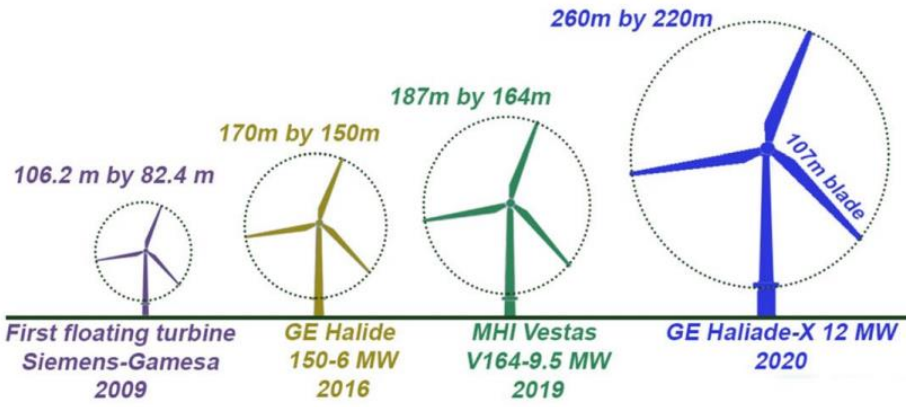

Figure 2.2: Growth in offshore wind turbine rated power and size [29].

2.1.3 Offshore Wind and the Atmospheric Boundary Layer

Wind turbines operate in a region of airflow whose characteristics are strongly influenced by the physical and thermal properties of the local ground or sea surface, known as the atmospheric boundary layer (ABL). The structure of this boundary layer is dependent on the thermal stratification. If the ground or sea surface is warm relative to the surrounding air, the warm air close to the surface rises, which subsequently increases shear driven turbulence and increases the boundary layer depth to the order of 1 km. This is known as a convective or unstably stratified boundary layer. A stable boundary layer occurs when the surface cools the nearby air, and is characterised by less turbulence and a

decreased boundary layer depth. If the air temperature is constant with height, the ABL is neutrally stratified. The stability of the ABL often varies with a diurnal cycle, particularly over land, where the ABL becomes unstable during the day and stable at night [31]. In offshore environments, the probability of stable, unstable or neutral ABL conditions is site dependent, although low wind speeds tend to correlate with more strongly stable or unstable conditions [32]. Measurements of offshore wind in the North Sea presented by Cheynet et al. [33] indicate that unstable conditions are prevalent, particularly at low wind speeds.

The wind profile in an atmospheric boundary layer is characterised by varying wind speed with height, known as vertical wind shear. In general, wind speed increases with height from the ground or sea surface. Stronger vertical wind shear is typically observed in stable conditions, whilst the unstable boundary layer may have close to zero and even occasionally negative vertical wind shear [32]. This variation in wind speed introduces cyclic loading on the rotating turbine blades, which may be particularly significant for large offshore wind turbines whose rotors cover a large range in height. In a recent review by Micallef and Rezaeiha [34], consideration of the coupled effects of complex inflow conditions (including turbulence and wind shear) and platform motions on FOWT loads and fatigue was identified as a significant future challenge for floating offshore wind research.

The International Electrotechnical Commission standard for wind turbine design IEC 61400-1 [35] specifies two statistical turbulence generation models for simulating turbulent wind inflow for wind turbines; the Kaimal spectrum exponential coherence model [36] and the Mann uniform shear turbulence model [37]. Both models are only able to model neutral atmospheric conditions.

The importance of atmospheric stability when studying offshore wind turbine loads has been highlighted. Putri et al. [38] found that unstable atmospheric conditions correspond to a significant increase in damage equivalent loads for a FOWT tower compared with neutral conditions, due to the increase in low frequency wind energy content and turbulence intensity. It was also shown that the yaw mode of a spar type FOWT is particularly sensitive to changes in turbulence. Doubrawa et al [39] showed that the turbine response is sensitive to atmospheric stability even when turbulence intensity does not change. In addition, they found that the Mann model matched more closely with LES at low

wind speeds whilst the Kaimal model showed a better match in high winds, suggesting that the Mann model may lead to overly conservative design due to higher predicted fatigue loads. However, this work did not include any validation against measured data, instead using LES as a benchmark.

2.1.4 Extreme Conditions

Extreme storm events such as hurricanes or typhoons are characterised by high wind speeds and gusts, high turbulence levels, changeable wind directions and very large waves [40,41]. This can cause damage to offshore structures including wind turbines. Many sites targeted for offshore wind development are in regions that are susceptible to such extreme events. For example, some regions of the South China Sea, which of China's seas is considered to have the highest potential for offshore wind development, experience up to seven typhoons on average per year [42]. Consideration of the impact of extreme storm events is therefore vital to ensure the survival of wind turbines.

For simulation of extreme conditions, the IEC 61400-3 standard for offshore wind turbine design specifies a number of extreme design load cases (DLC 6.x) to determine the ultimate and fatigue loads when the wind turbine is parked or idling [43]. These load cases involve the site-specific extreme wind and sea states with a 1- and 50-year return period. Performing a numerical analysis of floating offshore wind turbines in such conditions presents additional challenges, since many simplifications made in the numerical models may not be valid. For example, Nematbakhsh et al. [44] performed simulations of a spar type floating wind turbine in an extreme sea state using a high fidelity CFD approach, and found that the turbine experienced responses that would be very difficult for a linear solver to capture such as large platform pitch angles (larger than 10°), mooring tether slacking and complete submergence of the platform.

In an extreme event, such as a tropical cyclone or typhoon, the turbine rotor will most likely be idling with fully feathered blades due to the extreme wind speeds. Ma et al. [45] studied the aerodynamic performance of a fictitious spar type floating wind turbine in a typhoon using anemometer data recorded during typhoon Damrey. The sampled wind data covered the three hour period just before the wind speed rose above the turbine cut out wind speed, during which the aerodynamic loads would be largest since the turbine is still in operation. The

study indicated that a floating wind turbine operating in a typhoon may experience very large responses in the rotor thrust, rotational speed and power due to blade pitch angle errors in the control system. To mitigate this, it was suggested that the turbine is shut down in advance of extreme events. Only collinear wind and waves were modelled, and no changes in wind or wave direction were considered. A study by Li et al. [46] found that the maximum response of a semisubmersible FOWT in a typhoon does not necessarily correspond with the most extreme wind or wave state. They recommend that the sea state during the two hours before and after the maximum wind speed and wave height should be simulated in order to obtain a reliable estimate of the maximum response.

Tanaka et al. [47] validated an in house numerical code for simulating a floating offshore wind turbine in typhoon conditions against measured field data from the demonstration project turbine ‘Haenkaze’, which was exposed to typhoon Prapiroon in 2018. It was found that the numerical model was able to predict the response well apart from the platform yaw motion, which was significantly overpredicted compared to the measured data from the turbine, though the predictions were improved when spatial variation in the wind was taken into account.

2.2 Review of Numerical Modelling Approaches Applied to Floating Offshore Wind Turbines

In order to analyse the impacts of wind, wave and current loads on the dynamic behaviour of a floating offshore wind turbine, several approaches have been adopted in the literature. Many of the aerodynamic models frequently applied to wind turbines are no longer sufficient on their own for accurately describing the behaviour of floating wind turbines unless they consider the effect of platform motion on the relative inflow at the rotor. Also, as new designs for floating wind turbines follow the trend of increasing size and the structures become more flexible, analysis of structural response becomes more important. In this section, different approaches to modelling the different components of the dynamic behaviour of floating offshore wind turbines are reviewed in order of increasing levels of complexity and fidelity.

2.2.1 Wind Turbine Aerodynamics

2.2.1.1 Blade Element Momentum Theory

The blade element momentum method is the most widely used aerodynamic model in engineering tools for wind turbine analysis [48]. The model combines simple momentum theory with blade element theory [49]. Momentum theory forms the basis for the simplest models of wind turbine aerodynamics, where the rotor is modelled as an actuator disk that extracts momentum from the wind flow. The aerodynamic forces are then calculated based on the principle of momentum conservation. Using two dimensional blade element theory, the effects of rotor geometry on wind turbine aerodynamics are considered, and the local thrust and torque forces are calculated based on the lift and drag characteristics of the local aerofoil section. When the equations for the rotor forces from these two theories are combined, the induced axial and tangential velocity at the rotor can be estimated through an iterative procedure, and the power and thrust are subsequently calculated. The method involves splitting the rotor disk into a finite number of annular rings and calculating the forces at each radial position. The actuator disk and annular ring concepts are illustrated in Figure 2.3. The theory assumes that there is no radial interaction between the flows through neighbouring rings [50].

BEM theory based methods are simple and inexpensive to run, making them useful for the early stages of the design process where a large number of initial designs are analysed. However, BEM theory suffers from a number of limitations, and relies on empirical corrections to account for certain conditions. The theory assumes that the loading on the rotor is axisymmetric and that there is no radial component to the flow so that each radial element of the rotor can be treated independently, however this assumption is invalid for cases involving misaligned inflow [51]. A skewed wake correction model is applied to account for this, such as the Pitt/Peters correction [52]. However, this correction is known to be unreliable since it assumes a cylindrical wake, which is only valid for lightly loaded rotors [49].

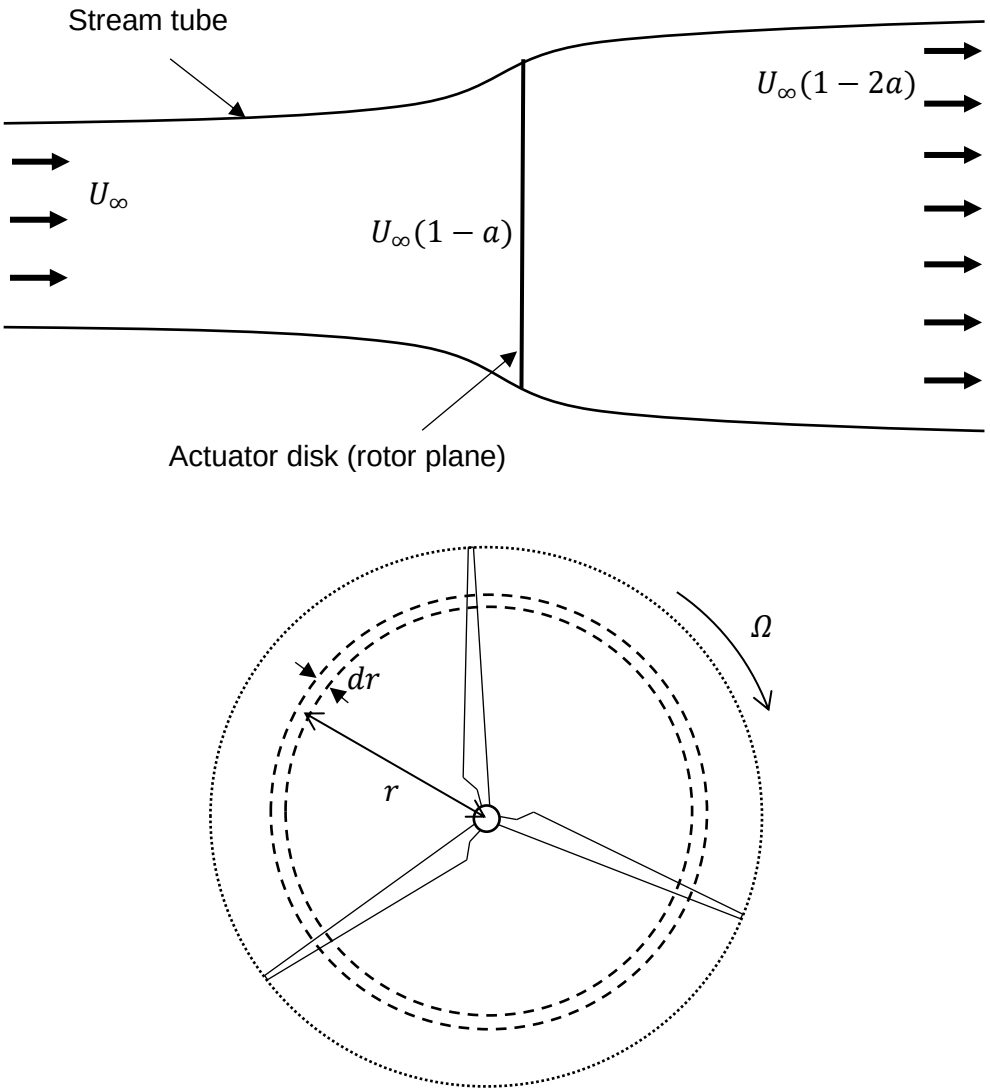

Figure 2.3: Actuator disk and annular ring representation of a turbine rotor used in BEM theory

The BEM method also does not take into account vortex shedding at the blade tip and root since the discrete blades are not modelled, and so loading in these regions is overpredicted [50]. The tip/hub loss correction factor developed by Prandtl is most commonly used to account for this; however, several alternative corrections have been proposed more recently that provide improved predictions of the force distribution at the tip region such as that proposed by Shen et al. [53].

BEM theory is based on the assumption of equilibrium between the momentum loss in the flow and the forces acting on the rotor blades, however this assumption breaks down when axial induction (described by a in Figure 2.3) is high since a turbulent wake develops due to the large difference between the freestream and wake velocities [50]. The turbulence in the wake increases due to additional flow from outside the wake being incorporated into it. Therefore, the velocity of the

flow behind the rotor decreases, but the thrust on the rotor continues to increase. In this case, BEM theory becomes invalid, and momentum theory instead assumes that some of the flow in the far wake begins to propagate upstream, which is physically impossible. The Glauert correction model for the thrust coefficient is usually applied to account for this, however this may also have limitations as this was developed initially as a correction for the entire rotor disk rather than for annular rings which are used in the BEM method [49]. The momentum balance assumption also becomes invalid when the flow is unsteady such as when dynamic stall occurs, and an empirical correction is required to account for this [54].

The quality of analyses performed using BEM methods are highly dependent on the aerofoil data provided; predictions can be improved by using data that is corrected for 3D flow effects such as flow separation and stall, or data that is a function of the flow Reynolds number in addition to the angle of attack [48].

For floating offshore wind turbines, the relative inflow at the rotor is inherently unsteady due to the motions of the floating platform, which requires a correction to the BEM model that accounts for dynamic inflow [34]. FOWT rotors are also more frequently misaligned with the incoming flow due to pitch and yaw motion, which increases the need for accurate skewed wake corrections. The momentum balance assumption is also more likely to break down for FOWTs with large platform motion amplitudes [25].

Even with the aforementioned empirical corrections, BEM may not be suitable for all load cases for FOWTs. Implementations of BEM with corrections typically involve decoupling the skewed wake correction from dynamic stall modelling, which is not appropriate for rotors operating consistently in unsteady or misaligned conditions, and therefore presents a potential issue for FOWTs [49,55]. BEM with common corrections is also not capable of capturing some of the complex aerodynamics conditions specific to FOWTs such as the vortex ring state that occurs when the rotor interacts with its own wake due to surge or pitch motion [9]. Furthermore, the actuator disk assumption that BEM relies on may be violated for rotors with highly flexible blades that experience large deflections, which is an increasingly important consideration as turbines continue to increase in size [56]. Therefore, higher order aerodynamic analysis may be necessary in order to accurately model the complex aerodynamics of FOWTs.

2.2.1.2 Potential Flow Methods

A higher order alternative to BEM is a vortex wake method such as a lifting line or surface model. The underlying theory behind these models is that lift force on the blades generates a bound circulation that determines the strength of the trailing and shed vorticity [57]. In a lifting line method, the bound circulation is concentrated in a line along the blade span that is usually at the quarter-chord location from the leading edge [58], and the lift is determined from tabulated aerofoil data as in the BEM method. Further information on the theory behind vortex methods can be found in Katz and Plotkin [59]. A lifting line method with a vortex lattice representation of the wake is illustrated in Figure 2.4 [60]. The lattice representation is formed of the trailing vortex filaments, which are related to the spanwise bound circulation gradients along the lifting line model of the blade, and the shed vortex filaments, which are determined by temporal variation in the bound circulation [25].

In vortex models of wind turbines, the wake is modelled using a discrete number of either vortex particles or filaments, where a vortex filament is a vorticity field with constant vorticity strength concentrated onto a curve. Vortex methods can be categorised as either prescribed wake methods, where the wake geometry is predetermined usually in order to fit experimental data, or free wake methods, where the vortex filaments move freely within the wake. Free wake methods incur a significantly higher CPU cost than prescribed wake methods, however they have the potential to give more accurate results [61].

Vortex methods are more computationally expensive than BEM models, but less expensive than computational fluid dynamics methods (discussed in the following section) since they are based on potential flow theory [62,63]. Using potential flow theory, the fluid flow is governed by Laplace's equation, which assumes that the fluid is incompressible, inviscid and irrotational. A limitation of vortex wake methods is that the inviscid flow assumption means that viscous flow effects such as skin friction cannot be captured, which may cause problems when flow separation occurs around the blades [64].

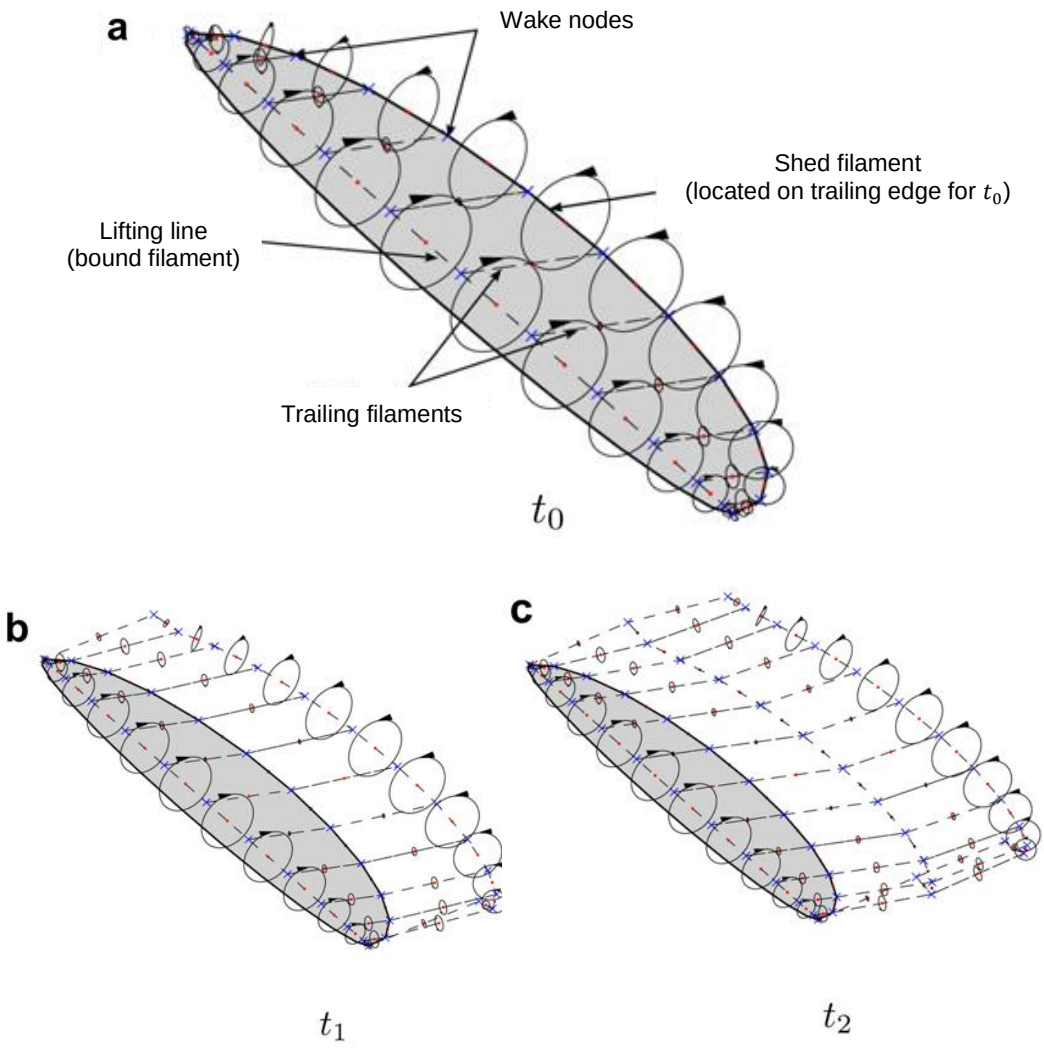

Figure 2.4: Illustration of lifting line model, including wake evolution using a vortex lattice method at three time steps (t_0, t_1, t_2) [60]

Vortex methods have the advantage of being able to capture 3D flow effects such as trailing and shed vortices around the rotor blades, meaning they may be better suited than BEM for modelling the unsteady aerodynamics of FOWTs [25]. An example of a free vortex wake (FVW) code developed for floating offshore wind turbines can be found in Sebastian and Lackner [60], which was found to show good agreement with experimental data for bottom fixed turbines, particularly when dynamic stall modelling was included [65], but still requires validation for floating applications. A FVW model has also been developed by the National Renewable Energy Laboratory (NREL) as an alternative to BEM in cases involving floating turbines or highly flexible rotors (where BEM is acknowledged to have limitations) [56], however this model also requires further validation.

2.2.1.3 CFD Methods

CFD approaches involve obtaining a solution to the governing equations for a fluid, known as the Navier Stokes equations. CFD allows for more realistic simulation of fluid flows than vortex wake methods allow since they include the effects of turbulence and viscosity which are not considered by potential flow theory. This makes it particular useful for complex fluid flow problems associated with wind turbines such as flow separation or wake interaction.

Due to the extremely high computational cost associated with the vast number of unknowns, obtaining a direct numerical solution to the Navier Stokes equation is near impossible for most complex fluid problems with currently available computing technology, and simplifications are usually made when simulating the fluid turbulence. CFD models therefore vary significantly in complexity. The simplest simulations of turbulent flows involve a Reynolds Averaged Navier Stokes (RANS) approach, where only the time averaged turbulent quantities are solved for. For cases where the turbulent structures and fluctuations are of interest, a more complex Large Eddy Simulation (LES) approach is usually applied, where the turbulent quantities are filtered and the turbulent structures larger than the filter width are directly resolved, whilst the behaviour associated with any smaller turbulent structures is represented by a turbulence model [66]. This incurs a larger computational cost than RANS but is less expensive than direct numerical simulation.

CFD models of wind turbines also vary in complexity; they may involve fully resolving the boundary layer around the structure's geometry, or may involve a more simple actuator approach where the turbine is represented by a force acting on the fluid.

2.2.1.3.1 Actuator Models

The simplest CFD models of wind turbines involve using the actuator disk concept described in section 2.2.1.1 to apply an axisymmetric force to the fluid based on an inflow velocity value sampled from the fluid domain. In order to include the effects of blade geometry on the aerodynamic forces generated by the actuator disk, the same blade element method used in BEM theory may be used to calculate lift and drag forces based on tabulated aerofoil data and the sampled

velocity information from the flow field. This approach has been implemented in Martinez-Tossas and Leonardi [67] and Wu and Porté-Agel [68].

The blade element coupled actuator disk approach was extended by Sørensen and Shen [69] to give the actuator line method. In this approach, the individual turbine blades are simulated by modelling the aerodynamic force distribution along discrete lines representing the blades that are rotated within the fluid domain, similar to the lifting line approach commonly used in vortex models of turbine rotors. The advantage of this approach over the actuator disk model (ADM) is that three dimensional flow effects due to discrete blades are resolved, such as the vortices formed at the blade root and tip. This means that the ALM in theory should not require a tip or root loss correction model. The ALM has been shown to improve predictions of the near wake compared to the ADM due to its ability to capture flow structured caused by the presence of individual blades [70]. Furthermore, unlike the ADM, the ALM does not rely on the assumption of axisymmetry, which may make an ADM unsuitable for modelling non-axial rotor conditions that are an important consideration for FOWTs. However, the computational cost of the actuator line model is higher than that of the actuator disk due to the constraint on the blade tip rotation, as the tip must not pass through more than one mesh cell each time step in order to maintain numerical stability.

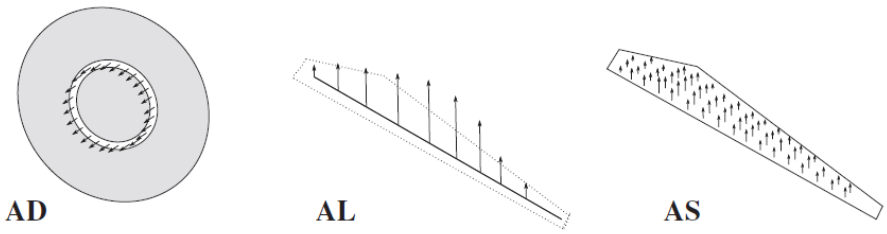

Figure 2.5: Illustration of actuator disk (AD), actuator line (AL) and actuator surface (AS) concepts [71]

Further improvements and alternatives to the standard actuator models have also been proposed. The actuator surface model [72] improves on the actuator line method by enabling the pressure distribution along the local blade chord to be modelled, however the computational cost is significantly larger than the standard actuator line model. The actuator disk, line and surface concepts are illustrated in Figure 2.5 [71]. An actuator sector model [73] has also been proposed, which is similar to the actuator line model in that the individual blades are modelled, but

with a decreased computational cost similar to that of an actuator disk model. However, the actuator line model remains a popular choice for mid fidelity CFD studies of wind turbines, and there exists a wide range of literature validating its use [74,75]. Actuator line modelling has also been shown to be capable of simulating vortex ring state, which gives them an advantage over BEM for floating applications [76].

Actuator approaches in CFD methods have the advantage of less complex mesh requirements than fully resolved methods (discussed in the next section), since a mesh of the turbine geometry is not needed and therefore the mesh cell count may be much lower. As a result they can be significantly less expensive to run. However, there are limitations associated with their reliance on tabulated 2D aerofoil data, as they are not able to capture 3D effects such as dynamic stall without a correction.

Micallef and Sant [77] compare three approaches that use blade element theory for predicting the aerodynamic loading of a floating wind turbine rotor with prescribed sinusoidal platform motion; a Navier Stokes based actuator disk approach, a free wake vortex model and blade element momentum theory. Considering only the surge motion, they found that the three models agree well for optimal and high tip speed ratio cases, but the BEM approach predicted significantly lower amplitudes for the power and thrust responses than the free wake vortex and actuator disk approaches for all sea states at low tip speed ratios. It was also found that the actuator disk model predictions for the time averaged power and thrust exhibited a much higher sensitivity to the sea state than the BEM and FWM predictions. However, the study was limited to a code to code comparison and the results were not validated against any experimental data.

Corniglion et al. [63] compare two lifting line model approaches for modelling a fictitious wind turbine experiencing surge motion; a CFD based actuator line model with a lifting line free vortex wake model. These models are also compared against quasi steady predictions based on the FVW method and high order blade resolved CFD. The primary difference between the two lifting line models is that the actuator line model includes turbulence and viscosity effects whereas the free vortex wake model does not, and so the most significant differences in the model predictions were seen in the far wake. A limitation was identified in both models'

ability to predict the rotor loads of a floating wind turbine experiencing dynamic stall due to large surge motions, which is a consequence of the local flow around the blade geometry not being resolved. Both lifting line models also predicted a higher mean thrust force than predicted by the quasi static model.

2.2.1.3.2 Fully Resolved Models

The most complex and expensive CFD models of wind turbines involve generating a mesh of the detailed turbine geometry and fully resolving the flow field generated around the structure. The advantage of this approach is that it does not rely on tabulated aerofoil data, and offers the potential for highly accurate and detailed simulations that capture complex flow effects without relying on empirical corrections [30,78].

The majority of examples of blade resolved CFD simulations of wind turbines from the literature used a RANS approach to model the flow around the blades, since resolving the turbulent boundary layer at the blade surface would require a much higher mesh resolution in this region that would make the simulation extremely computationally expensive [71]. However, RANS approaches have been shown to lack the capability to simulate stalled flow conditions [57,79]. An example of a LES study where the turbine geometry is resolved is found in Sedaghatizadeh et al. [80]. The simulation took approximately 200 hours using 40 CPU cores in order to run for long enough to achieve statistically stable results. For simulations where the full turbine geometry is resolved, mesh motion is also required in order to handle the rotation of the blades and other structural degrees of freedom where necessary, which adds further complexity to the simulation.

Due to the high computational cost associated with pure CFD analysis, there have also been attempts to develop hybrid numerical methods, such as a method combining CFD with BEM as demonstrated by Make et al. [81]. In this approach, a BEM method is used in combination with aerofoil data generated using CFD. It was found that whilst using 2D CFD aerofoil data does not have a significant effect on the BEM model results, including 3D flow effects from CFD computations in the aerofoil data can improve predictions.

2.2.2 Structural Modelling

The inclusion of structural modelling for wind turbine blades is important in order to take into account the structural response of increasingly large and flexible turbines, which may include large deformations or aeroelastic effects such as flutter. Through coupling aerodynamic models with structural models, fluid structure interaction (FSI) analysis can be carried out in order to understand this behaviour.

2.2.2.1 1D Beam Representation

Structural modelling of wind turbine components such as the blades and tower is typically simplified by modelling the 3D component as 1D beam elements, with cross sectional properties including stiffness and mass defined at discrete locations along the structure. Beam models vary in complexity. The simplest beam models used in wind turbine analysis are based on classical Euler-Bernoulli beam theory, which is capable of modelling extension, bending and torsion, but neglects shear deformations. More complex beam models are often based on the Timoshenko model, which includes shear deformation and is better suited to short and thick structures [30]. Both Euler-Bernoulli and Timoshenko beam models are based on linear assumptions, meaning they are not suitable for large deformations. An example of a nonlinear beam model is geometrically exact beam theory (GEBT) [82], which has demonstrated superiority for composite structures involving large deformations [83].

Discretizing the components into beam elements can be done using modal analysis, multi-body dynamics (MBD) representation, or 1D finite element analysis (FEA). In a modal representation of a wind turbine blade or tower, the structural response is described using a linear combination of a selected few modes of vibration, which are typically initially computed using finite element analysis [30]. The equations of motion are then solved for the full system. Example shapes of first and second bending mode for a wind turbine blade are shown in Figure 2.6 [84]. Modal analysis are one of the most efficient methods of structural modelling since the DoFs of the structure are limited. However, this approach may be inadequate in structures with complex behaviour that cannot be captured by lower order modes, such as flutter behaviour which depends on torsional eigenmodes that are generally not available in aeroelastic models based

on modal analysis [30]. The linear nature of the approach also means it may not be suitable for structures with large deflections where linear assumptions are not valid.

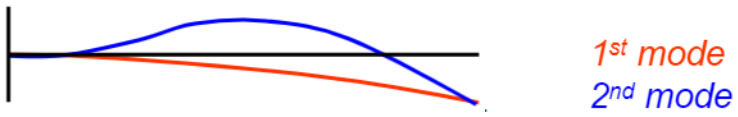

Figure 2.6: Examples of first and second bending modes of a blade [84]

In a multibody dynamics approach, the structure is discretized into an arbitrary number of components that can be flexible or rigid. The different components or bodies are connected to each other through kinematic constraints such as springs and hinges [85]. The MBD approach is more computationally demanding than the modal approach since the equations of motion are solved for each component separately, however the use of connections between bodies allows for more structural DoFs to be included, and it is possible to include some structural nonlinearities [57]. An example of a multibody representation of a wind turbine is shown in Figure 2.7 [30], where the blades are connected to the hub via hinges in order to allow pitching motion relative to the hub.

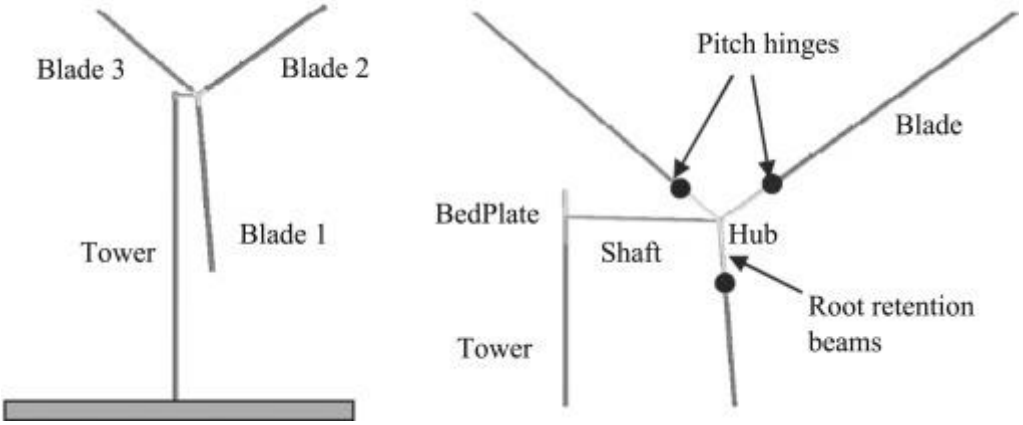

Figure 2.7: Multi-body system representation of a wind turbine [30]

A more accurate estimation of structural deformation can be obtained by discretizing the beam structure using 1D FEA [57]. In a finite element method, the structure is discretized by a number of elements, which are interconnected through nodes and the equations of motion are solved for each individual element. This is more computationally expensive than modal or MBD approaches, but is able to provide a more comprehensive description of deformation [3].

2.2.2.2 3D Finite Element Analysis

A high fidelity alternative to beam models of wind turbine blades is to use 3D finite element analysis, where the blade is discretised using shell elements that describe the composite layup of the structure. FEA is considerably more expensive than beam methods since the DoFs of the structure are not limited. However, they provide a more detailed description of the structural behaviour, and can be used to obtain information such as the stress distribution and specific load concentrations that cannot be obtained from beam models [86]. 3D FEA methods can also be used to determine accurate estimates of mode shapes in order to improve less computationally demanding modal methods. An example of blade deflection analysis using 3D FEA is shown in Figure 2.8 [87].

Faccio Júnior et al [88] compared 3D FEA with a geometrically exact beam model of a wind turbine blade, and found that whilst the beam model is capable of capturing the overall response well, it does not capture local buckling behaviour at the blade trailing edge in extreme load cases, which affects the blade bending stiffness. This highlights a limitation with the assumption of a rigid cross section used in beam models of wind turbine blades.

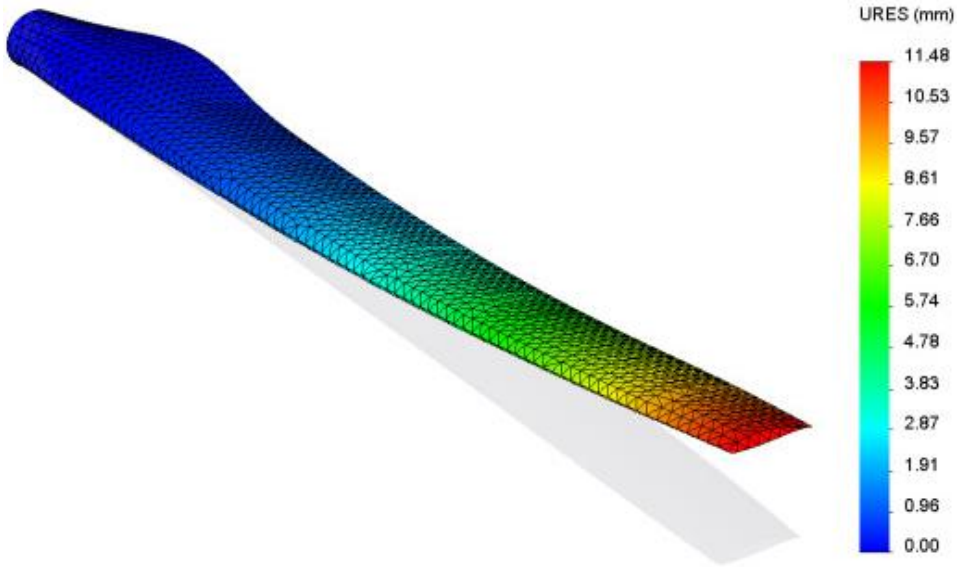

Figure 2.8: Deflection analysis of a blade using 3D FEA [87]

2.2.3 Floating Platform Motions

The hydrodynamic loads due to the ocean waves and currents excite the 6DoF floating platform modes, which strongly impact the wind turbine aerodynamic and

structural loads. Numerical models of floating wind turbines therefore must include a model of the platform motions due to these hydrodynamic loads.

2.2.3.1 Prescribed Motion Modelling

A frequent approach in CFD studies of floating offshore wind turbines is to superimpose prescribed motion to represent the floating motions rather than modelling the complex hydrodynamics of the support structure. Tran and Kim [89,90] studied the aerodynamics of a floating wind turbine by prescribing periodic pitching, yawing and surging motions using an overset grid technique to handle mesh motion. In their simulations, the wind turbine tower and rotor geometries are fully resolved. Liu et al [91] studied the impact of floating motions on FOWT aerodynamics by imposing three degrees of freedom of motion onto the turbine model. Li et al [92] presented a simpler model of a floating wind turbine represented by an unsteady actuator line model with prescribed sinusoidal pitch and surge motion.

Modelling FOWTs with prescribed platform motions reduces the complexity of the model, however this approach does not consider the two way coupling between aerodynamic loads and platform hydrodynamics. In order to achieve realistic simulation of FOWT response, the combined effect of wind and waves needs to be considered [93].

2.2.3.2 Potential Flow Methods and Morison's Equation

Many widely used codes for analysing floating wind turbine dynamics use low order models of platform hydrodynamics that are based on potential flow theory. The impact of waves on the structure is modelled using linear wave theory, and the wave-structure interaction is modelled by computing the diffraction and radiation components separately.

Due to the inviscid flow assumption, potential flow theory is not able to model the viscous drag due to flow separation. To address this, Morison's equation can be used:

$$f = C_m \Delta \mathbf{a_f} + \frac{1}{2} \rho C_d A |\mathbf{v_f}| \mathbf{v_f} \qquad (2.1)$$

Where f is the fluid force on a body, C_m and C_d are the body inertia and drag coefficients, Δ is the fluid mass displaced by the body, A is the drag area and $\mathbf{v_f}$

and $\mathbf{a_f}$ are the fluid velocity and acceleration relative to earth. Morison's equation is used to determine the inertial loads and viscous drag on a slender cylindrical body, and is frequently used to model hydrodynamic loads on bottom fixed offshore structures [9]. However, it has some limitations when applied to floating wind turbine support structures; it does not take into account wave diffraction effects, which become significant when the structure's diameter is large relative to the incident wave length, because the waves are disturbed by the presence of the structure. Therefore, a combination of potential flow theory and Morison's equation is frequently used in analysis codes, such as HydroDyn developed by NREL [94] or the SIMO code developed by MARINTEK [95].

The linear wave assumption in potential flow theory has several limitations; the waves and platform motions are assumed to be small, which makes the approach unsuitable for modelling extreme wave loading or large structural motions. It is also not able to handle nonlinear problems such as breaking waves or slamming loads on the structure. For these problems, a higher order approach may be necessary [9].

2.2.3.3 CFD Methods

In higher order models of hydrodynamics using CFD, the interaction between structure and the ocean waves and current is directly modelled by solving the Navier Stokes equations. CFD models of hydrodynamics may be a more suitable approach for problems involving extreme loads that result in large nonlinear waves and platform motions that potential flow methods are not able to handle. However, this also incurs a much higher computational cost.

CFD modelling of the fluid structure interaction for a floating platform creates various challenges such as multiphase flow due to the presence of both air and water, setting boundary conditions appropriate for modelling the free surface between the two fluids, and modelling mesh motion due to the floating platform motions [93].

2.2.4 Mooring Loads

In numerical models where the platform hydrodynamics are explicitly modelled, consideration of the mooring system dynamics is also vital in order to capture the platform stiffness and motion response. The existing approaches for modelling

the mooring system can generally be characterised as either quasi-static or dynamic models. In a quasi-static model, dynamic loads such as inertial forces and drag loads on the mooring lines are ignored. For shallow mooring systems where the total mass of the mooring system is small, the line motions are also small and the dynamic loads can be neglected. However, for mooring systems in deeper waters with a large mass, the line motions become large and a quasi-static approach is insufficient [96].

Anderson et al. [97] compare three different mooring analysis codes coupled with the wind turbine simulation tool FAST [98] for analysing a spar type model scale floating offshore wind turbine. The quasi static code MAP++ [99] and the lumped mass model used in the dynamic code MoorDyn [100] were validated against the commercial finite element software OrcaFlex. It was found that MoorDyn could predict results that were almost identical to those predicted by OrcaFlex, which has been validated extensively against real data [101]. MoorDyn has been validated for chains systems [102], and has recently been extended to include bending stiffness to allow for simulation of dynamic cable systems; validation of these capabilities is ongoing [103].

2.2.5 Full System Analysis of Floating Offshore Wind Turbines

The coupling between the aerodynamic loads on the wind turbine, hydrodynamic loads on the supporting platform and mooring loads for a FOWT is highly nonlinear and presents numerous challenges regarding predicting the power output and structural response. Development of FOWT designs therefore requires reliable models that capture the coupled dynamics [104].

FAST (Fatigue, Aerodynamics, Structures and Turbulence) [105] developed by NREL is one of the most widely used software for full system analysis of floating offshore wind turbines due to its open source nature. FAST was originally developed for modelling the dynamic behaviour of onshore and bottom fixed offshore turbines, though the capabilities of FAST have now been extended to allow for modelling of floating offshore wind turbines. Recently, FAST was renamed OpenFAST to reflect the transition to an open source software. The aerodynamics can be modelled in FAST using a blade element momentum model or, as of recently, a free vortex wake model. The structural dynamics are modelled using a combined modal analysis/MBS approach, where the blades can

be modelled using either classical Euler-Bernoulli linear beam theory with modal representation, or using nonlinear GEBT implemented through Legendre spectral finite elements [106]. The hydrodynamics are handled using potential flow model or Morison's equation, or a combination of the two [98].

FAST has a modular structure to enable handling of coupled dynamics, and many of the modules that constitute the FAST framework can also be used as standalone codes or coupled to external software. For example, Utsunomiya et al [107] use the aerodynamics module from FAST coupled with their in house hydrodynamics code and the commercial multibody dynamics code ADAMS [108], and partially validate this approach for simulating a spar type FOWT.

Various commercial codes have also been developed for floating offshore wind applications, such as Bladed, developed by DNV GL. Bladed uses a BEM model for the turbine aerodynamics with a dynamic wake model and an unsteady aerodynamics model to account for dynamic stall. Structural dynamics are calculated using a combined modal and multibody dynamics approach, where the modes of the blades and tower are computed through 1D FEA modelling using Timoshenko beams. The software capabilities have been extended to allow for modelling of floating wind turbines by including options to model hydrodynamics using Morison's equation and including a fully dynamic model of the mooring system. Alternatively, higher order hydrodynamic properties can be supplied externally.

The use of Bladed for designing a new control algorithm for a floating offshore wind turbine was demonstrated by Oh et al. [109]. Yoshimoto and Kamizawa [110] validated the use of Bladed for floating offshore wind turbine analysis against observation data from the Fukushima FORWARD floating offshore wind farm demonstration project, and showed that Bladed is capable of predicting motions of the floating turbine that show reasonable agreement with measured data.

Another widely used commercial code is HAWC2 (Horizontal Axis Wind turbine Code 2nd generation), developed by the Technical University of Denmark (DTU). In HAWC2, the structural dynamics are calculated using MBS dynamics and a 1D FEA approach for the blades, which are modelled as Timoshenko beams. Aerodynamics are modelled using a BEM method with various corrections, and

hydrodynamic loads using Morison's equation. Currently, HAWC2 does not have the capabilities to simulate mooring line dynamics, which therefore must be supplied externally. An example of the use of HAWC2 to simulate a FOWT is found in Skaare et al. [22], where HAWC2 was coupled with SIMO/RIFLEX. This is also a coupling of two codes developed by MARINTEK; the general purpose offshore structures code SIMO and the nonlinear finite element code RIFLEX, which are both distributed as modules of DNV's marine operations software SESAM [111]. Within this SIMO/RIFLEX/HAWC2 coupling, the aeroelastic response of the turbine is modelled in HAWC2, and the floating substructure and mooring lines are modelled in SIMO/RIFLEX. The coupled model was shown to be able to accurately simulate the response of an experimental scale turbine.

An example of a commercial analysis code for offshore structures that has recently been extended to enable modelling of offshore wind turbines is OrcaFlex [112,113]. OrcaFlex is an industry standard tool for dynamic analysis of offshore structures, and offers a range of modelling capabilities including a fully coupled nonlinear finite element model of the mooring lines, nonlinear analysis of floating structures including large displacement, and multibody analysis of structures. The turbine modelling capabilities in OrcaFlex include modelling aerodynamics using BEM theory with corrections, and modelling blade flexibility using beam elements that are similar to the line elements used to discretise the mooring lines. Alternatively, OrcaFlex can be coupled with FAST through the OrcaFAST coupling library [114]. The hydrodynamic modelling in this coupled approach (where the floating substructure and moorings are modelled in OrcaFlex and the turbine is modelled in FAST) has been validated against experimental data [115].

Recent advances in CFD have resulted in the development of several in-house codes for performing high fidelity full system simulations of floating wind turbines. Cheng et al [116] developed a fully coupled aero-hydrodynamic solver in OpenFOAM, FOWT-UALM-SJTU, that utilises two phase flow and RANS based turbulence modelling. The proposed solver uses an unsteady actuator line model for the turbine aerodynamics, a numerical wave tank system, and a quasi-static mooring system model. Structural flexibility in the blades and tower is not modelled. The model was shown to achieve good agreement with measured aerodynamic loads for a bottom fixed turbine and platform motions from the DeepCWind experiment. Liu [117] developed a FSI tool coupling geometry

resolved CFD with a multibody dynamics approach based on nonlinear beam theory to simulate a FOWT with flexible blades. Three degrees of freedom (surge, heave and pitch) were incorporated into this model. This work highlighted that platform motions have significant impact on the blade bending response. The inclusion of blade flexibility increased the computational cost of the model by around 60%.

One example of an open source code for modelling wind turbines using CFD is SOWFA (Simulator fOr Wind Farm Applications), developed by NREL. SOWFA is a toolbox used to perform CFD simulations of wind turbines and wakes in OpenFOAM, where the turbines are represented by actuator disk or line models. A fully coupled approach was also developed where the actuator model in SOWFA is two way coupled with FAST, so that only the aerodynamics are computed using CFD, whilst the structural response is computed by FAST. For offshore turbines, the platform hydrodynamics are calculated using a potential flow based method in FAST's hydrodynamics module, HydroDyn. SOWFA has been validated for simulations involving bottom fixed turbines [118], whilst research into the use of the code for floating offshore wind turbines is ongoing. Lee et al [119] compare a one way and two way SOWFA-FAST coupling for studying the impact of a downstream FOWT's position in a wind farm on the turbine's structural response and fatigue loading due to interacting with the wake of the upstream turbine. In the one way coupling approach, turbulent inflow data generated by SOWFA is used as input into FAST. Johlas et al [120] used a two way coupled SOWFA-FAST approach to compare the far wake characteristics for two different floating turbine platform types with a bottom fixed turbine in neutral and stable atmospheric conditions, and showed that wakes for floating wind turbines are deflected upwards more than for bottom fixed turbines, particularly in stable atmospheric conditions. Currently, there are no known comparisons between the SOWFA-FAST coupled approach and the standalone FAST approach for simulating the response of floating offshore wind turbines.

2.2.6 Experimental Data for Validation of Numerical Models

Numerical models are extremely useful for studying a wide range of designs and load cases at a much lower cost than would be incurred by physical testing.

However, in order to ensure that the accuracy of a numerical model's predictions, validation against experimental data is essential.

Several model experiments of floating offshore wind turbines have been conducted using wave tank and basin facilities. A comparison of some of these experiments was conducted by Steward and Muskulus [121] with the aim of identifying test cases that can be used to verify numerical and engineering codes. The experiments examined are most useful for studying hydrodynamics, since many of the experiments involved large simplifications in the rotor aerodynamics, or even no aerodynamics at all. An issue that was identified in this review is that public availability of experimental data for floating wind remains limited, however one experimental campaign for which the data is available is the DeepCWind project, in which a 1/50 scale model of a 5MW turbine was tested on three different model platforms; a semi-submersible, a spar buoy and a tension leg platform [122]. The experiments were performed in a wave basin at the Maritime Research Institute of the Netherlands (MARIN) test site and involved testing the model turbine in combined wind and wave loading. The results from the DeepCWind tests have been used extensively to validate numerical models of floating offshore wind turbines [123,124]. However, there were issues related to the use of Froude scaling in the experiments; due to the low Reynold's number resulting from scaling, the wind speed had to be increased to a value 80% higher than desired in order to achieve the correct aerodynamic thrust [8]. This large increase in wind speed meant that the sensitivity of the thrust force to turbulence and platform motion may not be represented correctly [126].

A recent example of an experimental investigation of FOWT aerodynamics is the UNAFLOW (UNsteady Aerodynamics of FLOating Wind turbines) experimental campaign [127], in which a 1:75 scale model of the DTU 10 MW reference wind turbine [128] was tested in a wind tunnel based at Politecnico di Milano (POLIMI). To avoid issues with the Reynolds number scaling, the model turbine featured an adjusted aerofoil profile with a lower Reynolds' number compared to the full scale reference turbine. This technique is known as performance scaling. In order to replicate the impact of waves on a floating platform, periodic surge and pitch motion was imposed onto the model turbine. The project provided valuable data on the unsteady aerodynamics of floating offshore wind turbines, including the

effect of pitching on aerofoil aerodynamics and the impact of surge motion on the full rotor response of a floating wind turbine.

A significant advantage of numerical models over experimental tests is that they are capable of modelling turbines at any scale including utility scale structures thereby avoiding similar scaling issues. Ideally, numerical models would be validated against measurements from full scale turbines, however, these are extremely limited as floating offshore wind energy is still a relatively new industry.

A number of utility scale floating offshore wind demonstration projects have been successfully carried out, such as the Hywind Scotland farm, the Goto Islands and Fukushima FORWARD projects in Japan, and the WindFLOAT projects that have been demonstrated in Portugal and Scotland. The most well-known example is the Hywind project, which involved the demonstration of a 2.3 MW spar type prototype turbine deployed off of the Norwegian coast, followed by the world's first floating wind farm consisting of five 6 MW spar type turbines deployed off the coast of Scotland in 2017 [7]. Most of the data from the conducted demonstration projects is proprietary, making validation of numerical models of full scale turbines difficult.

To address the problem of validating the codes developed for modelling floating offshore wind turbines whilst limited experimental data exists, the Offshore Code Comparison Collaboration (OC3) project was established to perform code-to-code comparisons for coupled simulations of offshore bottom fixed turbines on monopole and tripod supports, and a floating wind turbine on a spar buoy platform. This collaborative project ran from 2005 to 2009, and the results can be found in [129]. The work done in this project was extended in follow up projects;

- OC4 (Offshore Code Comparison Collaboration, Continued) focused on code comparisons for modelling a fixed jacket supported structure [130] and a semi-submersible floating wind turbine based on the DeepCwind experiments [131].
- OC5 (Offshore Code Comparison Collaboration, Continued with Correlation) focused on validation of hydrodynamic modelling by comparing code predictions against experimental data for hydrodynamic loads on cylinders and for the DeepCwind semi-submersible supported turbine [123]

- OC6 (Offshore Code Comparison Collaboration, Continued with Correlation and unCertainty) is still ongoing, though the outcomes from Phase I have been published [132], which examined the reasons for underpredicted platform response for a semi-submersible platform at the surge and pitch natural frequencies. Future phases will focus on modelling soil-structure interaction, and validating aerodynamic loading predictions when large floating structure motions are present [133].

2.3 Chapter Summary

In this chapter, an overview of some of the significant design challenges specific to floating offshore wind turbines is first provided. This includes the effect of a floating platform on turbine dynamics, the impacts of the trend of increasing turbine size and therefore flexibility, and the sensitivity of FOWT behaviour to the external environmental conditions. The challenges that these considerations present for numerical modelling are also discussed. Secondly, a range of established numerical methods used to model the different components of floating wind turbine dynamics are examined. This includes methods of modelling aerodynamics, structural dynamics, and floating platform behaviour. The progress made in developing models that consider the complex nonlinear coupling between the different dynamics is also reviewed, in addition to the efforts made to validate numerical models against experimental data.

It is noted that many of the aerodynamic models applied to wind turbines have been validated only against data for bottom fixed turbines, and require further validation against data specific to floating wind conditions. However, this is acknowledged to be currently difficult due to the lack of available physical data for FOWTs and scaling issues associated with small scale experimental studies. Therefore, there is a still lack of clarity on the extent to which turbine aerodynamic models, particularly lower fidelity models involving BEM and empirical corrections (which are still used in the majority of wind turbine codes), are capable of accurately simulating the aerodynamic loads of a FOWT that is subjected to many complex coupled dynamics.

In order to address this knowledge gap and improve confidence in numerical modelling, validation of models against available full scale data for FOWTs will

be extremely useful for considering the coupled aerodynamics and hydrodynamics without scaling issues. As relevant data remains limited at this stage, the capabilities of numerical models in FOWT applications can also be further investigated through comparative studies of low order models against higher fidelity models using CFD. This will help to quantify differences between model predictions and determine where high fidelity methods are needed in the design process and where low fidelity models are sufficient in order to reduce costs associated with numerical modelling.

Chapter 3

Numerical Background and Methodologies

This thesis features a comparison of several numerical methods of modelling the wind flow, aerodynamic loads and structural response of a floating offshore wind turbine. This chapter presents a review of the numerical methodologies that are studied in the work. Firstly, a brief introduction of the overarching modelling approaches that will be used is presented. The numerical background and implementation of the overarching methodologies is then presented, some of which was introduced in Chapter 2 and is examined further herein. This includes an overview of CFD and turbulence modelling, the details of the different applied models of the turbine loads, and the factors considered when modelling the offshore environment.

3.1 Overview of Thesis Methodology

In this work, three methods were chosen to model the aerodynamics of a floating offshore wind turbine, which are then compared in Chapters 4-6. The purpose of this approach is to understand and quantify the differences between models of different levels of fidelity, so that informed decisions on their use in the design process (taking into account accuracy and computational efficiency) can be made. The different aerodynamic modelling approaches are coupled with structural and hydrodynamic models in order to compute the load and motion response so that the coupled dynamics of a FOWT system can be analysed:

1. *Low fidelity model* – blade element momentum theory is used for rotor aerodynamics. The BEM method was chosen because of its computational efficiency, and because it is the most widely used approach for wind turbine analysis as described in the previous chapter. All turbine dynamics are simulated using FAST, where platform hydrodynamics are simulated using potential flow theory and Morison's equation, and the

turbine structural response is computed using a combined modal and multibody dynamics approach. For cases where a realistic offshore wind input is required, statistical turbulence models are used in TurbSim to generate wind fields with a predefined wind shear profile and hub height turbulence intensity. This approach is illustrated in Figure 3.1.

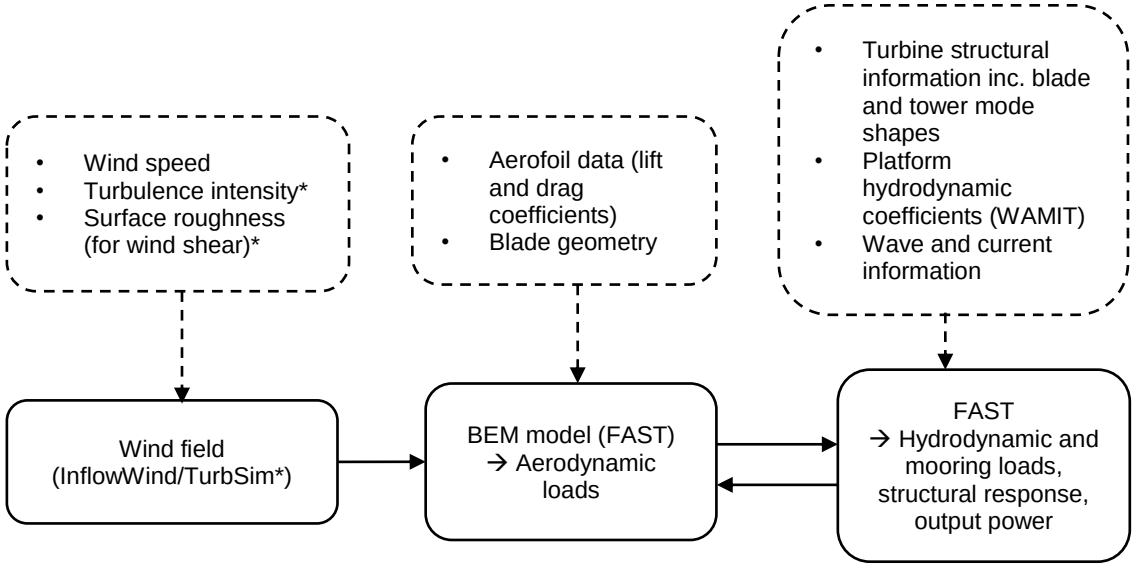

*Figure 3.1: Flowchart showing the different components and inputs of the low fidelity model. *not used in steady wind cases*

2. *Mid fidelity model* – a CFD based actuator line model from SOWFA in OpenFOAM is used for rotor aerodynamics. The ALM approach involves directly sampling the flow at the rotor, and therefore does not require many of the empirical corrections used in BEM modelling. The ALM also has several advantages over an actuator disk model, as it is able to capture 3D flow effects including the root vortex structure and vortex shedding at the blade tips, making it more suitable for modelling complex non axisymmetric flow conditions such as yaw misalignment. The ALM is two way coupled with the same structural and hydrodynamic models that are used in the low fidelity modelling approach. Realistic offshore wind inputs are generated using CFD simulations of atmospheric boundary layer flow. This approach is illustrated in Figure 3.2.

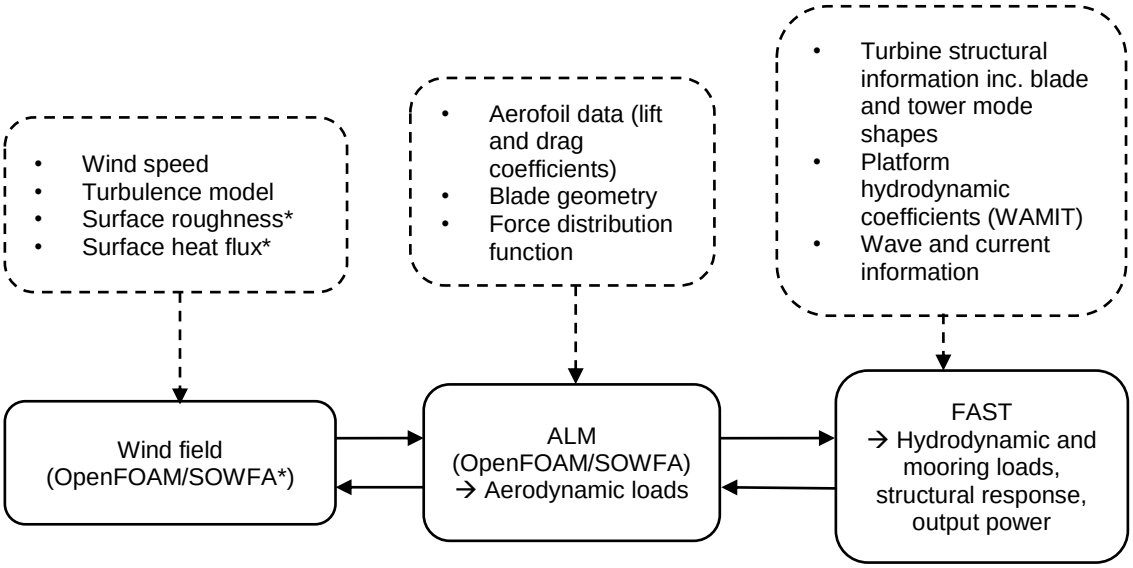

*Figure 3.2: Flowchart showing the different components and inputs of the mid fidelity model *not used in steady wind cases*

3. *High fidelity model* – the flow around the turbine blade is fully resolved using CFD simulation in OpenFOAM, which is two way coupled with a structural 3D FEA model in CalculiX. This is the most computationally expensive method available for modelling wind turbine rotor and blade dynamics, but in theory should offer the highest level of accuracy since it does not rely on assumptions such as beam behaviour and 2D flow at the rotor. This approach is illustrated in Figure 3.3.

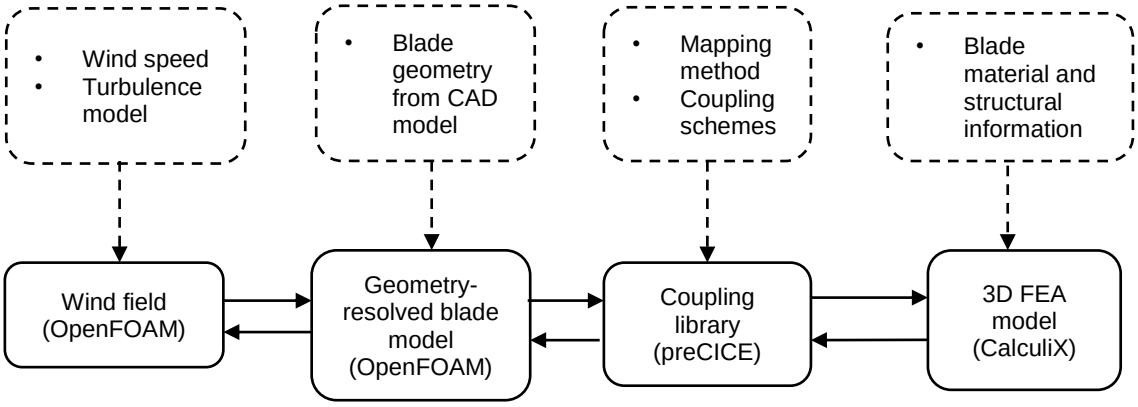

Figure 3.3: Flowchart showing the different components and inputs of the high fidelity model

3.2 Wind Flow Modelling

In this section, an overview of the methods used to model fluid flow, which in this research applies to the wind, is presented. The governing equations that form the basis of a CFD problem are presented, in addition to some of the simplifications

that are made in order to make it possible to obtain a CFD solution with available computing resources. The methods used to model realistic offshore wind are also introduced. The characteristics of atmospheric wind are examined, and an overview of the high order CFD approach and the simpler statistical models used to model the wind is given. The respective capabilities of each wind modelling approach are also described.

3.2.1 Governing Equations of Fluid Flow

All of the CFD simulations in this thesis are performed using OpenFOAM, which is an open source CFD toolbox written in C++ that is used to solve fluid flow problems using the finite volume method [66]. As an open source project, OpenFOAM is free to use and provides a framework where it is easy for the user to modify the code and implement new solvers and libraries to adapt the software to their specific requirements.

Using OpenFOAM, a solution to the Navier Stokes equations is obtained. These equations describe the fundamental physical laws of conservation of mass, momentum and energy in a fluid flow. All of the CFD problems in this work are treated as incompressible, meaning that the fluid density remains constant, and therefore the energy equation does not need to be solved. The governing equations of continuity and momentum for an incompressible fluid are as follows:

$$\nabla . \mathbf{u} = 0 \tag{3.1}$$

$$\frac{\partial \mathbf{u}}{\partial t} + \mathbf{u}\nabla . \mathbf{u} = -\frac{1}{\rho}\nabla p + \upsilon \nabla^2 \mathbf{u} + \mathbf{F} \tag{3.2}$$

where $\mathbf{u}$ is the fluid velocity vector, ρ is the density, p is the fluid pressure, υ is the kinematic viscosity and $\boldsymbol{F}$ represents additional forces acting on the fluid.

3.2.2 Turbulence Modelling

Obtaining an exact solution to the Navier-Stokes equations presented above, which is known as a Direct Numerical Simulation (DNS) approach, would require extremely fine grids in order to resolve the smallest turbulent structures in most

fluid flow problems. Most applications of CFD use numerical models to resolve all or some of the turbulence. In this work, both RANS and LES approaches to turbulence modelling are demonstrated, which are explained in this section.

3.2.2.1 RANS

The RANS modelling approach involves splitting each variable in the Navier-Stokes equations into two components; a mean and a fluctuating component. Using this approach, the instantaneous velocity $\mathbf{u}$ is written as:

$$\mathbf{u}(\mathbf{x},t) = \bar{\mathbf{u}}(\mathbf{x},t) + \mathbf{u}'(\mathbf{x},t) \tag{3.3}$$

where the mean and fluctuating components are given by $\bar{\mathbf{u}}$ and $\mathbf{u}'$ respectively. The mean value is determined through either time, spatial or ensemble averaging, depending on the nature of the flow [134]. Time averaging is most frequently used, however this approach is only suitable for time-independent turbulent flows. Spatial averaging can be used if the turbulence is homogenous, while ensemble averaging is suitable for any type of flow. Since the mean value of the fluctuating component $\overline{\mathbf{u}'} = 0$ by nature, the Reynolds averaged Navier Stokes equations are expressed:

$$\nabla . \bar{\mathbf{u}} = 0 \tag{3.4}$$

$$\frac{\partial \bar{\mathbf{u}}}{\partial t} + \nabla . \bar{\mathbf{u}}\,\bar{\mathbf{u}} + \nabla . \mathbf{R} = -\frac{1}{\rho}\nabla p + \upsilon \nabla^2 \bar{\mathbf{u}} \tag{3.5}$$

where $\mathbf{R} = \overline{\mathbf{u}'\mathbf{u}'}$ represents the Reynold's stress tensor, which describes the turbulence in the flow. This term is solved using a closure model.

Two different closure models are utilised to model turbulence in the RANS simulations presented in this work. In the RANS actuator line model simulations, where a uniform wind condition is specified and near wall flow does not need to be considered, the standard $k-\varepsilon$ closure model is used, because it is one of the most widely used and validated general-purpose turbulence models [66]. This model requires two additional transport equations for the turbulent kinetic energy k and rate of dissipation of turbulent kinetic energy ε to be solved in addition to

the Reynolds averaged Navier-Stokes equations. For incompressible flow simulations, the $k-\varepsilon$ model equations are as follows:

$$\frac{\partial k}{\partial t}+\nabla.\, k\mathbf{u}=\nabla.\left[\left(\upsilon+\frac{\upsilon_t}{\sigma_k}\right)\nabla k\right]+G-\varepsilon \tag{3.6}$$

$$\frac{\partial \varepsilon}{\partial t}+\nabla.\, \varepsilon\mathbf{u}=\nabla.\left[\left(\upsilon+\frac{\upsilon_t}{\sigma_\varepsilon}\right)\nabla \varepsilon\right]+C_{1\varepsilon}G\frac{\varepsilon}{k}-C_{2\varepsilon}\frac{\varepsilon^2}{k} \tag{3.7}$$

where υ_t is the turbulent viscosity, defined as:

$$\upsilon_t=C_\mu\frac{k^2}{\epsilon} \tag{3.8}$$

The production rate of turbulent kinetic energy G is defined as:

$$G=\upsilon_t(\nabla\mathbf{u}+\nabla\mathbf{u}^T)^2 \tag{3.9}$$

The standard values for the dimensionless model constants are provided by Launder and Sharma [135]:

$$\sigma_k=1,\qquad \sigma_\varepsilon=1.3,\qquad C_{1\varepsilon}=1.44,\qquad C_{2\varepsilon}=1.92,\qquad C_\mu=0.09 \tag{3.10}$$

The second closure model for turbulence used in this work is the Spalart-Allmaras model [136]. This model was chosen for use in geometry resolved simulations of wind turbine blades because it is designed and tuned for external aerodynamic flows. The Spalart-Allmaras model requires one additional transport equation to be solved for a kinematic eddy viscosity parameter $\tilde{\upsilon}$. For an incompressible flow, this is defined as

$$\upsilon_t=\tilde{\upsilon}f_{\upsilon 1} \tag{3.11}$$

Where $f_{\upsilon 1}=f_{\upsilon 1}(\tilde{\upsilon}/\upsilon)$ is a wall damping function. Near the wall, $\tilde{\upsilon}$ tends to zero. The transport equation for $\tilde{\upsilon}$ is defined:

$$\frac{\partial \tilde{v}}{\partial t} + \nabla . \tilde{v}\mathbf{u} = \frac{1}{\sigma}[\nabla . (v + \tilde{v})\nabla \tilde{v} + C_{b2}(\nabla \tilde{v})^2] + C_{b1}\tilde{v}\widetilde{\Omega} - C_{w1}\left(\frac{\tilde{v}}{\kappa y}\right) f_w \quad (3.12)$$

where the local mean vorticity $\widetilde{\Omega}$ is defined:

$$\widetilde{\Omega} = \mathbf{\Omega} + \frac{\tilde{v}}{(\kappa y)^2} f_{v2} \quad (3.13)$$

where $\mathbf{\Omega}$ is the mean vorticity tensor, $f_w = f_w(\tilde{v}/\widetilde{\Omega}(\kappa y)^2)$ and $f_{v2} = f_{v2}(\tilde{v}/v)$ are further wall damping functions, and y is the distance from the wall. The model constants have the following values [66]:

$$\sigma = 0.6667, \qquad \kappa = 0.4187, \qquad C_{b1} = 0.1355, \qquad C_{b2} = 0.622 \quad (3.14)$$

$$C_{w1} = C_{b1} + \frac{\kappa^2(1 + C_{b2})}{\sigma}$$

3.2.2.2 LES

In a LES approach, a spatially filtered form of the Navier-Stokes equations is used, where the velocity is decomposed into a resolved component and a residual sub grid scale (SGS) component. This allows for large scale turbulent structures to be resolved, whilst turbulent eddies that are smaller than the filter size are modelled using a closure model, referred to as an SGS model. The main argument for the LES approach is based on theory first proposed by Kolmogorov [137]; that the large scale turbulent structures contain most of the turbulent kinetic energy, whilst the small scale eddies act mainly to drain energy from the larger eddies through cascading and have a near universal form, and so can be reasonably approximated using a model. The size of the filter, and therefore the size of turbulent structures that can be resolved, is determined by the size of the grid cells in the mesh. It is recommended that the grid resolution is high enough that 80% of the turbulent energy is resolved [138]. LES is generally at least one order of magnitude more computationally expensive than RANS [139]. The spatially filtered incompressible Navier Stokes equations are defined:

$$\nabla . \overline{\mathbf{u}} = 0 \quad (3.15)$$

$$\frac{\partial \overline{\mathbf{u}}}{\partial t} + \nabla . \overline{\mathbf{u}}\,\overline{\mathbf{u}} + \nabla . \boldsymbol{\tau} = -\frac{1}{\rho}\nabla p + \upsilon \nabla^2 \overline{\mathbf{u}} \tag{3.16}$$

These take on the same form as the Reynolds averaged equations 3.4 and 3.5, except that $\overline{\mathbf{u}}$ is spatially filtered velocity rather than time averaged, and the sub grid scale turbulence is represented by the residual or sub grid scale stress tensor $\boldsymbol{\tau} = \overline{\mathbf{u}\mathbf{u}} - \overline{\mathbf{u}}\,\overline{\mathbf{u}}$. In the LES simulations presented in this work, the sub grid scale turbulence is modelled using a one-equation eddy viscosity that is specifically suited to turbulent atmospheric flows due to the inclusion of buoyancy effects, which is explained in the following subsection.

3.2.3 SOWFA Model of Atmospheric Boundary Layer Wind

For simulations in OpenFOAM where the turbulent characteristics of the wind are of interest, the atmospheric boundary layer is modelled using a high fidelity LES approach in SOWFA [140]. As described in section 2.2.5, SOWFA is a toolbox developed by NREL for analysing wind farms in OpenFOAM. The wind profile in the ABL is modelled using Monin-Obukhov similarity theory [141], where the level of wind shear is driven by the stability condition of the ABL and the surface roughness height parameter z_0, which is determined by the geometric features of the surface. The vertical wind profile within the boundary layer is described:

$$U(z) = \frac{u_*}{\kappa}\left[\ln\left(\frac{z}{z_0}\right) - \psi\left(\frac{z}{L}\right)\right] \tag{3.17}$$

where $U(z)$ is the wind velocity at height z, u_* is the friction velocity and κ is the von Karman constant, typically 0.4. $\psi(z/L)$ is an empirical thermal stratification function, where the Monin-Obukhov length parameter L is defined:

$$L = \frac{-u_*^3 \theta_0}{\kappa g Q_o} \tag{3.18}$$

where θ_0 is a reference potential temperature, g is acceleration due to gravity, and Q_o is the surface heat flux. L is positive in stable conditions, negative in unstable conditions, and tends towards infinity for neutral conditions due to zero heat flux at the surface.

The atmospheric boundary layer solver *ABLSolver* within the SOWFA framework is used for simulations of ABL wind. This is an incompressible solver that models buoyancy effects due to temperature distribution using a Boussinesq approximation. The theory behind the Boussinesq approximation is that changes in fluid density are due to thermal rather than pressure effects [142]. Using the Boussinesq approximation, variation in the fluid density is ignored in the Navier-Stokes equations for mass and momentum except for the buoyancy force term. *ABLSolver* uses the Pressure-Implicit Splitting Operation (PISO) algorithm [143] to solve the pressure and momentum equations, and uses Rhie-Chow interpolation [144] to avoid pressure-velocity decoupling. The momentum equation becomes:

$$\frac{\partial \overline{\mathbf{u}}}{\partial t} + \nabla . \overline{\mathbf{u}}\,\overline{\mathbf{u}} = -2\epsilon_{i3k}\bar{u}_k\omega\sin\phi - \nabla\tilde{p} - \frac{1}{\rho_0}\nabla p_0 - \nabla . \boldsymbol{\tau} - gz\nabla\left(\frac{\rho_k}{\rho_0}\right) + \frac{1}{\rho_0}F_i^T \tag{3.19}$$

The term $-2\epsilon_{i3k}\bar{u}_k\omega\sin\phi$ is the Coriolis force due to planetary rotation, where ω is the planetary rotational speed and ϕ is the latitude (ϵ_{ijk} is the alternating tensor). $\tilde{p}$ is a modified pressure variable, which represents the deviation in static (density-normalized) pressure from the horizontally averaged value. The term $gz\nabla\left(\frac{\rho_k}{\rho_0}\right)$ represents buoyancy forces using the Boussinesq approximation, where g is acceleration due to gravity. F^T represents additional forces, which in this case includes forces due to the actuator line model representing the turbine.

Fluid density in the buoyancy term is expressed as a function of potential temperature, where the ratio of buoyant density ρ_k to constant density ρ_0 is:

$$\frac{\rho_k}{\rho_0} = 1 - \frac{\bar{\theta} - \theta_0}{\theta_0} \tag{3.20}$$

where $\bar{\theta}$ is the resolved potential temperature. A transport equation for potential temperature is included in the ABL solver as follows:

$$\frac{\partial \bar{\theta}}{\partial t} + \nabla . (\overline{\mathbf{u}} \bar{\theta}) = -\nabla . q \tag{3.21}$$

where q is the temperature flux due to viscous and sub grid scale effects.

SOWFA uses a potential temperature model to account for atmospheric stability in the boundary layer. A negative, zero or positive vertical gradient of the potential temperature corresponds to unstable, neutral or stable stratification respectively. At the sea surface boundary, a surface shear stress model defined by Schumann [145] is used:

$$\frac{\tau}{\langle \tau \rangle} = \frac{\left| \overline{U}_{z1} \right|}{\langle \overline{U}_{z1} \rangle} \tag{3.22}$$

where $\overline{U}_{z1}$ is the resolved velocity vector at the cell centre closest to the wall and $\langle\ \rangle$ denotes horizontal averaging. A model for the temperature flux at the surface is also defined:

$$q_j = -\frac{\upsilon^{SGS}}{Pr_t} \frac{\partial \bar{\theta}}{\partial x_j} \tag{3.23}$$

where Pr_t is the turbulent Prandtl number. Pr_t is taken to be equal to 1/3 for unstable and neutral conditions, and is equal to 1 for stable conditions.

The height of the ABL is controlled by specifying a capping inversion layer. This inversion layer has strong stable stratification, with a linearly increasing temperature with height, and acts to slow boundary layer growth. For unstable conditions, the capping inversion is specified at a height of over 1 km, whilst in stable conditions the ABL height is capped at a few hundred meters [31].

The Schumann model and temperature flux model are used to account for sub grid scale and viscous stresses. The value of temperature flux at the surface controls the stability of the boundary layer and the level of turbulence, where a negative, zero or positive value of the z component of q_j corresponds to unstable, neutral or stable conditions respectively. The solver estimates friction velocity according to the Monin-Obukhov similarity theory based on the flow profile near

the surface, the surface roughness height and heat flux. The upper boundary of the fluid domain is located in the region above the ABL, and stress and temperature flux are set to zero. The sub grid scale turbulence is modelled using a one-equation eddy viscosity model developed by Deardorff [146] and Moeng [147]. The transport equation for sub grid scale kinetic energy k_{sgs} is defined:

$$\frac{\partial k_{sgs}}{\partial t} + \bar{u}_i \frac{\partial k_{sgs}}{\partial x_i} = -\tau_{ij}.S_{ij} - C_\varepsilon \frac{k_{sgs}^{\frac{3}{2}}}{\Delta} + \frac{\partial}{\partial x_i}\left(2\upsilon_t \frac{\partial k_{sgs}}{\partial x_i}\right) + \frac{g}{\theta_0}\overline{w'\theta'} \quad (3.24)$$

where w represents the vertical velocity, $S_{ij} = \frac{1}{2}(\frac{\partial \bar{u}_i}{\partial x_j} + \frac{\partial \bar{u}_j}{\partial x_i})$ is the resolved scale rate of strain tensor, Δ is the filter length scale, and $\upsilon_t = C_k\sqrt{k_{sgs}}\Delta$ is the turbulent eddy viscosity. The effects of buoyancy on turbulence production are represented by the $\frac{g}{\theta_0}\overline{w'\theta'}$ term. The constants are given the values $C_k = 0.0673$ and $C_\varepsilon = 0.93$.

In order to generate atmospheric turbulence for the turbine simulations using LES, precursor simulations are first run on a periodic domain to allow continual cycling of the flow back into the domain. This can be done on a coarse grid without any turbines present. Once the desired turbulence has been generated and the flow has stabilised, the precursor simulation is run for an additional period of time during which the flow profiles at the inlet are saved at regular intervals. These flow profiles are subsequently used as a library of time varying inlet conditions in the turbine simulations.

3.2.4 Sea Surface Roughness

Equation 3.17 shows that the wind profile is dependent on the surface roughness height parameter z_0. This parameter also drives the level of turbulence in the wind [148].The roughness of the sea surface is typically much lower than that of the ground, and recommended values of z_0 for a flat sea are typically between 0.0001 and 0.001 m [149]. However, the sea surface roughness is dependent on the wave conditions which in turn are dependent on the wind speed. This relationship can be expressed using the Charnock assumption [150], where the sea surface roughness is defined relative to the friction velocity u_*:

$$z_0 = \frac{\alpha u_*^2}{g} \tag{3.25}$$

where g is the acceleration due to gravity and α is an empirical constant known as the Charnock parameter. There have been many definitions proposed for estimating the friction velocity in the literature, some of which are reviewed by Weber [151], who suggests that a more accurate estimation of the friction velocity can be obtained using the Reynolds stress vector, however this information is difficult to obtain. For the simulations in this work where the desired turbulence intensity is known, the friction velocity is estimated for each simulation in this work using the following relationship given by Stull [149] based on the standard deviation σ of the wind speed.

$$\sigma^2 = 6.25 u_*^2 \tag{3.26}$$

3.2.5 Statistical Modelling of Turbulence

In the low fidelity modelling where CFD is not used, inflow turbulence is generated in TurbSim [152], which is an inflow turbulence code used for generating full field simulations of turbulent flow using statistical methods. Using TurbSim, turbulence is defined using the Kaimal model specified by the IEC standard for wind turbine design [35]. The Kaimal spectra for the three components $K = u, v, w$ of the wind velocity are defined:

$$S_K(f) = \frac{4\sigma_K^2 L_K / \bar{u}_{hub}}{(1 + \frac{6 f L_K}{\bar{u}_{hub}})^{5/3}} \tag{3.27}$$

where f is the cyclic frequency, σ is the standard deviation, $\bar{u}_{hub}$ is the mean wind speed at hub beight, and L is an integral scale parameter. The model does not include any temperature effects and therefore assumes neutral atmospheric stability, which limits its ability to accurately model realistic atmospheric boundary layer flow since the scale of turbulent structures is dependent on the atmospheric stability condition [153]. This may have an impact on the predicted loading on

FOWTs due to turbulence, particularly in low wind speeds where strongly stable and unstable conditions are more likely to occur in offshore environments [33].

3.3 Turbine Aerodynamic Load Modelling

In this work, three approaches are chosen from those introduced in Chapter 2 to model the aerodynamic loading on wind turbine blades. These include two approximations of the rotor, namely a BEM model and an ALM, which are described in more detail in this section. The implementation of the blade resolved CFD method used in the high fidelity approach, where the wind flow around the wind turbine geometry is resolved explicitly, is described in section 3.5.

3.3.1 Blade Element Momentum Model

The low order modelling of the rotor aerodynamics in this work is based on the blade element momentum theory, which is implemented in FAST's aerodynamics module AeroDyn [49]. The BEM method combines simple momentum theory with blade element theory in order to take into account the effect of blade geometry on the local lift and drag forces.

In the momentum theory, the forces acting on the rotor are expressed as a momentum deficit due to the rotor disk extracting energy from the flow passing through it. The thrust and torque forces acting on a radial element of the rotor are expressed as:

$$dT = 4\pi\rho U_{\infty}^{2} a(1-a) r dr \tag{3.28}$$

$$dQ = 4\pi\rho U_{\infty}\, \Omega a'(1-a) r^{3} dr \tag{3.29}$$

where U_{∞} is the free stream velocity, Ω is the blade rotational velocity, and a and a' are the axial and tangential induction factors respectively, defined as:

$$a = 1 - \frac{V_t}{U_\infty} \tag{3.30}$$

$$a' = \frac{\omega}{2\Omega} \tag{3.31}$$

where V_t is the wind velocity at the turbine and ω is the wake rotational speed. The relative airflow velocity and inflow angle at the blade element is therefore defined:

$$V_{rel}^2 = (U_\infty(1-a))^2 + (\Omega r(1+a'))^2 \tag{3.32}$$

$$tan\phi = \frac{U_\infty(1-a)}{\Omega r(1+a')} \tag{3.33}$$

This is illustrated in Figure 3.4. Blade element theory involves calculating the axial thrust force and rotational torque force on each radial section of the rotor (blade element) using the blade geometry characteristics including the 2D aerofoil characteristics and the local angle of attack, where $\alpha = \phi - \beta$ (ϕ and β are the flow angle and blade pitch angle respectively):

$$dT = \frac{1}{2}Bc\rho V_{rel}^2 C_n dr, \qquad C_n = C_L cos\phi + C_D sin\phi \tag{3.34}$$

$$dQ = \frac{1}{2}Bc\rho V_{rel}^2 C_t r dr, \qquad C_t = C_L sin\phi - C_D cos\phi \tag{3.35}$$

where C_n and C_t are the normal and tangential force coefficients respectively, C_L and C_D are the lift and drag coefficients, B is the number of rotor blades, c is the local chord length, ρ is the air density and V_{rel} is the resultant relative airflow velocity through the turbine based on the axial wind velocity and tangential velocity. The radial component of the velocity is assumed to be zero.

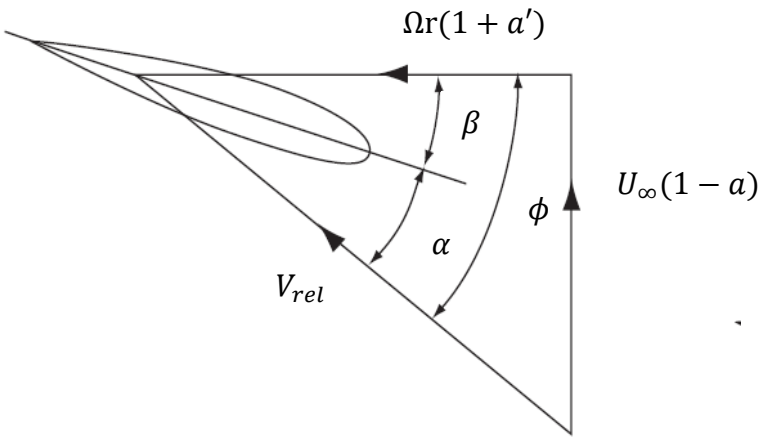

Figure 3.4: Axial and tangential components of the velocity at the rotor

In blade element momentum theory, the equations for momentum theory and blade element theory are combined to form the following expressions for the axial and tangential induction factors:

$$\frac{a}{1-a} = \frac{\sigma C_n}{4sin^2\phi} \tag{3.36}$$

$$\frac{a'}{1-a'} = \frac{\sigma C_t}{4sin\phi cos\phi} \tag{3.37}$$

where the local solidity $\sigma = Bc/2\pi r$. These equations are then solved iteratively and the torque and thrust elements at each radial station are calculated. The total power and thrust are then calculated, where the rotor power $P = \Omega Q$.

A major limitation of BEM theory is that it assumes the flow to be two dimensional, meaning it is not inherently able to account for 3D flow effects such as skewed wake due to yaw misalignment or losses due to vortices formed at the blade tip and root [50]. To account for these blade tip and root losses, the Prandtl correction factor [154] is added:

$$F_{tip} = \frac{2}{\pi}\arccos\left(e^{-\frac{B(R-r)}{2Rsin\phi}}\right) \tag{3.38}$$

$$F_{root} = \frac{2}{\pi}\arccos\left(e^{-\frac{B(r-R_{hub})}{2Rsin\phi}}\right) \tag{3.39}$$

In the presented FAST simulations, an empirical skewed wake correction model developed by Pitt and Peters is used to account for the effects of misaligned flow [155]. This correction is applied to the axial induction factor a after the BEM iteration procedure described by equations 3.36 and 3.37:

$$a_{yaw} = a[1 + k\tan\frac{\chi}{2}\frac{r}{R}\sin\psi] \tag{3.40}$$

where χ is the skew angle of the wake, ψ is the azimuth angle and k is a constant usually defined as $15\pi/32$ [156].

To account for the effects of dynamic stall, a semi-empirical unsteady aerofoil aerodynamics model based on the work of Leishman and Beddoes [54] is used, with modifications and simplifications defined by Minnema [157] and Pierce [158]. The implementation of this model in AeroDyn is described in detail in Damiani and Hayman (2019) [159].

The standard BEM method is quasi-steady, and so in order to account for the delay in the response of the rotor to changes in the inflow and loading, a dynamic wake model is used. The dynamic model of Øye is used, which is described in Snel and Schepers (1995) [156]. This is necessary for a floating wind turbine where the aerodynamics are inherently unsteady due to the motions of the floating platform [34].

3.3.2 Actuator Line Model

In the mid fidelity approach, the wind turbine is modelled using an actuator line model in SOWFA, which is a more sophisticated form of the traditional actuator disk model. Instead of representing the turbine rotor as an axisymmetric disk, each blade is distinctly modelled by a series of points distributed along a line representing the blade axis, and the blades are rotated each time-step.

The force f at each point along the actuator line is calculated using the blade element method as follows.

$$f = \frac{dF}{dr} = \frac{1}{2}\rho c V_{rel}^2 (C_L \boldsymbol{e_L} + C_D \boldsymbol{e_D}) \tag{3.41}$$

where $\boldsymbol{e_L}$ and $\boldsymbol{e_D}$ are unit vectors in the lift and drag force directions respectively. The lift and drag coefficients, C_L and C_D, for the relevant aerofoils are provided in tables as functions of the local angle of attack.

To avoid numerical instabilities caused by singularities, the forces calculated at each actuator point are distributed onto the fluid using a Gaussian projection function η_ϵ.

$$\eta_\epsilon(r) = \frac{1}{\epsilon^3 \pi^{3/2}} \exp\left[-\left(\frac{r}{\epsilon}\right)^2\right] \tag{3.42}$$

r is the distance between the actuator point and the cell centre and ϵ is the Gaussian width parameter that controls the width of the force projection. The velocity at the actuator point is determined by sampling the velocity using an integral of the local velocity field and the body force distribution function η_ϵ.

In the ALM from SOWFA used in this work, the turbine tower and nacelle are also modelled using drag-only actuator line representation. The tower is modelled as an additional actuator line with a circular aerofoil profile, and the computed drag force from each actuator element is distributed onto the fluid so that the force is radially constant up to a given value (the radius of the tower), and then decays beyond this radius according to a Gaussian projection function similar to that defined for the blades. As a result, the distributed force on the fluid due to the tower represents a cylinder. Similarly, the nacelle is represented by an additional actuator line from the front to the rear of the nacelle. The total drag force is determined by the area of the front of the nacelle and a user specified drag coefficient, and is distributed using the same cylindrical projection function as for the tower. Each nacelle actuator point projects an equal amount of drag force onto the fluid.

3.4 Coupled Modelling in FAST

A number of codes coupling turbine aerodynamics with structural dynamics and platform hydrodynamics have been introduced to address the problem of analysing the highly nonlinear behaviour of a floating offshore wind turbine [95], some of which are described in Chapter 2. Of these tools, one of the most widely used is FAST, a publicly available software developed by the National Renewable Energy Laboratory (NREL) [105]. FAST is a multi-physics engineering tool that is used to perform coupled aero-hydro-servo-elastic simulations of wind turbines in the time domain. In this thesis, the name FAST will be used to refer to OpenFAST, which is the open source version of the code. FAST was chosen for this project due to its open source nature, and the extensive validation that has been conducted [123,160,161].

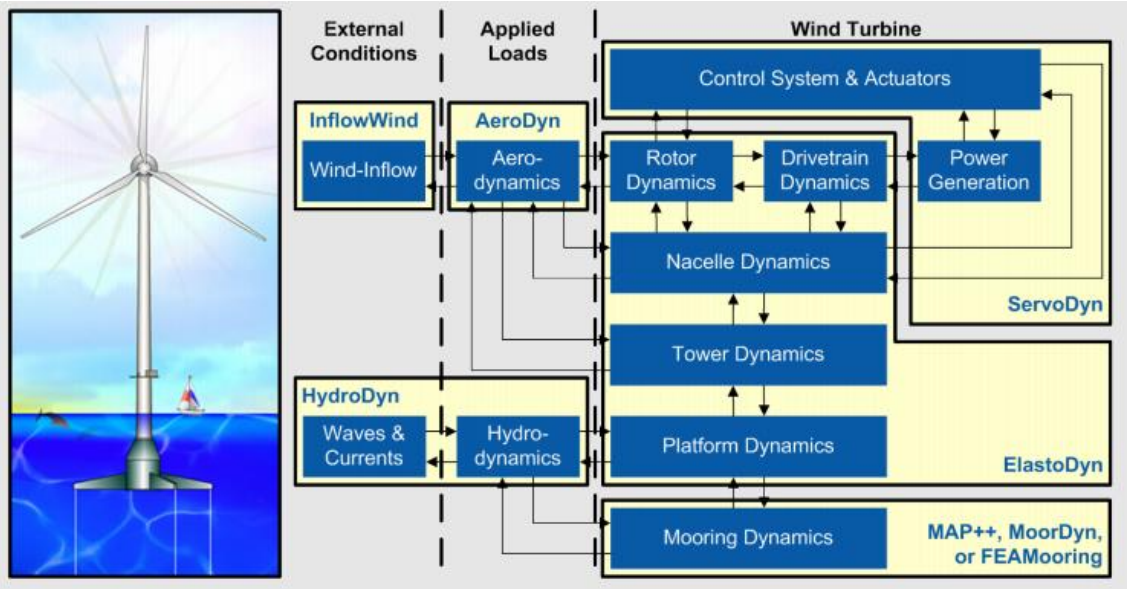

Figure 3.5: Interaction between different modules in FAST, from [162]

The coupled dynamics of a wind turbine in FAST are handled by using a modularization framework, with different modules developed to handle the aerodynamics, structural dynamics, hydrodynamics, control system properties and mooring loads. This framework and the coupling between modules is illustrated in Figure 3.5 [162]. In the low fidelity modelling approach used in this work, the wind input is defined and configured for input in FAST in the module InflowWind, which is able to read wind field files generated in external codes such as TurbSim or Bladed. The aerodynamic loads on the rotor and tower in response to the wind input are handled by the module AeroDyn. For offshore structures,

the hydrodynamic loads are calculated using the module HydroDyn, and mooring line dynamics are modelled using MoorDyn [100]. The turbine's structural response to the aerodynamic and hydrodynamic loads are computed in ElastoDyn, and the control system and electrical dynamics are computed by ServoDyn.

3.4.1 Structural Modelling

The structural model in ElastoDyn is one way coupled with the BEM method in the low fidelity approach (the BEM model in AeroDyn does not take into account structural deformation) and is two way coupled with the ALM in the mid fidelity approach. Structural flexibility is considered in the rotor blades, tower and drive shaft. All other components of the turbine are modelled as rigid structures, including the floating platform (except for the mooring lines, whose dynamics are considered in a separate module of FAST as described in section 3.4.2).

A combined modal and multibody dynamics approach is used, where modal analysis is applied to the blades and tower, and the multibody dynamics approach is applied to all other components. The blades are modelled with two flapwise bending mode DoFs, and one edgewise bending mode. The tower is modelled with two fore-aft and two side-to-side bending mode DOFs. The mode shapes are specified as 6^{th} order polynomials, which must be supplied externally from modal tests or finite element analysis.

The blades and tower are modelled as 1D beams using classical Euler-Bernoulli beam theory, which is valid for small to moderate deflections due to the small angle approximation (where $\cos\theta \approx 1$ and $\sin\theta \approx \theta$) with a nonlinear correction for orthogonality. No shear, torsion or extension DoFs are considered in the modelling of the tower and blades. The model is therefore best suited to straight, isotropic structures without mass or elastic offsets [84].

3.4.2 Wave and Hydrodynamic Modelling

The presented work focuses on floating wind turbines with spar platforms, which have simple cylindrical structures and catenary mooring systems. The feasibility of spar type FOWTs has been demonstrated in projects such as Hywind [163], and a recent review of the current technologies available for floating offshore wind

turbine support structures concluded that the spar concept is the most mature and has the highest 'technology readiness level' [15]. Due to the relatively small waterplane area of spar platforms, the impact of current loading on platform motion response is likely to be small [164].

The hydrodynamic loads on the floating platform due to waves and current are modelled in HydroDyn based on potential flow theory. To account for viscous drag due to flow separation, the relative form of Morison's equation is used.

The hydrodynamic loads are calculated on the structure based on added mass and damping due to linear wave radiation, incident wave excitation due to wave diffraction, and hydrostatic restoring. The hydrodynamic coefficients required to obtain a potential flow solution in HydroDyn are supplied externally by WAMIT [165], a commercial 3D panel method code that solves Laplace's equation in the frequency domain for a rigid body. The simulated waves and hydrodynamic forces are limited to first order calculations throughout this work in order to reduce computational expense. A small angle approximation is also applied to the calculated floating platform rotations.

Wave kinematics are modelled using linear Airy wave theory. Irregular waves are modelled using the JONSWAP (Joint North Sea Wave Project) spectrum [166], which is defined:

$$S(f) = 0.3125C(\gamma)\frac{H_s^2 f_p^4}{f^5}\exp\left[-\frac{5}{4}\left(\frac{f_p}{f}\right)^4\right]\gamma^{\exp\left[-\frac{(f-f_p)^2}{2\sigma^2 f_p^2}\right]} \quad (3.43)$$

where H_s is the significant wave height, f is the wave frequency, f_p is the peak frequency, σ is the spectral width parameter γ is the peak shape parameter, and $C(\gamma) = 1 - 0.287\ln(\gamma)$ is a normalizing factor. Recommended values for σ and γ are given in Annex B of the IEC standard for offshore wind turbine design [43].

Mooring line dynamics are modelled using MoorDyn, which uses a lumped mass approach that models each mooring line as a discrete number of concentrated masses connected by massless line segments. The MoorDyn model takes into account internal axial stiffness and damping forces, weight, buoyancy, hydrodynamic forces from Morison's equation and contact forces from the seabed on the line segments.

HydroDyn and MoorDyn are used to model the additional dynamics due to the floating platform in both the low and mid fidelity modelling approaches in this work, since they have been validated for floating offshore wind turbine analysis [97,167,168], and implementing a model with higher order hydrodynamics in OpenFOAM would be very expensive.

3.4.3 SOWFA-FAST coupling

The actuator model classes in SOWFA can be used in isolation to model wind turbines as rigid structures only, with no deformation of the tower and blades and no additional dynamics due to a floating platform. In the mid fidelity modelling performed in this project using SOWFA, the motions due to the floating platform are handled by using an implementation of the actuator line model that is two-way coupled with FAST, so that hydrodynamic loads can be calculated using HydroDyn. This two way coupling approach is detailed in Figure 3.6 [169]. The ALM coupled with FAST is implemented through a unique turbine model class provided in the SOWFA toolbox. In simulations using this coupling, OpenFOAM replaces InflowWind and the aerodynamic loading is calculated in SOWFA instead of AeroDyn. Each timestep, the actuator line model samples the inflow from the OpenFOAM domain at the location of the rotor, and feeds this information into FAST which computes the structural response. FAST then feeds this information back into OpenFOAM which updates the location and deformation of the turbine accordingly. The advantage of this approach is that mesh motion is not required in order to represent the flexible turbine components and the motions of the floating platform, which significantly reduces the computational cost.

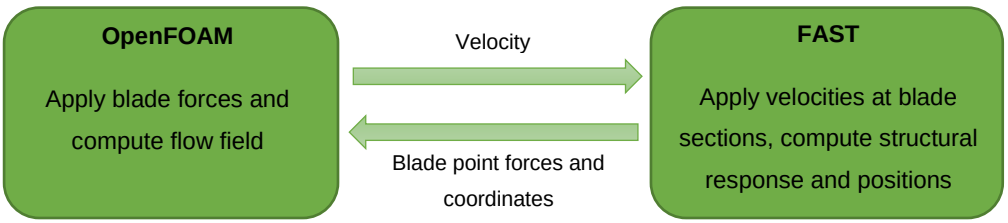

Figure 3.6: Two way coupling method between SOWFA and FAST, adapted from [169]

3.5 High Fidelity FSI Modelling

The most advanced modelling in this work involves fully resolving the fluid flow around the blade geometry using CFD, and computing the structural response using 3D finite element analysis. The implementation of this coupled model is described in this section.

3.5.1 CalculiX

The behaviour of the structure in response to the forces exerted by the fluid flow is calculated using the open source three-dimensional finite element code CalculiX [170]. The code is used to produce static, dynamic or thermal solutions to field problems involving structural mechanics or thermodynamics, and is capable of performing linear and nonlinear analysis. CalculiX was chosen because of its open source nature, and due to the existence of an adapter for the code coupling library preCICE (described in section 3.5.3). Information on the theory behind the finite element method in CalculiX can be found in Dhondt (2004) [171].

3.5.2 Geometry Resolved Modelling in OpenFOAM

3.5.2.1 Generation of Body-Fitted Mesh

To resolve the flow around the structure's geometry, a body-fitted mesh is generated using the tool *snappyHexMesh.* This requires a background hexahedral mesh and a geometry file (in STL format) describing the structure's surface as inputs. The *snappyHexMesh* algorithm generates a mesh of the geometry by refining the cells in the background mesh that intersect the geometry and aligning the cell edges with the geometry's surface by 'snapping' the grid points onto the surface. The quality of the surface mesh is improved by specifying additional refinement to capture feature edges and curvature, and adding layers of cells around the surface to define a boundary layer.

3.5.2.2 Mesh Motion

In order to account for the effect of the solid structure's deformation on the surrounding fluid flow, the fluid mesh will experience some level of deformation in each time window. The dynamic mesh motion is handled using OpenFOAM's

displacementLaplacian motion solver. The deformation of the structure boundary is given by the coupling with CalculiX, and the mesh motion solver calculates the motion of the surrounding cells by solving Laplace's equation for the cell displacement and diffusivity. The solver requires additional boundary conditions for the point displacement to be defined. For the presented simulations, quadratic inverse distance diffusion is defined, meaning that the diffusivity in Laplace's equation for any point in the mesh is inversely proportional to the squared distance of the point from the moving boundary.

3.5.3 preCICE

The coupling between OpenFOAM and CalculiX in the high fidelity modelling is handled using preCICE (**pre**cise **C**ode **I**nteraction **C**oupling **E**nvironment) [172], a library of functions to enable multi-physics coupled simulations. The main functions provided by the preCICE library are:

- Coupling schemes and acceleration methods for iterative coupling
- Mapping methods for interpolating data between the grids provided for each solver
- Communication between parallel processes

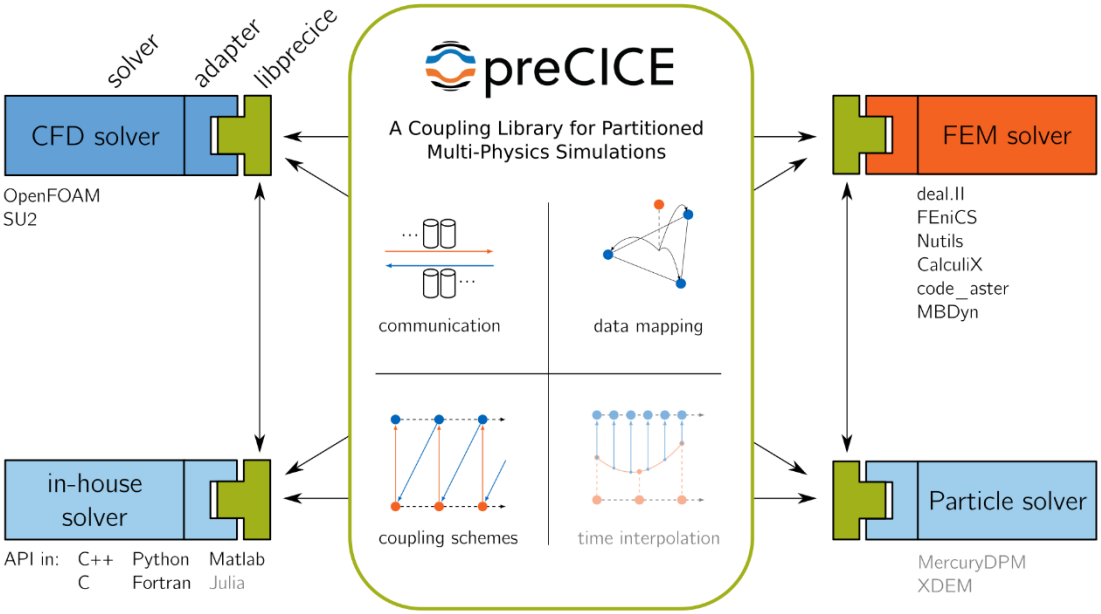

Figure 3.7: Coupling between different codes using preCICE, from [173]

preCICE is integrated with the solver codes to be coupled using glue codes referred to as adapters, as illustrated in Figure 3.7 [173]. The adapters used for

OpenFOAM and CalculiX in this work are the official adapters made publicly available by the preCICE developers [174]. The official preCICE adapter for CalculiX was originally developed by Cheung Yau [175] for conjugate-heat transfer (CHT) problems, and extended for use in FSI problems [174]. The fluid flow around the structure is solved in OpenFOAM using a preCICE adapter developed by Chourdakis [176].

The coupling between solvers can be either serial or parallel, and either implicit or explicit. Parallel coupling means that both solvers are executed simultaneously, whilst a serial coupling scheme means they are executed in turn. In implicit coupling, each solver is executed multiple times for each timestep until the convergence criteria are satisfied, whilst each solver is executed only once in explicit coupling.

For the mapping of data between different grids, preCICE provides three options for the mapping method; nearest neighbour, nearest projection, and radial basis function (RBF) mapping. Nearest neighbour mapping is first order accurate, whilst nearest projection and RBF mapping are second order accurate. Mapping between solvers can have either a consistent or conservative constraint. In consistent mapping, the mapped value at a node is the same as the value at the corresponding node in the other grid, regardless of the difference in grid resolution. This method is used for normalized quantities, such as displacement. In conservative mapping, the number of nodes in each mesh is taken into account, so that the total value of the quantity for the whole interface is conserved. This method is used for mapping absolute quantities such as force.

3.6 Chapter Summary

In this chapter, the numerical methods to be studied and compared for analysis of floating wind turbines are presented. The methodologies covered in this chapter describe the approaches that will be used to model the wind input, aerodynamic loads, structural response and hydrodynamic loads of FOWTs with spar platforms. The computational tools used to implement these methodologies are also introduced. The described methodologies form the basis of the work presented in Chapters 4-6.

Chapter 4

Comparison of an Actuator Line Model with Blade Element Momentum Theory in Uniform Wind

4.1 Introduction

In this chapter, an actuator line model of a wind turbine is defined and validated against experimental data. This chapter then investigates some of the known limitations associated with BEM theory applied to floating wind turbines. Predictions from the BEM method are compared with those from the actuator line model considering a range of simplified load cases covering those that have specific challenges for FOWTs or where the BEM method has known limitations. This includes the effects of platform motions due to waves, yaw misalignment, and misalignment between the wind and waves. This chapter aims to quantify the discrepancies between BEM and actuator line model predictions of floating wind turbine rotor loads where the wind input is identical for both models. The results of this chapter will indicate where the BEM model in tools such as FAST captures FOWT behaviour well and where a higher order model such as an ALM may be more appropriate choice in the design process, so that informed recommendations for the use of each model can be made.

4.2 Investigation of Actuator Line Model Parameters for Coupled SOWFA-FAST Model

In the OpenFOAM simulations, the turbine is represented using the actuator line model approach from SOWFA, which is described in section 3.3.2. The turbine blades are represented by a series of points along a line, and aerodynamic forces

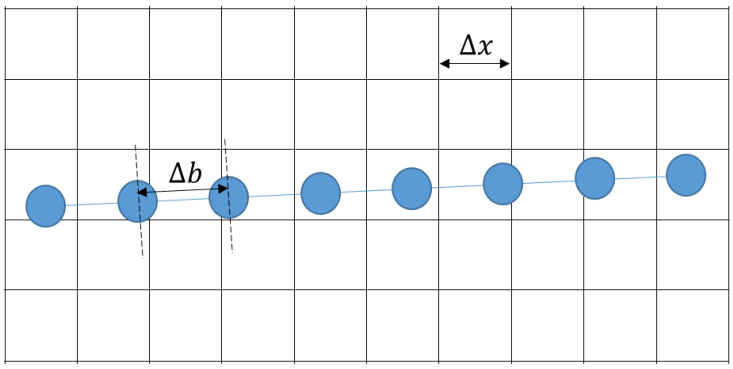

Figure 4.1: Visualization of actuator line model in the fluid mesh

are calculated for each point based on the lift and drag properties associated with the structure's geometry. The tower and nacelle are represented in a similar fashion, though the aerodynamic contributions due to these components will be small compared to the blades. The calculated point forces are projected onto the fluid using a Gaussian smoothing function η_ϵ, which is defined according to equation 3.42 in Chapter 3. The three model parameters that primarily influence the performance of the actuator line model are the Gaussian width parameter ϵ (see equation 3.42) which determines the distribution of force from each actuator point onto the fluid domain, the grid resolution at the actuator line location Δx, and the number of actuator points N_b used to discretise the blades (and the spacing between them, Δb, illustrated in Figure 4.1).

4.2.1 Existing Guidelines for ALM Parameters

Various guidelines and recommendations for defining an actuator line model and improving its accuracy have been published since the model was first introduced by Sørensen and Shen [69]. For the mesh resolution, Jha et al. [2] recommend choosing this so that $R/60 \leq \Delta x \leq R/30$, where R is the rotor radius, in order to ensure sufficient accuracy and computational efficiency. They also suggest a distribution of actuator points so that $\Delta b \geq 1.5\Delta x$ in order to avoid overpredictions in the blade tip loads. However, the advice from Martinez et al. [178] contradicts this, and recommends that $\Delta b \leq 0.75\Delta x$ to ensure a smooth distribution of forces. Since it is not possible to satisfy both recommendations, it is necessary to investigate the effect that this has on model predictions in order to determine a suitable value of Δb.

For the Gaussian width ϵ Troldborg [179] recommends $\epsilon \geq 2\Delta x$ to ensure numerical stability. Alternatively, Shives and Crawford [180] suggest that ϵ should

be proportional to the local blade chord length c, and present a guideline of $\epsilon = c/4$ in order to capture the blade tip vortex. In addition, they suggest that a grid resolution of $\Delta x \leq \epsilon/4$ is necessary in order to accurately capture the tip vortex. However, these recommendations require a very fine mesh resolution (more than 100 grid cells along the actuator line for most standard wind turbine blades). Jha et al. [181] propose an alternative method for improving tip load calculations by defining ϵ using an elliptical distribution function instead of a chord based function, which ensures that ϵ is kept small at the blade root and tip in order to avoid overpredicting the loads in these regions.

4.2.2 Calibration Using NREL Phase VI Experiment

Determining an actuator line model setup based on guidance from the literature is difficult since the recommendations vary or even directly contradict each other. Therefore, an investigation into the sensitivity of the model to some of these parameters was performed, where the model results are compared against experimental data from the literature. The objective of this study is to determine a model setup for the ALM that achieves good accuracy at a minimal computational cost, which will then be used to define an ALM to be used in a coupled SOWFA-FAST model of a floating wind turbine.

Due to the lack of available aerodynamic load data for floating offshore wind turbines, a fixed turbine case study from Phase VI of the NREL Unsteady Aerodynamics Experiment campaign was used [182]. The experiment featured a stall regulated turbine with a 10 m diameter two-bladed rotor and a power rating of 20 kW. The turbine was pitch controlled and operated at a constant rotational speed of 72 rpm, and was tested in the NASA Ames wind tunnel at wind speeds ranging from 5 to 25 m/s. The full details of the experiment can be found in Hand et al. [183]. In the parameter study presented here, the turbine is simulated with an upwind rotor in a uniform wind speed of 7 m/s. At this wind speed, there is no stall occurring at any point on the blade according to the experiment [182].

The actuator line model of the turbine was simulated in a fluid domain with the same dimensions as the NASA Ames wind tunnel, which has length 120 m, width 36.6 m and height 24.4 m. The inflow wind speed over the rotor area is assumed to be constant and unaffected by the walls of the wind tunnel. The impacts of mesh resolution Δx, number of actuator line points N_b, and distribution of the

actuator forces (by varying the ε parameter for the blades) on the performance of an actuator line model coupled with FAST are investigated in this study.

The impact of the number of actuator points N_b was investigated by studying the results of an actuator line model with 20 and 40 actuator points distributed uniformly along each blade for a grid resolution of $\Delta x = R/30$. This respectively corresponds to a relative resolution $\Delta b/\Delta x = 1.5$, which satisfies the guidelines from Jha et al. [2], and $\Delta b/\Delta x = 0.75$, which satisfies the guidelines from Martinez et al. [178]. The sensitivity of the actuator line model to the grid resolution was studied by increasing the mesh refinement to $\Delta x = R/60$. Two different approaches for determining ϵ are tested in this validation study based on recommendations from the literature. In the first approach, a constant value of ϵ along the blade is used, and in the second, ϵ is defined using an elliptical function proposed by Jha et al. [181]. The elliptical distribution of ϵ is defined as follows:

$$\varepsilon(r) = \max(n_{max}\Delta x\sqrt{1-\left(\frac{2r}{R}\right)^2}, n_{min}\Delta x) \tag{4.1}$$

where n_{min} and n_{max} are user defined constants. The guidelines presented in Jha et al. [177] suggest defining $n_{min} = 1$ and n_{max} such that:

$$\frac{n_{max}\Delta x}{R} \approx 0.08 \ldots 0.10 \tag{4.2}$$

For the uniform ϵ approach, ϵ is chosen to be twice the width of the local grid resolution in accordance with the recommendation presented by Troldborg [179]. For the elliptic function of ϵ, the constants are chosen according to the guidelines presented above, so that $n_{max} = 3$ for the cases with a grid resolution $\Delta x = R/30$ and $n_{max} = 6$ when $\Delta x = R/60$ in order to satisfy the guideline presented in equation 4.2.

4.2.3 Results

The estimated rotor loads from the experimental data are presented in Table 4.1. The mean rotor loads predicted using the actuator line model in SOWFA with different parameter configurations and the predictions from FAST are presented in Table 4.2.

Table 4.1: Estimated aerodynamic thrust and torque from UAE Phase VI [183]

	Mean	**Min.**	**Max.**
Thrust (N)	1128	1015	1206
Torque (Nm)	778	665	848

Table 4.2: Mean rotor thrust and torque predicted by FAST and SOWFA with different actuator line model setups for the UAE Phase VI turbine

	Thrust N)	**Torque (Nm)**
FAST (with BEM)	1196	795
ALM, uniform ϵ, $\Delta x = R/30$, $N_b = 20$	1170	783
ALM, uniform ϵ, $\Delta x = R/30$, $N_b = 40$	1149	772
ALM, uniform ϵ, $\Delta x = R/60$, $N_b = 40$	1035	621
ALM, elliptical ϵ, $\Delta x = R/30$, $N_b = 20$	1218	811
ALM, elliptical ϵ, $\Delta x = R/30$, $N_b = 40$	1211	804
ALM, elliptical ϵ, $\Delta x = R/60$, $N_b = 40$	1276	872

When a uniform ϵ value is used with a grid resolution of 30 grid cells along the blade, the total rotor torque and thrust predicted by the actuator line model coupled with FAST are both within the range of values from the experimental data. However, when the mesh is refined to $R/60$, the total rotor loads become too low compared to the experimental values when $\epsilon = 2\Delta x$. When ϵ is defined as an elliptical function, the rotor loads are again predicted well for a grid resolution of $R/30$, however the predicted loads are larger when the grid was further refined. This suggests that the choice of $n_{max} = 6$ used to define the elliptical function according to equation 4.1 was too large for this grid resolution and requires further investigation.

Increasing the number of actuator points along each blade from 20 to 40 led to a very small improvement in the mean rotor load calculations for both force distribution approaches, with a slightly increased computational cost of around 4% compared to the corresponding case with $N_b = 20$. Increasing the local grid resolution from $R/30$ to $R/60$ led to a CPU cost that was approximately four times larger than the cases with the coarser grid. Increasing the grid resolution results in a large increase in the CPU cost of an actuator line model because the time-step must also be reduced so that the blade tip does not pass through more than one mesh cell per time step.

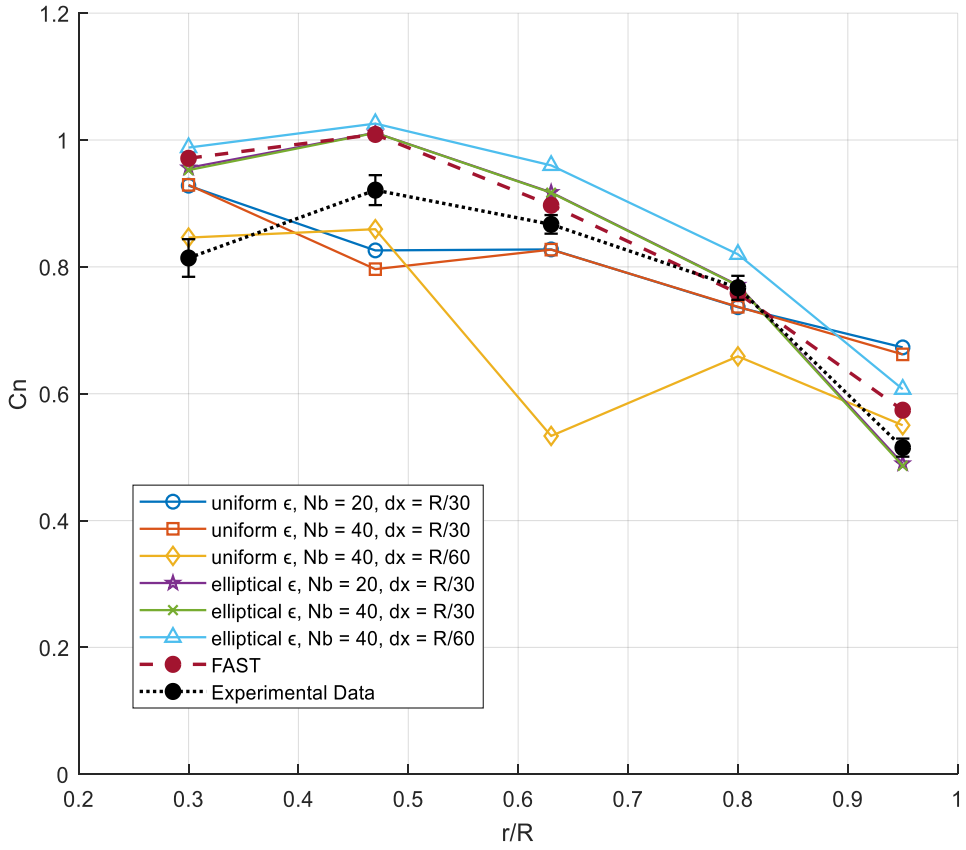

Figure 4.2: Normal force coefficients at different positions along the blade. The error bars represent one standard deviation either side of the mean for the experimental data

The experimental data for the aerodynamic loads has a high level of variability, as shown in Table 4.1, meaning it is difficult to tell which of the actuator line model setup gives the most accurate results based on this data alone. In order to give a better indication of the performance of each model setup, the local forces at different points along the blade were also examined. Figure 4.2 shows the mean normal force coefficients at five different points along the blade span for each actuator line setup, and how this compares with the experimental data and the BEM model in FAST. Likewise, Figure 4.3 shows the tangential force coefficients. FAST overpredicts the force in normal direction for the inboard half of the blade (close to the root), but the predictions improve for the outboard half. The tangential force is also overpredicted close to the blade root. The improved predictions close to the tip may be in part attributed to the use of the Prandtl tip loss correction in the FAST model. The use of a uniform value of ϵ without a tip loss correction model leads to overpredicted loads close to the blade tip for a grid resolution $\Delta x = R/30$. When an elliptical ϵ function is used, the loading at the low

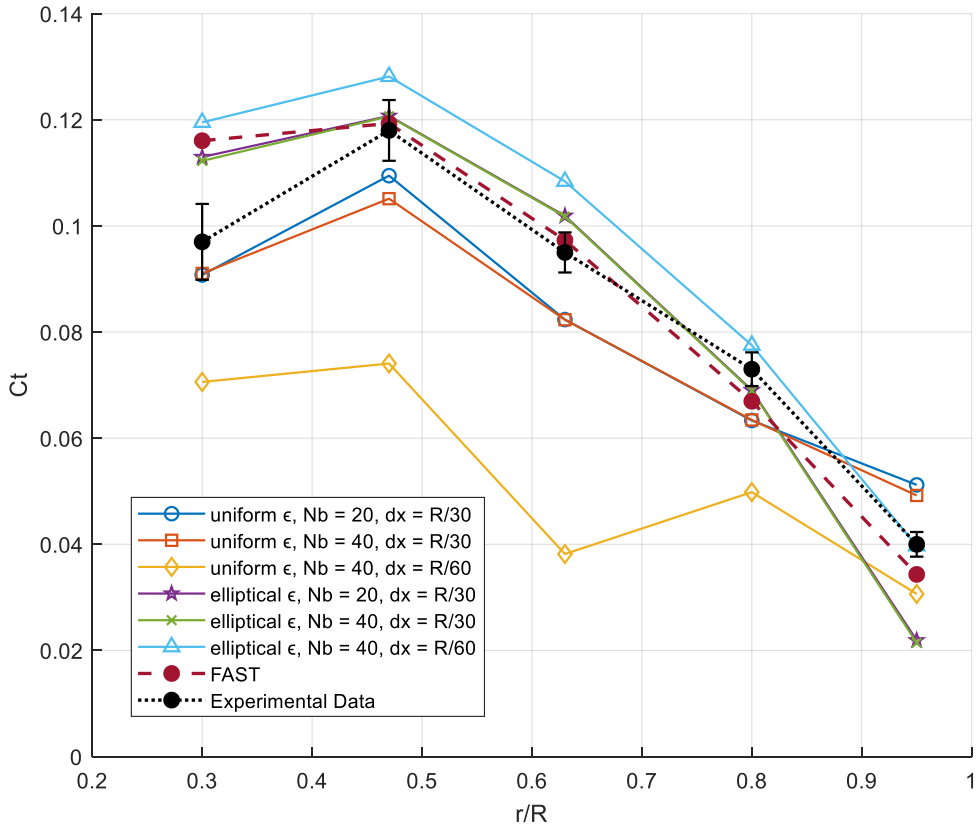

Figure 4.3: Tangential force coefficients at different positions along the blade. The error bars represent one standard deviation either side of the mean for the experimental data

to mid-span locations along the blade is overpredicted, however the estimated tip loading is significantly improved compared to the uniform ϵ cases and the overall 'shape' of the normal force distribution is closer to that of the experimental values and the predictions from FAST with the BEM method. Increasing the number of actuator points N_b defined along each blade to 40 was shown to have very little effect on the predicted load distribution.

When a uniform value of ϵ is used with a finer grid resolution, the tip loading is improved, but the predicted loads in the midspan region – particularly the tangential forces – are underpredicted. The forces predicted at the 0.63R location for this case are particularly low, which is suggested to be related to a numerical error since the normal force coefficient at this location was found to oscillate with a very large amplitude (with an approximate range $-2 < C_n < 3$. A negative value of the normal force coefficient implies a reverse in direction of the force, which is not physically possible). The same numerical behaviour was observed for the normal force coefficient at the 0.47R location in both of the uniform ϵ cases where $\Delta x = R/30$, but was not observed for any of the cases where an elliptical ϵ was

used. This may suggest that the relative value $\epsilon = 2\Delta x$ is not large enough in the midspan region of the blade where the force should theoretically be largest.

In the case of the elliptical distribution of ϵ and a fine grid, the tip loading is predicted well, and the 'shape' of the force distribution is similar to the cases with a coarser grid, but the force is significantly overpredicted in the low to mid-span region, which leads to overestimated total rotor loads as shown in Table 4.2. This further suggests that the choice of $n_{max} = 6$ used to define the elliptical distribution according to equation 4.1 is too large.

The results from this investigation suggest that the value of ϵ requires further tuning for actuator line models on fine grids, which was not conducted in this work due to time constraints. The definition of an elliptical distribution of ϵ with a smaller value of n_{max} for an ALM on a fine grid may result in more accurate force predictions that are in between those for the uniform function and the elliptical function demonstrated here. However, this would still incur a significantly higher computational expense than the coarser grid. The results from the cases with an elliptical ϵ function and a grid resolution of $\Delta x = R/30$ overall showed the closest match with the experimental data for the distribution of forces along the blade, and also showed good agreement with FAST; when $N_b = 40$, the difference between the ALM and FAST predictions was around 1% for both the total thrust and torque. It was therefore decided that this choice of a coarser grid resolution was sufficient for this study.

The actuator line model setups described above have been validated against a single case in this study. It is noted that these parameter configurations may not provide the same level of accuracy for different wind conditions or turbine geometries, and the optimal parameter configuration will be case dependent. However, the presented calibration study confirms that the ALM with a grid resolution $\Delta x = R/30$ is capable of predicting the total integrated aerodynamic loads and their distribution along the rotor blades with generally good accuracy, particularly when an elliptic distribution of ϵ is used, which helps to improve confidence in the model.

4.3 FOWT Simulation Setup

4.3.1 FAST Model Description

In the FAST simulations, the rotor aerodynamics are modelled using BEM theory. The BEM model estimates the apparent wind speed and induction at the rotor using an iterative procedure as described in Chapter 3, and uses a number of empirical corrections to account for complex flow effects that are not explicitly modelled. The influence of the tower on wind flow is accounted for using a potential flow model [49].

4.3.2 Floating Turbine Model Setup

The NREL 5 MW reference turbine [184] is modelled in all subsequent simulations presented in this chapter. This is a fictitious turbine that is based primarily on the REpower 5 MW turbine [185]. The key parameters are listed in Table 4.3.

Table 4.3: Key parameters of the NREL 5 MW turbine [184] on the OC3 Hywind spar platform [186]

Rated power	5 MW
Number of blades	3
Rotor configuration	Upwind
Rotor diameter	126 m
Hub diameter	3 m
Hub height above MSL	90 m
Cut-in, rated, cut out wind speed	3, 11.4, 25 m/s
Min, max (rated) rotor speed	6.9, 12.1 rpm
Platform draft	120 m
Spar diameter above cone section	6.5 m
Spar diameter below cone section	9.4 m

For the floating turbine simulations, the NREL 5 MW turbine is mounted on the OC3-Hywind spar platform [186], which was designed for Phase IV of the IEA Wind Task 23 Offshore Code Comparison Collaboration (OC3), and was based on the original spar buoy concept designed by Statoil for the Hywind Demo

project in 2009. The platform is anchored to the seabed via three catenary mooring lines.

In the SOWFA simulations, the actuator line model calculates the aerodynamic loads according to the blade element theory presented in Chapter 3, however instead of using an iterative procedure, the apparent wind speed is sampled directly from the blade element's location within the fluid domain. Unlike in the FAST simulations, the fluid flow in the OpenFOAM domain is affected by the presence of the turbine due to the forces exerted on the fluid by the actuator line model.

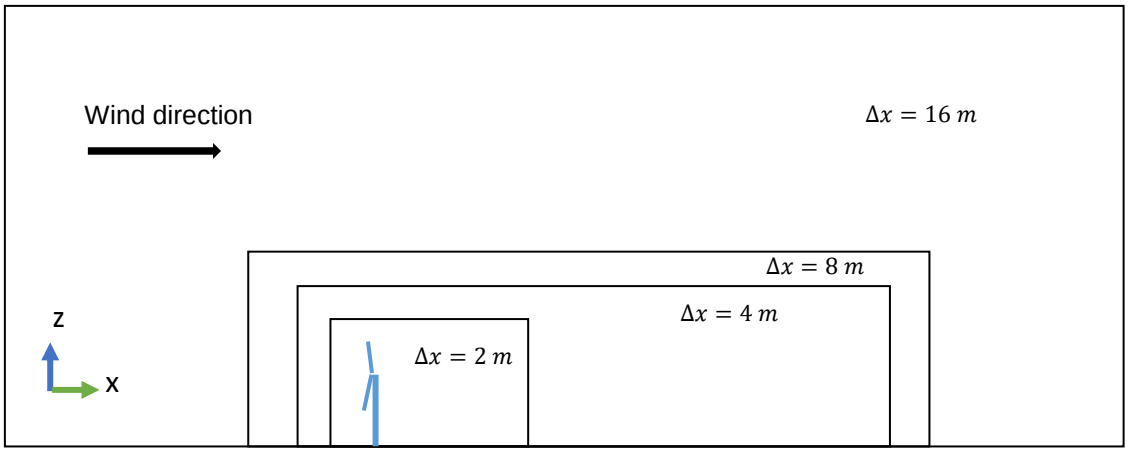

Figure 4.4: Visualization of the computational domain in OpenFOAM (not drawn to scale), showing regions of local mesh refinement of the computational mesh around the turbine location (represented by the blue lines)

In OpenFOAM, the actuator line model is positioned within a rectangular domain consisting of a hexahedral mesh which extends 1600 m in the horizontal x- and y-directions and 400 m in the vertical z-direction. The background mesh resolution is 16 m in each direction, and the mesh is locally refined three times by halving the cell width in each direction in the region where the actuator line model is positioned so that the mesh resolution in this region is 2 m, which equates to roughly 30 cells along each 61.5 m long blade in accordance with the chosen setup described in section 4.2. The computational domain is illustrated in Figure 4.4. The wind flows in the positive x-direction in all cases. Unless stated otherwise, the waves propagate along the same direction as the wind. The equilibrium position of the turbine is located at a distance equivalent to 5 times the rotor diameter from the inlet boundary. The actuator lines representing each blade consist of 40 actuator points uniformly distributed along the blade span, and the Gaussian width parameter ϵ is defined according to an elliptical function as described in section 4.2.

A uniform wind condition is specified in all presented simulations in order to limit additional sources of unsteady loading on the turbine. In the FAST simulations, a steady wind condition is used with a constant, uniform wind speed. The OpenFOAM simulations use free-slip conditions on the side, top and bottom boundaries, meaning that the boundaries have no effect on the flow velocity. A RANS approach with the $k-\epsilon$ turbulence model is used. All simulations are performed with the turbine initialised at the equilibrium position. The baseline control system for the NREL 5 MW turbine including adjustments for the OC3 Hywind platform [186] is enabled for all simulations, so that the rotor speed and blade pitch angle will be adjusted based on the inflow speed. The nacelle yaw angle is fixed for all simulations, where a yaw angle of 0° is aligned with the x-axis and therefore the wind propagation direction. In both the FAST and SOWFA simulations, the turbine is simulated for a total of 1200 seconds of simulation time, where the final 300 s are used for analysis in order to omit any start-up transients.

4.4 Impact of Wave Height and Period

A floating offshore wind turbine is subjected to platform motions due to wave excitation, which affects the relative wind inflow speed at the rotor and subsequently the aerodynamic loads and power production. The level of variation in the relative wind speed due to platform motions will depend on the amplitude and frequency of the incident waves. In particular, as the surge and pitch motion amplitudes increase, the effect of wake interactions on rotor aerodynamics may also increase [89,187]. It is therefore important that numerical models of floating offshore wind turbine aerodynamics are able to take into account the effect of waves and resulting platform motions. The impact of waves on the predicted aerodynamic loads of a FOWT using the BEM and ALM methods is investigated by simulating the NREL 5 MW on a spar platform in four different regular wave conditions. In addition, a control case featuring the NREL 5 MW on a fixed foundation without waves is simulated in order to directly demonstrate the additional effects that wave-induced floating platform motions have on FOWT aerodynamics according to each model. The wave kinematics are simulated using linear Airy wave theory and the hydrodynamic forces on the spar are calculated using potential flow theory and Morison's equation as described in Chapter 3. Wave heights of 4 m and 8 m and wave periods of 6 s and 12 s are

considered. The chosen parameters approximately represent mild and more extreme sea conditions for the spar platform [186,188], though it is acknowledged that not all combinations of the wave parameters examined in this study represent realistic sea states (in particular, a wave height of 8 m is larger than realistic values that would likely occur for a wave period of 6 s). Instead, the larger wave height and period values are chosen to be twice the magnitude of the smaller values so that their individual impact on model predictions of FOWT dynamics can be easily interpreted whilst limiting the number of simulations in order to reduce computational cost. The selected wave periods do not coincide with any of the floating platform natural periods, which are listed in Table 4.4. In each case, the NREL 5 MW turbine is simulated in a constant uniform wind speed of 8 m/s with the wind propagation direction aligned with turbine nacelle yaw angle. In the fixed turbine simulations, there are no waves or hydrodynamic effects considered. In the floating turbine simulations, the propagation direction of the regular waves is aligned with the wind direction.

Table 4.4: OC3 Hywind spar platform natural periods [189]

Platform mode	**Natural Period (s)**
Surge	125
Sway	125
Heave	31.3
Roll	29.4
Pitch	29.4
Yaw	8.3

4.4.1 Platform Motions

The platform motions predicted by each model for the floating turbine in the smallest waves simulated are shown in Figure 4.5. The wave propagation direction is aligned with the surge and pitch directions, so these are the modes that are predominantly excited by the waves in this case. However, the amplitudes of the floating platform motions in this case are small; the platform surge motion amplitude is around 0.7 m and the pitch motion amplitude is less than 0.5°. This is in part due to the constant uniform wind speed without explicitly modelled turbulent fluctuations. SOWFA predicts a slightly larger mean deviation

from the equilibrium position than FAST for almost all platform modes, but there is overall very little difference between the two model predictions for the platform response.

The platform surge and pitch motion in each wave condition are plotted in Figure 4.6. The floating platform response is directly related to the wave excitation; the motion period coincides with the wave period, and any increase in the wave amplitude will correspond with the same proportional increase in the surge and pitch amplitudes. Doubling the wave period alone leads to surge and pitch amplitudes that are four times the values for the baseline case. The mean deviation from the equilibrium position does not change significantly with wave height or period since this is driven primarily by the wind and the resulting rotor thrust force, which is examined in the following section. There is a small mean offset between the FAST and SOWFA predictions of both surge and pitch motions, which is due to differences in the mean rotor thrust force, however the amplitude and phase of the platform motions are almost identical in all cases. This is shown in Appendix A, where the offset is removed by plotting the FAST results with the mean offset added to all values.

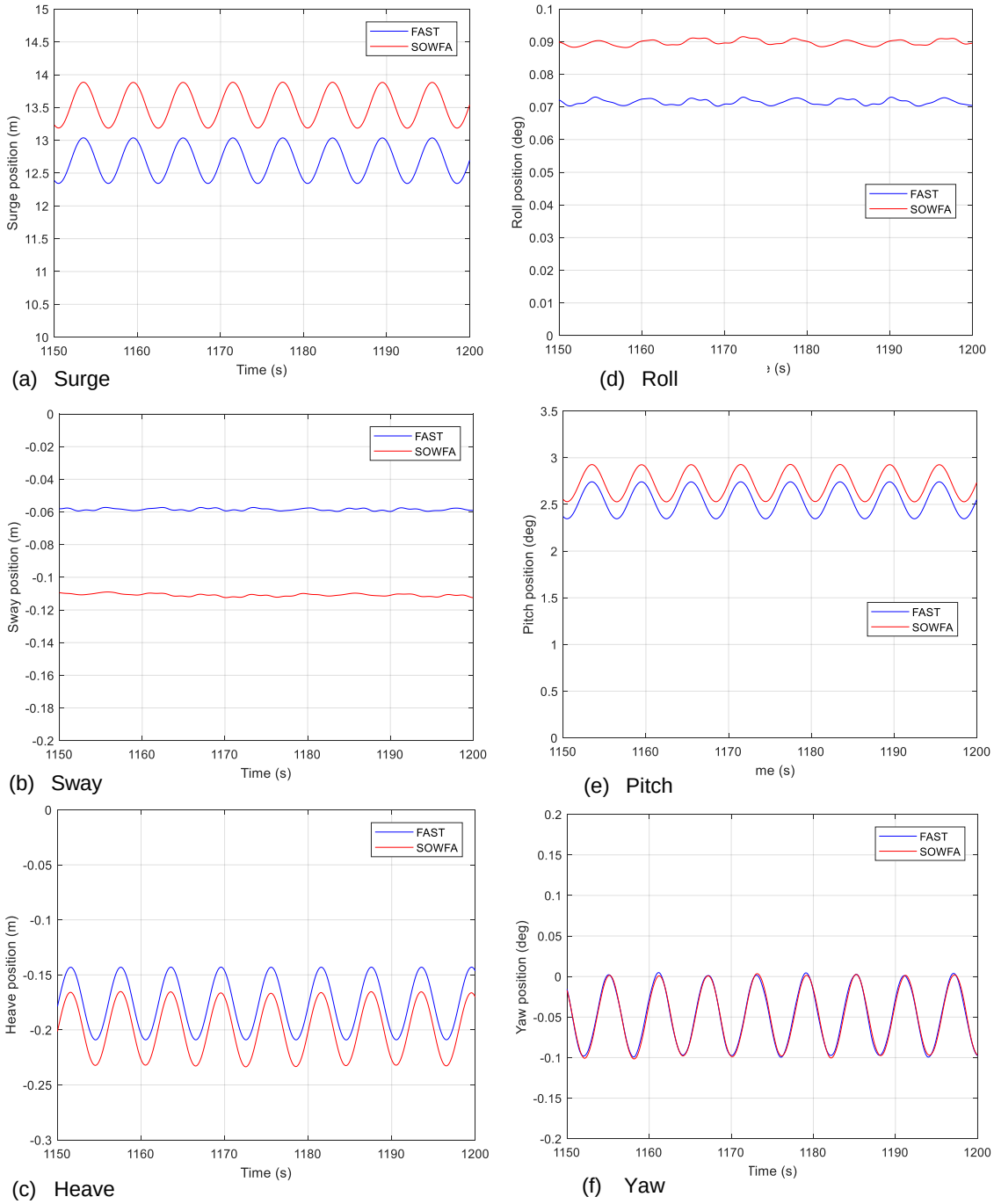

Figure 4.5: Platform motions for the floating spar turbine in waves with 4 m height and 6 s period

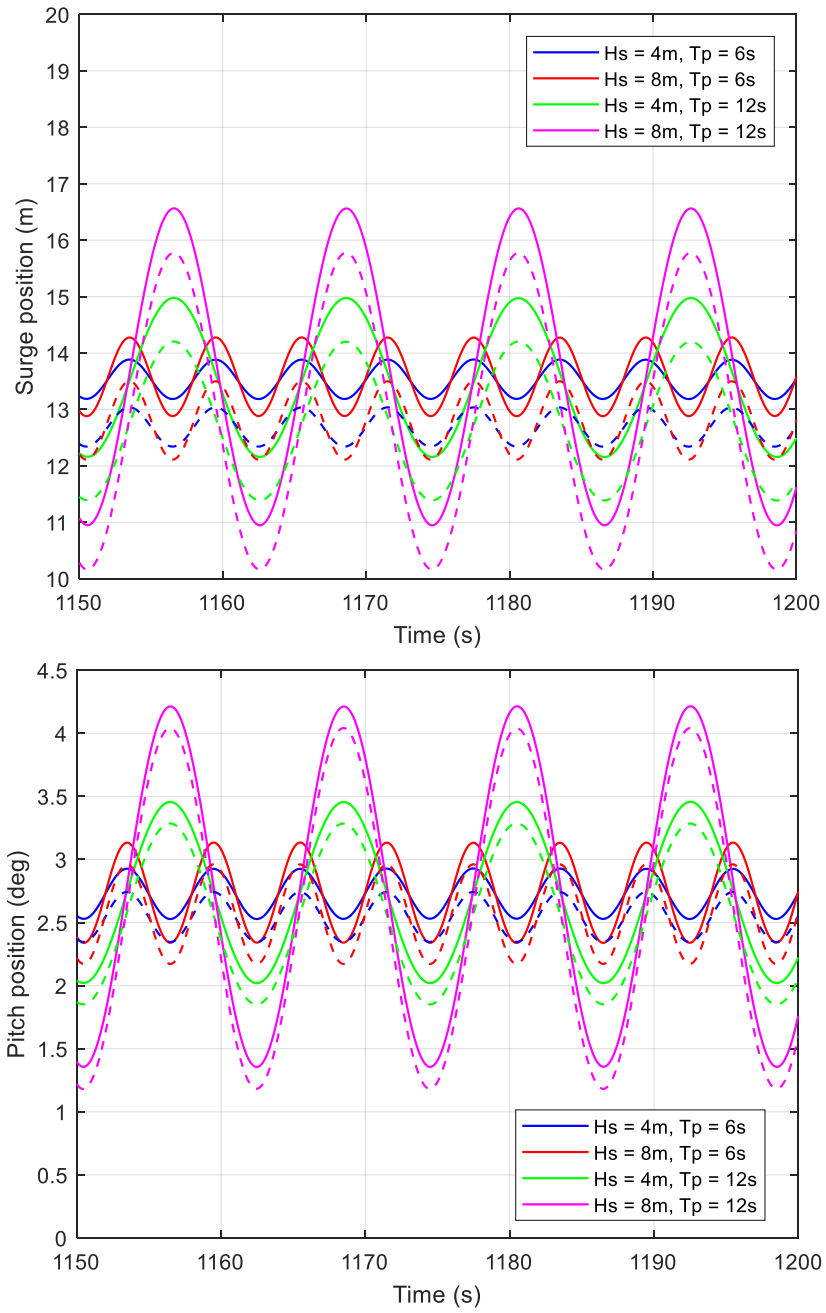

Figure 4.6: Surge and pitch motions of the floating platform under different wave conditions. Dashed lines represent predictions from FAST, solid lines represent SOWFA

4.4.2 Rotor Power and Thrust

The mean values and variation due to floating platform motion for the rotor aerodynamic power predicted in each wave condition are shown in Figure 4.7, while Figure 4.8 shows the axial thrust force. Aerodynamic or mechanical power is calculated as a product of the rotor torque and rotational speed, as described in section 3.3.1.

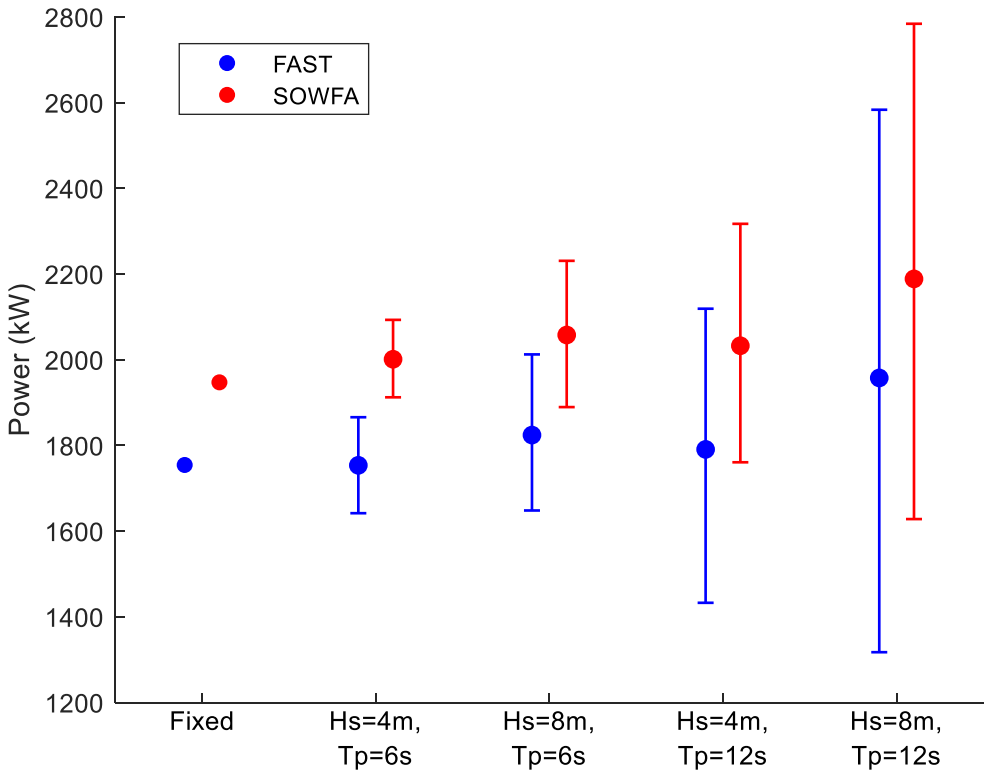

Figure 4.7: Rotor power in different wave conditions, U = 8 m/s. • represents the mean value, error bars represent the peak-to-peak variation due to floating motion

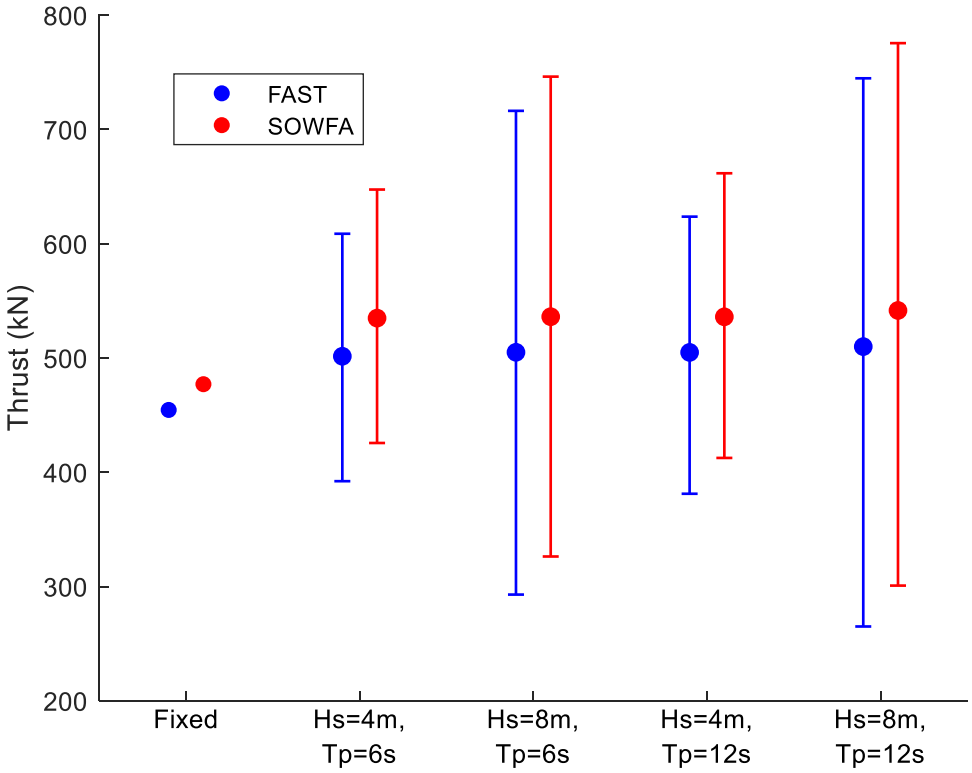

Figure 4.8: Rotor thrust in different wave conditions, U = 8 m/s. • represents the mean value, error bars represent the peak-to-peak variation due to floating motion

The actuator line model in SOWFA predicts higher mean loads than the BEM model in FAST for the NREL 5 MW turbine on both a fixed and floating foundation. This is consistent with observations from previous comparative studies in the literature where a tip loss correction factor is not used in actuator line modelling of the NREL 5 MW turbine [177,178,190]. In the present study, the average power and thrust predicted by SOWFA are respectively 10.9% and 4.8% higher than the FAST predictions for the fixed turbine. For the same ALM setup for the experimental UAE Phase VI turbine in section 4.2, the predicted torque and thrust were 1.1% and 1.3% higher than the respective FAST predictions. The larger differences observed in Figures 4.7 and 4.8 may be in part attributed to the more complex control system defined for the NREL 5 MW turbine; the experimental scale turbine operates at a fixed rotational speed, while the 5 MW turbine rotational speed varies with the apparent inflow wind speed. The average rotational speed for the fixed turbine in FAST was 8.96 rpm, while SOWFA predicted this to be 3.4% higher, at 9.27 rpm, which suggests a difference in the induced velocity calculated by each model. This will therefore result in a larger difference in the rotor loads, since they are a function of the rotor speed. Alternatively, it may be that a finer grid resolution and a smaller Gaussian width parameter would improve ALM predictions for this turbine. Since the NREL 5 MW reference turbine is fictitious, there is no experimental data available to validate the numerical models, and it is not possible to tell which model's predictions are closer to the 'true' values.

Figure 4.7 shows that the addition of platform motions due to wave excitation generally corresponds to an increase in the mean rotor power. This is consistent with previous numerical [63,191] and experimental findings [192] for high tip speed ratio cases. The difference between FAST and SOWFA predictions is larger for the floating turbine than the fixed case, with SOWFA predicting a larger increase in power due to platform motions. Notably, FAST predicts that the mean rotor power for a floating turbine in waves of 4 m height and 6 s period will be approximately the same as if the turbine was fixed, whilst SOWFA predicts a small increase of approximately 2.7%. Both models predict a substantial increase in the mean thrust force for a FOWT compared to a fixed turbine. This is because the thrust term includes effects from gravity and inertial loading of the rotor, which will be increased due to the nonzero mean pitch angle that increases the relative

rotor tilt. The increase in thrust force is similar for both models; in FAST, the predicted mean thrust for the floating turbine is 10-12% higher than for the fixed turbine (depending on the wave conditions), while in SOWFA the mean thrust increases by 12-13%.

When the floating platform oscillates with the waves, the rotor loads of a floating turbine experience periodic variation resulting from fluctuations in the relative wind speed and inflow angle [34]. The increase in platform motion due to increased wave height and period subsequently corresponds to an increase in the rotor load variation. It is observed that when the wave height is 8 m, the amplitude of the rotor power and thrust are nearly twice as large compared to the case where the wave height is 4 m (when the wave period does not change). When the wave period length doubles, the corresponding effect on the rotor power variation is significantly greater than the effect of increasing the wave height, as was observed for the surge and pitch motion amplitudes, however the increase in the thrust variation is much smaller than observed for the increased wave height, even though the platform surge and pitch amplitudes are larger in longer wave periods as shown in Figure 4.6. When both the wave height and period are doubled, the rotor power amplitude is more than six times larger than for the baseline case.

FAST consistently predicts a larger (by 7-24%) variation in the power than SOWFA for the floating turbine. This may be significant when estimating fatigue loads of components due to torque fluctuations, and the choice of model may have an impact for example in the design of a control system in order to reduce power fluctuations. It is possible that the empirical dynamic inflow model used in the BEM model overestimates the impact that platform motions have on the unsteady aerodynamics compared to the actuator line model which resolves more of the flow effects than the BEM method. However, it is difficult to know which model results in more accurate predictions without experimental validation.

4.5 Impact of Yaw Misalignment

The wind inflow direction is rarely aligned exactly with the rotor axis of a wind turbine for several reasons; the wind direction varies over time and will naturally have some fluctuation due to turbulence, and the yaw control system on a wind

turbine must have a delayed response to the instantaneous wind in order to ensure stable operation. In addition, turbines in wind farms may be intentionally yaw misaligned in order to redirect their turbulent wakes away from downstream turbines [193,194]. There have been numerous studies of impact of yawed inflow on the aerodynamic loads of fixed turbines [27,195], but floating wind turbines have an additional level of complexity due to the low yaw stiffness of many floating support structure designs [9]. This may result in additional motions that will further impact the response of a floating wind turbine. The impact of yawed conditions on floating wind turbine loads must therefore be understood.

When a wind turbine is operating in yawed flow, the aerodynamic loading on the rotor becomes asymmetric and experiences cyclic variation as a result of the variation in the angle of attack with azimuthal position. Yawed inflow conditions also generate a strong spanwise component of induced velocity across the rotor, which leads to a skewed wake structure being developed [50]. In the presented simulations, the rotor yaw angle of a floating wind turbine is varied from 0-30°, and the effect of this on the rotor and blade loads and platform motions is studied. The turbine is simulated in two wind conditions: a below rated wind speed of 8 m/s where the blade pitch controller will not be active, and an above rated wind speed of 16 m/s where the pitch controller will be actively pitching the blades, which will further impact the rotor loads. The purpose of this is to provide insight into the effect of yaw misalignment on model predictions of rotor loads in different wind conditions. The turbine is simulated in regular waves with a 4 m height and 6 s period, which were the smallest waves simulated in the previous section. The wave propagation direction is aligned with the wind for all simulations.

4.5.1 Rotor Power and Thrust

4.5.1.1 Below Rated Wind Speed

The results for the mean predicted power output and thrust force from the FAST and SOWFA models are shown in Figure 4.9. Increasing misalignment between the rotor and the wind flow direction causes the apparent wind speed at the rotor to decrease, since the component of the wind speed aligned with the rotor axis decreases in magnitude. For the below rated wind condition, this causes the rotor loads to decrease with increasing yaw misalignment.

The rotor power loss due to a yaw angle γ can be approximated according to the relationship $P_\gamma / P_0 = cos(\gamma)^x$, where P_0 is the power when the turbine is aligned. The exponent x is often assumed to have a value of 3 for small yaw angles [27], however experimental investigations have shown that this can vary widely [196]. A recent study by Simley et al. [197] demonstrated that the value of x is dependent on the wind speed, and estimated that x is between 1.3 and 2.3 for a wind speed of 8 m/s. In the simulations presented in this work, the power loss due to yaw was found to decrease with $cos(\gamma)^x$, where $x = 1.78$ according to SOWFA and $x = 2.68$ according to FAST, as plotted in Figure 4.9. For the rotor thrust, a curve of best fit (represented by dashed lines) is plotted for each set of model results, which is chosen to be a third order polynomial curve so that it passes through all four data points. Similar to the model predictions of the rotor power loss, FAST predicts a steeper decline in the rotor thrust with increasing yaw misalignment than SOWFA.

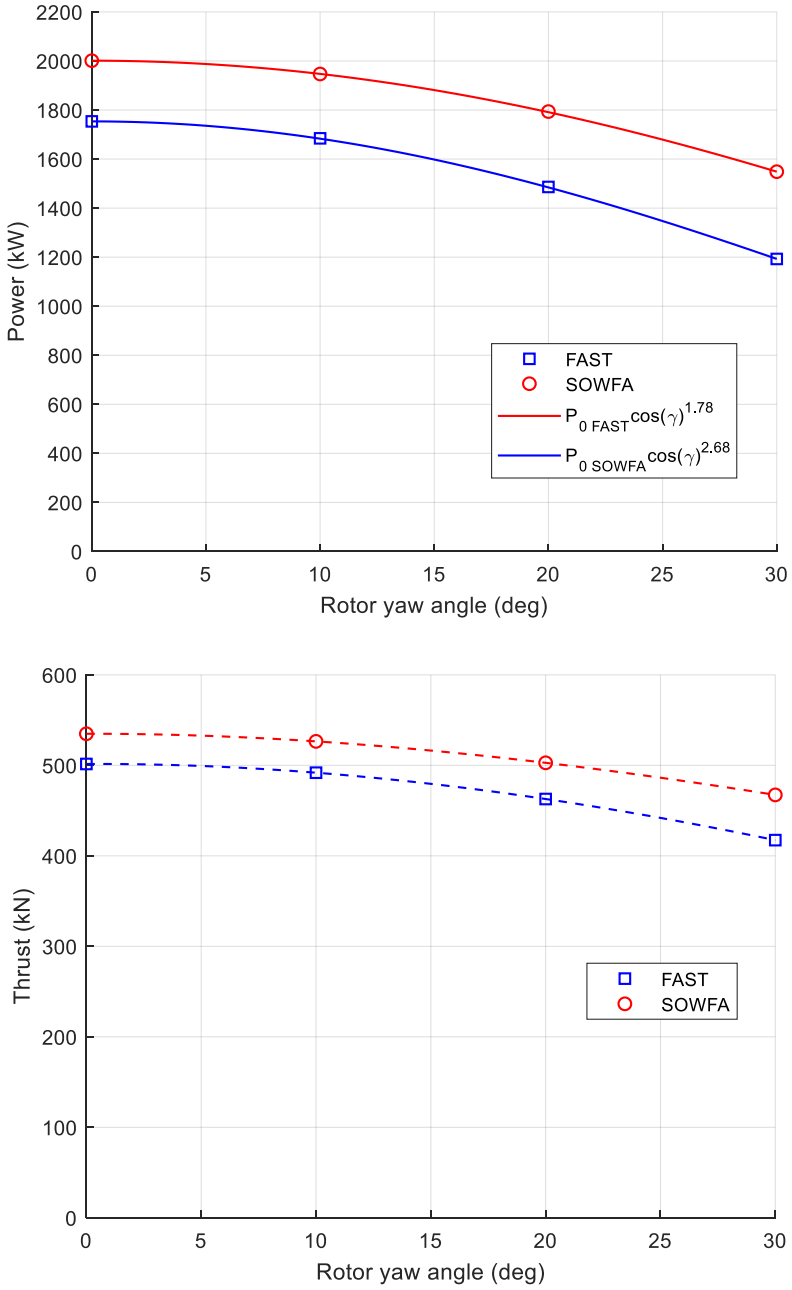

Figure 4.9: Mean rotor power and thrust at different rotor yaw misalignment angles, U = 8 m/s

The difference between FAST and SOWFA's estimations of the power and thrust decrease with increasing yaw misalignment suggests that the wind sampled in OpenFOAM by the actuator line model has a greater velocity component aligned with the rotor axis than that predicted by the BEM model with the Pitt/Peters skewed wake correction in FAST when the rotor is yawed. This may be significant when estimating the loading of floating turbines on platforms with a low yaw stiffness or intentionally yaw-misaligned turbines in wind farms that may spend a significant amount of time in yawed conditions. According to FAST, the mean

rotor power at a yaw misalignment angle of 30° is 32% lower than for the aligned case, and the mean thrust is 17% lower. According to SOWFA, the mean power and thrust drop by 23% and 13% respectively at 30° of yaw misalignment. The value of the exponent x from FAST is larger than the estimated values from the literature, meaning it is possible that the skewed wake model in FAST overestimated the power loss, though it must be reiterated that it is not possible to know for certain without experimental validation for this turbine. The larger power loss due to rotor misalignment predicted by FAST may also be a contributing factor in FAST predicting a smaller increase in power than SOWFA for a floating turbine compared to the fixed case, as observed in Figure 4.7. This is because the floating turbine experiences platform pitching about a nonzero mean pitch angle, which results in a larger and more variable rotor tilt misalignment.

The amplitude of the cyclic thrust variation due to wave induced platform motion is shown to decrease as yaw misalignment increases, and both FAST and SOWFA agree well on this, as shown in Figure 4.10. The impact of increased rotor misalignment on the power variation for a floating turbine is less obvious. FAST predicts a significantly larger variation in the rotor power than SOWFA for yaw angles up to 20°, then predicts a sharp decrease in the variation as yaw increases from 20° to 30°. According to FAST, the largest variation in power occurs at a yaw angle of around 10°, while SOWFA predicts that the largest power variation occurs when the rotor is aligned with the wind. SOWFA predicts that the power variation decreases as yaw misalignment increases up to 20°, but then increases when the yaw misalignment is further increased to 30°, which contradicts the results from FAST. This difference may again be significant in the design process when estimating fatigue loads for floating turbines that are frequently misaligned with the wind.

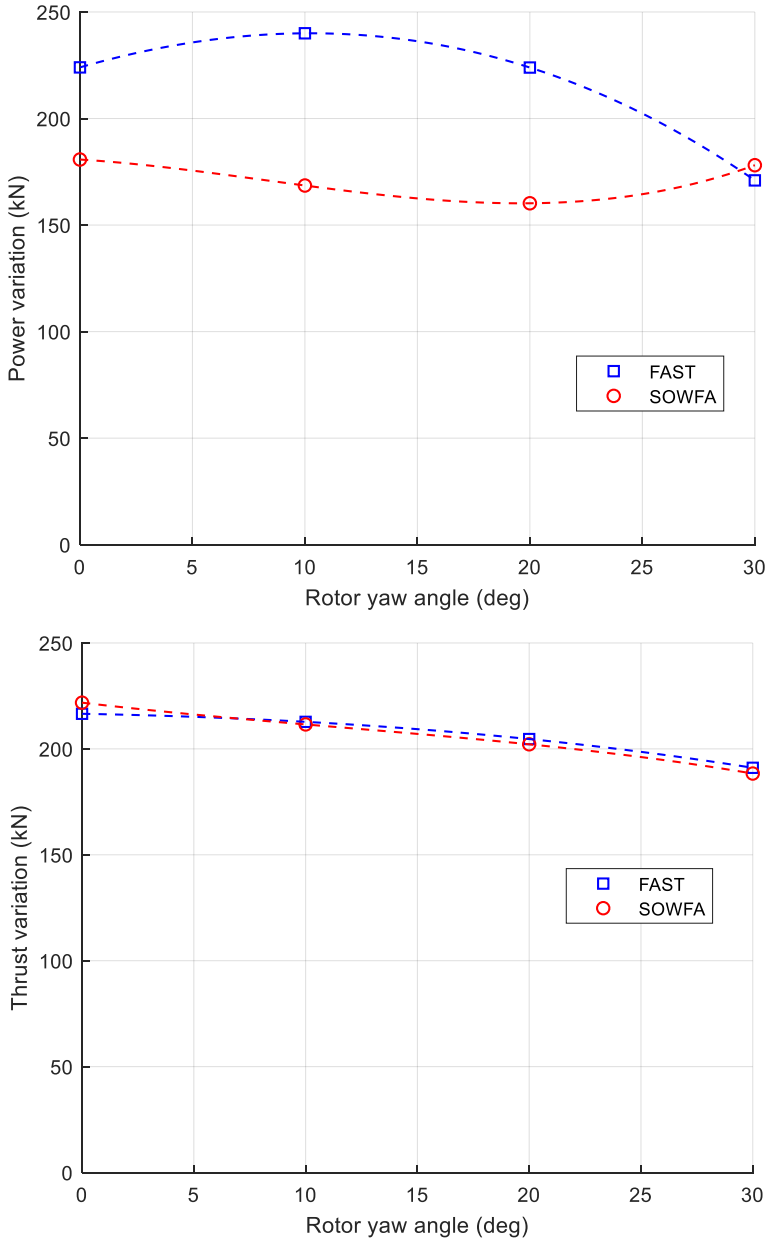

Figure 4.10: Variation in rotor power and thrust at different rotor yaw misalignment angles, U = 8 m/s

4.5.1.2 Above Rated Wind Speed

For the above rated wind condition, as yaw misalignment increases the blade pitch controller acts so that the power remains constant at the rated value. The thrust increases, since the apparent wind speed is closer to the turbine's rated wind speed value of 11.4 m/s, at which maximum rotor thrust occurs. For a large enough angle of misalignment, the apparent inflow wind speed would drop below the rated value and the rotor power and thrust would decrease.

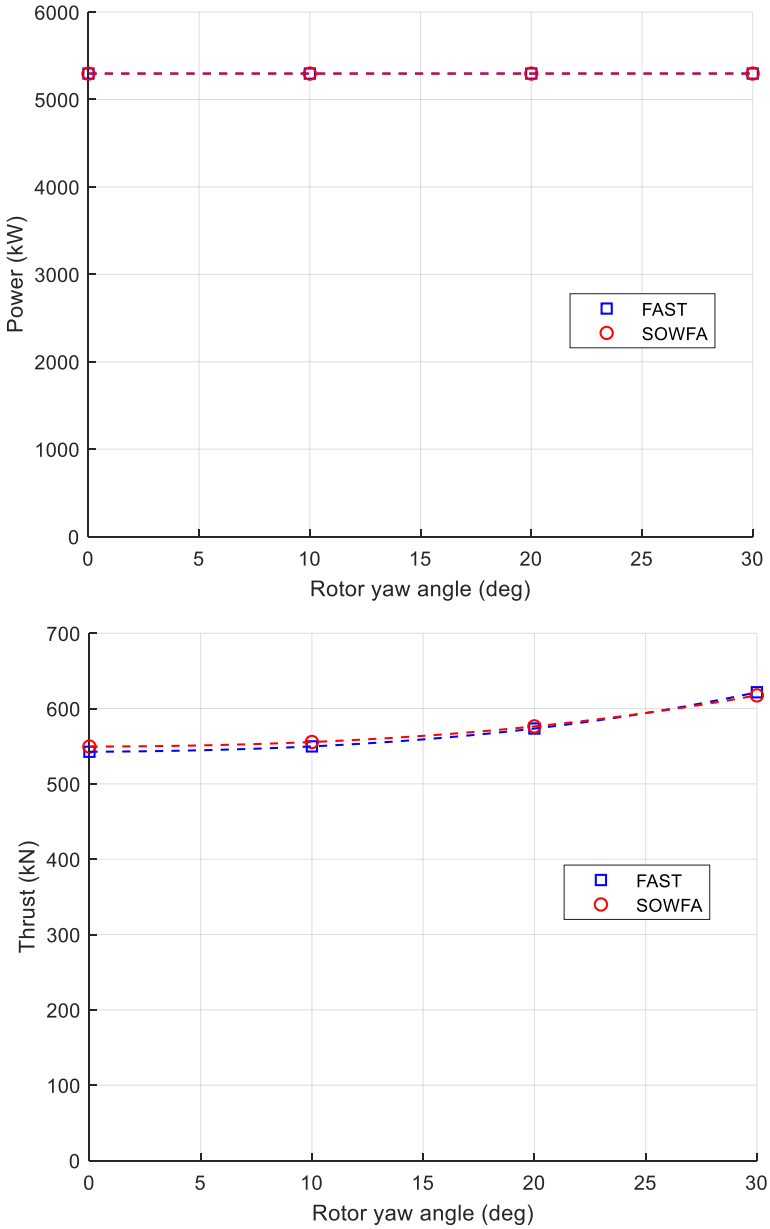

Figure 4.11: Mean rotor power and thrust at different rotor yaw misalignment angles, U = 16 m/s

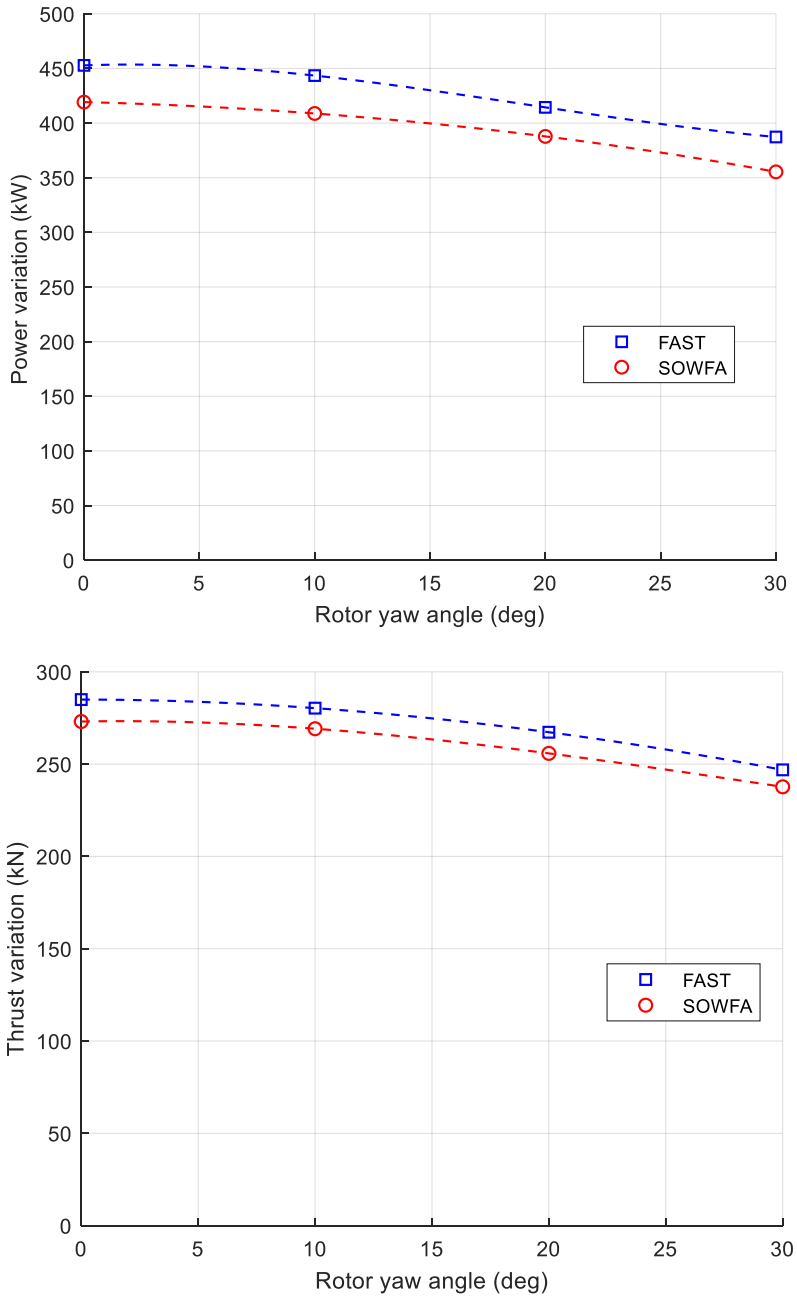

Figure 4.12: Variation in rotor power and thrust at different rotor yaw misalignment angles, U = 16 m/s

The mean power and thrust predicted by FAST and SOWFA for a wind speed of 16 m/s are shown in Figure 4.11. Figure 4.12 shows the power and thrust variation. The model predictions of the mean rotor power are identical, since this remains constant at the rated value for all yaw angles. FAST and SOWFA predict similar values for the mean rotor thrust, with less than 1.3% difference between the two models. Both models predict an increase in the mean thrust of around 12% at 30° yaw compared to the aligned case, and that the thrust and power oscillations decrease in amplitude with increasing yaw. However, FAST

consistently predicts a larger amplitude of both rotor load variations than SOWFA for all yaw conditions.

4.5.2 Blade Loads

4.5.2.1 Below Rated Wind Speed

The mean values for the blade root flapwise and edgewise bending moments are plotted in Figure 4.13, and the bending moment variation in each direction are plotted in Figure 4.14. The mean values for the flapwise and edgewise root bending moments both decrease as yaw misalignment becomes large, though SOWFA predicts that the mean edgewise bending initially increases for a small angle of yaw misalignment. Similar to the observed rotor power and thrust predictions, the difference between SOWFA and FAST predictions increases with yaw misalignment for both flapwise and edgewise bending mean values, with SOWFA predicting a smaller decrease than FAST with increasing yaw. In below rated conditions where the blades are not pitching, a flapwise bending moment at the blade root corresponds with out of plane bending, which is a function of the rotor thrust force, and so the effect of rotor yaw misalignment on the mean blade root flapwise bending moments is therefore very similar to that of the mean thrust.

A significant difference is observed for the model predictions of the blade root flapwise bending moment variation with increasing yaw misalignment. FAST predicts that the range of bending moment values at 30° yaw misalignment will be 39% larger than for the aligned case, whilst SOWFA predicts an increase of just 13%. This should be taken into account when estimating the blade fatigue loads, as it may suggest that the empirical skewed wake and dynamic inflow models overpredict the impact of yaw misalignment on the blade load fluctuations.

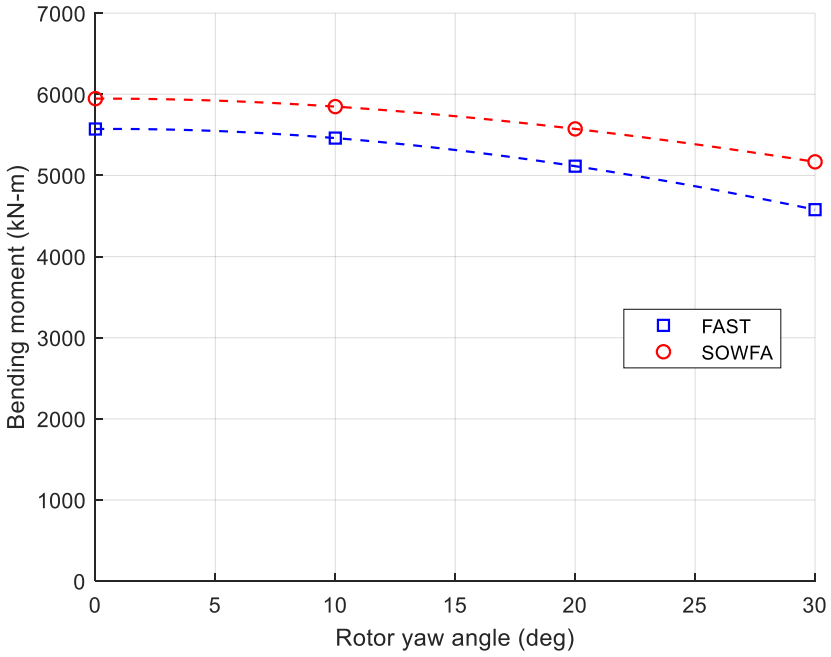

(a) Flapwise bending

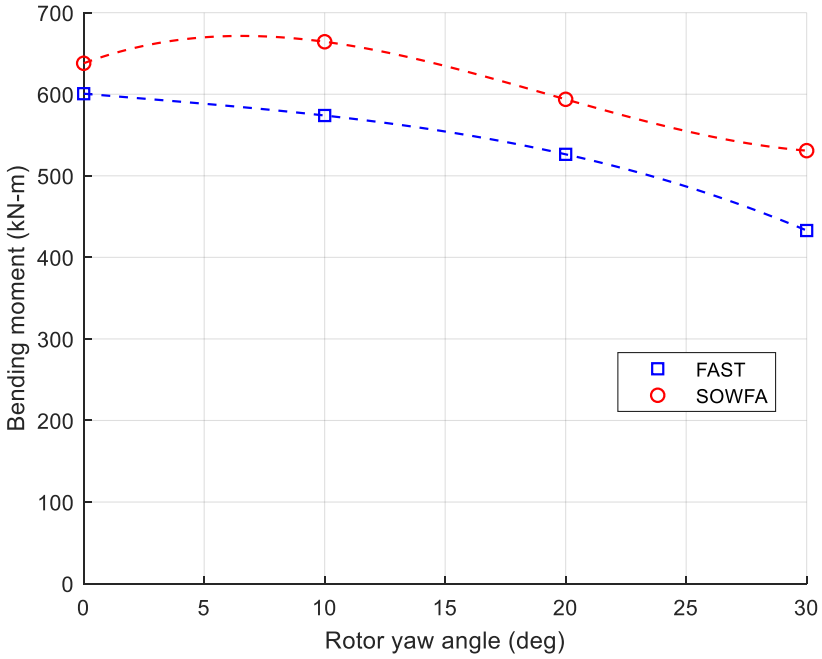

(b) Edgewise bending

Figure 4.13: (a) Mean blade root flapwise and (b) edgewise bending moment at different rotor yaw misalignment angles, U = 8 m/s

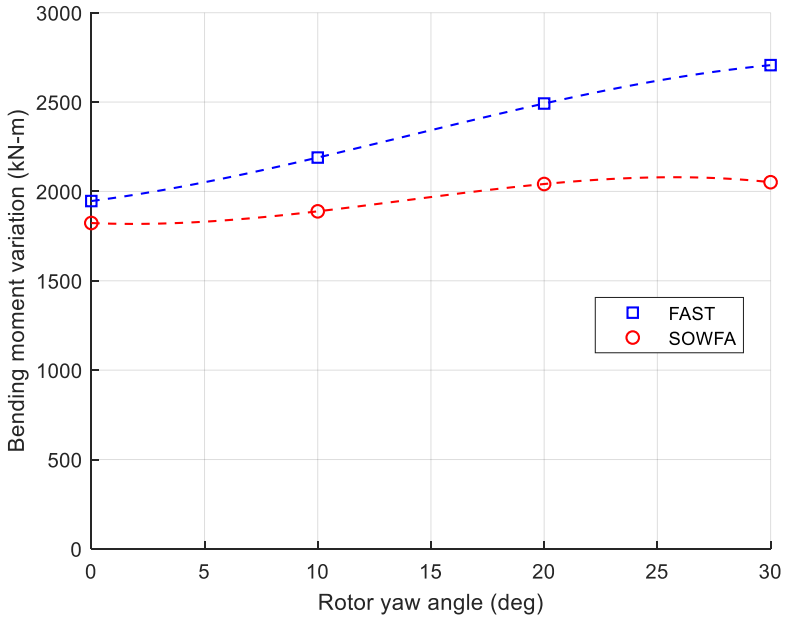

(c) Flapwise bending

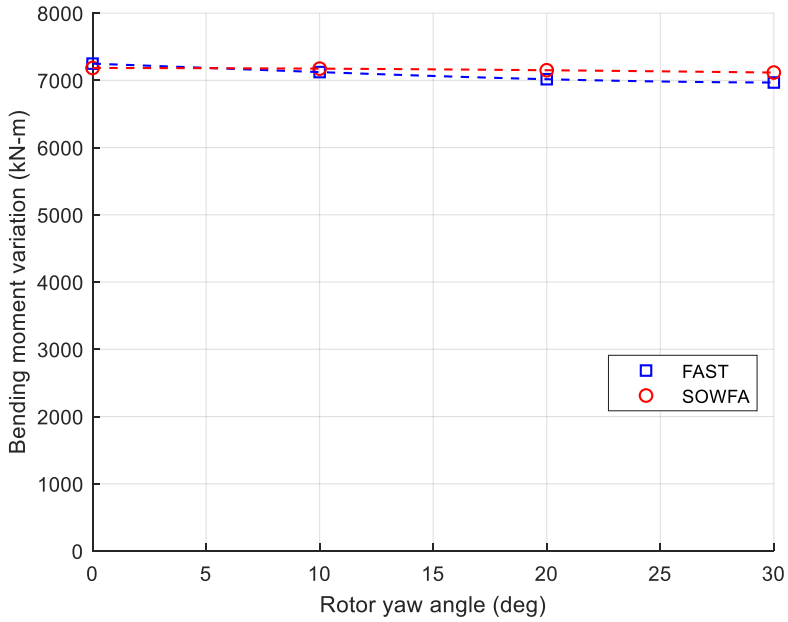

(d) Edgewise bending

Figure 4.14: Variation in blade root (a) flapwise and (b) edgewise bending moment at different rotor yaw misalignment angles, U = 8 m/s

4.5.2.2 Above Rated Wind Speed

The mean values for the flapwise and edgewise bending for the above rated cases with increasing yaw are plotted in Figure 4.15, and the variations for each bending direction are shown in Figure 4.16. Both the mean flapwise and edgewise bending moment values increase with increasing yaw misalignment at this wind speed.

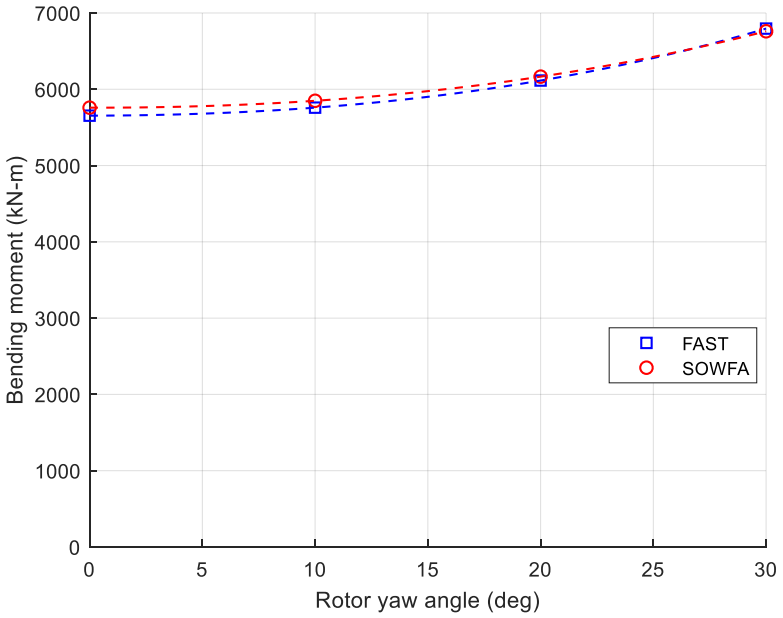

(a) Flapwise bending

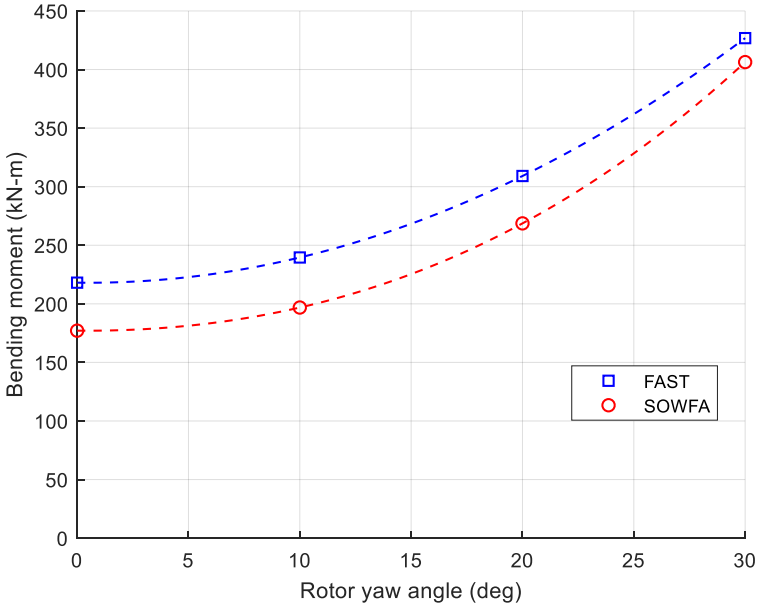

(b) Edgewise bending

Figure 4.15: (a) Mean blade root flapwise and (b) edgewise bending moment at different rotor yaw misalignment angles, U = 16 m/s

The two models disagree on the effect that increasing yaw misalignment has on the cyclic variation in the blade flapwise bending moment. Whilst SOWFA predicts that the variation decreases consistently as yaw misalignment increases, FAST predicts little change overall in the variation, and the largest variation in the bending moment is observed for a yaw angle of 20°. At the largest simulated yaw angle (30°), FAST predicts a noticeably larger variation in the blade root flapwise

bending moment than SOWFA, similar to that observed in the below rated case. There is little change in the cyclic variation for the edgewise bending moment.

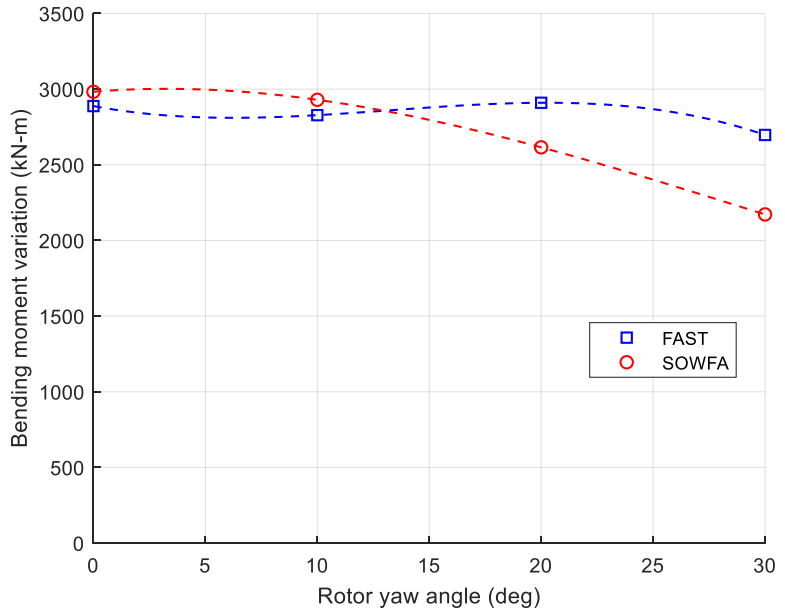

(a) Flapwise bending

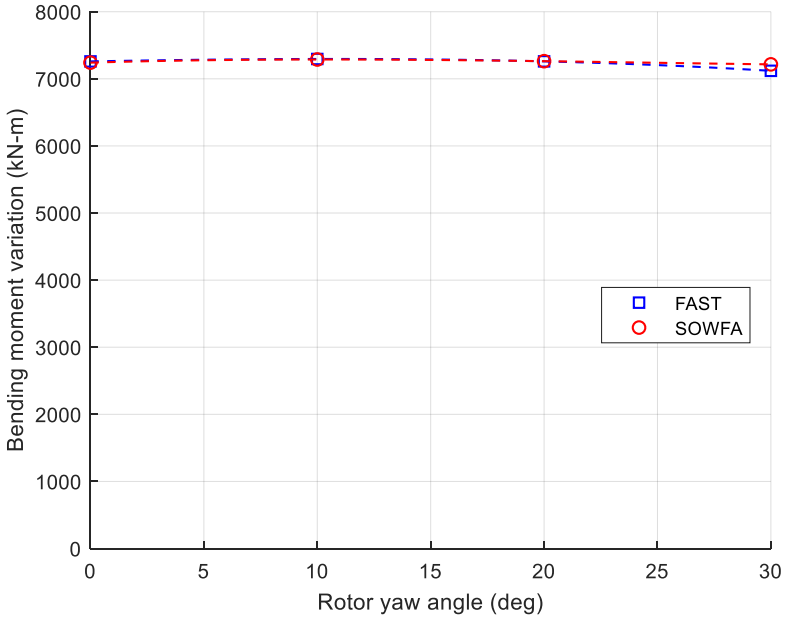

(b) Edgewise bending

Figure 4.16: Variation in blade root (a) flapwise and (b) edgewise bending moment at different rotor yaw misalignment angles, U = 16 m/s

4.6 Impact of Wind/Wave Misalignment

The IEC 61400-3-2 standard for floating offshore wind turbine design [198] states that misalignment between the wind and waves interacting with a floating wind

turbine may lead to bi-directional wave loading which can have a significant effect on tower base fatigue. Previous work has shown that while most extreme loading on a spar platform occurs when the wind and waves are aligned, it is important to consider wind and wave misalignment in order to estimate the side-side bending behaviour of the tower when calculating fatigue loading [199].

The effect of misaligned wind and waves is investigated by simulating the spar-mounted NREL 5 MW turbine in conditions where the wind is aligned with the turbine rotor axis and the wave propagation direction is perpendicular to the wind. The results from this simulation are compared against the baseline case with aligned wind and waves.

4.6.1 Platform Motions

The alignment of the wind and waves has a negligible effect on the mean position of the turbine, as shown in Figure 4.17. However, the propagation direction of the waves strongly affects the fluctuations in the floating platform response. In the aligned wind and waves case, the waves (and wind) propagate in the direction aligned with the surge axis, so surge and pitch are the dominant motions. However, in the 90° misaligned case, the waves propagate along the sway axis, so the sway and roll modes are excited and the surge and pitch motions become very small. A significant increase in the yaw response is also observed, since this is coupled with the roll motions [200]. The sway and roll amplitudes in the misaligned wind and wave case are roughly equal to the surge and pitch amplitudes respectively in the aligned cases.

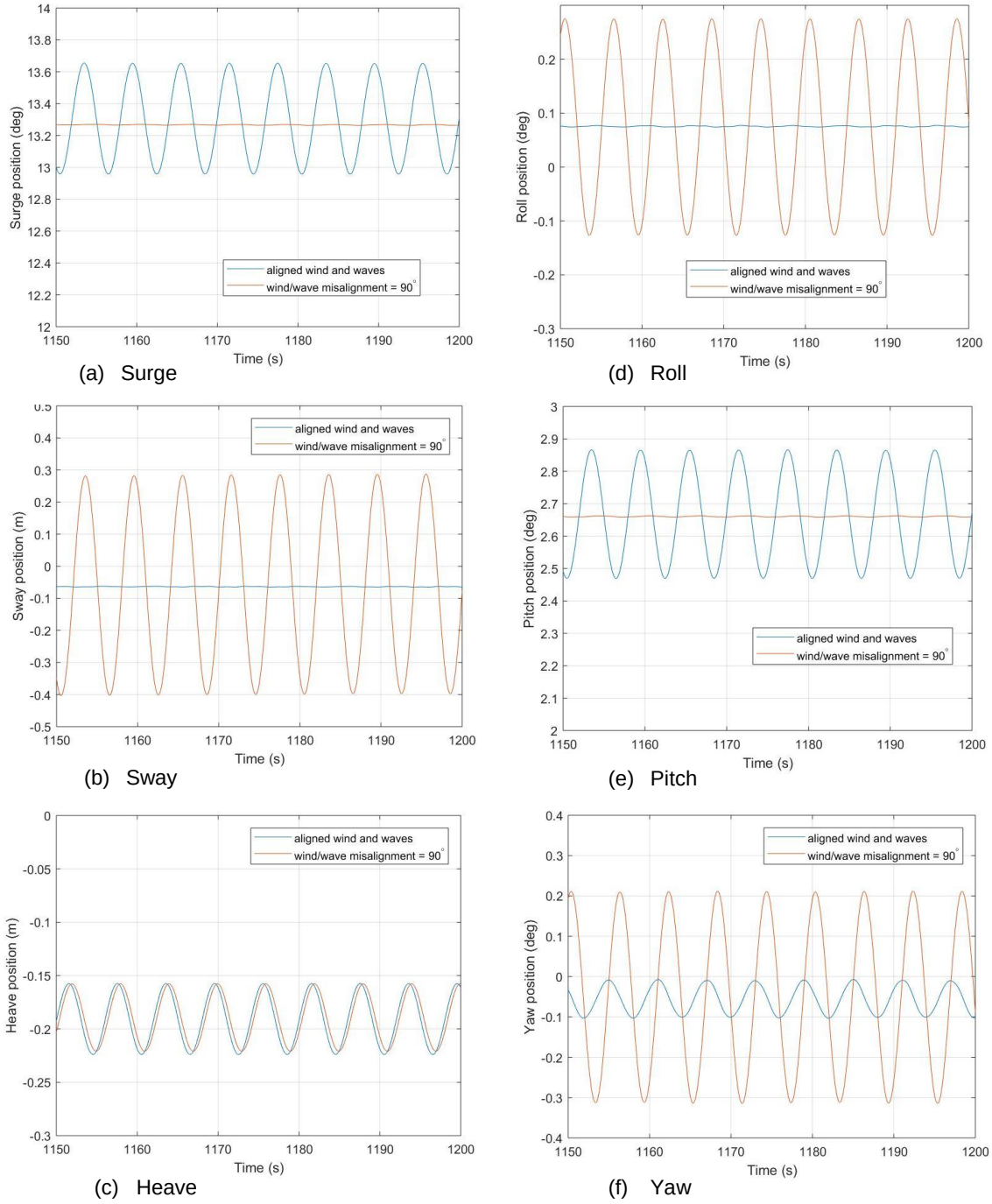

Figure 4.17: Platform motions for the floating turbine in aligned and misaligned wind and waves

4.6.2 Rotor Power and Thrust

The rotor power and thrust for the aligned and misaligned wind and wave cases are plotted in Figure 4.18. The fluctuations in rotor loads are significantly smaller for the wave misalignment case than for the aligned case, since the axial

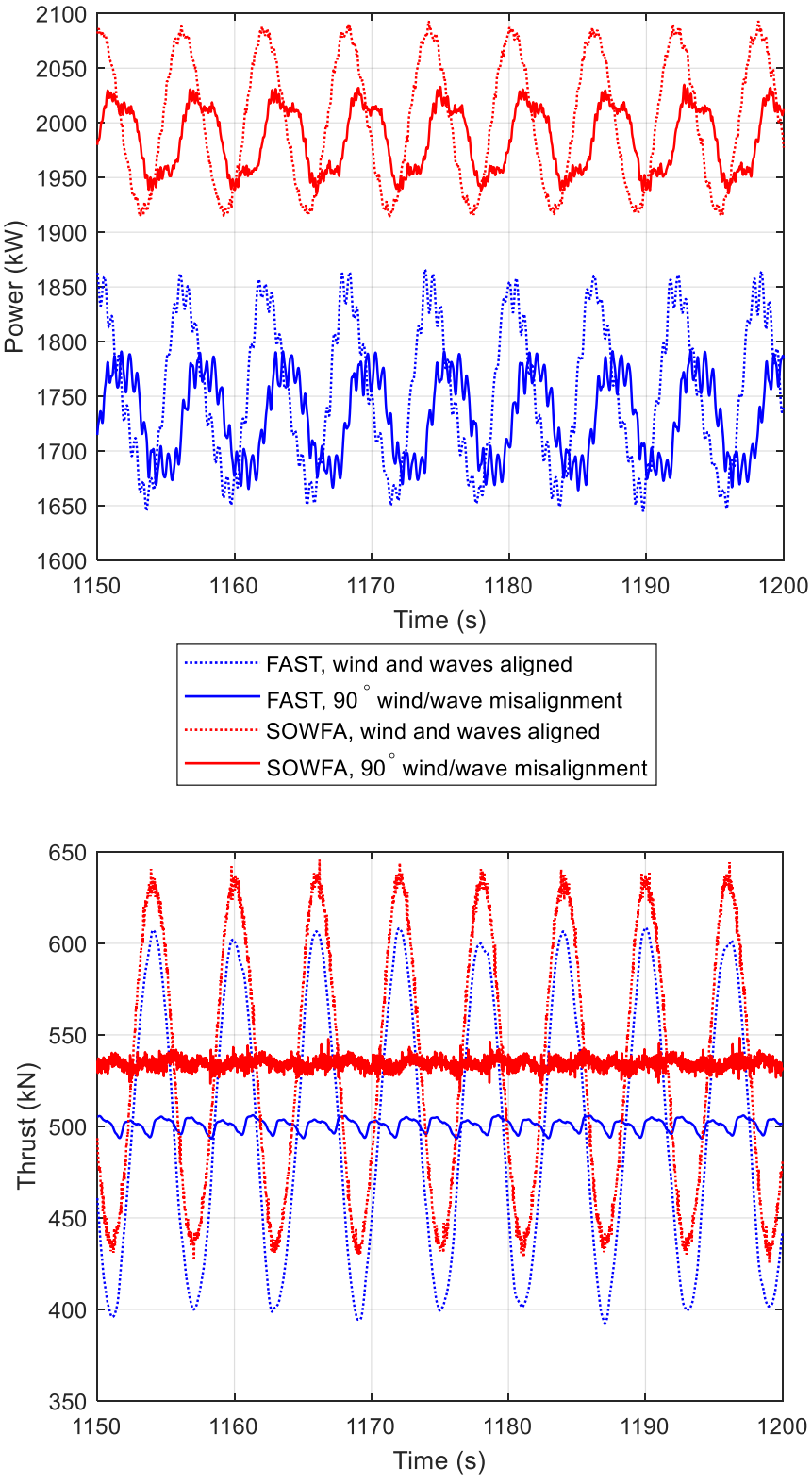

Figure 4.18: Rotor power and thrust in aligned and misaligned wind and waves, U = 8 m/s

component of the relative wind speed at the rotor strongly depends on surge and pitch motions and is mostly unaffected by sway and roll motions. The rotor thrust amplitude is decreased by around 90% in the perpendicular wind and waves case compared to the aligned case, whilst the rotor power amplitude is decreased by nearly a half. A small decrease (around 2%) is observed for the rotor power in

misaligned wind and waves compared with the aligned case, whilst the mean rotor thrust does not change.

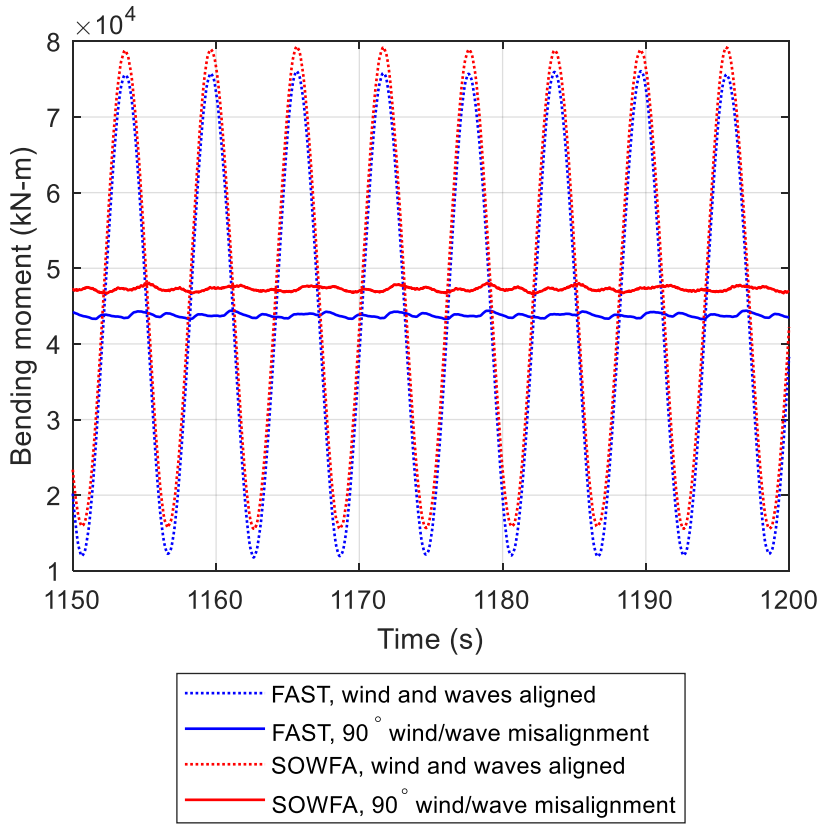

(a) Fore-aft bending

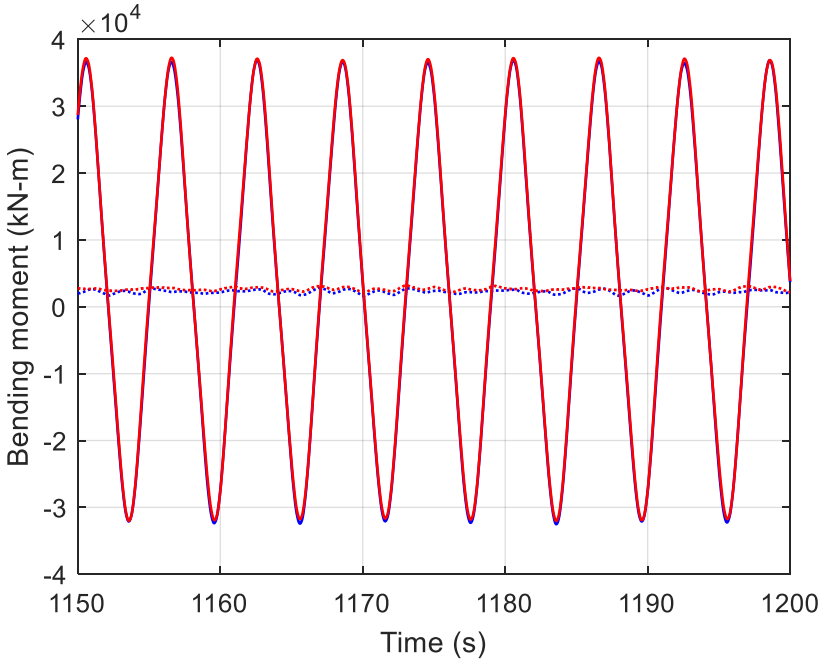

(b) Side-side bending

Figure 4.19: Tower base bending moment in the (a) fore-aft and (b) side-side directions in aligned and misaligned wind and waves, U = 8 m/s

4.6.3 Tower Base Bending

The bending moment in the fore-aft and side to side directions at the tower base for the aligned and misaligned wind and waves is plotted in Figure 4.19. For a floating wind turbine, the fore-aft tower base bending is strongly influenced by the platform pitch response, so when the wind and waves are perpendicular to each other and the pitch motions become very small, the tower fore-aft bending response also drastically reduces. However, the side-side bending response becomes much larger due to the increased roll and yaw motions. It should be noted that whilst the tower side-side bending response does become much larger than the fore-aft bending response in the misaligned case, the fore-aft bending moment was still larger than the side-side bending moment at any point in time. SOWFA predicts slightly larger mean and maximum values for both bending moments than FAST in both the aligned and misaligned wind and wave cases, which can be attributed to the larger mean aerodynamic loads that are consistently predicted by SOWFA.

4.7 Chapter Summary

In this chapter, the use of an actuator line model approach for analysing floating offshore wind turbines is investigated and the results are compared against those from FAST for a range of load cases. The results of this chapter highlight the discrepancies between model predictions using BEM and ALM approaches. Furthermore, the results indicate the load cases for FOWTs where these discrepancies are amplified, potentially due to shortcomings associated with the empirical corrections used in the BEM approach. The key findings from this chapter are as follows:

1. The actuator line model is capable of achieving good agreement with experimental data, particularly for the rotor torque and therefore mechanical power, however the model is highly sensitive to a number of setup parameters, particularly the grid resolution and the ϵ parameter which determines the distribution of the actuator forces onto the fluid domain. Defining ϵ as an elliptical function along the blade leads to improved predictions of the loading in the blade tip region compared to cases with uniform value of ϵ, and may help to avoid errors associated

with numerical oscillations. Using finer grids does not necessarily improve the performance of the model, and may require the tuning of additional parameters.

2. When the wind speed is below the rated value, both the BEM model in FAST and the ALM in SOWFA generally predict that a floating spar-mounted turbine will have a higher mean power output than its bottom fixed equivalent. The predicted increase is slightly larger in SOWFA than in FAST, which may be in part due to the platform pitching motion and nonzero mean pitch (or heel) angle in the floating case, which causes the overall rotor misalignment about the tilt axis to be larger and more variable.
3. An increase in the wave height leads to a near proportional increase in the rotor load variation, whilst an increase in the wave period leads to a large increase in the rotor power but a much smaller increase in the thrust. FAST predicts a rotor power variation that is 7-24% larger than the prediction from SOWFA, which may suggest that the empirical dynamic wake model in FAST overpredicts unsteady aerodynamics due to platform motions.
4. The most significant differences between the FAST and SOWFA predictions for floating wind turbines were found in the cases involving rotor yaw misalignment. BEM method predicts a steeper decline in the mean rotor and blade loads with increasing yaw misalignment than the ALM, and it has been demonstrated that the empirical skewed wake model in FAST may overestimate power losses due to yaw. BEM also predicts a larger variation in the blade bending moments at high yaw angles, which may lead to larger predicted fatigue loads than if an ALM is used.
5. Misalignment between the wind and waves increases the roll and yaw motions which subsequently increase the tower base side-side bending moment, however the tower bending in the fore-aft direction remains dominant.
6. Experimental validation is necessary to determine the extent to which observed differences between FAST and SOWFA are due to inaccuracies in the empirical models used in FAST or the need for further tuning of the actuator line model parameters in SOWFA.

Based on the findings in this chapter, the following recommendations are made:

1. The BEM method in FAST is shown to be capable of modelling the effect of wave-induced floating platform motions on the aerodynamic loads with similar predictions to the ALM used in the SOWFA-FAST coupled model, and is therefore indicated to provide a satisfactory approximation of FOWT aerodynamic behaviour in these simplified conditions.
2. The ALM may be more suitable than BEM for cases involving significant yaw misalignment, where differences between model predictions of blade bending behaviour become significant. This would be important for wind turbines that are intentionally misaligned in order to deflect their wake from downstream turbines, and FOWTs with a low platform yaw stiffness that may result in large angles of rotor yaw misalignment. This may also be significant for FOWTs that experience a large heel angle due to platform pitching.
3. If an ALM is used, careful attention must be paid to the parameter set up, because the optimal numerical configuration may not be the same for all turbines, as indicated by the significantly larger difference between the two models for the NREL 5 MW compared to the NREL UAE Phase VI. It is recommended that the chosen configuration is validated for multiple experimental cases in order to increase confidence in the modelling.

Chapter 5

Impact of Turbulent Wind Input on Model Performance

5.1 Introduction

Chapter 4 featured a model to model comparison for simplified load cases, however, the results could not be validated against any real world data since the NREL 5 MW turbine is fictitious. In this chapter, the performance of the numerical models examined in Chapter 4 are assessed by validating against measured environmental data and platform motions from large scale floating offshore wind turbines. The performance of coupled numerical models for predicting floating offshore wind turbine behaviour is investigated firstly in operational conditions involving power production, and secondly for extreme conditions where the turbine rotor is idle. Unlike the previous chapter which considered only steady, uniform wind and regular periodic waves, this chapter considers floating offshore wind turbine behaviour in realistic turbulent wind and irregular sea states based on measured conditions. The objectives of this study are to investigate how the simulated wind input impacts the ability of numerical wind turbine simulation tools to predict the behaviour of a FOWT, and determine if there are any advantages to using high order numerical modelling such as large eddy simulation in CFD over a lower order alternative for simulating wind inputs. The contributions of this chapter to the overall aims of this work are an assessment of the performance of different levels of numerical modelling compared against full scale field data when realistic environmental conditions are considered.

5.2 FOWT Behaviour in Operational Conditions

In this work, a spar mounted floating offshore wind turbine is simulated in wind and waves typical of operational conditions. The effect of turbulent wind with different speeds and turbulence levels on power production and the turbine and platform response is investigated. Two numerical modelling approaches are compared; a lower order method involving FAST with the BEM method for calculating aerodynamic loads and turbulent inflow wind generated using TurbSim, and a higher order method involving an actuator line model in SOWFA coupled with FAST and turbulent wind simulated using LES in OpenFOAM. The details of these numerical methods are explained in Chapter 3.

5.2.1 Case Study – Hywind Scotland

The performance of each model is assessed against real world measurements using recorded data from the Hywind Scotland Pilot Park [201], which consists of five Siemens 6 MW turbines. The park is located in the Buchan Deep, approximately 25 km from the coast in northeast Scotland, and has an average water depth of 105 m. The data used to validate the numerical models was recorded for turbine HS4 and made available by ORE Catapult in collaboration with Equinor [202]. The field data available for the HS4 turbine consists of time series of the wind speed, platform motions, nacelle yaw angle, nacelle rotational displacement and mooring line tensions recorded over several 30 minute periods between January and July 2018. The environmental conditions averaged over each 30 minute period are also provided, including the mean propagation direction of the wind, waves and current. The wind speed and direction are measured by the turbine's anemometer, and the wave and current conditions are measured by a wave buoy. The rotational motions of the platform are measured using a motion reference unit within the turbine tower, and the translational motions are measured by a GPS antenna. HS4 is positioned furthest south out of the five turbines within the wind farm, and is located approximately 2.5 km west from the wave buoy, as illustrated in Figure 5.1 [163].

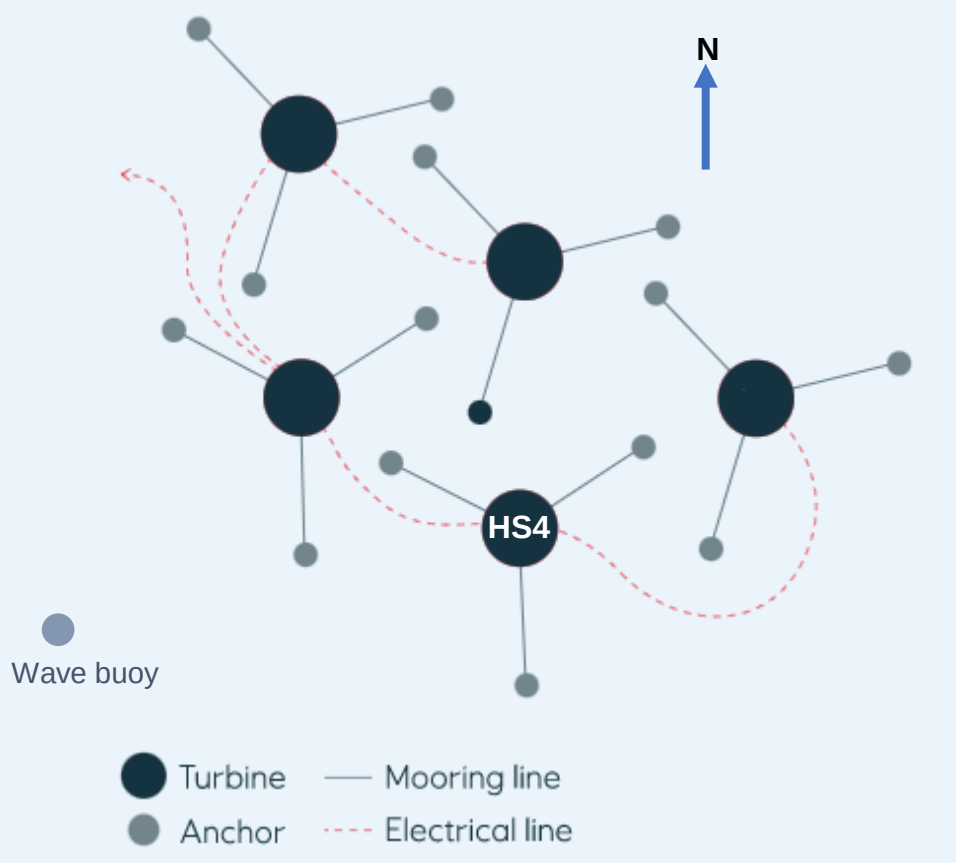

Figure 5.1: Location of turbine HS4 and approximate position of the wave buoy within the Hywind Scotland Pilot Park, adapted from [163]

5.2.2 Simulation Setup

A model 6 MW turbine was created based on the available information for the SWT-6.0-154 turbine developed by Siemens and the floating platform and mooring system used in the Hywind Scotland wind farm. A summary of the turbine properties is provided in Table 5.1. It should be noted that the control system for the model turbine used in this study was defined based on the pitch controller for the fictitious NREL 5 MW turbine installed on the OC3 Hywind spar platform (scaled up from a 5 MW to a 6 MW turbine) [186], and so will not be the same as that developed for the floating Siemens 6 MW wind turbine, since this data is not available. The controller gains and inputs were determined using the formulae given in the NREL 5 MW turbine report [184] and recommendations for adjustments for a spar type platform [186]. The blade geometry for the Siemens turbine is also proprietary, so this was defined in the numerical model by scaling up the length of the blades for the NREL 5 MW turbine to the desired length of 75 m (from 61.5 m). The structural properties for the blade are defined using a

structural concept of the NREL 5 MW blade developed by Sandia National Laboratories [203] and scaling up the length accordingly. The modal frequencies and mode shapes for the adjusted blade are then calculated using the 1D finite element code BModes [204] to be used as input in FAST's structural dynamics module ElastoDyn. It should therefore be noted that the model turbine in this study will not have exactly the same aerodynamic and power performance as the SWT-6.0-154 turbine.

The turbine is simulated in four different 30 minute cases chosen from those measured at the site for HS4. The environmental conditions for each case are listed in Table 5.2. These case studies were chosen to represent a variety of wind speeds within the turbine's operational range. U_{hub} is the mean wind speed at hub height, σ_{hub} is the longitudinal standard deviation of the hub height wind speed, H_s is the significant wave height and T_p is the peak period.

Table 5.1: Key parameters of SWT-6.0-154 turbine used in Hywind Scotland project

Rated power	6 MW
Number of blades	3
Rotor configuration	Upwind
Rotor diameter	154 m
Hub height above MSL	98 m
Cut-in, rated and cut out wind speed	4, 13, 25 m/s
Min, max rotor rotational speed	5, 11 rpm
Platform draft	78 m
Spar diameter above cone section	9.45 m
Spar diameter below cone section	14.4 m

C1 and C2 both represent below rated conditions. The average wind speed of 5.24 m/s in C1 is just above the cut in wind speed and so the rotor loads and power output will be very low, while the 8.49 m/s wind speed in C2 will result in higher power and thrust, but not high enough that the blade pitch controller is active. C3 represents a case where the wind speed is close to the rated value, while C4 represents a high wind speed case close to the cut out condition.

Table 5.2: Environmental conditions simulated, based on those recorded for HS4. All directions are defined as the compass direction from which wind, waves and current are propagating from

	Date & time recorded	U_{hub} (m/s)	σ_{hub} (m/s)	Wind direction (°)	H_s (m)	T_p (s)	Wave direction (°)	Current speed (m/s)	Current direction (°)
C1	14th Apr 2018, 00:25-00:55	5.24	0.74	171	2.1	10.5	107	0.32	15
C2	26th Mar 2018, 23:15-23:45	8.49	0.75	172	2.2	10.6	14	0.24	196
C3	6th Jan 2018, 07:45-08:15	13.72	1.33	11	4.4	10.9	17	0.21	199
C4	14th Jan 2018, 15:25-15:55	20.44	2.07	174	4.2	8.7	165	0.32	204

5.2.2.1 Generating the Turbulent Wind

In the low order modelling, the turbulent wind is generated in TurbSim to be used as input in FAST. As described in Chapter 3, TurbSim generates turbulent wind flow using statistical turbulence models. In this study, the turbulent wind is generated in TurbSim using the Kaimal spectrum model, which is one of the two models specified in the IEC standard for wind turbine design IEC 61400-1 [35] (the other model being the Mann uniform shear turbulence model). As discussed in section 2.1.3, both models assume neutrally stable atmospheric boundary layer flow. Using the Kaimal model, the turbulent fluctuations in the wind flow are scaled to achieve a user defined turbulence intensity at the hub height. Each case study listed in Table 5.2 is run 5 times in FAST using different random seeds for the turbulent wind generation in TurbSim. The turbulent wind is simulated for a 10 minute period, which generates a periodic wind input for the FAST simulations.

The turbulent atmospheric flow in OpenFOAM is simulated using SOWFA's *ABLSolver*, which is an incompressible solver based on the PISO algorithm as described in Chapter 3. Turbulence is modelled using a LES approach. A one-equation eddy viscosity model developed by Deardorff [146] and Moeng [147] is used for the sub grid scale turbulence, which is described in section 3.2.3. Each case from Table 5.2 was initially simulated with a neutral stability condition (CN1 – CN4), since the thermal stratification of the boundary layer in the recorded data is not known. In SOWFA, where a boundary layer height must be specified, the

neutral boundary layer has a height of 800 m in each case, and a capping inversion layer is specified from 800 m to 900 m height above the sea level as described in Chapter 3. Case C2 was also simulated in stable atmospheric conditions (CS2), since the data was recorded at night when the ABL is more likely to be stable, and the recorded wind speed variation was relatively low which suggests low turbulence levels typical of stable atmospheric flow. Likewise, case C4 was also simulated in unstable conditions (CU4), since the data was recorded during the day and the recorded wind speed variation is high, which is typical of unstable ABL flow.

The turbulent wind in OpenFOAM was first generated in precursor simulations involving periodic boundary conditions on all boundaries except for the top and bottom of the domain, and no turbines present. The lower boundary represents the mean sea level, and is represented by a flat surface with a rough wall function. The wall roughness is determined by the surface roughness height parameter z_0, which is described in the following section. The neutral and unstable precursor simulations were run for 20000 s of simulation time in order to allow the flow field to reach a state of quasi-equilibrium. The precursor simulation for the stable ABL required longer in order for the flow field to reach quasi-equilibrium, and was run for 40000 s, as shown in Figure 5.2 where time series of the mean velocity at different heights during the precursor simulations for the neutral and stable simulations of case C2 are plotted. Similar plots for the remaining cases can be found in Appendix B. A variable timestep was used in order to keep the Courant flow number below 0.75 as the turbulent wind develops. The precursor simulations are then continued with a much smaller timestep, and the velocity, temperature and SGS kinetic energy data at the inflow boundary is stored at regular intervals to be used as a time varying turbulent inlet boundary condition in the turbine simulations.

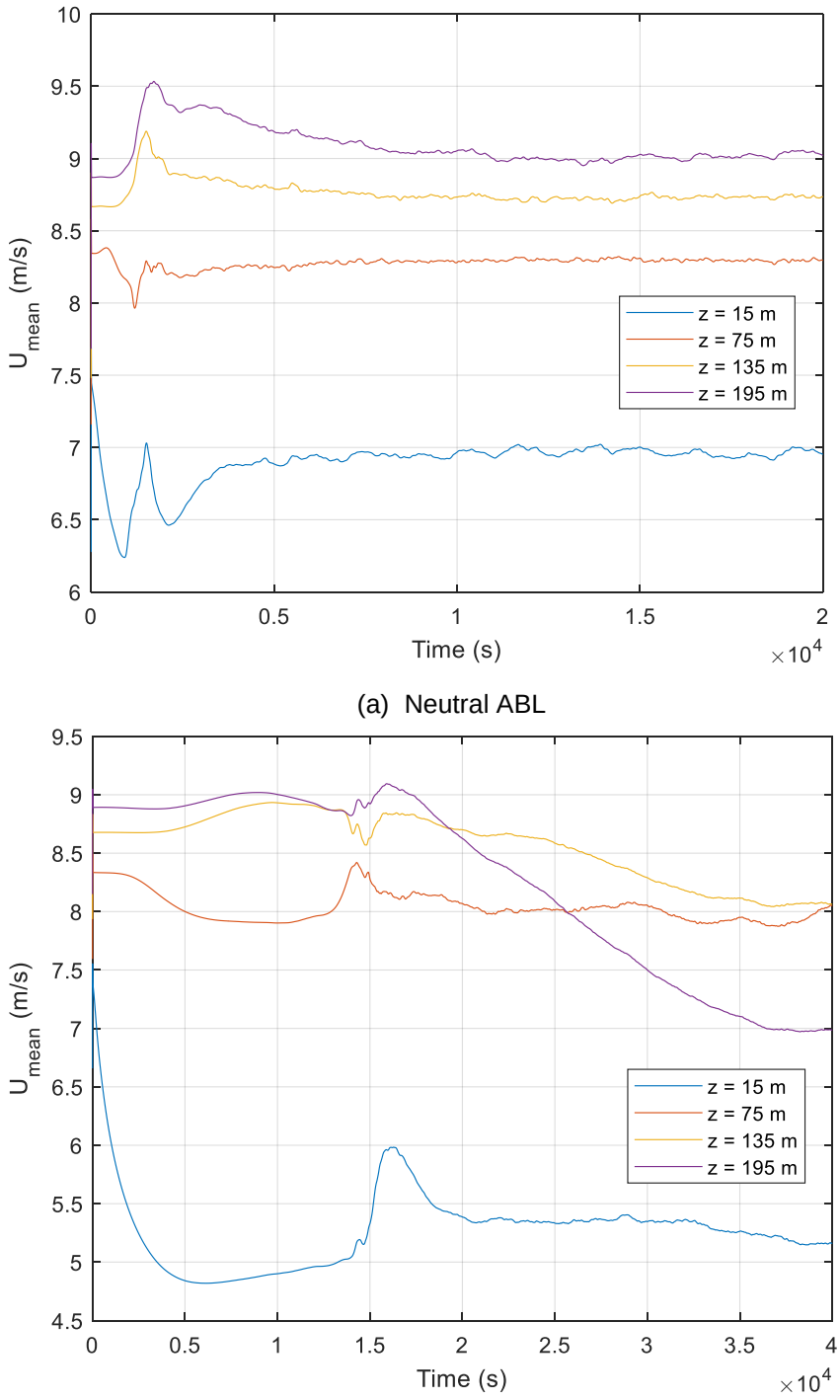

Figure 5.2: Mean velocity in precursor simulations of (a) neutral and (b) stable ABL flow. U_{hub} = 8.5 m/s in both cases.

In the neutral stability ABL simulations, the simulation domain is 3 km long in both the x- and y-directions, and extends 1 km in the upwards z-direction. A uniform 10 m mesh resolution was used in order to ensure that 80% of the turbulence was resolved in accordance with best practices for LES simulation [138], which was estimated by sampling the velocity and SGS turbulent kinetic energy using

probes at selected locations in the fluid domain. This resulted in a mesh size of 9,000,000 cells.

The stable atmospheric boundary layer was simulated in SOWFA by specifying a surface cooling rate, resulting in temperature flux out of the simulation domain and a positive vertical potential temperature gradient ($\partial\theta/\partial z > 0$). The height of the capping inversion layer was reduced to 300 m, which is a more typical boundary layer height for a stable ABL [205]. The domain size can be reduced due to the smaller turbulent length scales, so a simulation domain extending 1 km in the horizontal x- and y- directions and 500 m in the vertical z-direction with a uniform 10 m resolution was used, which satisfies the guidelines for simulating a stable ABL in SOWFA presented by Churchfield (2017) [169]. The mesh size is 500,000 cells.

The unstable boundary layer was simulated by specifying temperature flux into the simulation domain, and increasing the boundary layer height to 1500 m, which is more typical of unstable conditions [31]. The simulation domain must be larger in all directions to accommodate for the longer turbulent length scales and thicker boundary layer, so a domain size of 5 x 5 x 2 km was used in accordance with the guidelines for the use of SOWFA [169]. The unstable boundary layer is typically characterised by larger turbulent structures than the neutral or stable ABL [153]. Therefore, the mesh cell size was increased to give a uniform 20 m grid resolution, which was found to be sufficient in ensuring that less than 20% of the turbulence was resolved using the SGS model. The total mesh size is 6,250,000 cells.

5.2.2.2 Estimating the Roughness Height z_0

The turbulence intensity, TI, in the cases from the field data listed in Table 5.2 is not known, and so is estimated based on the measured value of σ_{hub}, where $TI_{hub} = \sigma_{hub}/U_{hub}$. It should be noted that this estimation gives a 1-D turbulence intensity, since only the longitudinal (*u*) component of the wind speed is given in the data. This means that the lateral (*v*) and vertical (*w*) turbulent fluctuations, which lead to variation in the horizontal and vertical direction of the wind, are not considered.

Unlike in TurbSim where the TI is a direct input in the Kaimal model, the level of turbulence in the atmospheric flow simulated in SOWFA is dependent on the tuning of key parameters, which include the surface heat flux due to the atmospheric stability condition and the aerodynamic roughness height z_0. However, the sea surface roughness is dependent on the wave conditions which in turn are dependent on the wind speed. In the presented simulations, the roughness height of the sea surface is estimated based on the Charnock relation [150] using the methodology presented in section 3.2.4. The Charnock constant α in equation 3.25 was chosen to have a value of 0.017 based on the estimation by Wu [206] for a von Karman constant value $\kappa = 0.4$. The estimated roughness heights for the four cases simulated are listed in Table 5.3.

Table 5.3: Estimated friction velocity and roughness height based on the Charnock relation for each condition

Case	Wind speed (m/s)	Estimated u_* (m/s)	z_0 (m)
C1	5.24	0.30	0.00015
C2	8.49	0.30	0.00016
C3	13.72	0.53	0.00049
C4	20.44	0.83	0.0012

5.2.2.3 Turbine Modelling

The turbine aerodynamics are modelled using the same approaches as those used to model the NREL 5 MW turbine in the previous chapter. In the FAST only simulations where TurbSim wind fields are used as input, aerodynamics are modelled using the BEM theory with various empirical corrections to account for blade tip/root effects, skewed wake due to rotor yaw, and unsteady aerofoil aerodynamics.

For the turbine simulations using an actuator line model in SOWFA, the computational domains have the same background mesh resolution as the corresponding precursor simulations (uniform 10 m in neutral and stable flow, 20 m in unstable flow). The turbine is positioned at the horizontal centre of the domain, and the mesh was locally refined to give a grid resolution of 2.5 m at the location of the turbine. For the Hywind turbine, this gives a grid resolution $\Delta x = R/30$, which is the same relative grid resolution as that used to study the NREL

5 MW turbine in Chapter 4. The domain size for the turbine simulations in neutral ABL flow was reduced to 1.2 x 1.2 x 1 km in the x-, y- and z- directions, and in unstable flow was reduced to 3 x 3 x 2 km in order to reduce the computational cost. The turbine rotor is discretized using 40 actuator points for each blade, which equates to a spacing $\Delta b = 1.875$ m between each point, and an elliptical function of ϵ as described in Chapter 4 is used to define the distribution of actuator point forces onto the fluid. A time varying inflow condition is defined at the inlet boundaries using the stored data from the precursor simulation with linear interpolation in time to account for the different timesteps used in the precursor and turbine simulations. In all cases, the turbine is simulated for 40 minutes, where the first 10 minutes are removed from the results in order to omit start up transient effects.

The platform hydrodynamics in both methods are modelled using first order potential flow theory and Morison's equation in HydroDyn [94]. The waves are modelled without directional spread using the JONSWAP spectrum with a significant wave height and peak period corresponding to the conditions listed in Table 5.2. The default values of σ and γ as described in IEC 61400-3 [43] are used in all cases.

5.2.3 Results

5.2.3.1 Wind Field Characteristics

The one dimensional hub height turbulence intensities from the SOWFA simulations for each case is shown in Table 5.4. The calculated turbulence intensity at the hub height for the neutral cases is consistently lower than that estimated from the variation in the wind speed recorded by the anemometer for HS4. However, the variation in the field data may not be solely due to freestream turbulence, and may have been influenced by additional factors such as shadow effects from the rotor blades passing in front of the anemometer. As expected, the stable ABL has a lower TI than the corresponding neutral case, and unstable conditions lead to a higher TI.

Table 5.4: Turbulence intensities estimated from the provided data compared against LES wind field

Case	Estimated TI from field data (%)	TI from LES (%)
CN1	14.1	8.2
CN2	8.8	7.0
CS2	8.8	2.7
CN3	9.7	7.9
CN4	10.1	7.7
CU4	10.1	10.3

In TurbSim, wind fields with the estimated TI from the field data are generated for each of the four cases C1-C4. In order to determine that any observed differences between FAST and SOWFA predictions of turbine response are not solely due to differences in turbulence intensity, TurbSim is then used to simulate separate wind fields for cases CN1-CN4 and CS2 in which the hub height turbulence has been scaled to match to the corresponding TI from SOWFA. A TurbSim wind field corresponding to case CU4 is not generated since the turbulence intensity from the SOWFA simulation for this case was very close to the estimation from the field data. It should be noted once again that the wind fields in TurbSim are all simulated using the Kaimal model, which only models neutral conditions, so it is only the hub height turbulence intensity that has been matched with the SOWFA simulations.

The mean wind shear profiles for each case is shown in Figure 5.3. The wind shear profile in TurbSim is predetermined according to the log law for the reference wind speed at the hub height and the roughness height given in Table 5.3 (see equation 3.17). The wind shear profile in the neutral ABL simulations in SOWFA is close to the TurbSim wind shear for the rotor disk region. The unstable ABL simulation shows slightly less shear than the neutral profile, whilst an inversion in the wind shear can be observed for the stable ABL due to the presence of a low level jet. Wind shear is important to consider as this may impact the cyclic loading on the blades due to the variation in wind speed with azimuthal position.

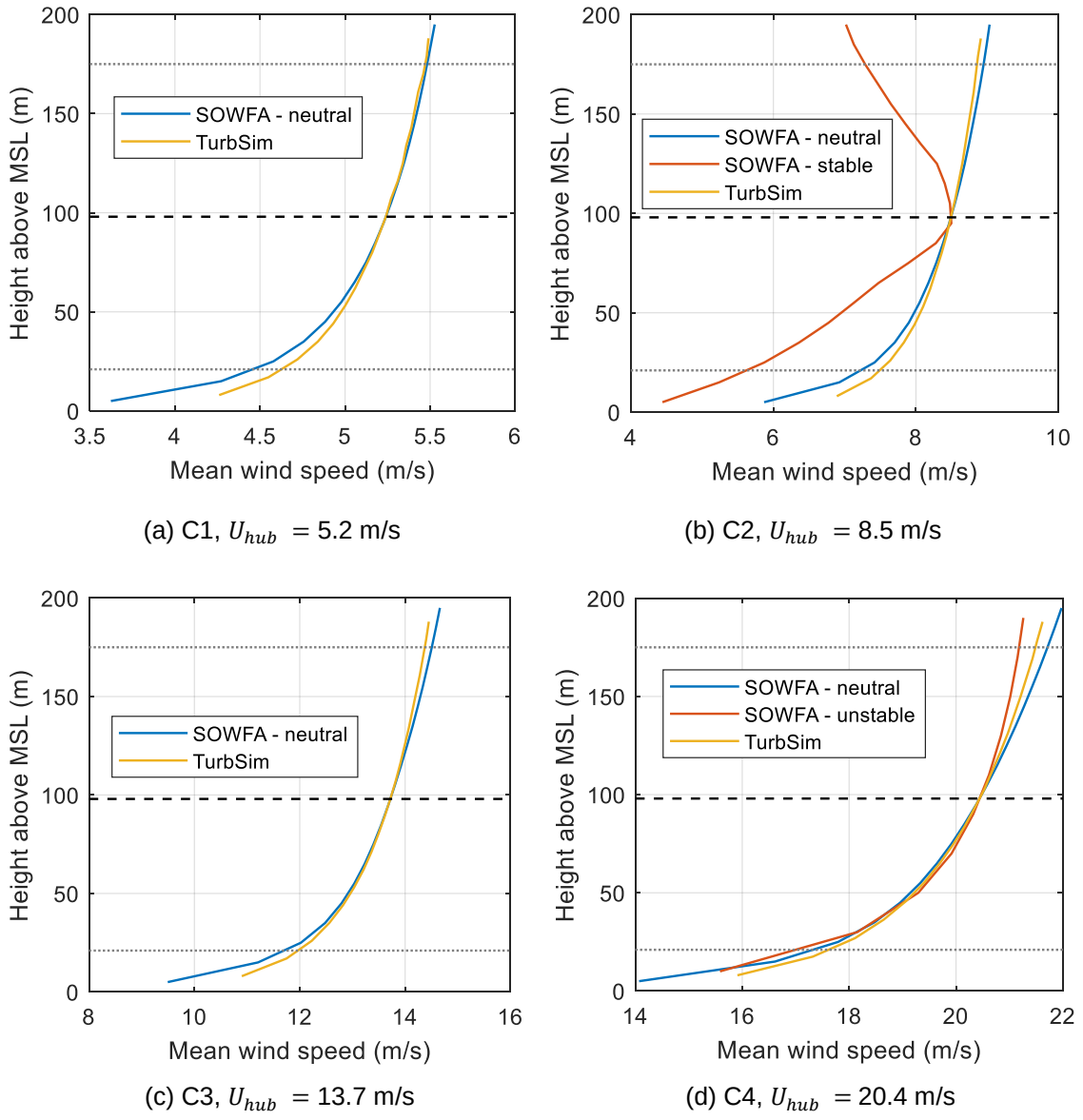

(a) C1, U_{hub} = 5.2 m/s

(b) C2, U_{hub} = 8.5 m/s

(c) C3, U_{hub} = 13.7 m/s

(d) C4, U_{hub} = 20.4 m/s

Figure 5.3: Simulated wind shear profiles for each of the four sets of conditions listed in Table 5.2. The dashed black line represents the turbine hub height, and the dotted lines represent the top and bottom of the rotor disk area.

Figure 5.4 shows the change in mean wind direction with height, known as wind veer, and how this varies depending on the atmospheric stability condition for cases C2 and C4. In the TurbSim wind fields, the mean wind direction is constant across the grid. A low level of wind veer is observed for the neutral SOWFA cases, which is primarily due to the Coriolis force term. The unstable case shows very low veer, whilst the stable ABL exhibits significantly higher wind veer, with a change in wind direction of around 25° across the rotor disk area. This may affect turbine loads due to the additional cyclic variation in the inflow angle of attack, particularly in the tip region of the blade.

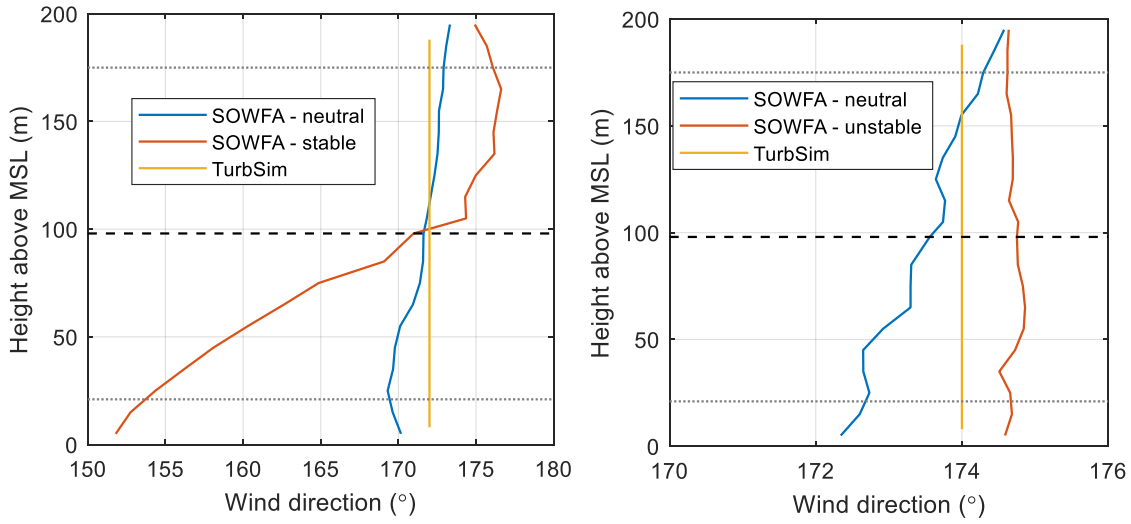

(a) C2, U_{hub} = 8.5 m/s (b) C4, U_{hub} = 20.4 m/s

Figure 5.4: Wind veer profiles for cases (a) C2 and (b) C4. The dashed black line represents the turbine hub height, and the grey lines represent the top and bottom of the rotor disk area.

The standard deviations of the u-, v- and w- components ($\sigma_u, \sigma_v, \sigma_w$) of the simulated wind speed for case C2 are plotted in Figure 5.5. The plotted values from SOWFA include the contributions from sub grid scale kinetic energy k_{sgs}. The plotted standard deviations for the other cases can be found in Appendix C.1. These indicate how the level of turbulence varies with height; σ_u describes the variation in the axial wind speed, whilst σ_v and σ_w describe the variation in the horizontal and vertical wind direction respectively. The wind profiles simulated using the Kaimal spectrum in TurbSim have constant values of σ_v and σ_w with height, whilst σ_u shows some variation due to the IEC spatial coherence model used [152]. In the SOWFA simulations, the horizontal turbulence (u and v components) is generally highest close to the sea surface, and decreases with increasing height. It can be seen that even when the hub height longitudinal turbulence in TurbSim is matched with the value from SOWFA, this does not mean that the wind at hub height is the same in each model; the lateral component of turbulence is approximately the same in each model at low wind speeds, but in cases C3 and C4 the v- component in SOWFA is generally smaller than in TurbSim, while the vertical component from SOWFA is larger in all cases.

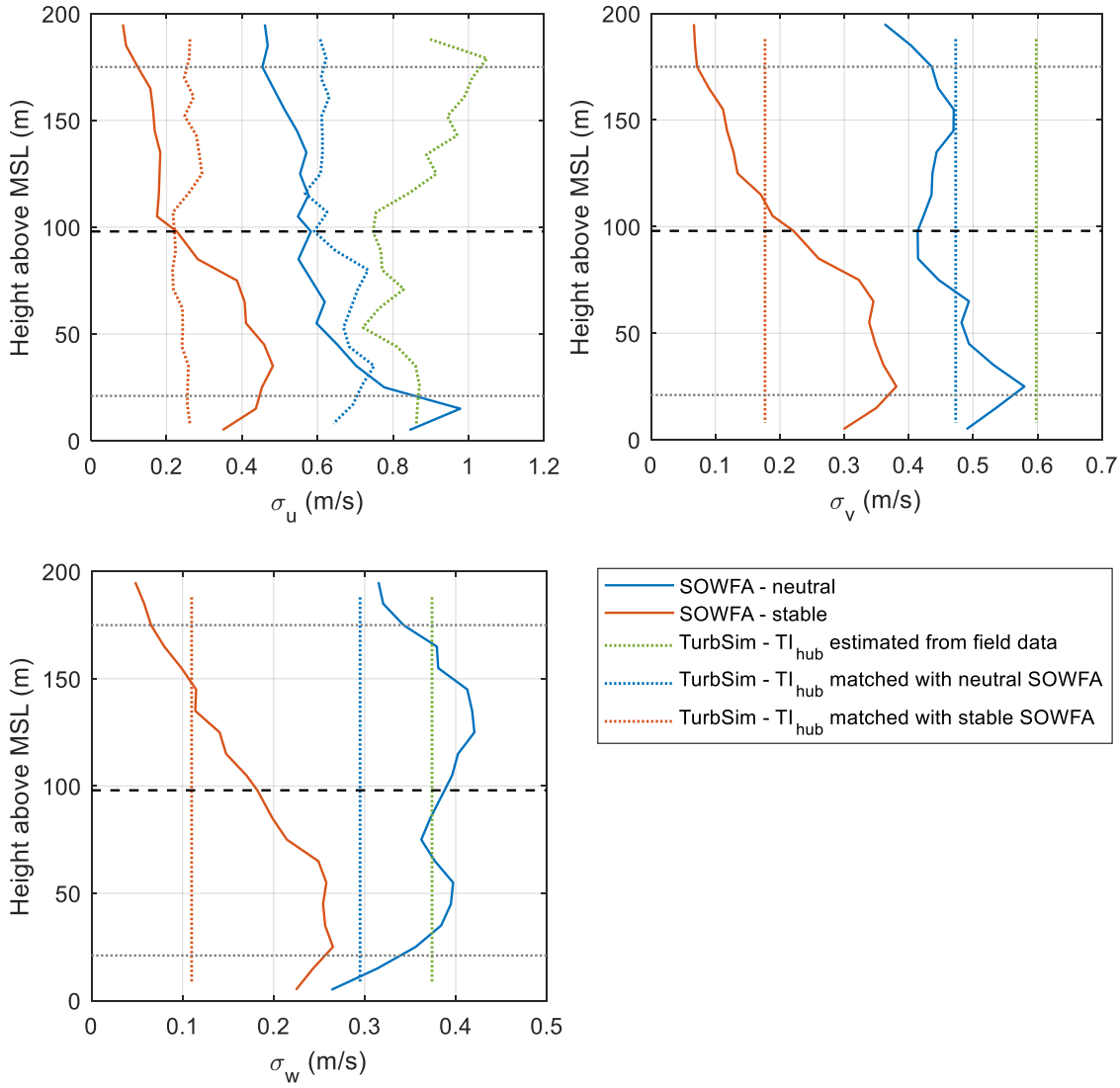

Figure 5.5: Standard deviation of the u-, v- and w- components of the wind speed for case C2. The dashed black line represents the turbine hub height, and the grey lines represent the top and bottom of the rotor disk area.

5.2.3.2 Platform Motions

The platform response is measured in the global coordinate system for all cases. The reference point is the turbine's equilibrium position at the mean sea level. Surge motion is defined along the x-axis and sway motion is defined along the y-axis, where positive surge and sway motion corresponds to the turbine positioned south and east respectively from the equilibrium position. Likewise, roll and pitch motions are defined about the x- and y-axes respectively. This is important to note as it means that the coordinate system of the platform does not coincide exactly with the rotor axis, since the nacelle yaw angle is fixed in the simulations so that the rotor axis is aligned with the mean wind direction listed in Table 5.2 in each case. The apparent wind speed at the rotor will therefore be affected by

sway and roll motions. However, since the mean wind direction is always aligned close to directly north or south in this study, sway and roll motions will have little influence on the apparent axial wind and power production.

The simulated platform response from each numerical model is compared against the field data in Figures 5.6 to 5.8. The heave motion of the platform is not shown here since the heave data for the Hywind turbine was not available. The data for the measured platform yaw motion prior to April 2018 showed a mean value of approximately 9°, which is noted by Equinor as an error in the data [207], and so the yaw data for the affected cases (C2, C3 and C4) is plotted with a 9° yaw offset removed in order to be able to compare the data more easily.

The results from FAST plotted in Figures 5.6-5.8 show the platform response does have some correlation with the turbulence intensity; in case C2 when the TI is matched with the low value from the stable SOWFA simulation (indicated by the red and dark red lines), the platform response in all degrees of freedom was lower than in the cases with higher TI. However, the highest TI does not always correspond with the largest response. For example, in case C3, FAST predicted larger sway and pitch motion response in less turbulent wind (dark blue line).

The platform response is shown to be sensitive to the atmospheric stability condition; the SOWFA simulation CU4 with the unstable ABL shows a larger response in all platform degrees of freedom than its neutral ABL equivalent CN4, and the platform response in the stable case CS2 is significantly smaller than in the neutral equivalent SOWFA case CN2.

FAST and SOWFA generally predict very similar mean values for the platform displacements, particularly at higher wind speeds. The maximum difference between model predictions at each wind speed is around 0.8 m for the mean translational (surge and sway) displacement and 0.8° for the rotational (roll, pitch and yaw) displacement. The largest differences in mean platform displacement are between the neutral and stable ABL simulations of case C2 in SOWFA, which suggests that the stable ABL results in lower aerodynamic loads (discussed in the following section) than the neutral case.

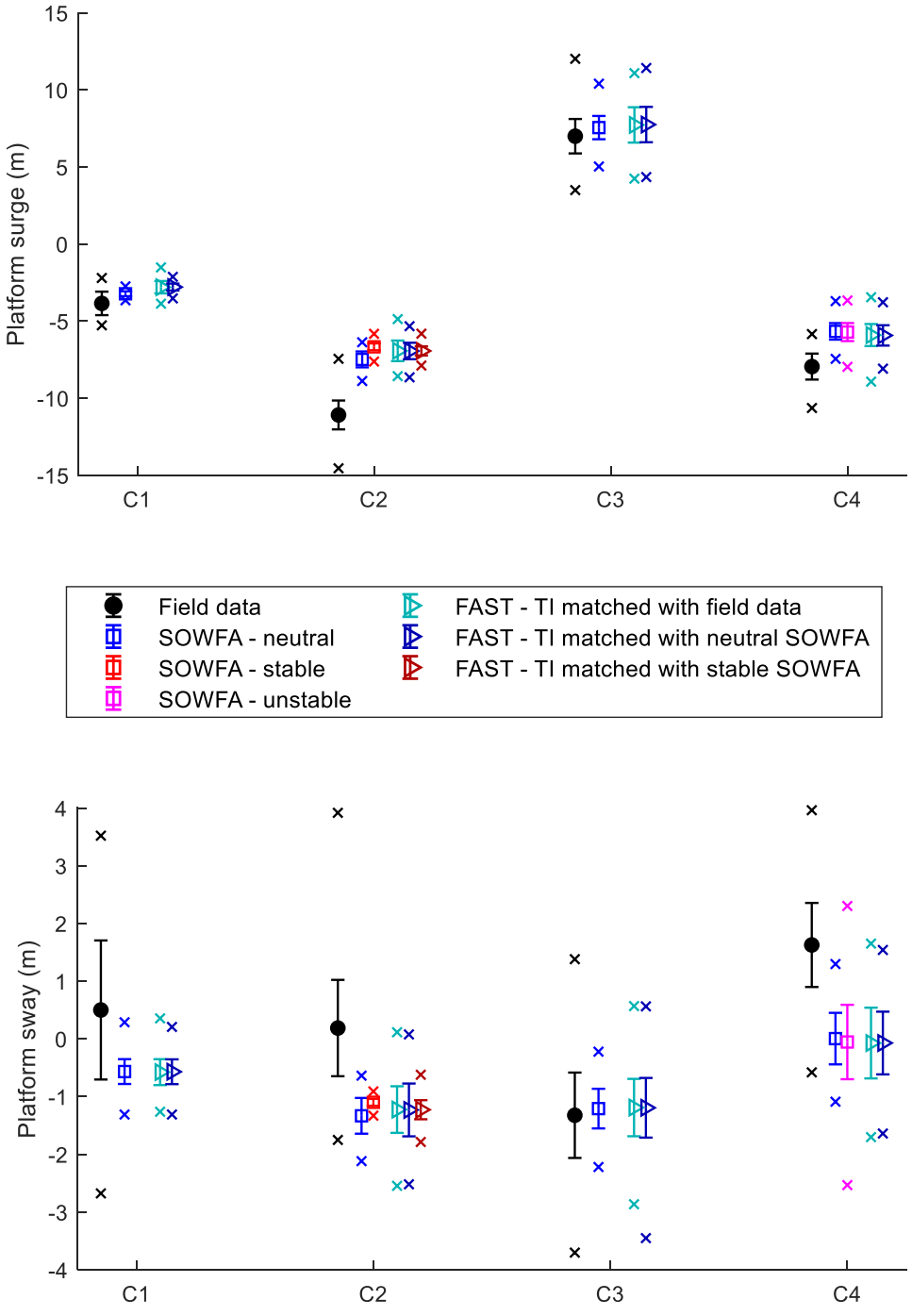

*Figure 5.6: Platform surge and sway motions from the field data and numerical modelling. The circle, square and triangle symbols denote the mean value, error bars show one standard deviation above and below the mean, and **x** denotes the minimum and maximum values.*

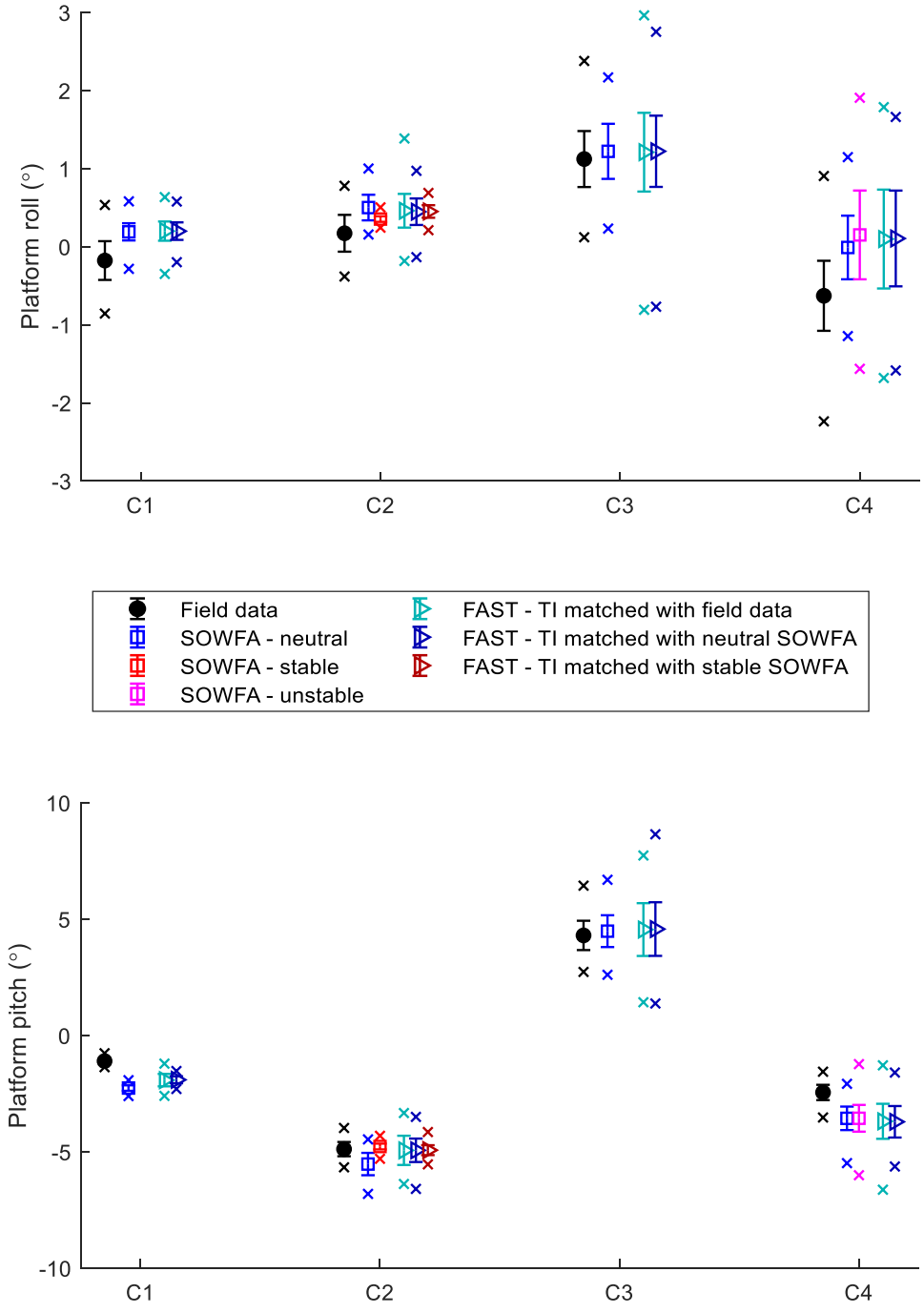

Figure 5.7: Platform roll and pitch motions from the field data and numerical modelling

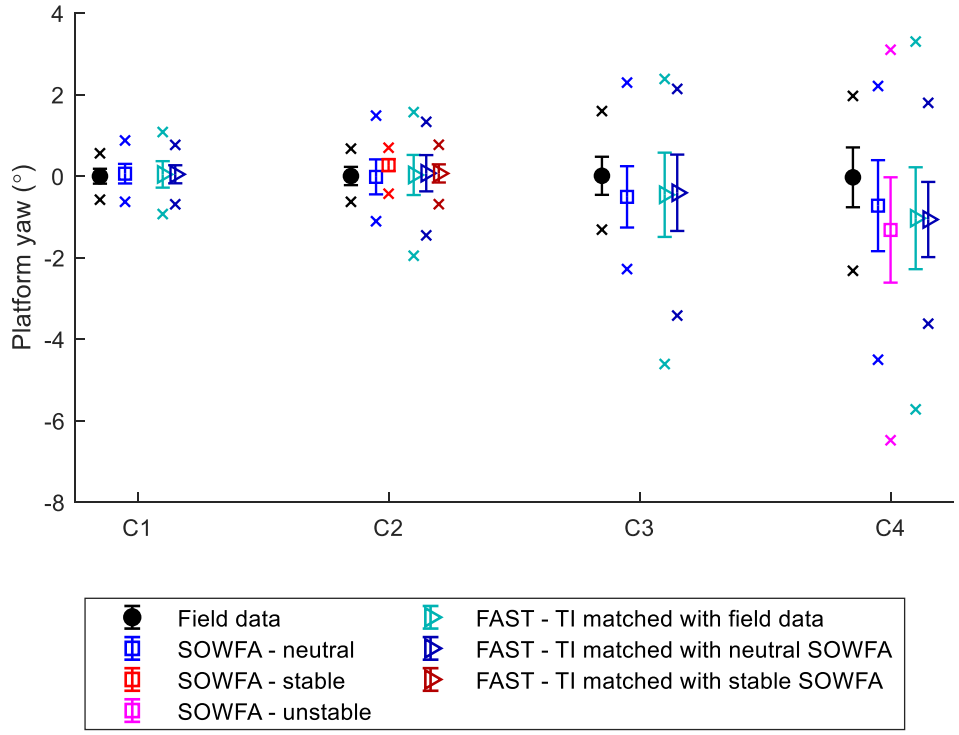

Figure 5.8: Platform yaw motion from the field data and numerical modelling. An offset of 9° has been removed from the field data for cases C2, C3 and C4 because this is noted as an error in the data

Due to the direction of the wind and therefore the axial thrust force produced by the rotor, the mean surge displacement is much larger than the mean sway in all cases, and this is captured by the numerical models. In cases C1 and C2, where the wind speed is below rated, all of the numerical modelling significantly underpredicts the translational (surge and sway) motion as shown in Figure 5.6. The sway motion in particular is poorly predicted, with all numerical modelling predicting a range of values that is less than half of the measured range in both C1 and C2.

The GPS device measuring the translational motion is positioned approximately 15 m above the mean sea level on the turbine tower, and so the measured surge and sway motions may be influenced by rotational motions. However, the pitch and roll motions are small, with a maximum range of roughly 7° so this would not influence the translational motions enough to explain the large differences between the measured surge and sway response and the numerical predictions. The mean pitch position of approximately 5° in case C2 is also not large enough to fully account for the noticeable error of more than 3 m in the mean surge

displacement. This offset implies that there is an error in the calculated aerodynamic loads (examined in the following section), which is expected since the blades and the control system are not the same as those for the Hywind turbines (since this information was not available). The differences between the measured and numerical values for the mean surge and sway displacement can also be in part attributed to starting the simulations with the turbine at the equilibrium position.

The hydrodynamic modelling may be another source of error in the platform surge and sway response. Directional variation in the waves was not included in the numerical simulations, which is likely to be a reason for the underestimated sway response [208]. It should also be noted that in the provided data, the mean propagation directions of both the wind waves and the swell were reported [207], whereas the numerical modelling only considered the 'total' propagation direction since it is not possible to separate the wind sea and swell components in HydroDyn. The difference between the direction of the two components was small in most cases (less than 5°), but for case C2 was reported to be approximately 70°, which may impact the platform response.

For the rotational motions, the agreement between the numerical models and the measurements is generally good for the mean displacements. In all cases, the largest rotational motion is the platform pitch, and the maximum error in the mean pitch angle is around 1.3°. In cases C2 and C3, where platform pitch is largest, all of the modelling predicts a mean error of less than 0.7° compared to the field data. However, in all simulations except for the stable SOWFA case CS2 and the corresponding FAST case with the same low TI, the platform pitch and yaw motion response is overpredicted compared to the measurements. In all wind speed cases, the standard deviation of the pitch motion when the TI matches the estimated value from the field data is at least twice as large as that for the measured pitch motion. The roll response is also overpredicted by FAST in above rated wind cases (C3 and C4). These discrepancies may be partly due to differences between the controller defined for the numerical models and that implemented in the Hywind Scotland turbines, meaning that the rotational motions of the numerical model turbine are not sufficiently damped in above rated conditions. However, this does not explain the overestimated pitch and yaw

motions at below rated wind speeds in cases C1 and C2 where the pitch controller is not active, which suggests that the Hywind turbines have additional damping in these rotational modes that has not been included in the presented numerical models. Another contributing factor may be that the Hywind turbines have nacelle yaw control which could have further damped the platform yaw motions. The nacelle yaw angle was defined as a fixed value in all simulation cases to reduce model complexity, and because in most cases the recorded nacelle yaw variation was small (among the chosen case studies, the case with largest nacelle yaw response was case C3 with a range of approximately 12° during the 30 minutes of recorded data). The nonzero response of the nacelle yaw control system also indicates a gradual change in the mean wind direction over time, which would not be reflected by the turbulence modelling and may therefore be another reason for the underpredicted surge and sway motions as seen in Figure 5.6

It is noted that FAST generally predicts larger sway, roll and pitch responses than SOWFA in neutral cases when the longitudinal TI is the same in both models, except in the lowest wind speed case C1. The difference is most significant in the pitch motion from case C3, where the pitch standard deviation from FAST is 69% larger than that from SOWFA. This may be partially caused by the use of multiple random seeds in the generation of wind fields in TurbSim, whilst the SOWFA models were simulated only once. Alternatively, this suggests that the lateral component of the turbulence does have an effect on platform motions, since σ_v was shown to be higher on average in the TurbSim wind fields than SOWFA (see Figure 5.5 and Appendix C.1) in all cases except C1. It is however noted that the unstable SOWFA simulation CN4 (pink line) does not result in lower motion response than the FAST simulation with a similar longitudinal TI despite having lower σ_v (see Appendix C.1), and that the sway response is in fact larger in the unstable SOWFA-generated wind than in any of the neutral wind simulations for case C4. This suggests that the turbine response is also affected by the larger turbulent flow structures characteristic of unstable conditions compared to the neutral case, which would exert a larger dynamic force on the turbine as discussed by Sathe et al. [32]. The sway motions from FAST show closer agreement with the field data than the neutral cases in SOWFA, whilst the opposite is true for the pitch motions, so it is not possible to say which wind field has lateral turbulence that is closer to that of the actual measured wind.

5.2.3.3 Rotor Loads

The numerical model predictions of the rotor power and thrust variation for each case are plotted in Figure 5.9. The field data for HS4 did not contain any measurements of the rotor loads or power production, so the numerical models can only be compared against each other.

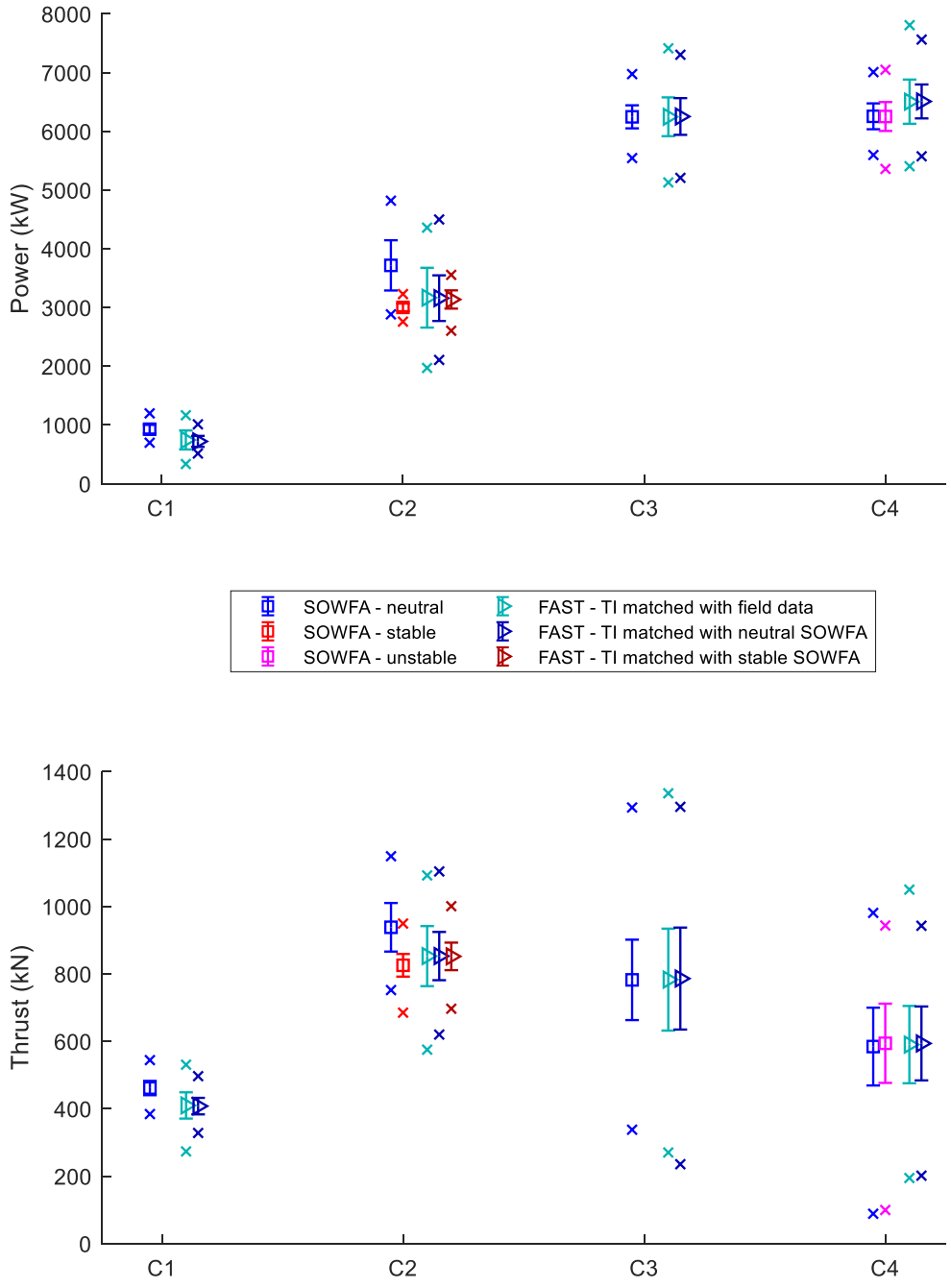

Figure 5.9: Model predictions of rotor power and thrust

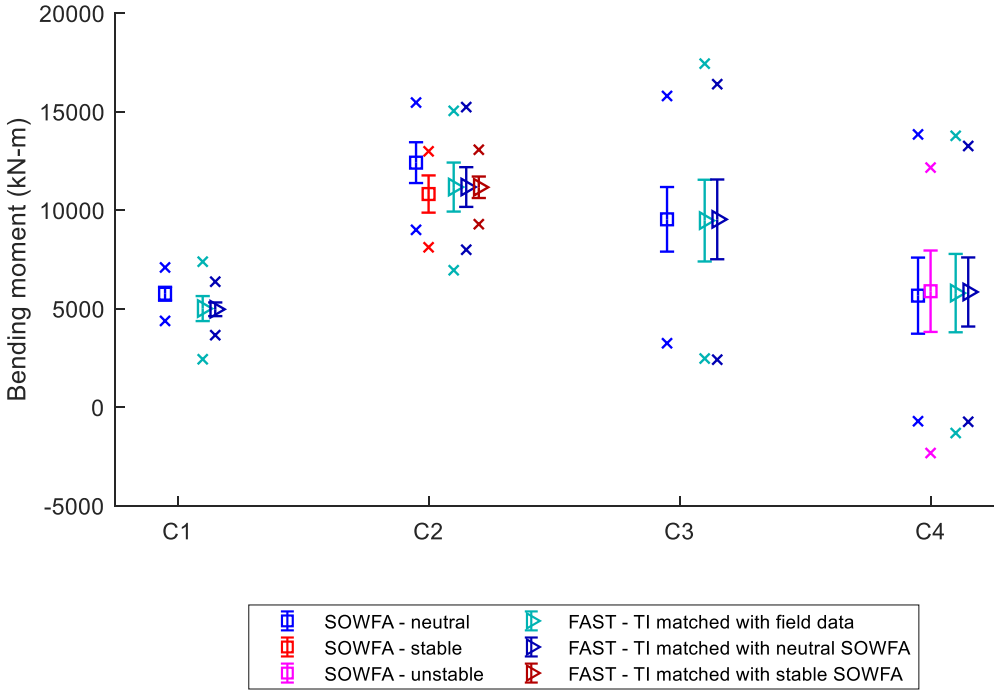

(a) Out-of-plane bending

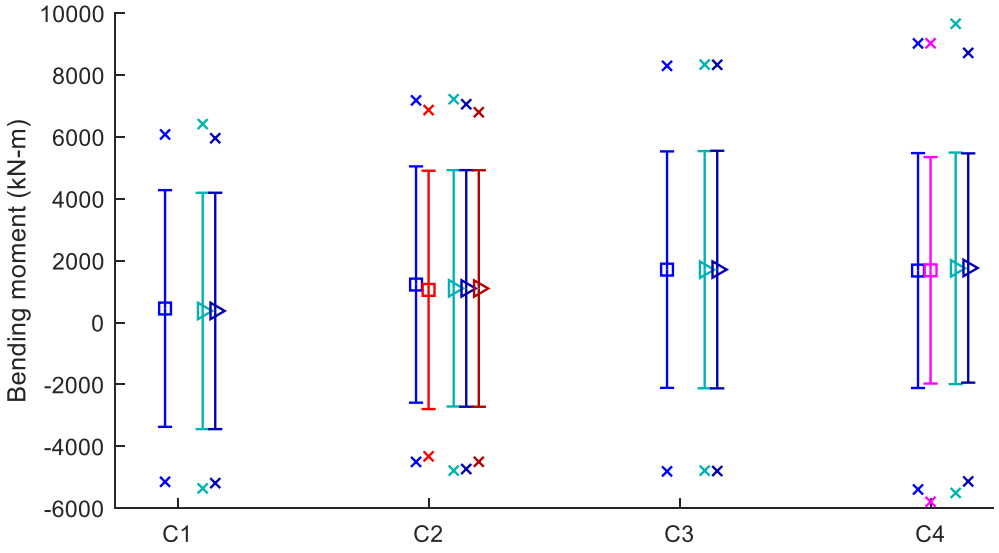

(b) In-plane bending

Figure 5.10: Model predictions of (a) out-of-plane and (b) in-plane bending moment at the blade root

Similar to the platform motions, higher turbulence intensity generally results in larger variation in the rotor loads, since this means there is a larger variation in the wind speed experienced at the rotor. In the below rated cases C1 and C2, FAST predicts a lower average rotor power and thrust than the neutral cases in

SOWFA. This is consistent with the results observed in Chapter 4. Both models show that the highest mean rotor thrust occurs in case C2, but the largest variation in the thrust and the peak values occur in case C3, when the wind speed is closest to the rated value. The lower turbulence levels in the stable atmospheric conditions present in case CS2 lead to decreased fluctuations in the rotor loads compared with the neutral case. The higher turbulence in the unstable conditions in case CU4 result in larger power variations than in neutral conditions, though the thrust is relatively unaffected since the wind speed is above rated and so the blade pitch controller acts to limit rotor thrust fluctuations. The ranges of simulated values for the thrust force in the above rated conditions C3 and C4 are particularly large, with the FAST simulations for case C3 showing a range of over 1000 kN. This corresponds with the overestimated pitch and roll motions in these cases observed in Figure 5.7, and further suggests that the control system specified for the numerical modelling does not accurately represent that of the Hywind turbines and could be improved. The stable case CS2 results in lower mean rotor loads than the neutral case at the same wind speed (8.5 m/s), which explains the lower mean platform displacement observed in Figures 5.6 and 5.7. This may be caused partly by the low level jet wind profile which results in a lower wind speed above the hub height than in the log law wind shear profile observed for the neutral wind field.

The blade root bending moments in the in-plane and out-of-plane directions are plotted in Figure 5.10. The statistics are calculated from one blade, labelled blade 1 in FAST, which is initialized at the 0° azimuth position in each simulation. It can be assumed that the bending behaviour will be roughly the same for all three blades in operational conditions because any fluctuations due to rotor rotation will be averaged out over the 30 minutes of simulation time. Out-of-plane bending follows a very similar trend to rotor thrust, as was also seen in the cases with steady wind in Chapter 4. The variation in the out-of-plane bending moment in the stable SOWFA simulation is larger than the corresponding FAST case with the same TI (indicated by the dark red line plot). This may be due to the strong wind shear and wind veer in the stable ABL as shown in Figures 5.3 and 5.4, and is evidence that stable atmospheric conditions have an effect on turbine loading beyond simply having lower levels of turbulence as previously shown by Doubrawa et al. [39].

Both models predict that the peak values for the blade out-of-plane bending occur in case C3, when the wind speed is closest to the turbine's rated value. The in-plane bending on the other hand continues to increase with wind speed, with the maximum values observed in case C4.

5.3 FOWT Behaviour in Extreme Conditions

When the wind reaches a speed above the turbine's cut out wind speed, the turbine stops producing power and switches to either a parked or idling state, and a shutdown strategy is implemented to reduce the aerodynamic loads on the rotor in these extreme conditions. This usually involves pitching the blades to close to 90° to provide aerodynamic braking, known as a pitch-to-feather strategy [50]. This work investigates the use of numerical modelling methods for simulating extreme winds typical of a typhoon event, and the effect that this has on the simulated behaviour of a floating offshore wind turbine in extreme environmental conditions. The aim of this case study is to determine how well FAST performs for predicting the behaviour of a FOWT in extreme conditions, and to determine if simulations of a FOWT using an aeroelastic code such as FAST can be improved by using a higher fidelity wind input.

5.3.1 Case Study – Goto Islands Project

For the simulation of floating offshore wind turbines in extreme conditions, the behaviour of a 2 MW spar mounted FOWT in a typhoon was considered. The numerical simulation of a typhoon and the resulting FOWT response in FAST and SOWFA was compared against data from the Goto Islands floating offshore wind turbine demonstration project recorded during Typhoon Prapiroon in July 2018.

The Goto Islands project [209] was a demonstration project for floating offshore wind that was funded by Japan's Ministry of the Environment. The project involved the testing of two downwind spar-type floating wind turbines installed close to Kabashima Island; firstly a 100 kW turbine (referred to as the half scale turbine) was installed in 2011, and in 2013 this was replaced by a 2 MW turbine referred to as Haenkaze. Both turbines were subjected to several typhoons whilst in operation, the most severe being the Typhoon Sanba which hit the 100 kW

turbine in 2012, and Typhoon Prapiroon which hit the 2 MW turbine in 2018. However, both turbines survived these typhoon events without damage. The response of both turbines to the severe typhoons were recorded and published by Utsunomiya et al. [210] and Tanaka et al [211], who performed simulations of each turbine's response to the typhoons using the commercial multibody-dynamics simulation tool ADAMS coupled with their in-house code SparDyn, and compared their simulated results to the measured response of the real turbines. In their work, the recorded time series of the wind from the turbine anemometer and the water surface elevation measured by a nearby wave buoy was used directly as input in the numerical modelling. In the work presented in this chapter, the waves are simulated using the JONSWAP spectrum, and wind is simulated both using the Kaimal spectrum in TurbSim and using LES modelling of atmospheric boundary layer flow.

5.3.2 Simulation Setup

A model turbine was defined based on the demonstration FOWT Haenkaze, which is a Hitachi HWT2.0-80 turbine installed on a spar platform designed by the Toda Corporation [212]. The spar platform is a hybrid spar concept; the upper sections are made from steel and the lower portion from prestressed concrete. The mooring system consists of three catenary chains with drag anchors, where two of the chains are equipped with clump weights. The key parameters of the turbine are listed in Table 5.5. The nacelle, hub and blade geometry information from the 2 MW reference turbine UT80d-2.0MW [213] was used for the model turbine defined in this study, which may not be exactly the same as that of the Haenkaze turbine (since the information for the Hitachi turbine is proprietary). This is unlikely to have a significant effect on the model results, because the rotor is not operating in the simulations and aerodynamic loading on the feathered blades is expected to be low.

Table 5.5: Key parameters of Haenkaze [211]

Rated power	2 MW
Number of blades	3
Rotor configuration	Downwind
Rotor diameter	80 m
Hub height above MSL	56 m
Platform draft	76 m
Spar diameter above cone section	4.8 m
Spar diameter below cone section	7.8 m

*Table 5.6: Environmental conditions used for each simulation, based on the measured conditions averaged over each hour of the typhoon duration at the site of the turbine, adapted from Tanaka et al. [211]. *All data was measured on the 3rd July 2018. **Average conditions are estimated based on interpolation due to lack of data (except for H_s and $T_{1/3}$ which are known)*

Case	Time period*	$\bar{U}_{hub}$ (m/s)	TI (%)	Mean wind direction (°)	H_s (m)	$T_{1/3}$ (s)	Wave direction (°)	Sub surface current speed (m/s)	Current direction (°)
1	07:00-08:00	25.7	9.9	85.2	5.2	10.7	160.3	0.14	213.4
2	08:00-09:00	26.6	9.2	106.9	5.7	10.7	248.9	0.14	232.8
3	09:00-10:00	31.9	10.1	112.4	6.2	11.6	264.4	0.17	293.4
4	10:00-11:00	37.5	9.7	127.6	6.6	12.1	200.4	0.17	289.0
5	11:00-12:00	41.0	9.1	143.5	7.1	12.3	152.6	0.22	295.1
6**	12:00-13:00	38.0		161.3	7.1	12.2	130.8	0.22	294.6
7**	13:00-14:00	34.5		179.0	6.6	11.9	109	0.22	294.1
8	14:00-15:00	31.5	6.6	196.8	4.9	10.6	87.2	0.22	293.6
9	15:00-16:00	27.8	9.4	211.9	3.9	9.5	154	0.19	111.5
10	16:00-17:00	22.7	7.6	229.8	3.1	9.4	151.2	0.24	248.2

The FAST model of the 2 MW turbine was simulated in typhoon conditions using hourly averages of the measured environmental conditions from typhoon Prapiroon for the 7:00-17:00 period on the 3rd July 2018, shown in Table 5.6. This time window covers the period during which the turbine was in a shutdown state, which was from 7:06-16:38. The conditions listed for 7:00-8:00 include only the data averaged from 7:30-8:00 in order to omit the period where the turbine is still producing power. Likewise, the conditions listed for 16:00-17:00 are actually averaged from 16:30-17:00. These are the same conditions that are used as

inputs into the numerical model in Tanaka et al. [211], except for the data for the time period between 12:00 and 14:00 (simulations 6 and 7), where there was a gap in the data due to a power outage, and only the wave buoy data was made available. For the simulations covering this period, the wind and current information and the wave direction are estimated based on interpolation. The wind turbulence intensity in TurbSim for these cases is determined by the value obtained in the SOWFA simulations, which is explained in more detail in the following section. The water depth is assumed to be constant at 106.5 m in all simulations. The turbine is simulated in each case for 1 hr 10 minutes, where the first 10 minutes are removed from the results in order to omit start up transient effects.

The turbulent wind fields representing the typhoon in SOWFA are generated using the same method used for the operational cases in section 5.2. According to Zhang et al. [214], the typhoon boundary layer has near neutral stability, and therefore each case listed in Table 5.6 is simulated in neutral atmospheric conditions only.

Although the JONSWAP spectrum is specific to wave conditions in the North Sea, previous work has found that this can fit well with typhoon wave spectra provided that the shape parameters (particularly the peak enhancement factor γ) are modified from the default values [215,216]. A value $\gamma = 2.4$ is used in all presented simulation cases, which is approximately consistent with observations of typhoon waves in the northwestern Pacific Ocean [216].

The actuator line model simulations in this work are performed on a coarse grid relative to the turbine size; the cell width at the rotor is 2.5 m, which equates to a local grid resolution of $\Delta x = R/16$ for this turbine. The number of grid cells along each blade is therefore roughly half the minimum value of 30 cells recommended by Jha et al. [177] as discussed in Chapter 4. This was done in order to reduce the computational cost of the simulations, since complying with the recommended grid resolution would have required several weeks of computational time for each case, which is discussed further in section 5.3.3.4 where the impact of the grid resolution on the results is examined. The justification for the choice of a coarse grid resolution is that it is less important for

the integrated rotor loads to be calculated accurately for the idling turbine, because it is not producing power and the rotor loads are small and will not have a significant effect on the structure's response to the typhoon.

5.3.3 Results

5.3.3.1 Characteristics of the Simulated Extreme Wind

Table 5.7 shows the turbulence intensity calculated from the LES simulations compared with the target values from the field data. The surface roughness height z_0 is estimated based on the wind speed using the Charnock relation as described in section 5.2.2.2. In cases 6 and 7, where field data for the wind was unavailable, z_0 was estimated by interpolation. The maximum instantaneous wind speed at the hub location (56.0 m/s in TurbSim and 53.5 m/s in SOWFA) occurred during the 5th hour of the typhoon in both models. The maximum instantaneous wind speed recorded by the turbine anemometer during the typhoon was 52.2 m/s [211].

Table 5.7: Turbulence intensities from the LES wind field compared against target values from the field data

Case	Target TI from field data (%)	TI from LES (%)
1	9.9	8.3
2	9.2	10.5
3	10.1	11.6
4	9.7	11.2
5	9.1	12.2
6	-	8.7
7	-	8.4
8	6.6	9.3
9	9.4	9.9
10	7.6	15.5

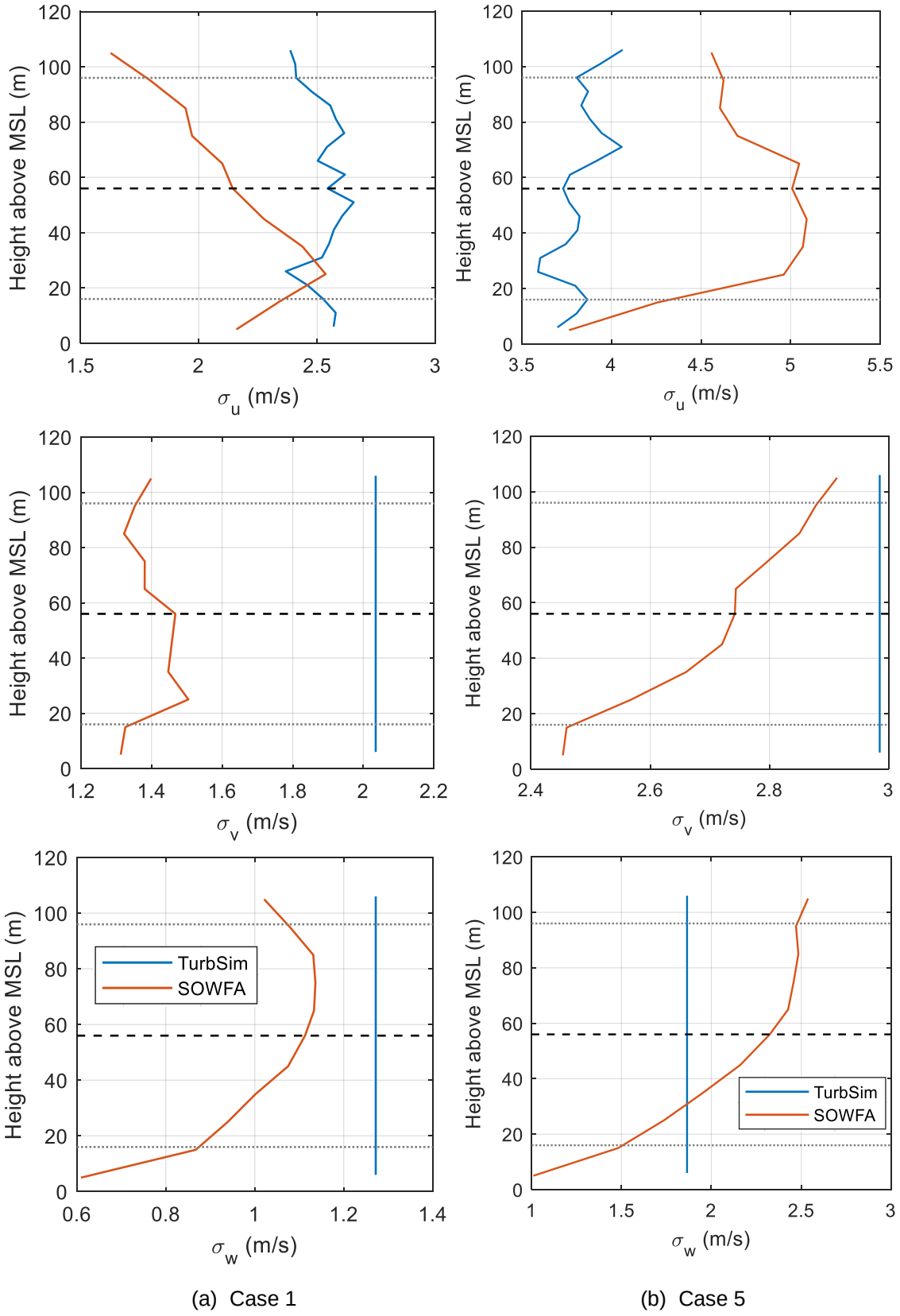

Figure 5.11: Standard deviation of the u-, v- and w- components of the wind speed for (a) case 1, U_{hub} = 25.7 m/s and (b) case 5, U_{hub} = 41.0 m/s. The dashed black line represents the turbine hub height, and the dotted lines represent the top and bottom of the rotor disk area.

In the FAST only simulations, the turbulent wind was generated in TurbSim using the Kaimal spectrum with a turbulence intensity corresponding to the value from the field data listed in Table 5.6, except for cases 6 and 7 where the value from the LES wind field is used. In all cases except for case 1, the TI from the SOWFA simulations is overpredicted compared to the target value from the field data. The error is particularly large in case 10, where the turbulence intensity is around twice as large as the value from the field data. One explanation for the relatively high TI values compared to those obtained in the operational cases (listed in Table) is that the 56 m hub height of the 2 MW turbine used in this case study is lower than that of the 6 MW turbine (98 m) studied in section 5.2. It was observed in Figure 5.5 and Appendix C.1 that according to SOWFA, longitudinal variation in the wind speed decreases with increasing height from around 20-30 m above the mean sea level. The variation in the u-, v- and w- components of the wind speed with height are shown in Figure 5.11 for case 1, which occurs at the start of the typhoon, and case 5 where the maximum wind speed occurs. The remaining cases are presented in Appendix C.2. It can be seen that the variation of each component of the wind speed continues to increase up to a larger height above sea level in case 5 than in case 1. This is likely to be due to the considerably larger roughness height z_0 used in the simulation of the very high wind speed in case 5, which leads to higher shear stress near the wall boundary representing the sea surface.

5.3.3.2 Comparison of Simulated Platform Response with Field Measurements

The statistics for the floating platform motions from the numerical modelling is compared against the data from the field measurements from Tanaka et al. [211] in Figures 5.12 to 5.14. Platform motions are measured in the global coordinate system for all simulations, where positive values for surge and sway correspond to the turbine positioned south and east of the equilibrium position respectively.

The level of agreement between the numerical simulations and the field data varies depending on the environmental conditions. At the beginning of the typhoon, there is an offset of around 2 m between the surge displacement from the numerical modelling and the field data, which may be attributed to the fact that the numerical modelling does not take into account any of the loading prior to the turbine shutdown. The field data for case 1 (07:00-08:00) is recorded from

shortly after the turbine stops producing power, meaning that the rotor was producing a thrust force that would result in a surge offset from the equilibrium position, which may influence the results at the beginning of the typhoon. The agreement between the numerical modelling and the field data for the surge displacement improves as the typhoon increases in severity, with a mean difference of around 0.6 m for cases 3, 4, 5 and 8 (where field data is available),. An offset of around 2 m between numerical modelling and field data is present again in the final two cases, which suggests there is a loading contribution that is not considered in the numerical modelling. It is noted that only sub-surface components of the current are included in the numerical modelling, since wind generated current could not be measured during the typhoon, which may have an effect on the numerical predictions. In the pitch motion, it is noted that there is a consistent offset of 1-1.7° between the numerical modelling and the field data. This was also observed in the numerical modelling performed by Tanaka et el. [211], who suggested that this may be due to differences in the initial tensions in the mooring lines due to the slope and general unevenness of the seabed [47]. The sway and roll displacements are generally predicted well, except for in the final two simulated hours where, similar to the observed surge displacement, there is an error of over 1 m in the mean sway displacement. The error between the average values for the measured roll displacement and the numerical predictions is less than 0.3° in all cases.

The heave response (Figure 5.13) predicted by the numerical modelling is consistently underpredicted compared to the field data, more so than any of the other platform motions. The standard deviation of the results from FAST and SOWFA is less than 50% of that from the field data in all cases except one (case 4, where the standard deviation from SOWFA is 53% of that from the field data). This may suggest that the waves predicted using the JONSWAP spectrum and linear wave theory in HydroDyn did not accurately represent the extreme waves present during the typhoon. Prediction of the heave response could also be improved by including second order hydrodynamics and drift [217]. In the simulations performed by Tanaka et al. [211], where the measured sea surface elevation from the field site was used as a direct input and wave stretching was included, the heave response showed better agreement with the measured data

near the peak of the typhoon than in the simulations performed in this study, but was still underpredicted overall.

The SOWFA predictions of the mean surge and sway displacement from the equilibrium position are on average about 12% lower than the FAST predictions, and the mean roll and pitch angles are approximately 8% lower in SOWFA compared to FAST. This suggests that the calculated aerodynamic loads on the turbine in SOWFA are smaller than in FAST. Since the turbine is not operational in this study, a large proportion of the aerodynamic loading is due to drag forces on the tower, so this may suggest that the actuator line representation of the tower requires further study. With this exception, there is little difference between the predictions of the platform response from FAST and SOWFA. The platform response also appears to be relatively unaffected by turbulence intensity when the turbine is in shutdown mode, as evidenced by the results for the 10th and final hour of the typhoon, where there is little difference between the model predictions despite the large difference in TI as described in section 5.3.3.1.

The highest wind speeds and largest wave heights and periods occurred during the 5th hour of measurements (11:00-12:00), however this did not correspond with the most extreme values simulated for all platform motions. The largest simulated yaw response was observed during the 4th hour, where there was a significantly larger misalignment between the wind and waves than in the 5th hour. The extreme yaw response simulated during the 4th hour is overpredicted by both FAST and SOWFA compared to the measured yaw motion from the field data, which may suggest that the real turbine had additional yaw damping that was not included in the numerical model. However, yaw motion is underpredicted by both numerical models at other times, particularly in the two hours at the beginning and end of the typhoon, where the wind is less extreme, and the 5th hour of the typhoon where the wind and wave direction are closely aligned. A possible explanation for this underprediction is that the waves were simulated without directional variation, since this was not known from the recorded data, which may result in underestimated excitation of the platform yaw mode.

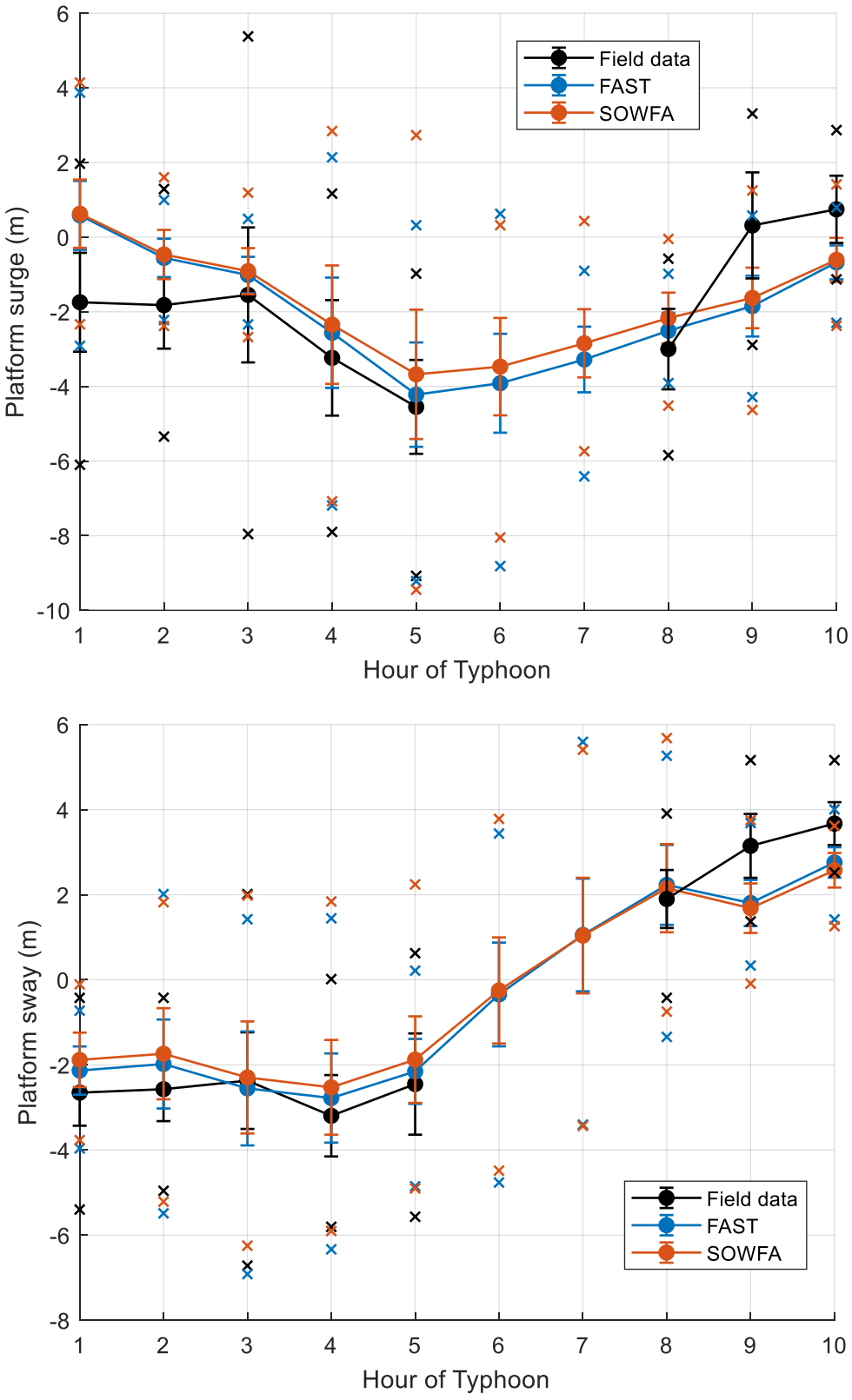

Figure 5.12: Platform surge and sway motion during each hour of the typhoon. • represents the mean position, error bars represent one standard deviation above and below the mean, x represents the minimum and maximum values for each hour.

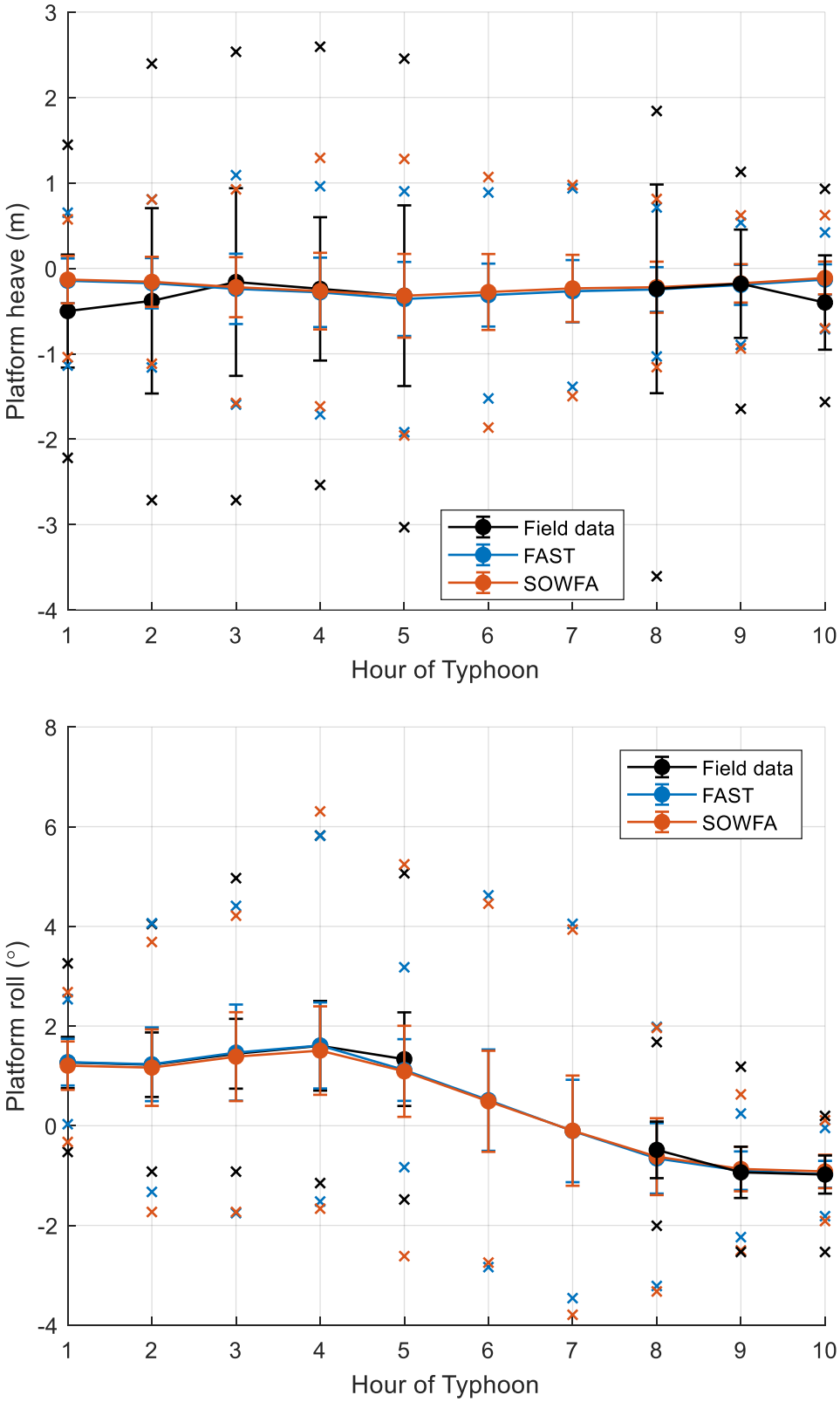

Figure 5.13: Platform heave and roll motion during each hour of the typhoon

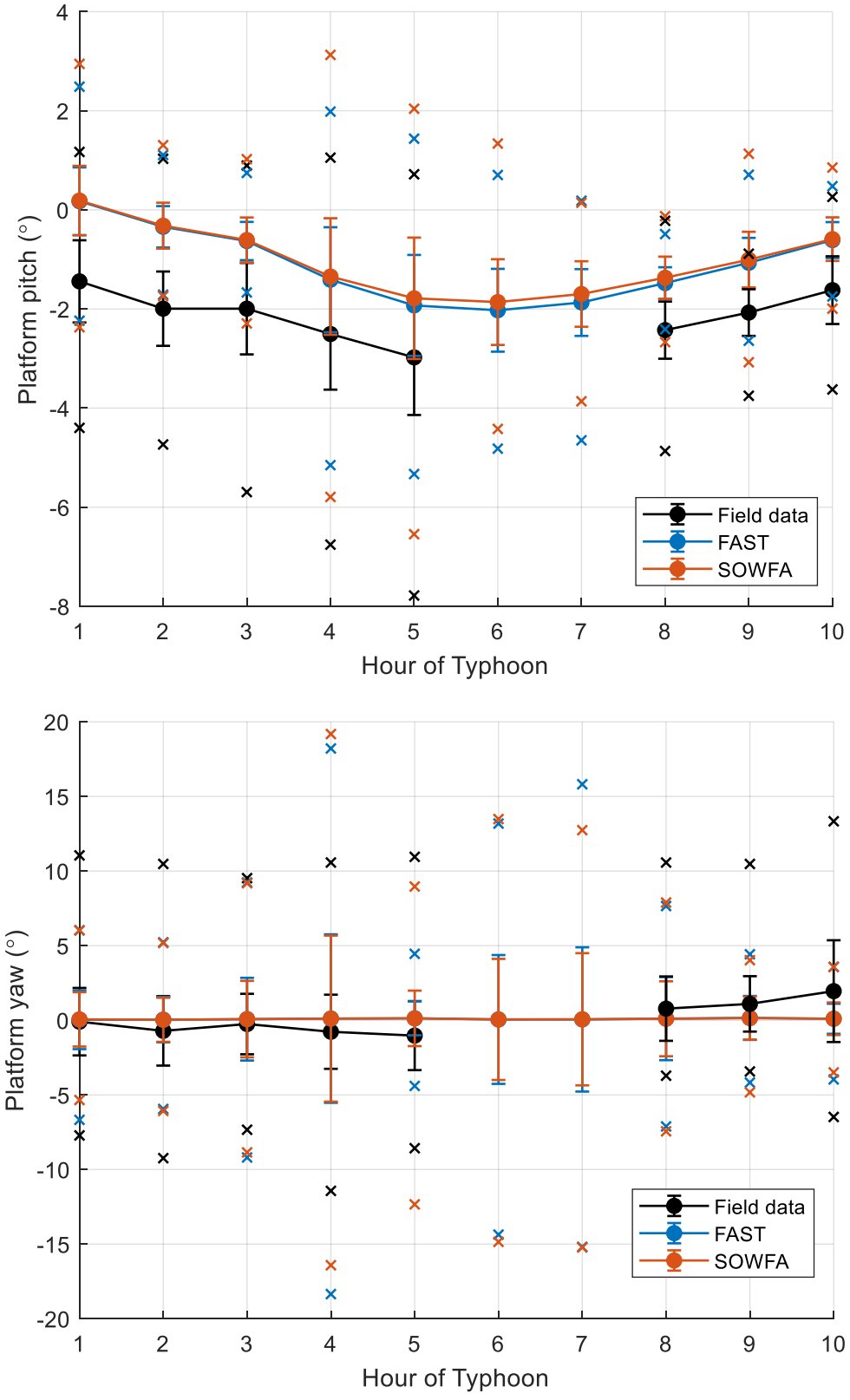

Figure 5.14: Platform pitch and yaw motion during each hour of the typhoon

5.3.3.3 Extreme Blade Loads

The flapwise and edgewise bending moment statistics for each hour of the typhoon are plotted in Figure 5.15. The statistics are calculated for all three blades of the idling rotor. It should be noted that since the blades are pitched at near 90° to reduce aerodynamic loads on the blade, the flapwise bending is now nearly aligned with the in-plane bending direction, and edgewise bending now results in more out-of-plane deflection.

The overall agreement between FAST and SOWFA is good for both the edgewise and flapwise bending moment. The difference between the standard deviation of the edgewise bending moment is less than 10% for all simulated hours of the typhoon, and the difference for the flapwise bending moment is less than 5% Some difference between the two models is noted in the minimum and maximum edgewise bending moment in each hour of the typhoon, however neither model consistently predicts a larger range than the other. The two models agree well on the extreme values of the flapwise bending moment, with less than 10% difference between model predictions across all hours of the typhoon. The blade loads of the idling turbine also appear to be largely unaffected by turbulence intensity differences between the two model inputs. The blade flapwise bending response increases with increasing wind speed, and the both largest variation and maximum value for the flapwise bending moment occur during the 5th hour of the typhoon (11:00-12:00), which corresponds to the highest mean wind speed. The edgewise bending moment response on the other hand is not linked to the wind speed; both models predict that the largest response and maximum values occur in the 1st hour of the typhoon.

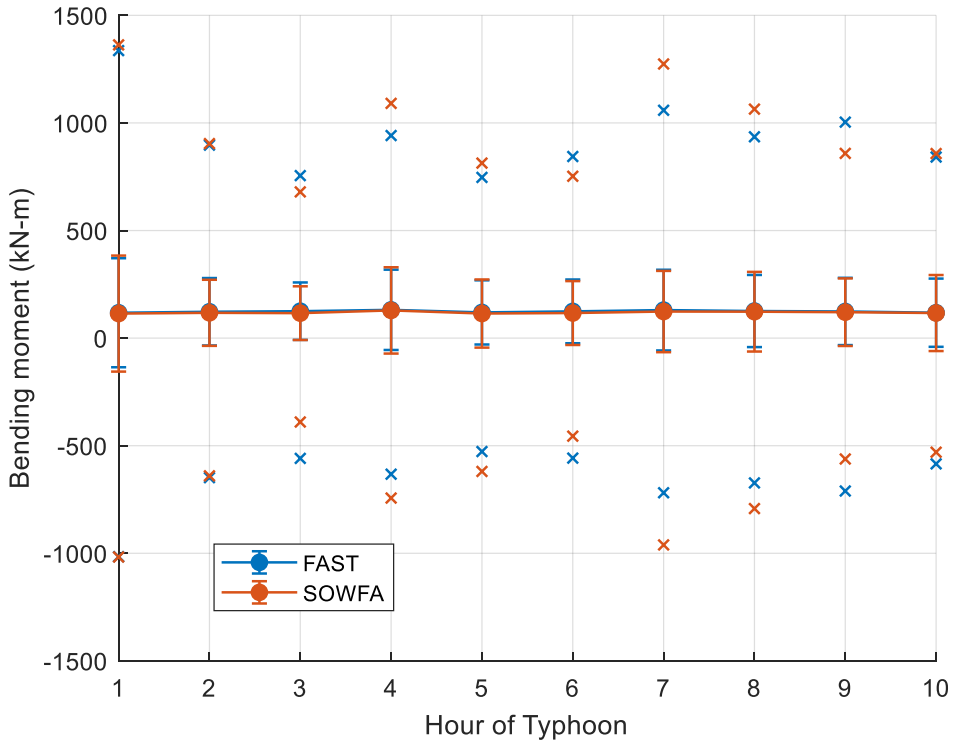

(a) Edgewise bending

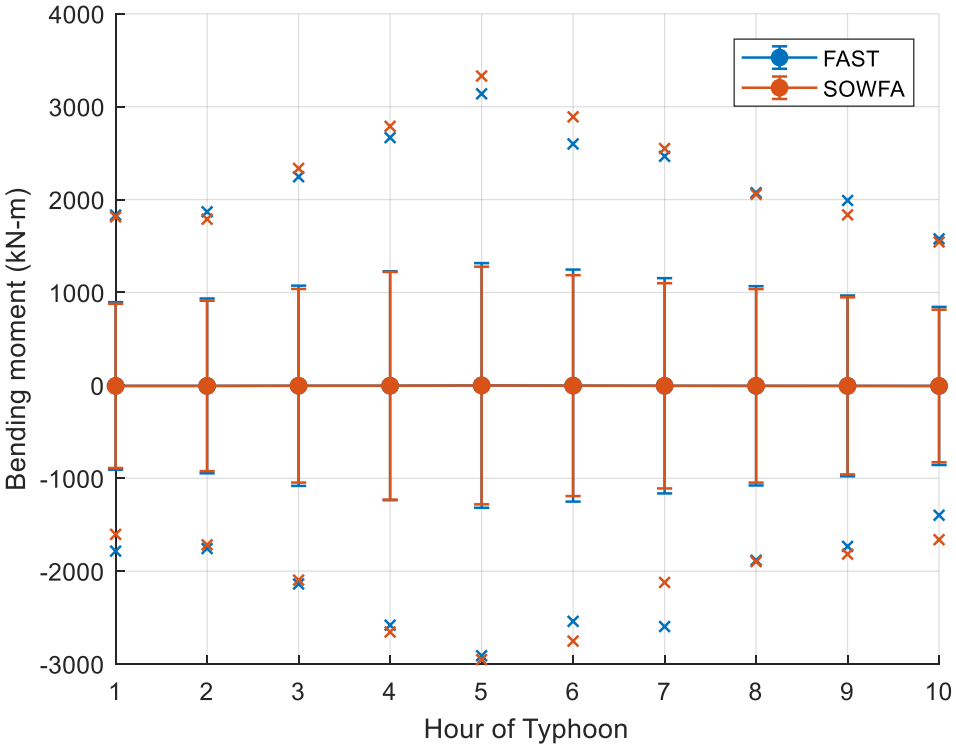

(b) Flapwise bending

*Figure 5.15: Blade root bending moment in each hour of the typhoon. • represents the mean position, error bars represent one standard deviation above and below the mean, **x** represents the minimum and maximum values for each hour.*

5.3.3.4 *Impact of Grid Resolution*

To investigate the impact of using a relatively low mesh resolution, Case 1 from Table 5.6 was simulated once with the coarse mesh and once with an additional level of refinement so that the local resolution was $R/32$, which is within the recommended range of local mesh resolutions for actuator line simulations as suggested by Jha et al. [177], and the results from each mesh are compared. The additional level of refinement increased the total cell count from 2.96 million to 7.48 million, and the required computational time running in parallel on 28 cores increased from around 4.5 days to approximately 22 days for 70 minutes of simulation time. Case 1 has one of the lowest average wind speeds of the presented simulation cases, and other cases with higher wind speeds would have taken longer due to the smaller timestep required to keep the Courant flow number low enough to avoid numerical instability for the duration of the simulation. It was therefore not feasible to simulate all cases with the increased mesh resolution.

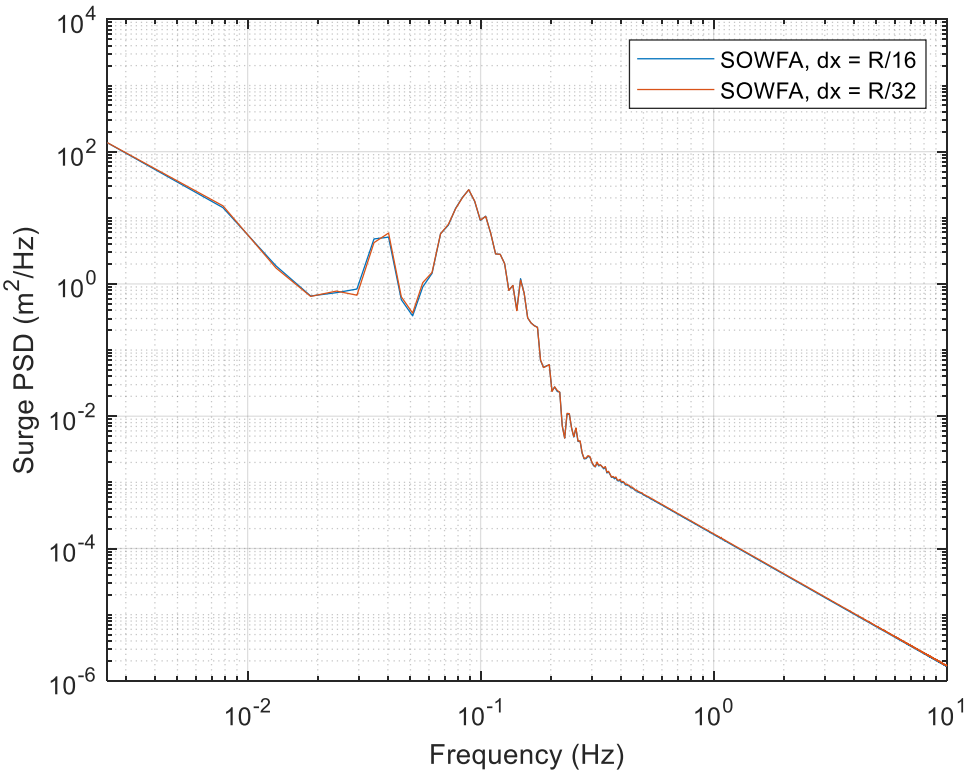

Figure 5.16: Power spectral density (PSD) of the surge motion predicted by SOWFA during the first hour of the typhoon (07:00-08:00) using two different grid resolutions.

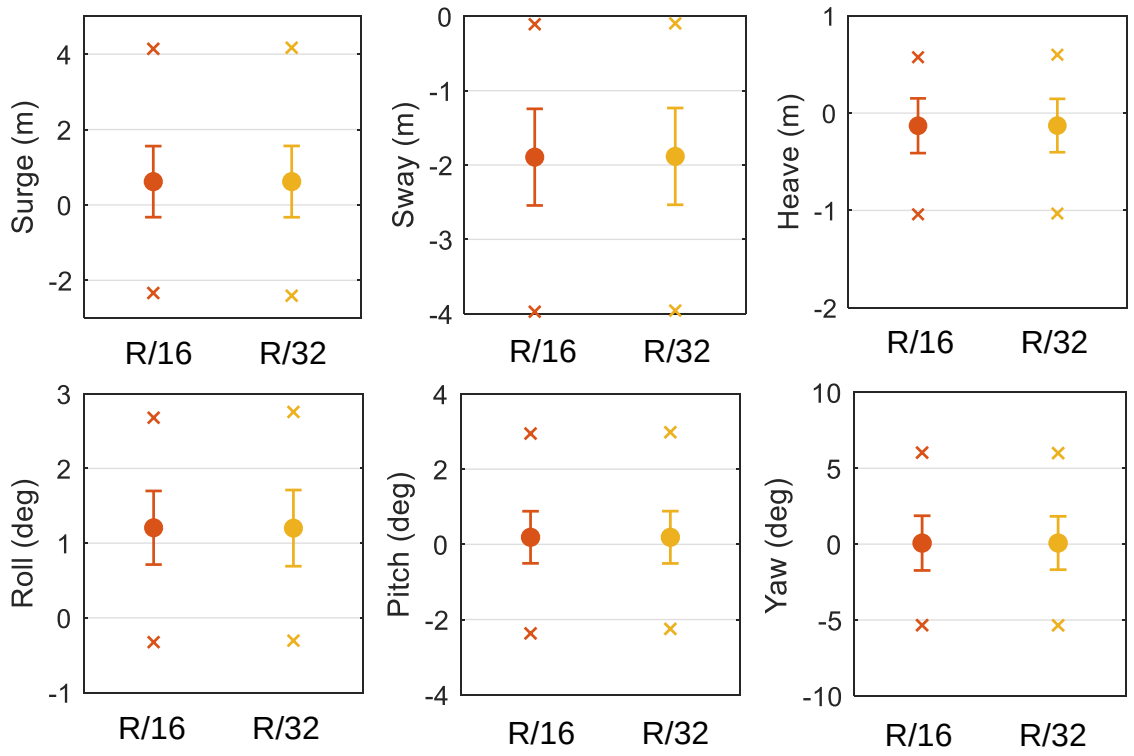

*Figure 5.17: Platform motions in the first hour of the typhoon (07:00-08:00) predicted by SOWFA for two grid resolutions, $\Delta x = R/16$ and $\Delta x = R/32$. • represents the mean position, error bars represent one standard deviation above and below the mean, **x** represents the minimum and maximum values.*

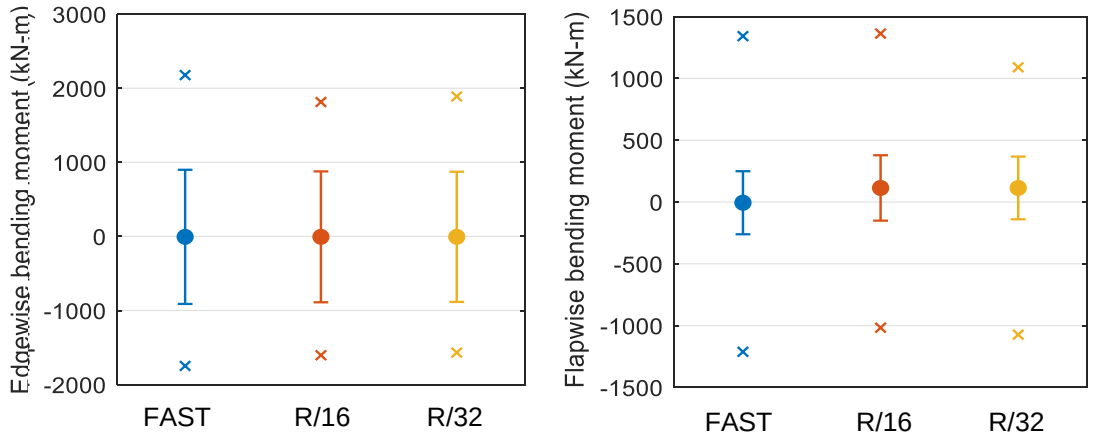

*Figure 5.18: Blade root bending moments in the first hour of the typhoon (07:00-08:00) predicted by SOWFA for two grid resolutions, $\Delta x = R/16$ and $\Delta x = R/32$. • represents the mean position, error bars represent one standard deviation above and below the mean, **x** represents the minimum and maximum values.*

The change in grid resolution results in negligible change platform motion response, as shown in the power spectral density (PSD) of the surge motion plotted in Figure 5.16, which is almost identical for both meshes. Figure 5.17 shows that there is a negligible difference in the mean position and overall

variation predicted for all platform modes for the duration of each simulation. This is not unexpected, since changing the grid resolution results only in changes to the aerodynamic forces due to the wind, while the platform response is primarily driven by hydrodynamic forces.

The grid resolution has a larger influence on the blade loads, since these are more heavily influenced by the wind loading. The statistics for the blade root flapwise and edgewise bending moment are plotted in Figure 5.18. The simulation performed on a grid with local resolution $\Delta x = R/32$ resulted in a maximum blade root flapwise bending moment that was approximately 20% lower than for the coarser mesh. The predictions from FAST for the maximum edgewise bending moment show closer agreement with the SOWFA predictions using the coarser mesh than the finer mesh. There is little difference between the two meshes for the flapwise bending moment. The PSDs of the edgewise bending moment plotted in Figure 5.19 show that the finer mesh results in a small decrease in the response at high frequencies. It is interesting to note that differences between the predictions of the blade bending moment were only observed from approximately 18 minutes (1080 s) into the simulation, and that before this point the predictions are almost identical, as observed in Figure 5.20.

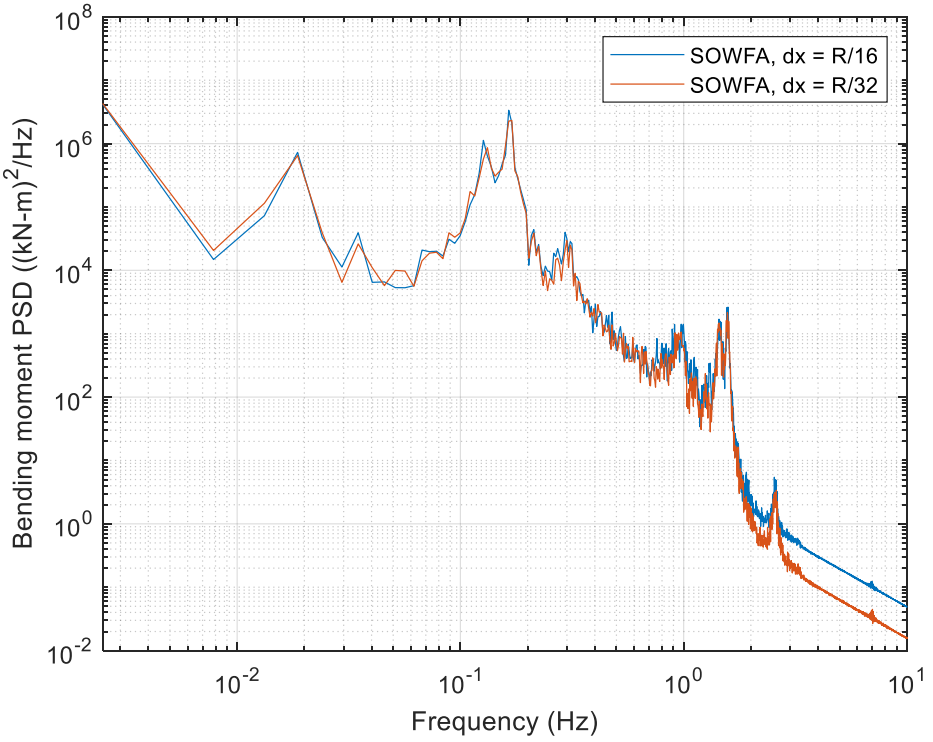

Figure 5.19: Power spectral density of the blade root edgewise bending moment predicted by SOWFA during the first hour of the typhoon (07:00-08:00) using two different grid resolutions.

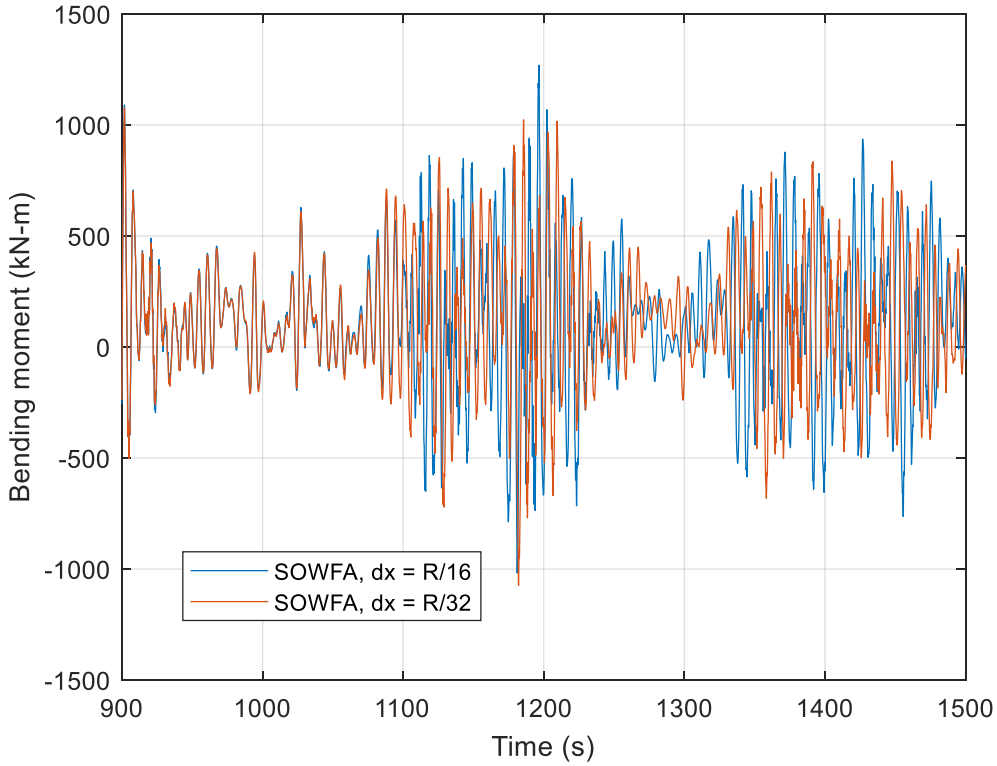

Figure 5.20: Time series of the blade root flapwise bending moment predicted by SOWFA during the first hour of the typhoon (07:00-08:00) using two different grid resolutions.

5.4 Chapter Summary

In this chapter, the influence of the turbulent wind input on platform motion and rotor load response for a floating offshore wind turbine has been studied using two modelling approaches, namely a statistical wind model and high fidelity ABL simulation using LES. The model predictions are compared against each other and against available field data, firstly for a range of operational conditions and secondly for an extreme typhoon event. The key findings of this chapter are summarized as follows:

1. FAST with BEM for aerodynamics and FAST coupled with the ALM in SOWFA are both capable of achieving good overall agreement with recorded rotational displacements for a turbine within the Hywind Scotland floating wind farm, with a maximum error of 1.3° observed for the predicted mean pitch angle compared to the recorded data. The results of the numerical modelling do however suggest that the platform pitch and yaw

modes are not sufficiently damped, which is likely in part due to discrepancies in the turbine controller used in the modelling compared to that of the actual turbines (since this data from Hywind Scotland is not available).

2. The numerical modelling underpredicts the translational motions, particularly the sway motion, suggesting possible limitations in the numerical modelling such as not including directional variation in the waves and starting each simulation with the turbine at the equilibrium position.
3. In operational conditions, the simulated platform motions and rotor loads when a TurbSim wind input is used are generally similar to those obtained from an actuator line model simulation in neutral atmospheric flow at the same longitudinal turbulence intensity. This suggests that the Kaimal spectrum is suitable for simulating wind inflow for a FOWT in neutral conditions. The agreement between FAST and SOWFA is also generally good when unstable ABL conditions are simulated in SOWFA, except for the sway response, which is indicated to be sensitive to the larger turbulent structures present in unstable conditions.
4. For extreme wind speeds where the turbine is not producing power, there is overall little difference between FAST and SOWFA's predictions of a floating spar turbine's motion and load response, even when there are large differences in the turbulence intensity between TurbSim and LES wind fields. There may however be limitations associated with using first order potential flow theory for hydrodynamics, which consistently underestimated the heave motion of the spar platform.
5. The blade loads in extreme environmental conditions predicted from LES simulations using an actuator line model become sensitive to the grid resolution after a certain period of simulation time, which was found to be approximately 18 minutes in this case.

Based on the findings in this chapter, the following recommendations are made:

1. If a specific value of the turbulence intensity is desired, a statistical model such as the Kaimal model available in TurbSim is more appropriate, since the random nature of turbulence means that it is difficult to accurately

match physics based turbulence models such as LES with measured values.

2. The Kaimal spectrum is suitable for simulating wind inflow for a FOWT in neutral conditions, and may be acceptable for simulating FOWT response in unstable conditions with above rated winds, provided that the turbulence intensity is adjusted to an appropriately high value. The Kaimal model would not be suitable for simulating stable conditions even if the turbulence intensity is adjusted to an appropriately low level, because it does not capture the strong wind shear and wind veer characteristic of stable conditions which may have a significant effect on the blade bending response.
3. For operational cases, CFD modelling using an ALM does not offer significant benefit over the lower fidelity modelling options available in FAST for cases involving a single turbine, since there was overall little difference between rotor and blade loads predicted by each model that was not due to differences in turbulence intensity.
4. The ALM is not recommended for use in cases involving extreme environmental conditions with a parked or idling rotor, where the aerodynamic loading is primarily due to forces acting on the tower. This is particularly significant for FOWTs because the surge and sway displacement are driven by the aerodynamic forces; if these are not predicted accurately, this may result in underestimation of the extreme mooring forces.
5. The discrepancies between the field data and numerical modelling results suggest that there are a number of ways in which the modelling presented in this chapter can be improved. In both operational and extreme conditions, it is recommended to consider a more accurate starting position of the turbine rather than starting all simulations with the turbine at the equilibrium position. This may help to reduce errors in the predicted translational displacements. Including second order effects such as mean and slow drift contributions may also improve these predictions. For simulation of cases involving extreme environmental conditions with large waves, higher order hydrodynamic modelling is likely to be necessary in order to capture the heave response of a spar-type FOWT.

Chapter 6

High Order Coupled Fluid-Structure Interaction Modelling of Blade Behaviour

6.1 Introduction and Motivation

In previous chapters, the performance of a low order BEM method has been compared with an actuator line model for analysis of a floating offshore wind turbine in order to determine where the BEM approach is sufficient and where a higher order model would be a more appropriate choice. The ALM captures more of the complex flow effects associated with wind turbines than traditional BEM, for example it is able to capture root and tip vortices and does not require an empirical correction when the turbine rotor is not aligned with the wind [218]. However, generalized actuator disk approaches including the ALM also have their limitations. Like the BEM method, ALM predictions of rotor aerodynamics depend on the quality of the tabulated aerofoil data supplied, which can be difficult to obtain [48]. The aerofoil data used in BEM and generalized actuator disk modelling usually comes from 2D wind tunnel measurements, and so requires corrections in order to account for 3D geometrical and rotational effects [219]. The alternative to relying on aerofoil tables is to fully resolve the blade geometry.

All of the numerical modelling presented in the previous chapters has used FAST's ElastoDyn module to account for the structural response of the wind turbine rotor, which may also have limitations. The structural model in ElastoDyn is best suited to straight isotropic blades dominated by bending, and may only be able to handle moderate deflections [106]. ElastoDyn also does not include axial, shear or torsional degrees of freedom, so may not be suitable for highly flexible or aeroelastically tailored blades involving bend-twist coupling, for example. As current design trends for offshore wind turbines lead to increasingly large rotors, the blades tend to become more flexible in order to reduce the weight and cost

of materials, and aeroelastic effects become more important [30]. Therefore, higher order structural models may be needed in order to accurately predict blade behaviour.

In this chapter, a two-way coupled fluid structure interaction (FSI) model is used to investigate the structural behaviour of a single large flexible wind turbine blade. The fluid dynamics are solved in OpenFOAM, where the blade geometry is resolved, and the structural dynamics are solved using CalculiX [170]. The interaction between the two solvers is handled using the code coupling library preCICE [172], which is described in detail in Chapter 3. The observations of the blade response from the FSI simulations are compared against those from FAST, where the forces on the blade are calculated using BEM theory and a steady, uniform wind is used as input, similar to the FAST method demonstrated in Chapter 4. The objectives of this chapter are to demonstrate the use of high fidelity numerical modelling for analysing wind turbine behaviour and to provide insight into the behaviour of a large flexible wind turbine blade in extreme environmental conditions. This study should be viewed as a 'proof of concept' for a high fidelity method for wind turbine analysis, which will help to inform recommendations on where high order numerical modelling may be necessary in the design process for large flexible blades used in offshore wind turbines.

6.2 Validation of Methodology

A wind turbine blade that is fixed at the hub can be considered as a cantilever structure that experiences deformation due to wind loading in addition to rotor rotation in operational conditions. It is therefore necessary that the numerical methodology investigated in this work is able to accurately simulate the deflection of a cantilever structure. In order to determine this, the use of preCICE with CalculiX and OpenFOAM is investigated for a simple fluid structure interaction case from the literature involving a cantilever plate bending in cross flow.

The study is based on an experiment that was conducted by Luhar and Nepf [220] to investigate the deformation of aquatic vegetation. In the experiment, a flexible plate representing seagrass was subjected to cross flow in a flume, and the resulting deflection and drag force was measured. In a subsequent numerical

study, Tian et al. [221] used one of the cases from this experimental campaign to validate an FSI model, and also presented simulations in the absence of gravity and buoyancy to serve as benchmark validation cases for FSI studies. These cases without gravity and buoyancy from [221] are chosen to validate the simulations presented herein in order to simplify the CFD modelling.

In the presented numerical simulations, a flexible plate was fixed at one end and subjected to a uniform fluid flow of $U = 0.16\,m/s$. The plate had a height of $h = 50\,mm$, width $b = 10\,mm$ and thickness $t = 1.9\,mm$. The plate is made from a silicon foam with density $\rho = 670\,kg/m^3$ and Young's modulus $E = 500\,kPa$.

The fluid domain in OpenFOAM represented a section of the flume in which the experiment was performed, and is shown in Figure 6.1. The domain consists of a hexahedral mesh of 400,750 cells, which is linearly graded to give wider cells near the outer boundaries of the domain and finer cells close to the location of the plate as shown in Figure 6.2. The top, bottom and side boundaries are given free slip conditions, and the plate boundaries are treated as solid walls. Water flows in the positive x-direction, and is treated as a laminar flow.

Using CalculiX, the structural dynamics are solved using full 3D finite element analysis. The plate is modelled as a solid structure with a mesh consisting of 1196 tetrahedral elements. The equations of motion for the structure are integrated in time using a revision of the α method originally developed by Hilber, Hughes and Taylor [222], where α lies in the interval [-1,3].

The force data is mapped from OpenFOAM to CalculiX using conservative mapping, meaning that the number of nodes in each mesh is taken into account and the total value of the force at the interface is conserved when mapping. Consistent mapping is used to map the structural displacement from CalculiX back to OpenFOAM, meaning that different mesh resolutions at the interface are not taken into account, and the value at a node in a coarser mesh is the same as for the corresponding node in the finer mesh.

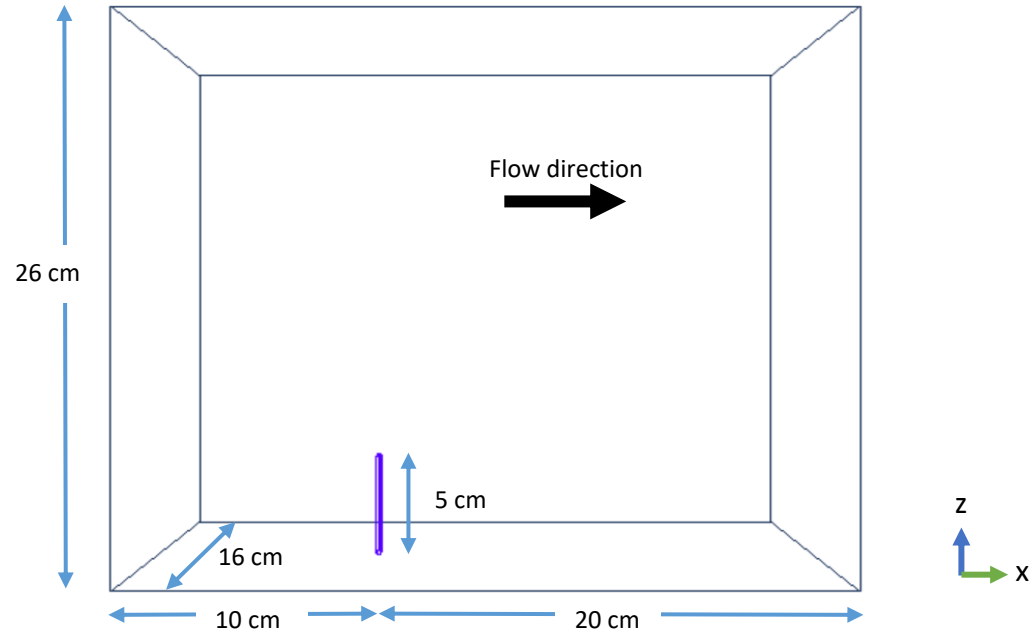

Figure 6.1: Dimensions of the fluid domain representing a section of the flume with the plate fixed at the bottom

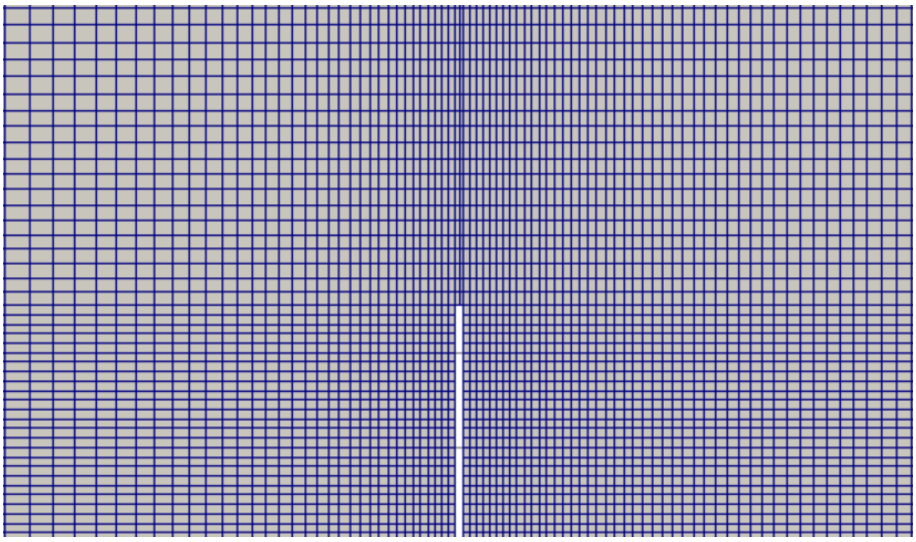

Figure 6.2: Fluid mesh grading around the plate

The deflection of the plate and the deformation of the fluid mesh is shown in Figure 6.3 for three numerical configurations, which are listed in Table 6.1. The fluid structure interaction was investigated using two-way nearest neighbour and two-way nearest projection mapping, and using a geometrically linear and nonlinear structural solver in CalculiX. In nearest neighbour mapping, the values from the source mesh are projected to the nearest nodes on the target mesh regardless of differences between the two meshes. In nearest projection mapping, the points on the target mesh are projected onto the source mesh

elements, and the values are determined using linear interpolation. Nearest neighbour mapping is a first order accurate scheme, and nearest projection mapping is usually second order accurate [172]. As Figure 6.3 shows, nearest projection mapping leads to a more numerically smooth deformation of the plate than the nearest neighbour mapping shown in (a). Since the plate experiences a large deflection, treating the case as a linear problem as shown in (a) and (b) leads to a perceived elongation of the deformed plate relative to the undeformed structure.

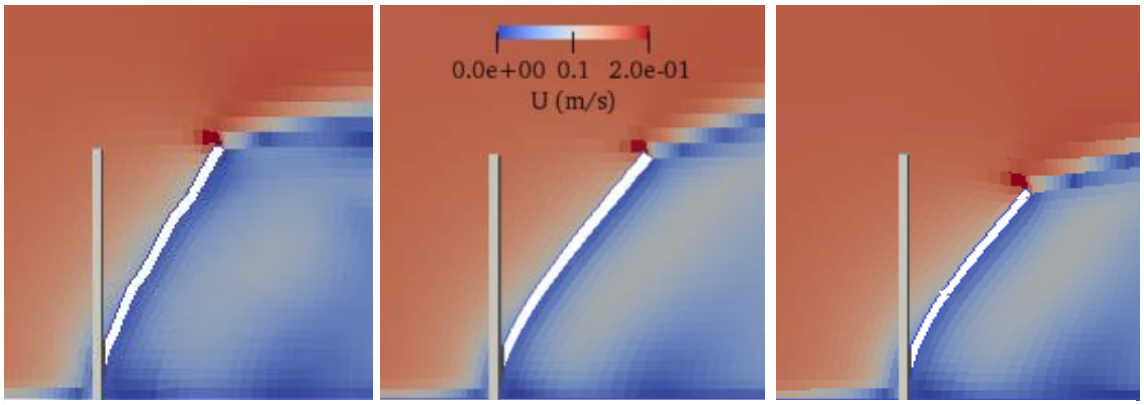

(a) (b) (c)

Figure 6.3: Structural deformation of the cantilever plate for three preCICE configurations: (a) nearest-neighbour mapping and geometrically linear structural solver, (b) nearest-projection mapping and linear structural solver, (c) nearest-projection mapping and nonlinear structural solver

Table 6.1: Numerical model settings used in validation study

Configuration	Description
A	Nearest-neighbour mapping, linear structural solver
B	Nearest-projection mapping, linear structural solver
C	Nearest-projection mapping, nonlinear structural solver

Table 6.2: Results of the preCICE simulations compared against experimental data [220] and numerical study from [221]

	Experiment	**Simulation from [179] (with buoyancy)**	**Simulation from [179] (no buoyancy)**	**preCICE (no buoyancy)**		
				A	**B**	**C**
C_D	1.15 ± 10%	1.03	0.94	1.17	1.15	0.958
Tip displacement in x-direction (mm)	21.4	21.2	24.5	23.8	31.3	25.3
Tip displacement in z-direction (mm)	-5.9	-5.4	-7.5	0.6	0.8	-7.3

The tip deflection and calculated drag coefficient from the preCICE simulations are shown in Table 6.2. The drag coefficient C_D is calculated from the force F_D exerted on the plate using the following equation:

$$F_D = \frac{1}{2}\rho_f U^2 C_D bh \tag{6.1}$$

where ρ_f is the fluid density. It can be observed from the simulations from Tian et al [221] that neglecting buoyancy effects leads to a larger deflection and a larger negative tip displacement in the vertical (z) direction. The simulations with buoyancy included agree well with the experimental results, with approximately 1% and 9% error for the x- and z-displacement respectively.

The tip displacement and drag force coefficient from the simulations performed using preCICE with a nonlinear structural solver in this work show good agreement with the numerical benchmark case where buoyancy and gravity are neglected, with a difference of 2-3% for all quantities. It is noted that the model has only been validated for a single case study, and further validation may be required in order to ensure the model gives reliable results in a range of flow conditions and in cases with more complex structural behaviour. However, this study demonstrated that the model is capable of accurately predicting simple structural bending due to fluid flow.

6.3 Investigation of Blade Behaviour

6.3.1 Simulation Setup

6.3.1.1 Fluid Modelling in OpenFOAM

The model blade used in this study is based off the reference blade for the DTU 10 MW wind turbine [223], which has length 86.35 m. The blade model has identical geometry to the DTU 10 MW reference turbine blade in terms of the aerofoil profile, chord and twist distribution. Unlike the DTU blade, the presented blade model does not feature any prebend in order to reduce complexity. This may have an effect on the dynamic behaviour of the blade, since prebending can increase the coupling between the edgewise bending and torsional modes and

reduce the torsion loads on the blade [224]. The chord and twist distributions are plotted in Figure 6.4. The blade features aerofoil sections from the FFA-W3 series, with relative thickness ranging from 60.0% near the cylindrical root section to 24.1% at the tip.

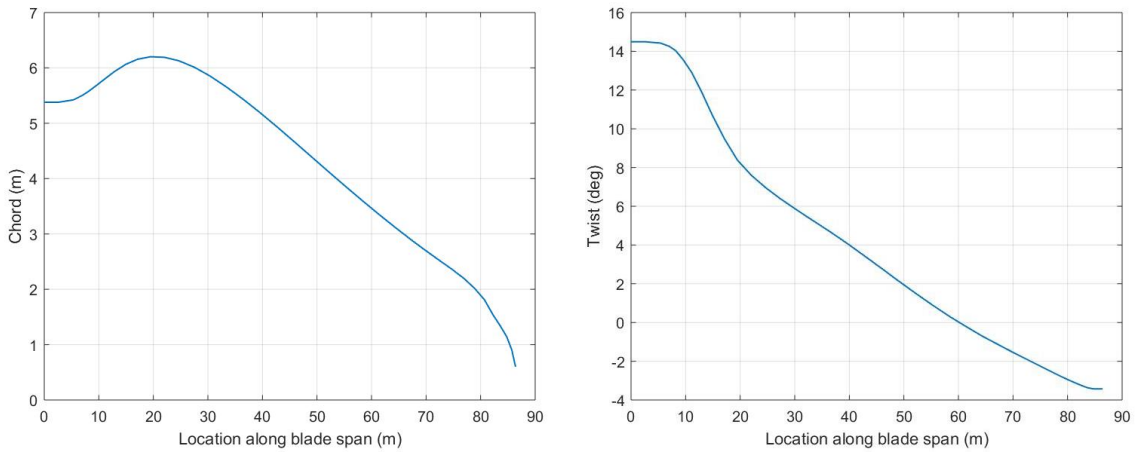

Figure 6.4: Chord and twist distribution for the DTU 10 MW blade and model used in this study

The simulations are performed using a RANS approach, and turbulence is modelled using the Spalart-Allmaras closure model, which is described in section 3.2.2.1. The rotor does not rotate in these simulations, and the simulated blade is pitched at 90° as if it were in the parked, fully feathered position in order to represent blade behaviour in extreme conditions when the turbine control system has performed a shutdown operation. In the interest of simplicity, the presented simulations also do not explicitly model any motions due to a floating platform. This means that the aerodynamic loading on the structure due to the fluid flow will be steadier with smaller fluctuations than if floating motions were included, as shown in Chapter 4.

Simulations are performed in two uniform turbulent wind speeds (i.e. without wind shear). The chosen high wind speed of 50 m/s represents an extreme event, whilst the chosen lower wind speed of 12 m/s would typically be a mid-level wind speed within a turbine's operational range. It should be noted that a parked rotor in a wind speed of 12 m/s is likely to occur only if the turbine is shut down for maintenance or due to a fault. The different wind speeds are simulated to enable comparison of the turbine blade response in different load cases.

The fluid domain in the blade simulations features a cylindrical domain, referred to as an O-mesh, as shown in Figure 6.5. The domain has 150 m height and 200 m diameter. The fixed end of the blade is positioned at the centre of the bottom boundary of the domain. The top and bottom boundaries are given free slip conditions, and the outer circular boundary is given freestream conditions. The blade mesh is treated as a solid wall boundary, where a wall function for the turbulent viscosity is used so that the mesh does not need to be fine enough at the wall to resolve the viscous sublayer. The wind flow direction is aligned with the negative x-axis.

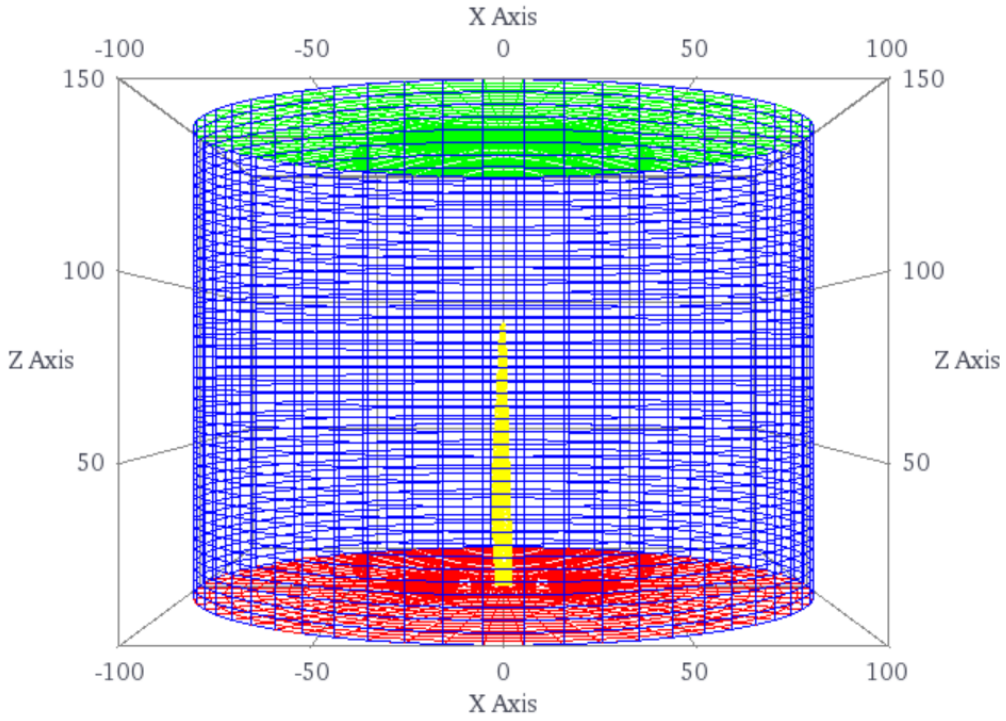

Figure 6.5: Fluid domain in OpenFOAM. The yellow region represents the meshed blade.

The blade geometry is resolved in OpenFOAM by generating a refined mesh around the structure using the tool *snappyHexMesh*, which is described in Chapter 3. Three different fluid meshes are generated using this method, which have different levels of local refinement around the blade surface. In order of increasing refinement, the three meshes have 486 000 (mesh 1), 2.05 million (mesh 2) and 3.69 million cells (mesh 3). In mesh 1, no boundary layer cells are included, whilst two layers of cells are inserted around the blade geometry in meshes 2 and 3. In mesh 2, the cell width at the blade boundary is 0.042 m and the height of the first layer of cells at the blade boundary is 0.025 m. In mesh 3,

the cell width and height in the first boundary layer of cells are 0.031 m and 0.018 m respectively. The blade is simulated at both wind speeds using each mesh in order to investigate the influence of the fluid mesh resolution on the resulting structural behaviour, which is examined in section 6.3.2.1.

The average value of the non-dimensional wall distance y^+ for each case is shown in Table 6.3, where:

$$y^+ = \frac{u^* y}{\nu} \tag{6.2}$$

u^* is the friction velocity at the wall, y is the distance between the wall and the first grid point, and ν is the local kinematic viscosity. In order for the wall function in the turbulence modelling to be accurate, it is recommended that the first grid point is positioned in the region where the log-law applies, generally estimated to be approximately $30 < y^+ < 500$ [66]. However, studies of experimental data have revealed that the log law region for boundary layer flows may be located much further from the wall. Österlund et al. [225] suggest a lower limit of $y^+ \approx 200$ and George and Castillo [226] suggest $y^+ \approx 300$, while the outer bound of the log law region is located up to $y/\delta \approx 0.2$ [227], where δ is the turbulent boundary layer width. As shown in Table 6.3, the average y^+ value for all mesh configurations is relatively high, particularly in the higher wind speed since y^+ is dependent on this as equation 6.1 shows. Whilst this may be acceptable for the proof-of-concept study presented in this work, the impact of this should be considered in future study, as the near wall turbulence may not be captured accurately, which may limit the accuracy of the calculated forces on the blade.

Table 6.3: Average y^+ values for each simualtion

Mesh	Number of Cells	$U = 12\ m/s$	$U = 50\ m/s$
1	486,287	1289	4615
2	2,049,027	391	-
3	3,694,028	295	1183

6.3.1.2 Structural Modelling in CalculiX

The structural model of the blade used in this analysis has a uniform structure involving only one material of uniform thickness along the blade span, and it does not have shear webs or spars. This differs significantly from the DTU blade internal structure, which features a composite layup with three shear webs running along the blade span for added structural support. The uniform structure was chosen in order to simplify the model, improve numerical stability, and increase computational speed in CalculiX. The structural characteristics of the blade are listed in Appendix D, which were calculated from the model of the blade used in the analysis in FAST using NREL's blade structural design tool PreComp [228]. The resulting blade has stiffness characteristics that differ significantly from the DTU 10 MW, as shown in Figure 6.6, and is less stiff overall, particularly in the flapwise direction. This difference is to be expected, since the model blade in this study does not have a varying composite layup to reflect the stiffness requirements at different locations along the blade, and does not have shear webs that add stiffness. The deformation of this model blade is therefore expected to be large, which will make results easier to interpret, and will help to indicate the limitations of linear models that assume small to moderate deformation such as those used in FAST. However, the resulting deformations may be larger than those currently expected for most modern wind turbine blades. As stated at the beginning of this chapter, the purpose of this study is not to calculate the stresses and deformation of a realistic turbine blade, but rather to demonstrate the use of preCICE for a coupled fluid-structure interaction of a large flexible wind turbine blade and investigate how this compares to predictions from lower order engineering tools.

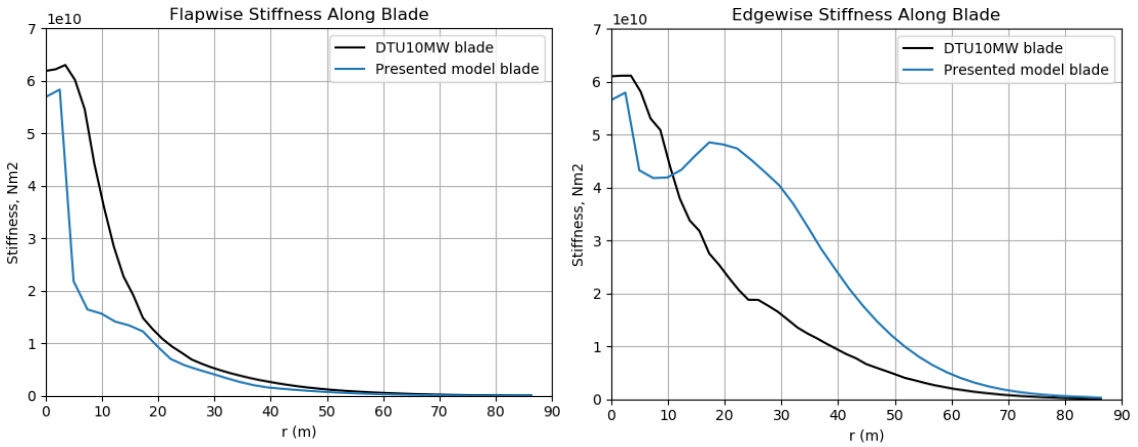

Figure 6.6: Stiffness along the model blade in the flapwise and edgewise direction, compared with the DTU 10MW blade

The blade is represented in CalculiX as a hollow structure defined using first order tetrahedral 2D shell elements. When the simulation is initialized, these shell elements are extruded to form 3D 'wedge' elements based on the user defined material thickness, as shown in Figure 6.7 [170].

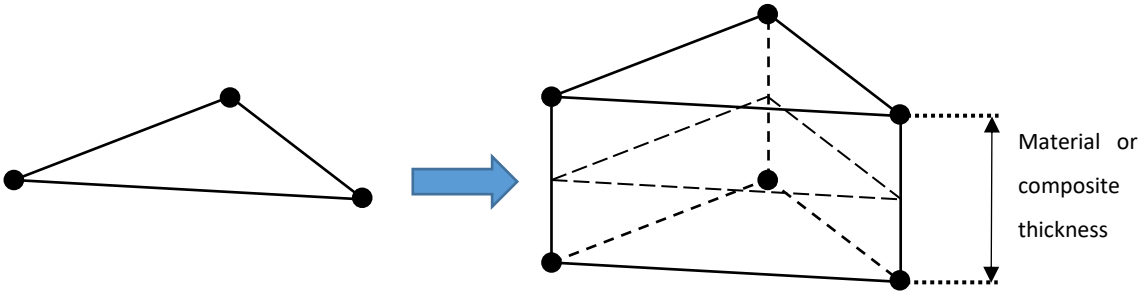

Figure 6.7: Expansion of 2D shell element to 3D wedge element during solver initialization in CalculiX, adapted from [170].

The geometrically nonlinear solver is used in CalculiX to account for possible large deformations that may occur. Each element in the CalculiX mesh has two integration points positioned across the element thickness, for which the stress information is given. The displacement and stress information for the structure is recorded at regular intervals.

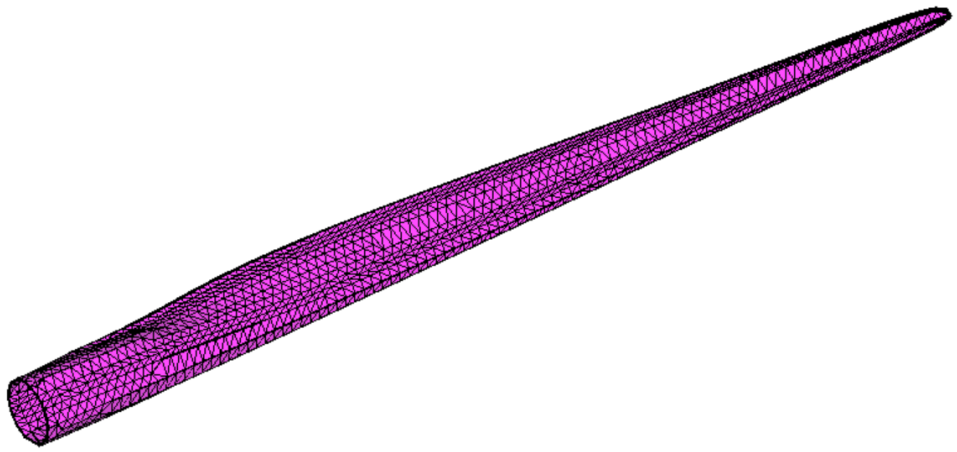

Figure 6.8: 3D finite element model of the blade used in CalculiX

Due to time constraints, the impact of the structural mesh resolution was not investigated in this study, and the same structural mesh was used for all simulations. The mesh used for the structural calculations in CalculiX is relatively coarse compared to the fluid mesh resolution, consisting of 2254 nodes and 4465 elements, in order to improve the computational speed of the model. The finite element mesh of the blade is shown in Figure 6.8.

The natural frequencies of the model blade are obtained by performing a modal analysis in CalculiX. A modal analysis on the FAST model of the blade is also performed using the 1D finite element code BModes [204], which uses a beam representation of the blade. The five lowest natural frequencies of the model blade calculated in each code are presented in Table 6.4, in addition to the natural frequencies of the original DTU 10 MW blade.

Table 6.4: Natural frequencies calculated for the model blade, compared with the DTU 10 MW blade

Mode	Model blade (CalculiX) (Hz)	Model blade (BModes) (Hz)	DTU 10 MW (Hz)
1st flap mode	0.40	0.31	0.61
1st edge mode	0.87	0.83	0.93
2nd flap mode	1.33	1.01	1.74
2nd edge mode	3.35	3.04	2.76
3rd flap mode	2.91	2.07	3.57

The natural frequencies of the flapwise bending modes are significantly lower for the model blade than the DTU reference blade, which corresponds to the lower stiffness observed in Figure 6.6. The natural frequencies of the CalculiX model are also consistently higher calculated for the NuMAD model that is used in

FAST, The reason for this is unclear, but may be in part due to the coarse mesh used in CalculiX. This may affect each model's prediction of the blade behaviour and should be taken into account when the two models are compared, since each blade will have different excitation frequencies.

6.3.1.3 preCICE Configuration

The force from the fluid mesh in OpenFOAM is interpolated onto the solid mesh in CalculiX using conservative radial basis function (RBF) mapping with a compact thin plate splines function, of which more detail can be found in [229]. Similar to nearest projection mapping, this RBF mapping scheme is second order accurate. A consistent form of this interpolation function is used to map the displacement from the solid mesh to the fluid mesh. The compact thin plate splines function has local support, and requires a support radius to be defined. This is chosen to be approximately 4x the average mesh cell width at the interface in accordance with the guidelines in the preCICE documentation [230].

The two solvers are coupled in preCICE using parallel implicit coupling. The convergence of the implicit coupling is accelerated using the interface quasi-Newton least squares (IQN-ILS) approach, of which more detail can be found in [231].

The simulation timestep dt is dependent on the fluid mesh resolution dx and the wind speed U, since this had to be chosen so that the Courant flow number $CFL = dt * U * dx < 1$ for the duration of the simulation; this ranges from $t = 0.001\ s$ to $t = 0.000025\ s$ for the presented simulations. No subcycling is incurred in the presented simulations, meaning that OpenFOAM, CalculiX and preCICE all use the same timestep.

6.3.2 Results

6.3.2.1 Blade Deflection and Impact of Grid Resolution

The resulting blade deformation from the preCICE modelling is compared against FAST for each of the fluid meshes investigated, in order to determine how the preCICE model differs from a low fidelity engineering model in its prediction of blade behaviour. Estimating the blade deformation accurately is important as this can alter the surrounding flow field, which can lead to additional fluctuation in the

loading on the blade. This two way fluid-structure interaction may lead to aeroelastic instabilities such as flutter, which can damage the structure.

6.3.2.1.1 Low Wind Speed

The time series of the blade tip displacement in the lower wind speed in the x- and y- direction, which correspond to edgewise and flapwise bending respectively, is plotted for each mesh in Figure 6.9. The simulation on the coarsest mesh (mesh 1) is simulated for an additional 10 seconds in order to demonstrate that an approximate steady state response is achieved by the model for this time period. The blade tip oscillates in the y-direction at approximately the same frequency for all three mesh configurations, which roughly coincides with the first blade flapwise bending eigenfrequency listed in Table 6.4. This does not agree with FAST, which predicts that the blade oscillates at the second flapwise eigenfrequency. The preCICE model also captures numerical damping behaviour which is not observed in FAST. There is some variation in the amplitudes of these oscillations between the three mesh configurations in preCICE, but there is good agreement on the mean tip y-displacement and the level of damping. However, the mean tip deflection and oscillation amplitude in all of the preCICE simulations is significantly lower than that observed in FAST. For the edgewise bending, the finer mesh configurations (mesh 2 and 3) show higher frequency second order oscillations which are not observed in the results for coarsest mesh or in the FAST model. The modal model of the blades used by ElastoDyn considers only the first edgewise mode, so this model is not capable of capturing higher order oscillations for this mode. Similar to the flapwise bending, the edgewise bending oscillations in preCICE have a lower amplitude than in FAST. The preCICE model predictions of the mean blade deflection in both directions show little change with increasing fluid mesh resolution, and the predictions of the oscillating behaviour using mesh 2 and 3 in particular show good agreement, which suggests that a reasonable level of fluid mesh convergence has been achieved. It will be interesting to see if the model predictions of the structural response change with increasing refinement of the structural mesh.

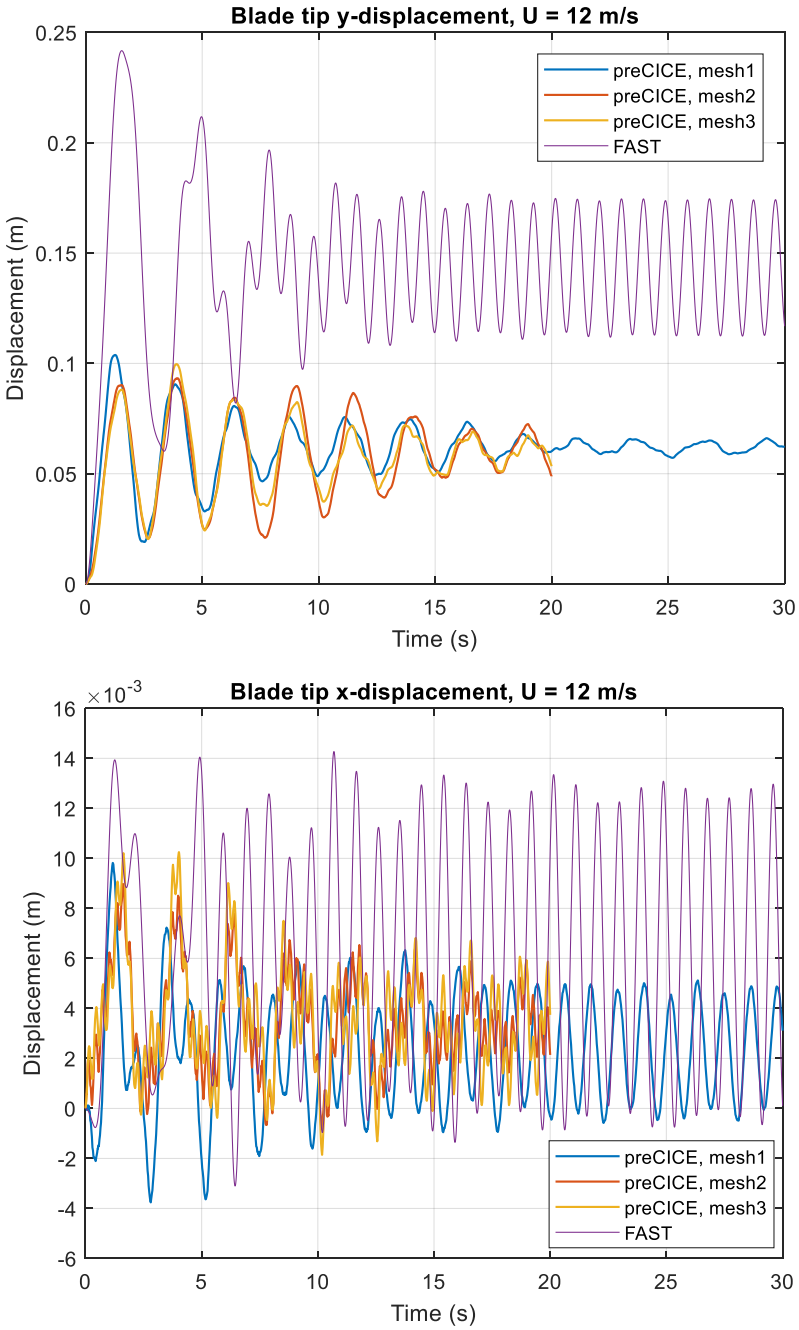

Figure 6.9: Tip displacement over time for U = 12 m/s

It should be highlighted once again that a parked wind turbine in 12 m/s wind is an unlikely event, and that a turbine would usually be producing power at this wind speed, meaning that the blades would experience significant additional loading due to rotor rotation. The implications of this are discussed in Chapter 7.

6.3.2.1.2 Extreme Wind Speed

The blade tip deflection for a wind speed of 50 m/s is plotted in Figure 6.10 for the coarsest and finest fluid mesh. Both FAST and the preCICE model show that

the blade tip deflection in both directions is at least an order of magnitude larger in a wind speed of 50 m/s compared to 12 m/s. The flapwise deflection oscillation frequency in the preCICE simulations is also higher in this extreme wind speed than in the lower wind speed, whilst the frequency in FAST is the same for both wind speeds. The mean deflection predicted by the preCICE model is once again significantly lower than that observed in FAST. The amplitude of the tip edgewise bending oscillations from the preCICE simulations show closer agreement with FAST in this case than for the lower wind speed, although second order higher frequency oscillations are again only observed at the higher mesh resolution.

The lower deflections predicted by preCICE in both wind speeds may suggest that the ElastoDyn module in FAST overpredicts structural deformation for a highly flexible blade. If this is true, this may lead to overly conservative blade designs for floating wind turbines where large blades with low stiffness. Alternatively, this may suggest that the structural mesh resolution used in CalculiX is too coarse to capture the deformation behaviour correctly. Validation against experimental data for a flexible wind turbine blade is needed in order to confirm the accuracy of each model.

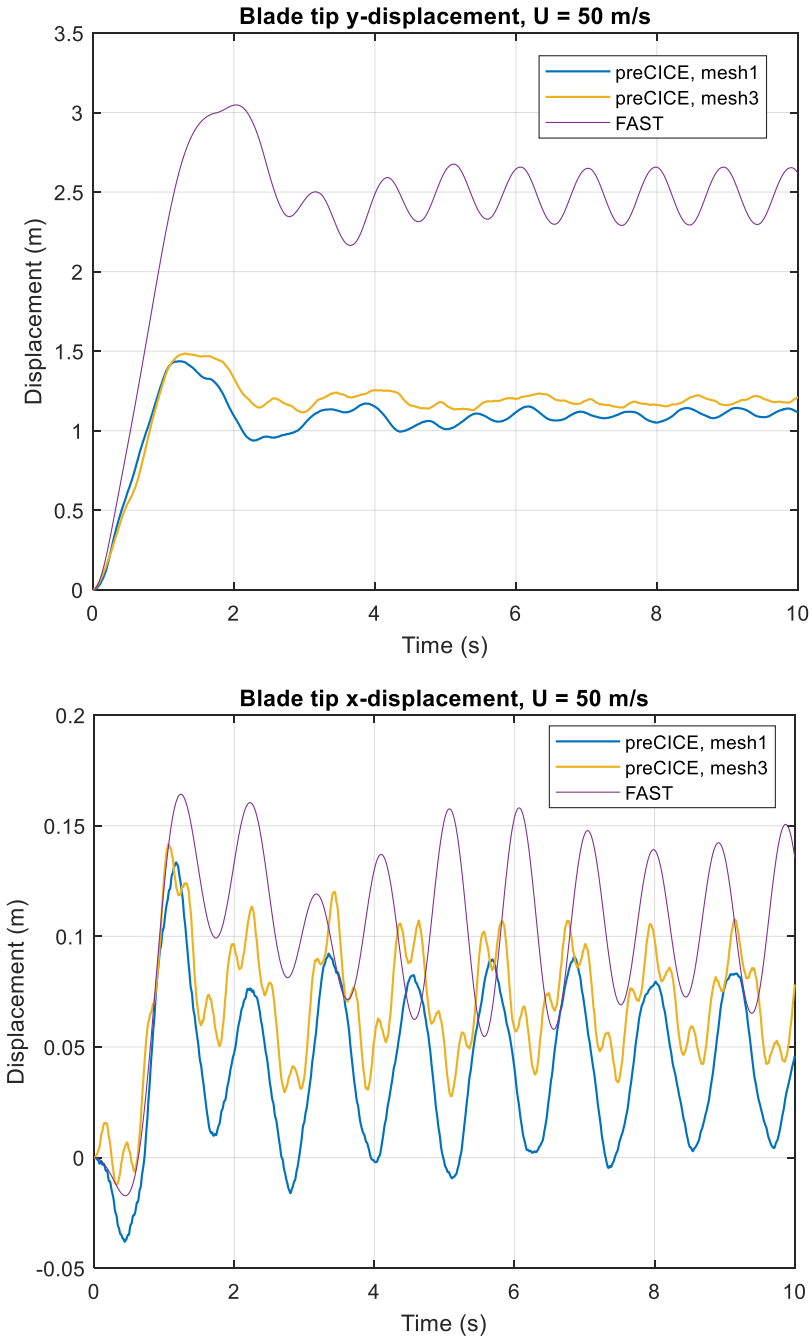

Figure 6.10: Tip displacement over time for U = 50 m/s

6.3.2.2 Load Distribution

Figures 6.11 and 6.12 show a snapshot of the kinematic pressure distribution on each side of the deflected blade due to the fluid flow at each wind speed. Figures 6.13 and 6.14 show the pressure distribution around a cross section of the blade close to the tip. The pressure distribution indicates the magnitude and direction of the forces that are acting on the blade.

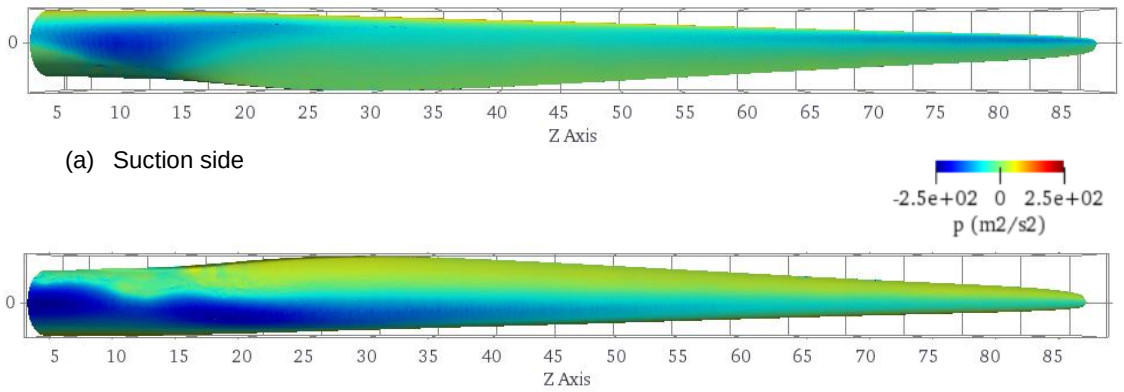

(a) Suction side

(b) Pressure side

Figure 6.11: Kinematic pressure distribution along the blade, U = 12 m/s

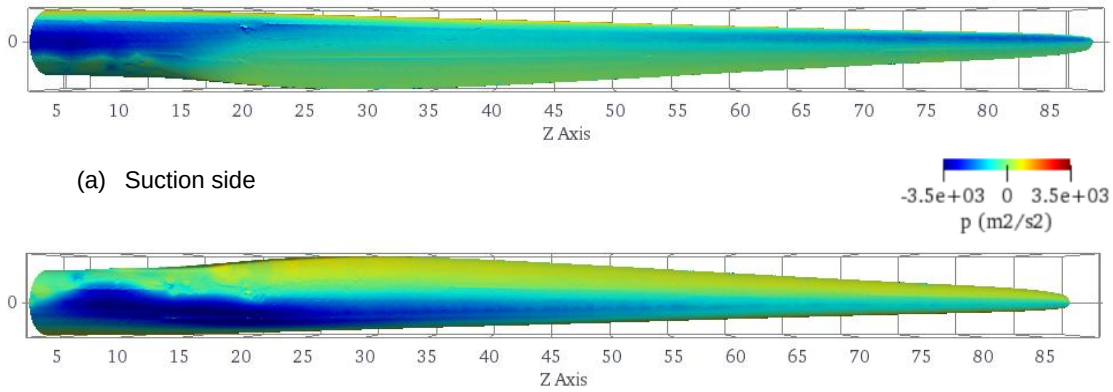

(a) Suction side

(b) Pressure side

Figure 6.12: Kinematic pressure distribution along the blade, U = 50 m/s

In a typical operational case, positive pressure would be observed on the lower side of the aerofoil whilst the upper side would experience negative pressure (suction), which generates a lift force on the aerofoil. This is observed close to the blade tip, as shown in Figures 6.13 and 6.14. In Figures 6.11 and 6.12, higher levels of suction are observed on the pressure side than the suction side near the blade root, which is due to the blade being feathered at 90° to represent an extreme case. This results in a negative local angle of attack up to approximately 60 m from the blade root (see Figure 6.4), which means that the pressure sign is reversed on each side of the blade section. Positive pressure is highest at the leading edge of the aerofoil section along the blade. Except for the root section where the blade cross section is a cylinder, an area of positive pressure is also observed on the pressure side of the aerofoil section trailing edge. As expected,

the fluid pressure and suction on the blade is significantly larger in the extreme wind case, which leads to a larger force acting on the blade.

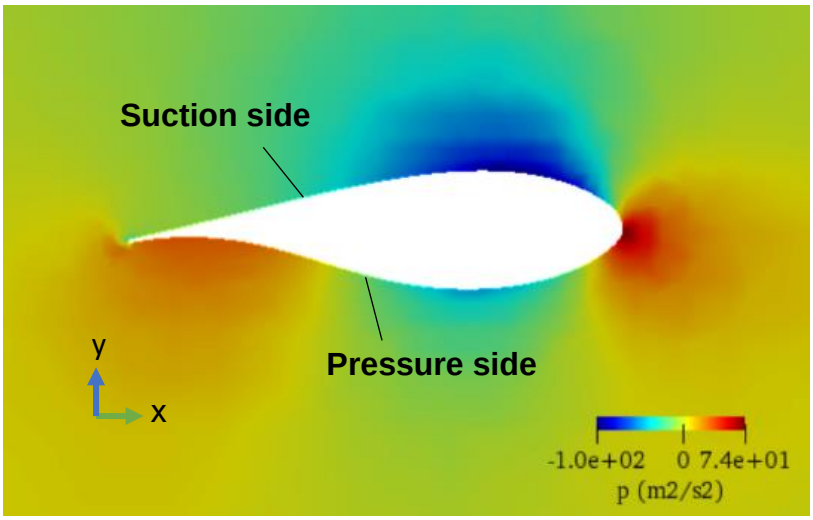

Figure 6.13: Pressure distribution around the blade at r = 75 m, U = 12 m/s

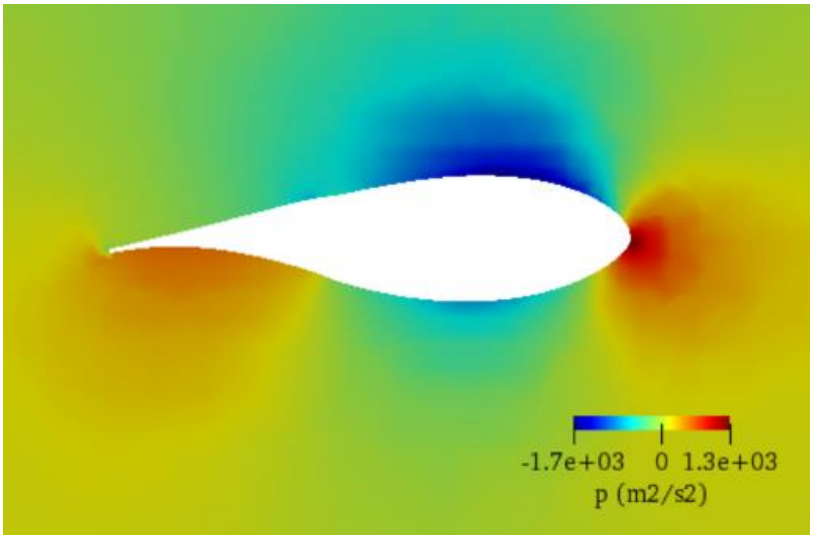

Figure 6.14: Pressure distribution around the blade at r = 75 m, U = 50 m/s

The forces on the blade due to the fluid pressure are converted to stresses in CalculiX. The load output available from CalculiX consisted of a stress tensor for each of the mesh elements. The distribution of bending stresses about the x- and y-axes are plotted in Figures 6.15-6.18. By viewing the stresses over the whole blade, it is possible to analyse detailed information on the load distribution for the structure, and identify locations on the structure that may be most at risk of failure by locating areas with high stresses where loading is concentrated. This is a key advantage of using a 3D FEA approach to structural modelling, since it is not possible to identify the exact locations of stress concentrations using a simplified 1-D beam model of the blade. For example, Figure 6.17 shows an area of high

bending stress about the x-axis (flapwise bending) at approximately 15-20 m along the span from the root. In this region, the blade cross section transitions from a cylinder to a thick aerofoil section, and a typical blade internal structure would have shear webs in this region to add stiffness. This explains why there is a particularly large difference in flapwise stiffness between this blade and the DTU 10 MW reference turbine blade close to the root, as shown in Figure 6.6. It is therefore expected that loading would be high in this region for the model blade. The maximum stresses in the blade structure observed in 50 m/s wind case are approximately an order of magnitude higher than in 12 m/s wind. However, the exact values of the local stresses may be mesh-dependent.

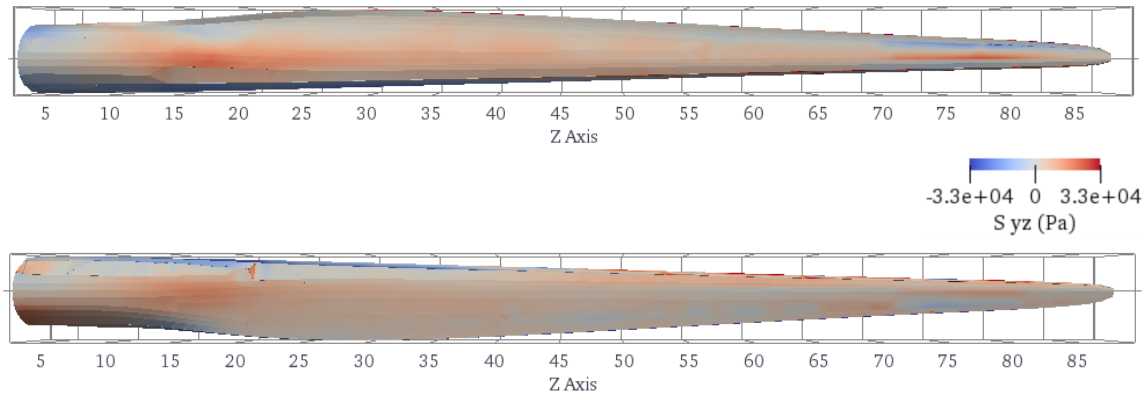

Figure 6.15: Bending stress about the x-axis, U = 12 m/s

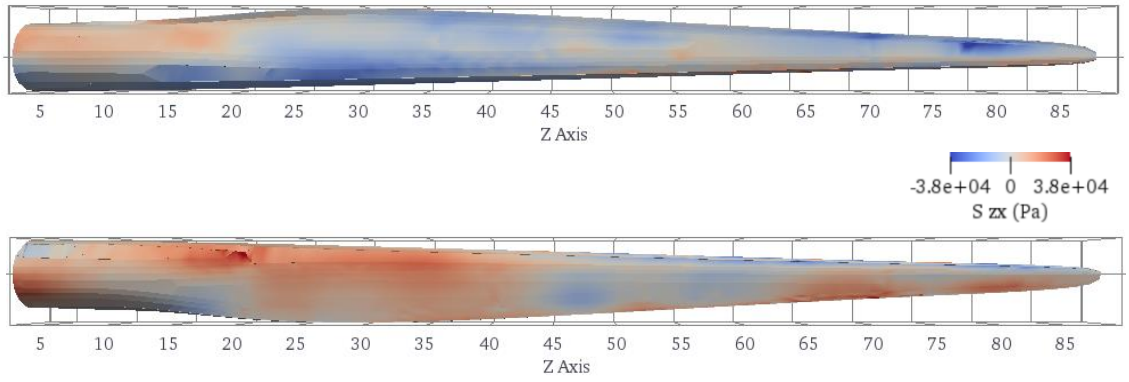

Figure 6.16: Bending stress about the y-axis, U = 12 m/s

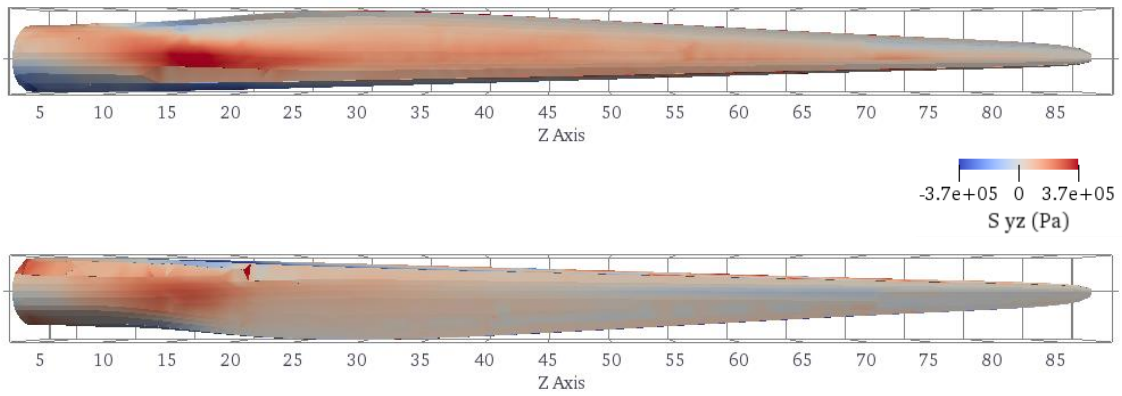

Figure 6.17: Bending stress about the x-axis, U = 50 m/s

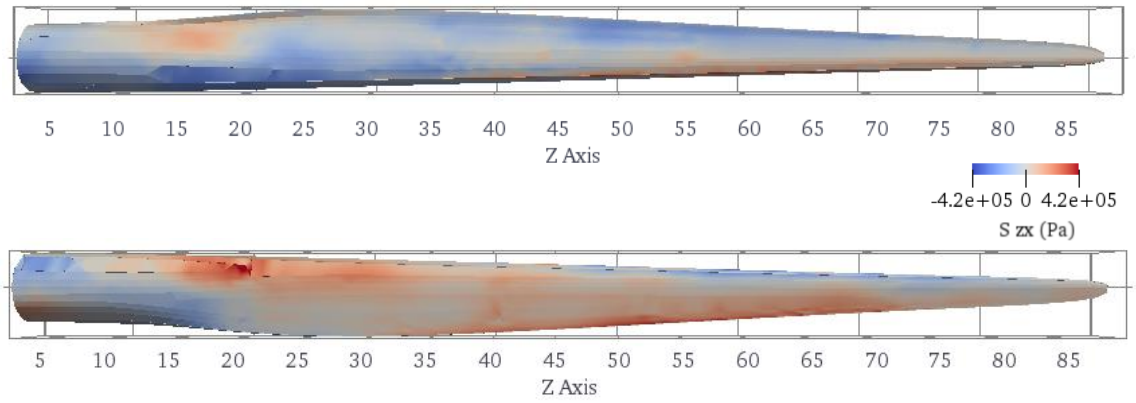

Figure 6.18: Bending stress about the y-axis, U = 50 m/s

The available output from ElastoDyn, the structural model in FAST, is less detailed than that from a finite element model such as CalculiX, and consists of shear force and bending moment information at the blade root or at specified blade nodes. The blade root bending moments for each wind speed according to FAST are plotted in Figure 6.19. Similar to the bending stresses observed in the FEA model in Figures 6.15-6.18, the maximum values of the blade root bending moment are approximately an order of magnitude higher in 50 m/s wind compared to the 12 m/s wind. From these figures, it is difficult to obtain a reliable value of the peak bending moment, since spikes due to numerical instabilities are observed with each cycle. This is especially true for the flapwise bending. This suggests that it is possible that the specific blade model used in this study, which has low flapwise stiffness as shown in Figure 6.6, is too pliant for FAST to be able to model accurately. The numerical spikes are also significantly larger at the high wind speed (50 m/s), which further suggests that ElastoDyn may not be able to handle large deformations.

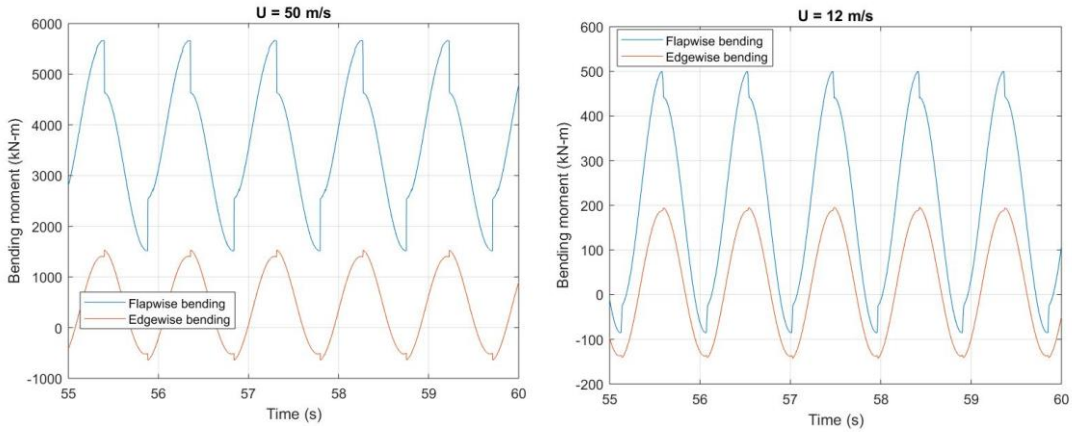

Figure 6.19: FAST predictions of blade root flapwise and edgewise bending moments

6.4 Chapter Summary

In this chapter, an approach for fluid structure interaction simulation using high fidelity CFD with fully resolved structure geometry and 3D FEA for structural modelling has been introduced and demonstrated. The outcomes from this chapter are summarised as follows:

1. The methodology was partially validated against a benchmark study for a cantilever structure with a simple geometry, and was shown to be capable of capturing large deformations due to bending.
2. Through simulation of a large flexible wind turbine blade in different wind speeds without rotation, the model predicts a load distribution that is consistent with what would be expected for a stationary blade given the simplified structure.
3. A reasonable level of mesh convergence has been achieved for the fluid solver, however the influence of the structural mesh still needs to be investigated, as the coarse mesh used in this analysis may limit the accuracy of the results.
4. The preCICE model gives noticeably different results to FAST in predictions of the blade deflection in both simulated wind speeds, with FAST predicting larger deflections in the flapwise and edgewise directions. This may suggest that ElastoDyn overestimates deformations for highly flexible structures, but also may be due to the coarse structural mesh used in CalculiX. The preCICE model is also shown to capture higher frequency

vibration response which is not captured in FAST due to the limited degrees of freedom considered in the modal model used in ElastoDyn.

High fidelity FSI models such as that presented in this chapter are generally recommended for cases involving complex conditions, such as flow separation that is not captured by models that rely on 2D aerofoil data or local buckling behaviour that cannot be captured by beam models. Such models can also provide information such as 3D aerofoil data or modal frequencies that can be used to tune and improve less computationally intensive models without the need for expensive physical testing. The results from this study indicate that the high fidelity model has potential to capture structural behaviour such as high frequency vibrations and damping that is not captured by lower order models. However, it is also clear that the model presented in this work requires extensive further work before it is ready to be used to produce a reliable analysis of blade behaviour. This includes a full grid convergence study (including both fluid and structural meshes), consideration of rotor rotation which will significantly change the loading conditions, and validation against experimental data for structures with more complex behaviour than simple bending. In particular, there is a need for validation to determine the extent to which difference between the proposed model and FAST are due to limitations related to the mesh configurations used in OpenFOAM and CalculiX.

Chapter 7

Discussion

In this chapter, the strengths and weaknesses of the modelling approaches investigated in Chapters 4-6 of this work are discussed in greater detail. The limitations of this work are also considered. Recommendations for the use of each modelling approach are then presented in Chapter 8.

7.1 BEM and ALM Approaches in Coupled Simulations of FOWT Systems

Whilst BEM and ALM approaches have limitations associated with their reliance on 2D aerofoil data, their relatively low computational cost compared to geometry resolved CFD means they can be used to simulate a wide range of load cases as shown in Chapters 4 and 5. Furthermore, the integration of these models in multiphysics tools such as FAST enables simulation of the complex coupled dynamics of floating offshore wind turbines. The effects of floating platform motions were not considered in the geometry resolved modelling presented in Chapter 6 since this would dramatically increase the complexity and computational cost of an already very expensive modelling approach, which highlights the advantages of lower fidelity models in FOWT simulation.

An actuator line model has been compared with a BEM model for several different turbines in operational conditions in this work. A consistent difference between the BEM and ALM is that the ALM predicted higher rotor power and thrust in below rated wind speeds when the pitch controller is not active. For the experimental scale NREL Phase VI turbine, the difference between the rotor load predictions from FAST and SOWFA was less than 2% for the chosen parameters (Table 4.2), but when the same ALM setup was used for utility scale 5 MW and 6 MW turbines, the differences are more significant (Figures 4.7, 4.8 and 5.9). This implies that there is not a ‘one size fits all’ approach to the tuning of the actuator line model parameters, and that the chosen setup should be validated for multiple

turbines in order to increase confidence in the accuracy of the ALM and to avoid over-calibration of the model to one specific validation case.

Whilst the rotor loads predicted by an ALM were found to be higher than those from BEM modelling, the results from investigating FOWT behaviour in extreme conditions (presented in section 5.3) suggested that the aerodynamic loads on the turbine tower were smaller when calculated using an ALM as opposed to the potential flow model used to calculate tower loads in FAST, leading to discrepancies in the mean platform displacement. This was particularly apparent in the surge and sway displacement (shown in Figure 5.12), which is significant as this could lead to errors in the predicted mooring loads during an extreme event. This highlights a potential flaw with modelling a non-slender structure such as a turbine tower using an actuator line representation, where the structure is modelled as a drag force on the fluid rather than a physical boundary, since this still allows the fluid to potentially pass through the modelled tower, which is not realistic [232]. A more advanced actuator line model of the tower such as the method proposed by Churchfield et al. [232] based on pressure around a cylinder may improve predictions.

Chapter 4 showed that BEM and ALM predictions of the rotor loads diverge slightly for a floating turbine compared to bottom fixed configuration. The platform motion in response to wave loading resulted in a larger increase in the mean power in SOWFA than in FAST, and a larger power variation in FAST than in SOWFA (Figure 4.7). The reason for this discrepancy cannot be confirmed without validation data, however this may indicate a limitation in the empirical dynamic inflow model used in the BEM model in FAST, and requires further investigation.

The rotor load predictions from FAST and SOWFA were also found to diverge with increasing yaw misalignment. Misaligned conditions are an important issue for floating offshore wind turbines since they are more frequently misaligned with the wind than bottom fixed turbines due to platform pitch and yaw motion. Misaligned rotors experience unsteady loading due to the cyclic variation in relative velocity and angle of attack, which negatively impacts power production and fatigue loading [27]. It is therefore important that numerical models are able to capture the effects of misaligned conditions accurately. The rotor power loss due to a yaw misalignment angle γ is shown to be proportional to $\cos(\gamma)^x$, where

$x = 2.68$ according to FAST and $x = 1.78$ according to SOWFA (Figure 4.9). The misaligned rotor aerodynamics are computed in the BEM model using an empirical correction which is acknowledged to be unreliable [49], whilst the ALM directly samples the wind flow at the rotor, which means that in theory the ALM should be more accurate than the BEM model in predicting aerodynamics in yaw. This finding therefore indicates that BEM models overestimate power loss due to yaw. This study also indicated that the BEM model may overpredict the cyclic variation in the blade flapwise bending moment in large yaw angles, which has implications for fatigue loading and may lead to overly conservative design choices. When realistic turbulent conditions were considered in Chapter 5, there was directional variation in the wind due to turbulent fluctuations that would have led to the turbine operating in yawed conditions, since the nacelle yaw angle was fixed to align with the target mean wind direction for each simulation. However, neither TurbSim nor SOWFA predicted an instantaneous wind direction that varied more than 15° from the mean (target) wind direction, meaning there was negligible difference between the BEM and ALM predictions of the rotor response due to yaw misalignment in the presented cases.

The presented work focused on the behaviour of spar type FOWTs in order to be able to compare numerical model results against real data for full scale FOWTs from the Hywind Scotland and Goto Islands projects. However, the motion response of a FOWT is strongly dependent on the platform and mooring configuration. A TLP FOWT typically has smaller platform motions and higher natural frequencies than a spar, and so the aerodynamic behaviour will be closer to that seen for a bottom fixed turbine, whilst a semi-submersible may experience larger motions. Novel platform designs and floater geometries may also experience their own unique dynamic behaviour, such as Floatgen [233], a floating turbine installed off the coast from France which features a semi-submersible platform with a damping pool to reduce motions. In order to fully understand the interaction between aerodynamics and different floating substructure dynamics, adaptive numerical models are needed which consider the two-way coupling. Fully coupled models using geometry resolved CFD are extremely expensive, so lower fidelity models such as BEM and ALM approaches, and the structural and hydrodynamic models used in FAST play an important role in understanding the behaviour of FOWTs.

7.2 Simulating Realistic Offshore Wind Loads on FOWTs

In Chapter 5, turbulent wind fields were simulated based on statistics of wind turbine anemometer data for a range of operational conditions from the North Sea and an extreme typhoon event offshore from the Goto Islands, Japan. In SOWFA, different atmospheric stability conditions were considered by modifying the temperature flux. It was found that the simulated neutral and stable ABL conditions tended to result in lower TI than the estimated value from the field data for the North Sea, whilst the unstable ABL simulation resulted in a closer match. This may suggest that unstable conditions are a more suitable assumption than neutral conditions for wind fields in the North Sea where the Hywind Scotland wind farm operates, which is supported by measurements presented by Cheynet et al. [33]. However, it was also shown that floating platform motions and rotor loads are sensitive to the turbulence intensity in operational conditions. A key disadvantage of using SOWFA is that it is more difficult to tune the atmospheric boundary layer model to achieve desired conditions such as a specific turbulence intensity, since this is not an input in SOWFA but rather depends on the tuning of several parameters. The Kaimal model is much simpler to set up and fit to measured conditions, and is therefore preferable to LES for neutral atmospheric conditions if parameters such as the turbulence intensity are known and wake effects on downstream turbines are not important.

The study of the typhoon impact on a FOWT indicate that there is no apparent benefit to using LES over less computationally expensive statistical methods, since there was overall very little difference in the turbine response predicted by FAST and SOWFA. It was also observed in this study that in extreme conditions when the turbine is in a shutdown state, the platform response and blade loads appear to be insensitive to the turbulence intensity. An environmental factor that may have a significant effect on FOWT response in a typhoon event (in addition to the extreme wind speed and wave height) is the misalignment between the wind and wave direction. This was shown to be particularly important when calculating the extreme yaw response of the spar platform, and implies that models where only aligned wind and waves are considered would not be adequate for simulating FOWTs in extreme conditions. To confirm this, future work should consider wave models with directional spread to see if this can

achieve an estimate of the yaw response that matches more closely with field measurements.

The impact of atmospheric stability was only investigated in this work using SOWFA, however it should be noted that it is also possible to simulate non-neutral atmospheric conditions using statistical methods which were not investigated in this work. In TurbSim, stable and unstable conditions can be modelled based on the work of Høstrup [234] and Olesen et al. [235]. It was observed in Chapter 5 that there were differences in the impact of the stable SOWFA wind field and the Kaimal wind field on the turbine response (notably the sway response and the blade flapwise bending moment) even when the hub height TI is the same, which suggests that atmospheric stability should be taken into account. However, unlike for the Kaimal model, it is not possible to directly scale the hub height turbulence intensity to a desired value in the non-neutral statistical models available in TurbSim which, as was shown for the LES wind fields, makes comparison against field data difficult.

A benefit of using SOWFA with the LES method that was not investigated in this work is the ability to capture the complex flow physics involved in wake dynamics. This is necessary for wind farm simulations involving multiple turbines, where some turbines will be affected by the turbulent wakes of upstream turbines within the farm. A recent development in wind energy simulation tools is FAST.Farm [236], which is an extension of FAST for modelling wake physics in wind farms at a lower computational cost compared to full LES. The code requires a turbulent wind input using either an LES precursor or synthetic turbulence generated using a statistical model such as TurbSim. Validation of FAST.Farm is ongoing [237].

If the SOWFA approach is used to model ABL wind, the turbulence intensity is determined by the atmospheric stability condition and the ground or sea surface roughness. In the work presented in Chapter 5, the roughness height parameter z_0 was estimated based on the Charnock relationship, where the friction velocity u_* was estimated based on the target turbulence intensity using an approximation from the literature [149]. This approach was found to result in a hub height TI that was lower than desired in operational cases with neutral stability, and higher than desired in most cases involving typhoon wind. One reason for this is that the standard deviation σ of the wind speed is implied to be constant with height. In

general, the simulations using LES presented in this work show that σ_u decreases with height above the sea surface. The 2 MW turbine that was studied in the typhoon simulations has a lower hub height than the 6 MW Hywind turbine (56 m vs 98 m), but the height at which turbulence intensity and therefore σ is measured is not considered when estimating friction velocity. The approach used in this work may therefore result in a poor estimation of the surface roughness, and is not recommended for generating atmospheric wind with a target turbulence intensity.

7.3 Considerations for High Fidelity Modelling of Turbine Blades

In Chapter 6, a high fidelity method involving geometry resolved CFD and 3D FEA was proposed, which provides the opportunity to study the loading on the blades in detail without relying on tabulated 2D aerofoil data. The limitations associated with the aerofoil data required for BEM and ALM methods, such as the need for a correction to account for dynamic stall, therefore do not apply. In addition, the use of 3D finite element modelling of the structural behaviour means that detailed information on the local stresses can be obtained, which has been shown to be important when investigating blade buckling behaviour in extreme conditions [88]. Based on the significant differences between the presented high fidelity model and FAST, and the lack of experimental data to confirm which result is more accurate, the proposed model is not yet ready for use in the wind turbine design process. However, as offshore wind turbines continue to increase in size and blade aeroelasticity becomes more significant, high fidelity models that are able to capture this behaviour will become more important. In order to improve the reliability of the model, several modelling aspects must be considered in future work, which are described in this section.

The presented results in Chapter 6 demonstrated that the simulated structural deflection behaviour of the blade is at least partially dependent on the fluid mesh configuration (Figures 6.9 and 6.10), with higher resolution meshes resulting in larger mean deflections in high wind speed cases as well as higher frequency oscillations. Due to time constraints and limited available computing resources, it was not possible to investigate finer structural mesh configurations in CalculiX. In order to obtain reliable results for the blade behaviour using preCICE, future work

will also require simulations with increasingly fine structural mesh until convergence is achieved. The computational costs of each simulation are presented in Table 7.1. All simulations were performed on 72-core dual Intel(R) Xeon(R) Gold 6254 CPU @ 3.10GHz processors, and OpenFOAM was run in parallel using 35 CPUs. The most computationally expensive simulation, which was of the extreme wind case on mesh 3, took approximately 21 days to complete 10 seconds of simulation time. It should also be noted the fluid mesh resolution in the presented simulations is relatively low compared to guidance from the literature (Table 6.3), which suggests that more powerful computing resources are needed to study turbine behaviour using this modelling approach. It may also be possible to reduce computation time by running CalculiX in parallel to enable simulation of finer structural meshes.

Table 7.1 Total runtime for each preCICE simulation required to reach the simulation time (given in parentheses)

Number of fluid mesh cells	$\boldsymbol{U = 12\ m/s}$	$\boldsymbol{U = 50\ m/s}$
486,287	41 hrs (30 sec)	52 hrs (10 sec)
2,049,027	158 hrs (30 sec)	-
3,694,028	194 hrs (20 sec)	508 hrs (10 sec)

The preCICE model has been demonstrated to be capable of simulating the bending of a simple cantilever plate in this work, however this single case may not be sufficient to consider the methodology validated. Additional validation cases are necessary in order to ensure that the method produces consistently accurate results. The model predictions of wind turbine blade bending have not been validated against experimental data since this was not available. A typical wind turbine blade has more complex structural behaviour than simple bending, such as shear forces or torsion. Therefore, the preCICE model should be validated further against experimental data that includes these effects in order to make it a reliable model for use in the design process for large flexible blades suitable for offshore wind turbines.

The conditions simulated in this study provide insight into the behaviour of a parked blade during wind turbine shutdown, which occurs when the wind speed is outside of the operational range, and may also occur due to a fault or during turbine maintenance. If blade behaviour in operational conditions is of interest,

future work will need to include the effects of rotational speed on blade loading. This may be done using a single rotating frame approach in OpenFOAM if only rotating structures are to be modelled, or using a multiple reference frame or sliding mesh approach if stationary components such as the turbine tower are also modelled.

When the rotor rotates, the loading on the blades will differ significantly compared to the parked case, because relative velocity of the flow interacting with the blades increases with radial distance from the hub, and the angle of attack also varies. At the lowest rotational speed (6 rpm) of the DTU 10 MW turbine [223], on which the model blade studied in this work was based, the blade tip speed would be 56 m/s. The relative speed of the wind flow at the blade tip would therefore be higher than in the extreme wind speed case in which the stationary blade was simulated in this work, and resulting deflections are likely to be larger than when the turbine is parked in extreme wind conditions. This would also require a higher grid resolution in the blade tip region in order to keep the y^+ value sufficiently low enough to capture the effects of near-wall turbulence, which would subsequently increase the computational cost of simulations.

A higher order structural code BeamDyn has been developed for FAST that addresses some of the limitations of ElastoDyn, and is designed to be better suited for highly nonlinear composite beam problems [106]. Whilst ElastoDyn is based on Euler-Bernoulli beam theory, BeamDyn uses geometrically exact beam theory based on the Legendre spectral finite element method, which models a beam using a single high order finite element, and is capable of modelling full geometric nonlinearity. The BeamDyn model requires more detailed input than ElastoDyn and incurs a computational cost that is roughly one order of magnitude higher, and so due to time constraints this was not investigated in the presented work. In future work it will be interesting to compare the 3D finite element approach in CalculiX presented here with BeamDyn or another mid fidelity code that takes into account more structural nonlinearity than ElastoDyn.

7.4 Limitations of Presented Research

A limiting factor of this work is that the aerodynamic calculations using different numerical models cannot be directly compared against real world data for floating

offshore wind turbines, since this is not available. This is an ongoing issue in floating wind research, and makes it difficult to determine which aerodynamic model is more accurate or more suitable. It is difficult to explain the consistent offset between the two models' predictions of the rotor power and thrust, and determine the extent to which this is due to the need for further tuning of the ALM parameters examined in section 4.2. As discussed in Chapter 2, there is a need for reliable aerodynamic data for FOWTs to be made readily available in order to improve confidence in numerical modelling.

Due to constraints on time and available computing resources, simulations involving the ALM were restricted regarding grid resolution; the majority of simulations of operating rotors featured a local grid resolution $\Delta x \approx R/30$, which is the lower bound of the guideline provided by Jha et al. [177], and the refinement of the elliptical ϵ distribution for a grid resolution of $R/60$ discussed in section 4.2.3 was not investigated. Some of the recent developments proposed to improve ALM performance were also not considered in this work as they require finer grids that are more computationally intensive. For example, the recommendation by Shives and Crawford [180] of $\varepsilon < c/4$ would require more than 100 grid cells along each blade length for most modern large scale wind turbine designs in order to keep $\varepsilon > 2 * \Delta x$ to avoid numerical instabilities. A possible solution is to vary the grid resolution at the rotor location to take into account the chord length, however this would be complicated if the blades are able to move within the domain such as in the SOWFA-FAST coupled model used in this work, and may require some form of mesh motion.

For the simulations presented in Chapter 5, model turbines were developed based on the SWT-6.0-154 and Hitachi HWT2.0-80 turbines, however much of the information for these turbines is proprietary and therefore many of the parameters for the models were estimated, such as the blade geometry, blade and tower structural properties, and control system properties. It is therefore expected that the numerical model of the turbine will not behave in exactly the same way as their physical counterparts. This limits the ability to validate the numerical models against the field data, particularly in the case of aerodynamic loads in operational conditions and their effect on platform motions.

The impact of the atmospheric stability condition on the load and motion response of a floating offshore wind turbine was considered in Chapter 5, however the impact of stable and unstable conditions were not considered for the same wind speed. The combined impact of wind speed and atmospheric stability therefore cannot be determined from the simulated cases. In numerical studies by Doubrawa et al. [39], it was shown that blade loads are more sensitive to the atmospheric stability condition in low winds.

All of the hydrodynamic calculations performed in this work considered first order effects only, since previous work has shown that second order effects on spar concepts are negligible [217,238]. However, higher order effects are likely to be more important in extreme conditions, where the aerodynamic loads are small due to the idling rotor [239] and the large waves mean that platform motions are not small relative to the platform diameter, meaning linear assumptions are not valid [44]. The reason that second order forces were not calculated in this work is that this would have required more detailed information on the spar platforms such as the mass distribution, which is difficult to obtain accurately for the turbines simulated in Chapter 5 where many of the parameters were estimated based on the availability of information from the Hywind and Goto Islands projects. In addition, the accuracy of the hydrodynamic coefficients required from WAMIT for second order calculations could not be guaranteed, since WAMIT does not include structural flexibility which may affect the calculated second order quantities [238]. The inclusion of second order hydrodynamic effects is also estimated to increase the computational expense of the simulations by an order of magnitude [217].

The high fidelity model was used to investigate the behaviour of a turbine blade with a simplified structure, featuring one material with a uniform shell thickness and no internal structural support such as shear webs. Modern wind turbine blades are typically composite structures with layups that vary along the blade span in order to increase stiffness near the root and reduce mass near the tip. The resulting deflection and stress distribution for a realistic offshore wind turbine blade design is therefore expected to differ significantly from the results presented in Chapter 6. In addition, the simplified blade structure does not experience the complex effects associated with composite blades such as bend twist coupling or cross sectional coupling due to anisotropic layups [106]. Further

work is needed to confirm that the high fidelity model is able to accurately capture the behaviour of composite blades that are applicable for offshore wind turbines.

Chapter 8

Conclusions and Future Work

8.1 Summary of Outcomes

In this work, low order numerical modelling using the engineering tool FAST has been compared with CFD models for a range of load cases for floating offshore wind turbines. The outcomes of this work in relation to the research questions set out in section 1.2 that this thesis aimed to answer are summarised as follows:

How does the widely used blade element momentum theory compare with higher fidelity CFD based actuator line modelling for simulating the aerodynamic loads of a FOWT?

- Chapter 4 demonstrated that when a uniform wind input is used, the difference between BEM and ALM predictions of rotor aerodynamics is larger for a FOWT than a bottom fixed turbine, and is sensitive to the rotor yaw misalignment angle. The BEM method predicts a larger rotor power fluctuation due to platform motion than the ALM, and BEM predicts a sharper decrease than the ALM in the mean aerodynamic loads with increasing yaw misalignment.
- In the study of extreme conditions presented in Chapter 5, when the turbine is idling, it was found that actuator line modelling of a turbine tower may in fact result in less accurate platform translational displacement compared to the potential flow method used in FAST.

How well do numerical models perform against experimental data for FOWT behaviour in realistic operational and extreme conditions?

- Through comparison against field data from one of the turbines within the Hywind Scotland pilot park in Chapter 5, it was shown that the FAST framework using either a BEM or ALM approach for aerodynamic modelling is capable of simulating mean rotational platform displacements

of a spar type FOWT in response to different wind and wave conditions that match well with measured values. However, the large simulated pitch and yaw motions suggest that the numerical models require additional damping of these modes. Large errors were also observed in the translational motions in below rated conditions, indicating limitations in the modelling approach such as starting simulations at the turbine equilibrium position and considering only unidirectional waves.

- The investigated numerical models were shown to be capable of simulating the platform motions of a spar FOWT in extreme environmental conditions with reasonable agreement with measured values, with the exception of the heave response, which was significantly underpredicted when first order hydrodynamic modelling was used

To what extent does the modelling approach for the wind input impact the behaviour of numerical models of FOWTs?

- It was found that that the use of the Kaimal model for the turbulent wind will result in similar results overall for the turbine response as when LES of a neutral atmospheric boundary layer wind is used, provided that the hub height longitudinal turbulence intensity is the same. However, the Kaimal model was shown to predict higher levels of lateral turbulence in high wind speeds that may have a small effect on sway, roll and pitch modes in neutral conditions
- In simulations of a FOWT during a typhoon, it was shown that the choice of wind model has very little impact on the extreme response of a FOWT, suggesting there is no significant benefit to using LES modelling instead of more efficient statistical methods for the wind input. The misalignment between the wind and waves may however have a significant impact on the platform yaw response.

How can high fidelity fluid structure interaction modelling help to inform on FOWT behaviour compared to more commonly used low fidelity models?

- In Chapter 6, it was shown that high fidelity FSI modelling using geometry resolved CFD and 3D FEA can capture simple bending behaviour with results that agree well with established benchmark results, and can provide valuable information on stress concentrations in a parked wind

turbine blade during extreme loading which is not possible with simple beam models.

- Early simulations using the high fidelity model showed significantly smaller deflections for a highly flexible wind turbine blade than those predicted using the BEM method and linear beam approach in FAST, though this may be related to the relatively coarse mesh configurations used.

8.2 Research Contributions

The original contributions to research of this project are summarized as follows.

- The widely used numerical tools FAST and SOWFA have been used to compare BEM and ALM implementations within a coupled aero-servo-hydro-elastic modelling approach for floating offshore wind turbine load cases. The presented study revealed a small increase in the difference between each model's estimation of rotor loads for a FOWT subjected to platform motions compared to a fixed turbine.
- Numerical models were compared against field data for full scale floating offshore wind turbines. To the author's knowledge, this is the first study of its kind to validate coupled numerical models against the data from Hywind Scotland which was distributed by Equinor and ORE Catapult in 2019. It was confirmed in this study that the numerical models used in FAST are capable of modelling the platform displacements of a spar mounted FOWT in a range of different wind conditions with reasonable agreement with measured values, although there is scope for improvement.
- As part of the effort to validate the numerical tools against field data, FAST models of two spar mounted turbines with 6 MW and 2 MW power ratings were developed based on the turbines used in the relevant floating wind projects. These models also included the hydrostatic restoring, added mass and damping coefficients from WAMIT for each spar platform to enable first order hydrodynamic analysis. The novel input files for these models are available at github.com/rachaelesmith.
- A framework for FSI modelling of wind turbine blades using open source software for geometry resolved CFD and 3D FEA was developed, where the two way coupling is configured using preCICE. The results from the

proposed tool were also compared against FAST for a case involving a stationary blade. Through partial validation against a benchmark case, this approach has been shown to be capable of handling large structural deformations, and with further validation this tool can be used to investigate the structural response and detailed loading information of the increasingly large and flexible blades that are used in offshore wind applications.

- Guidance and recommendations for the use of the studied models with focus on floating wind considerations are presented, which are summarized in the following section.

8.3 Recommendations for Use of Numerical Models

Low Fidelity Modelling with BEM

The validation of numerical models against field data presented in Chapter 5 demonstrated that there is overall little difference between the predicted platform motion response when a TurbSim wind input is used compared to LES in neutral conditions (provided that the longitudinal turbulence intensity is the same in operational conditions). The use of the Kaimal model may also provide an acceptable approximation of the impact of unstable conditions on FOWT response provided that an appropriate turbulence intensity is specified. In addition, the difference between the BEM and ALM predictions of aerodynamic loads appears to have little impact on the mean platform displacement. This is also found to be true in typhoon conditions, where the aerodynamic modelling method was found to have no significant impact on the extreme values of the platform response or the loading on the parked blades. This suggests that the use of BEM (with appropriate corrections) with the Kaimal model is suitable for FOWT simulations in most load cases, at least when the hydrodynamic response is of interest, and may even provide better results than the presented ALM approach in extreme conditions when considering the mean platform displacement.

CFD Modelling with ALM

For floating offshore wind turbines that experience a large heel angle, or turbines that are intentionally misaligned with the wind in order to redirect their wakes away from downstream turbines, it may be beneficial to use an ALM to understand their behaviour, at least in the cases where misalignment is expected to be largest.

In above rated conditions where the rotor is not operating and the aerodynamic loading is primarily due to forces on the tower, it is not recommended to use an ALM of a FOWT with a drag-only actuator line representation of the tower, since this may result in poor predictions of the platform displacement. There is also no apparent benefit to using computationally expensive LES over lower order models for simulating extreme typhoon wind impacts on FOWTs.

FSI with Geometry-Resolved CFD

Despite limitations associated with the use of relatively coarse mesh configurations, the high fidelity model has been shown to estimate a stress distribution that would be expected based on the internal structure of the investigated blade. Due to the very high computational cost, it is not recommended to use this model early in the design process for FOWT blades when many designs are being considered.

At this stage, the model is not ready for use in wind turbine design applications, since the exact reasons for the observed disagreement with FAST are not yet known. However, once a full mesh convergence study has been completed and the model has been validated against relevant experimental data, it may be extremely useful for investigating blade structural response in detail and identifying specific areas for improvement in blade design after the conceptual design stage. In particular, this may be a valuable tool for analysing blade behaviour where large deformations are expected, such as in extreme wind conditions, where low order models may be less reliable and have been shown in this work to lead to numerical spikes that may compromise the results. Large deformations and complex behaviour are increasingly likely to occur as offshore wind turbines become larger and blades become longer and more flexible. This level of modelling may limit future need for rigorous experimental testing of prototype blades, which ultimately helps to reduce the cost of wind turbine design.

8.4 Future Work

Based on the outcomes of this research and the acknowledged limitations, several proposed areas for future work have been identified:

1. *Experimental validation of FOWT aerodynamics and blade structural response:* The data from the Hywind Scotland and Goto Islands floating wind projects provides valuable information on the platform motion response. However, there is still a need for experimental validation of numerical aerodynamic models for floating wind applications. In addition, the high fidelity coupled numerical model for fluid structure interaction simulation has not yet been validated for analysing wind turbine blade response. It is therefore necessary to obtain experimental data that describes the impact of floating platform motions on power production and aerodynamic loads, and data that describes the structural deformation of a flexible wind turbine blade.

2. *Validation of hydrodynamic models against full scale field data:* A limitation in the validation of numerical models against field data that was identified in this work is that only first order waves and hydrodynamics were considered, which may explain the significant underpredictions for the translational motions, particularly the heave motion in the simulation of typhoon conditions. It is therefore recommended that further validation of the numerical models presented in this work against the Hywind Scotland field data is conducted with higher order hydrodynamic modelling included. This will help to determine the extent to which the errors in this work are due to the hydrodynamic model and how much they are influenced by the aerodynamic modelling.

3. *Extension of high fidelity coupled FSI model:* The approach for modelling the fluid structure interaction behaviour of a wind turbine blade using geometry resolved CFD and 3D FEA has so far only been used to investigate a stationary blade with a very simple internal structure. Future work will therefore focus on modelling more realistic blade structures using FEA, and including blade rotation through the use of moving meshes or

reference frames in OpenFOAM. A full mesh convergence study including the impact of the structural mesh in CalculiX is also necessary in order to improve confidence in the model results.

Appendices

A Platform Motions in Regular Waves and Uniform Wind

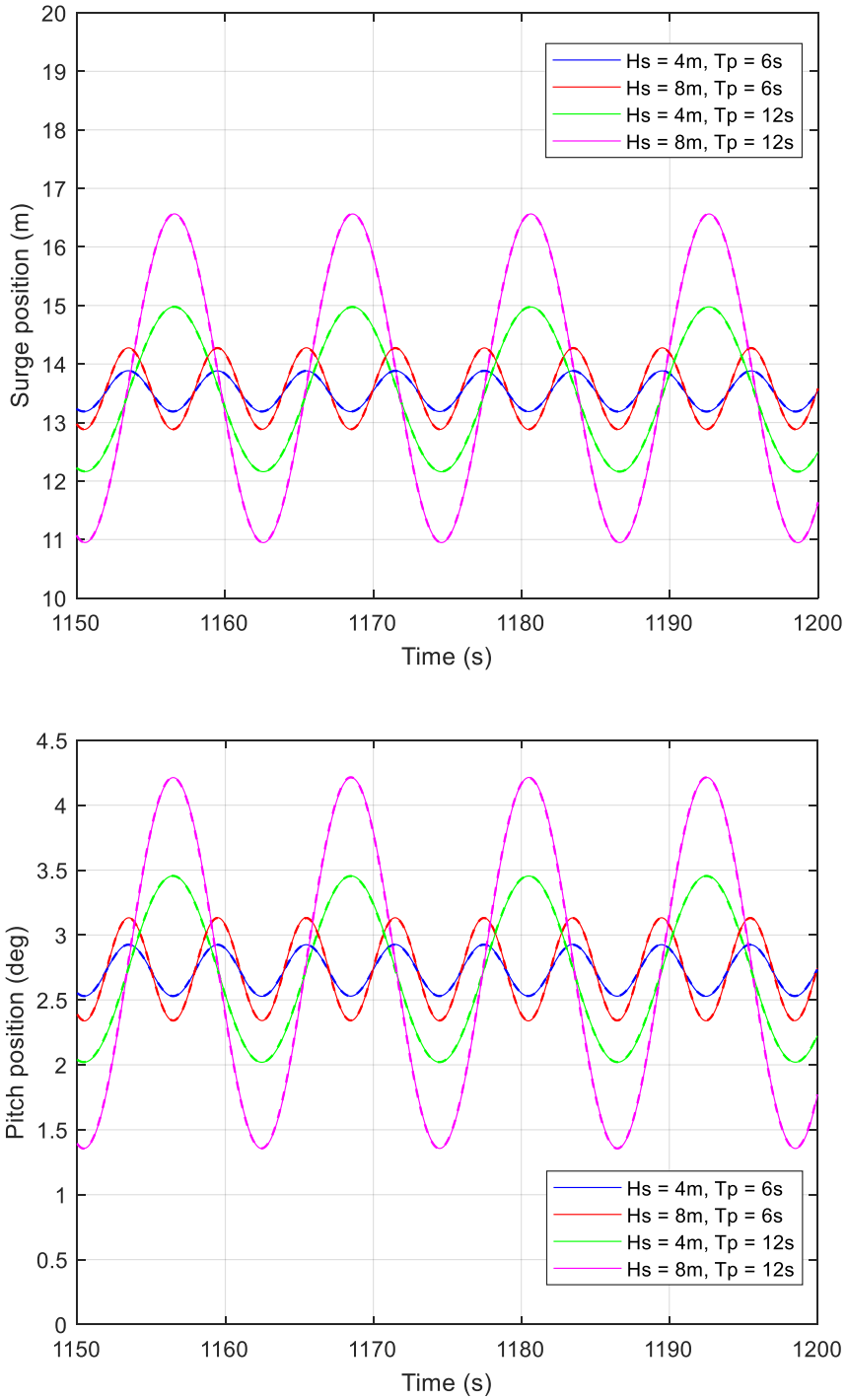

Figure A.1: Surge and pitch motions of the floating platform under different wave conditions, with mean offset between FAST and SOWFA removed. Dashed lines represent predictions from FAST, solid lines represent SOWFA

B Development of Quasi Equilibrium in Precursor Simulations

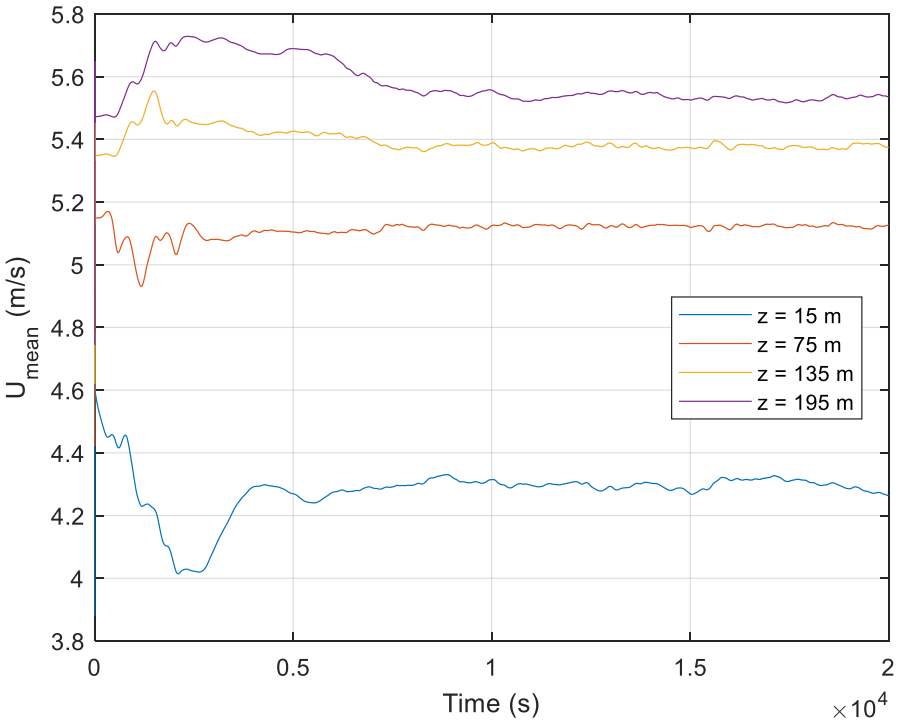

(a) CN1

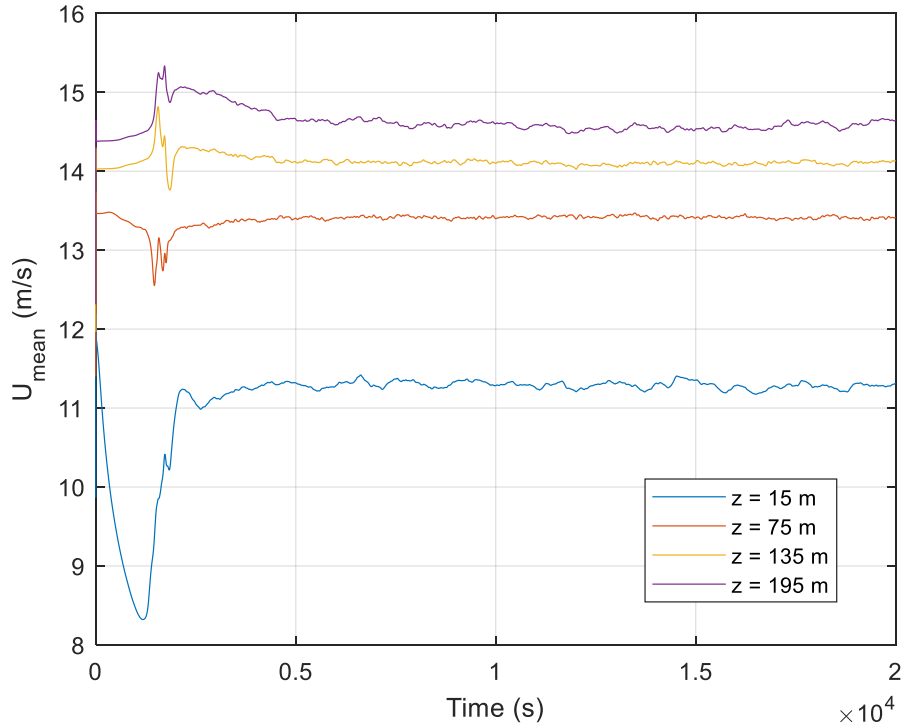

(b) CN3

Figure B.1: Mean velocity in precursor simulations of cases (a) CN1 and (b) CN3

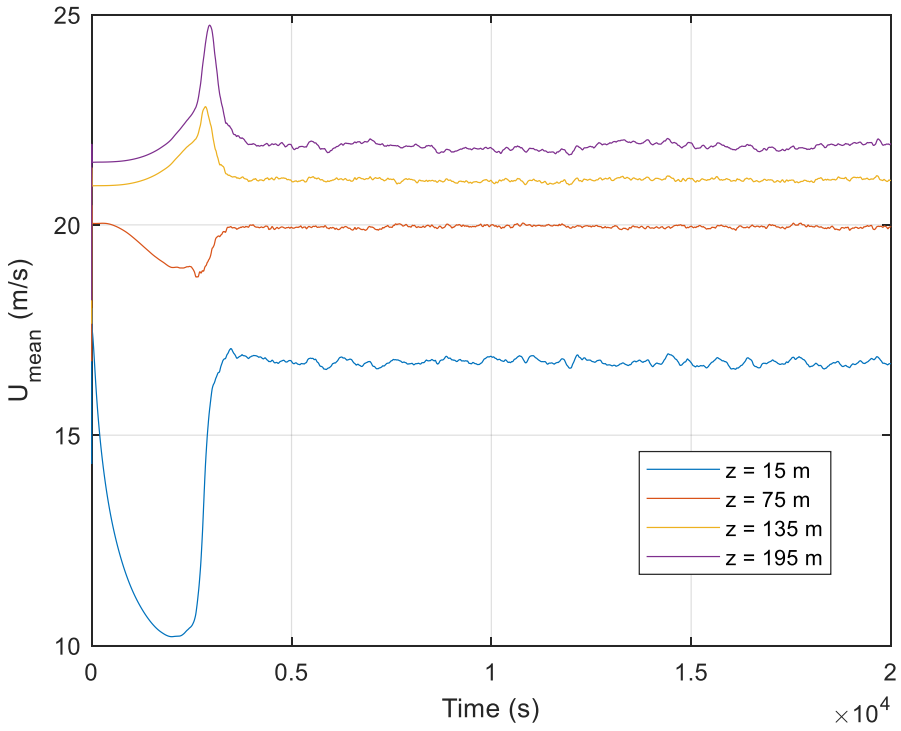

(b) CN4

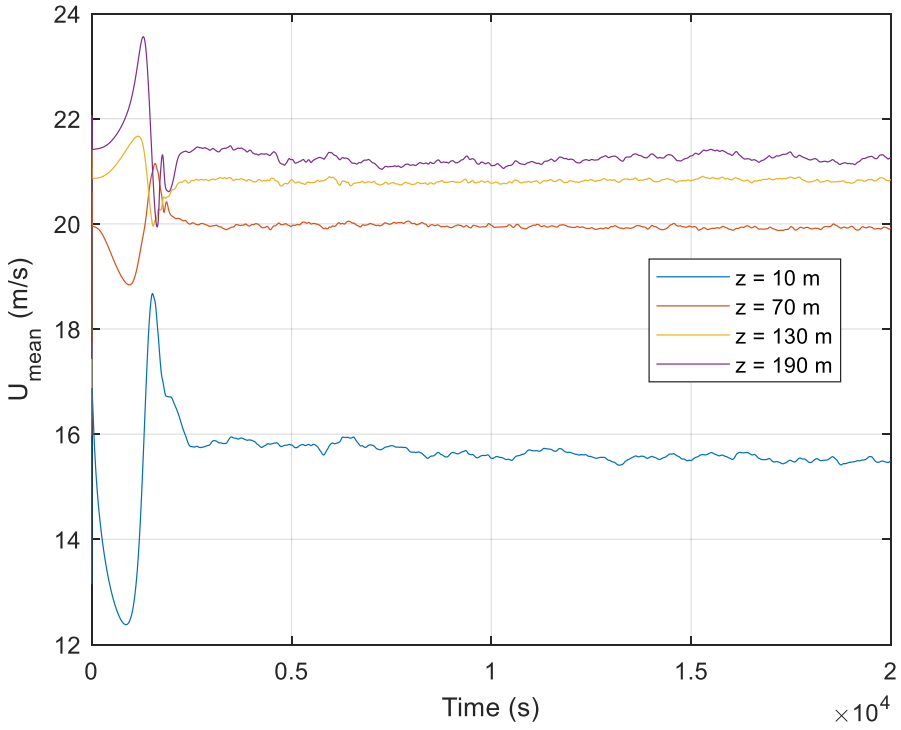

(a) CU4

Figure B.2: Mean velocity in precursor simulations of cases (a) CN4 and (b) CU4

C Standard Deviations of Wind Speed Components

C.1 Operational Wind Fields

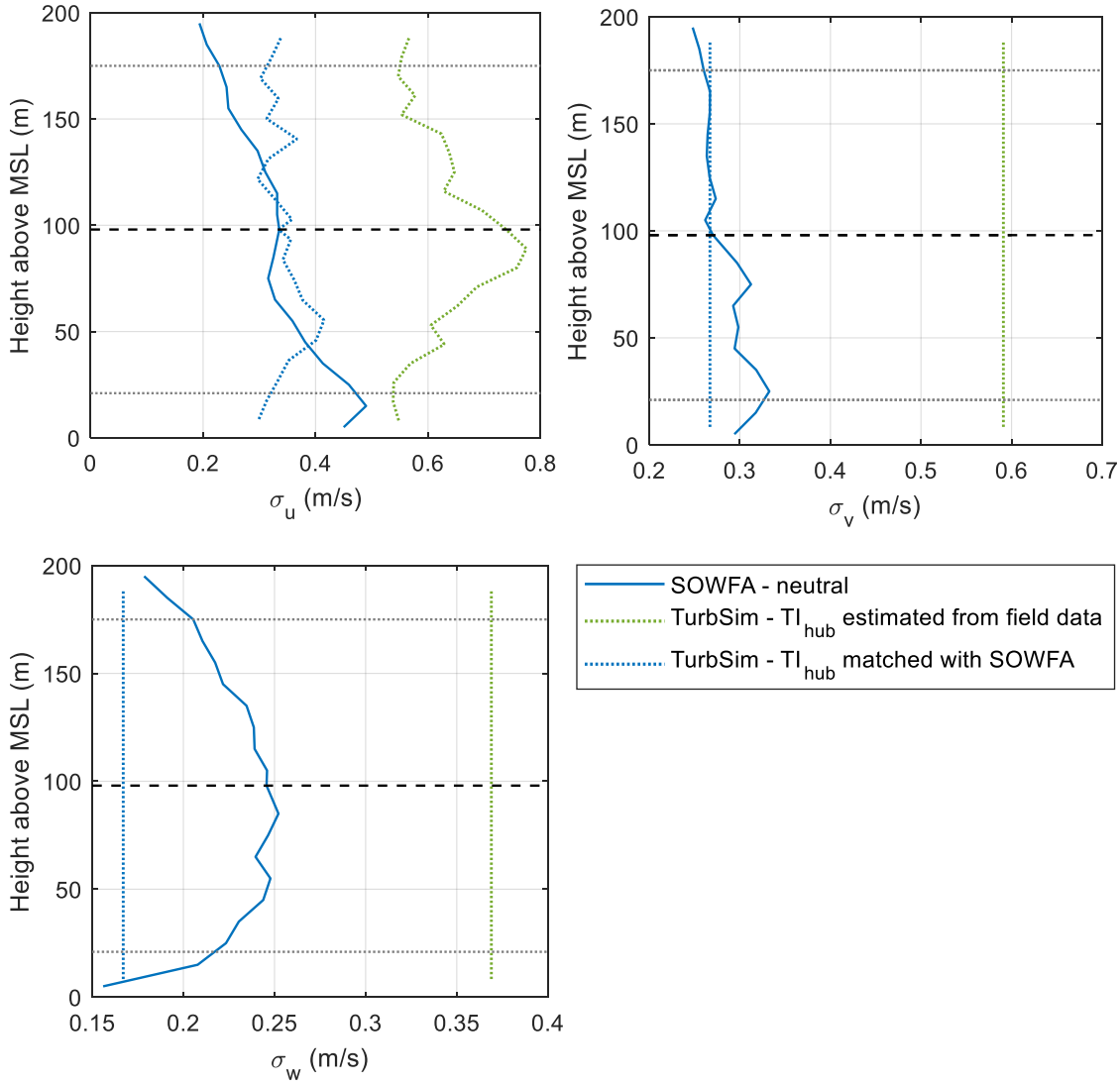

Figure C.1: Standard deviations of the u-, v- and w- components of the wind speed for case C1, U = 5.2 m/s

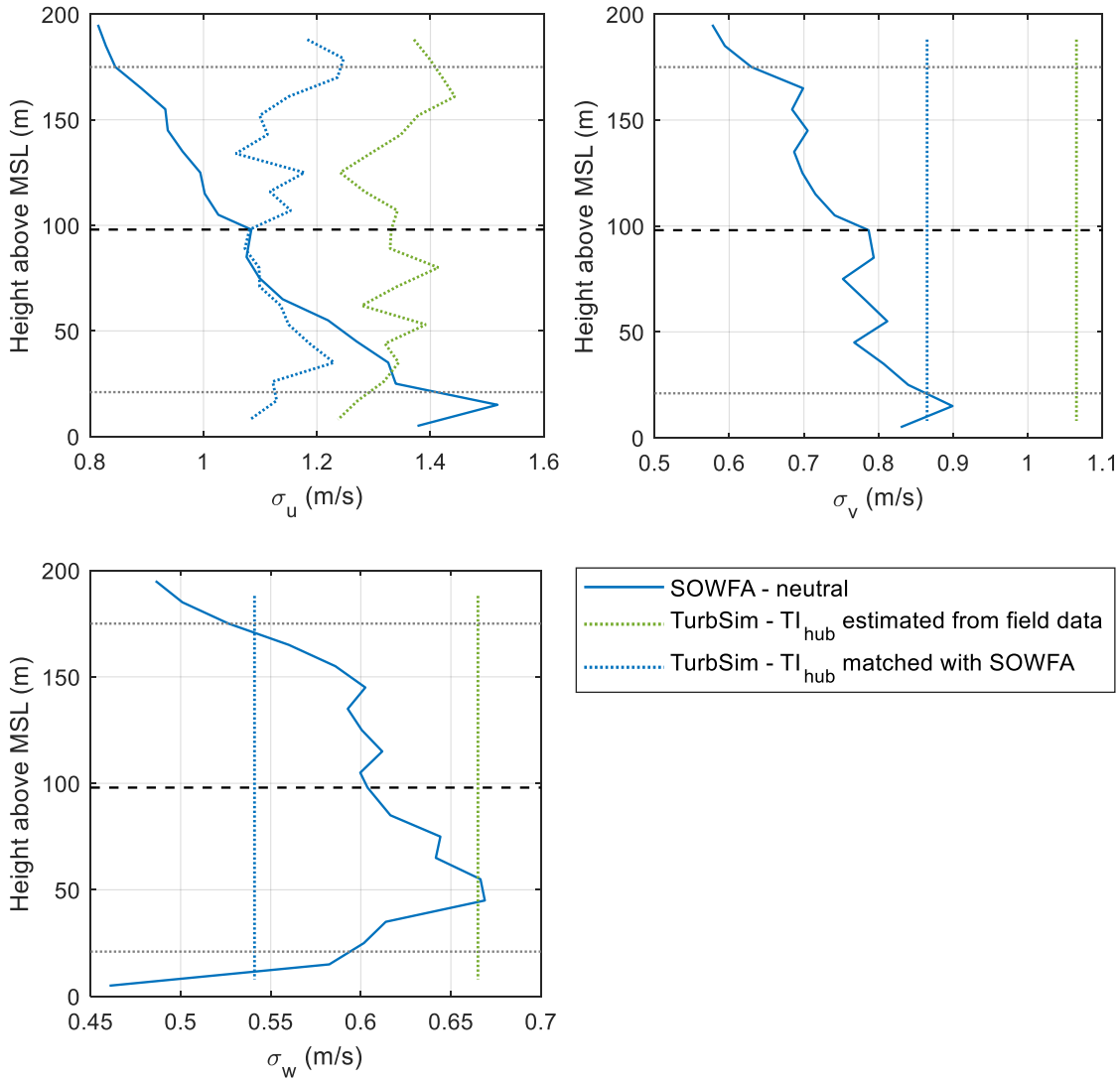

Figure C.2: Standard deviations of the u-, v- and w- components of the wind speed for case C3, U = 13.7 m/s

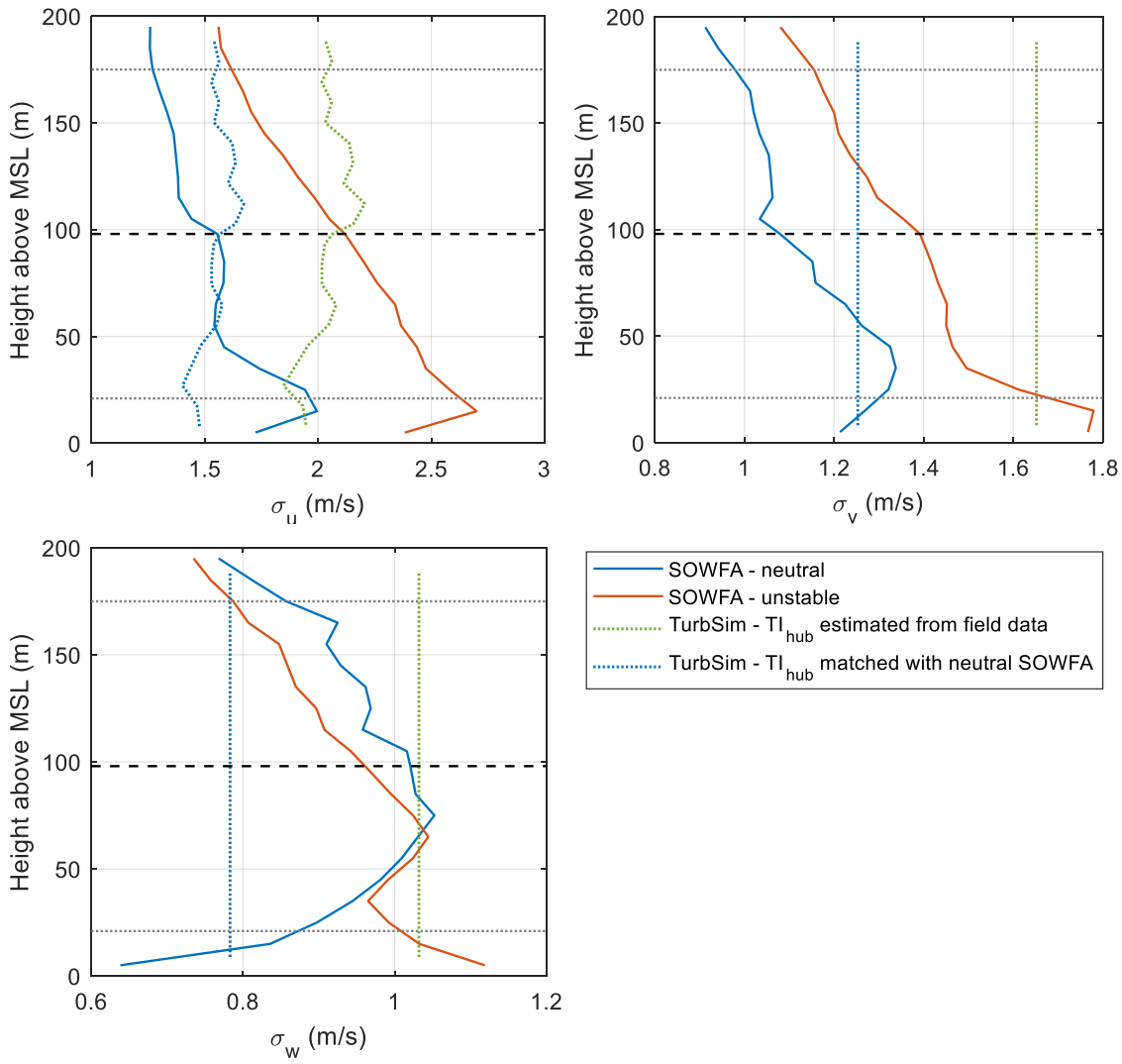

Figure C.3: Standard deviations of the u-, v- and w- components of the wind speed for case C3, U = 20.4 m/s

C.2 Typhoon Wind Fields

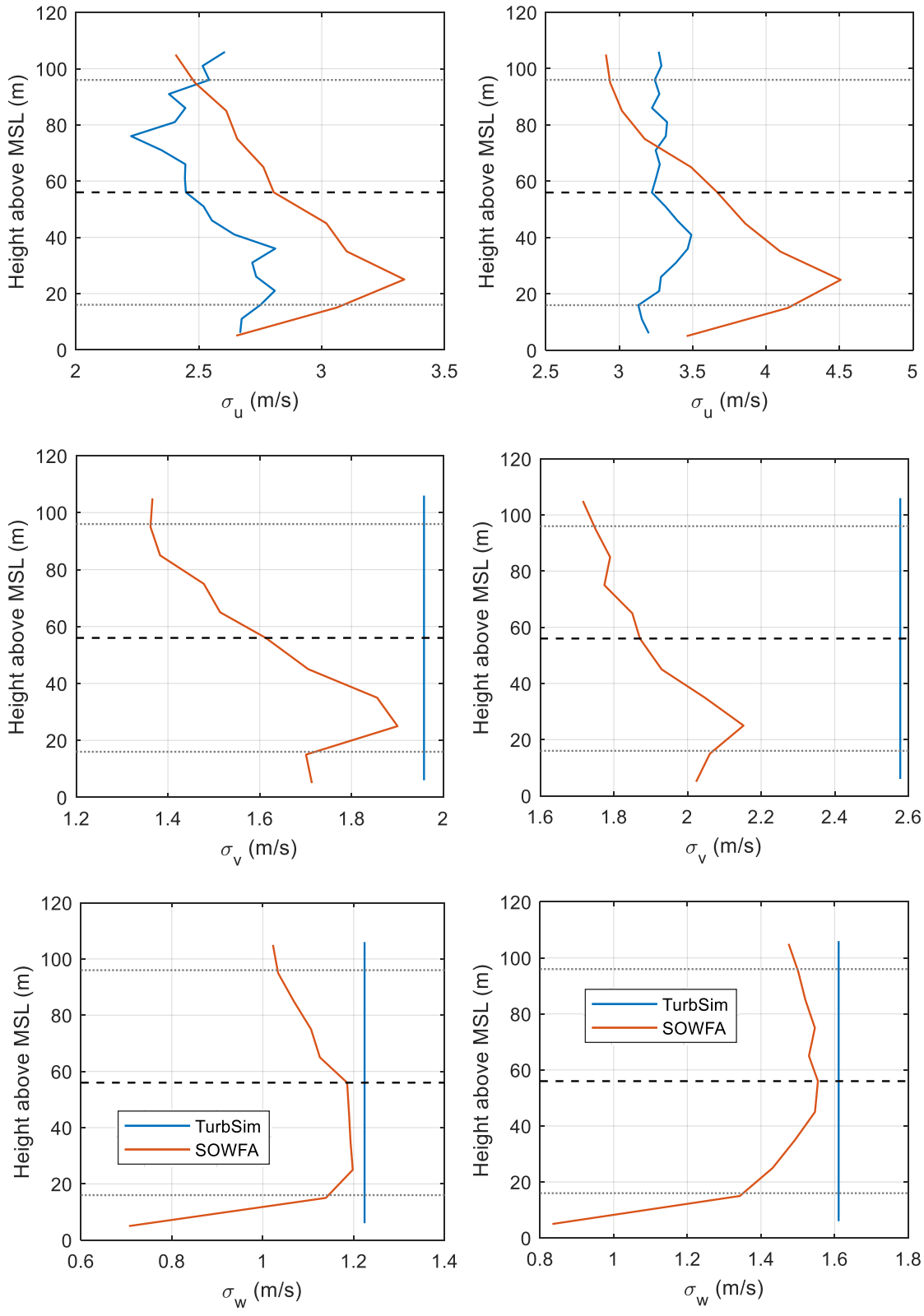

(a) 08:00 – 09:00, U_{hub} = 26.6 m/s (b) 09:00 – 10:00, U_{hub} = 31.9 m/s

Figure C.4: Standard deviations of the u-, v- and w- components of the wind speed for (a) case 2, U_{hub} = 26.6 m/s, and (b) case 3, U_{hub} = 31.9 m/s

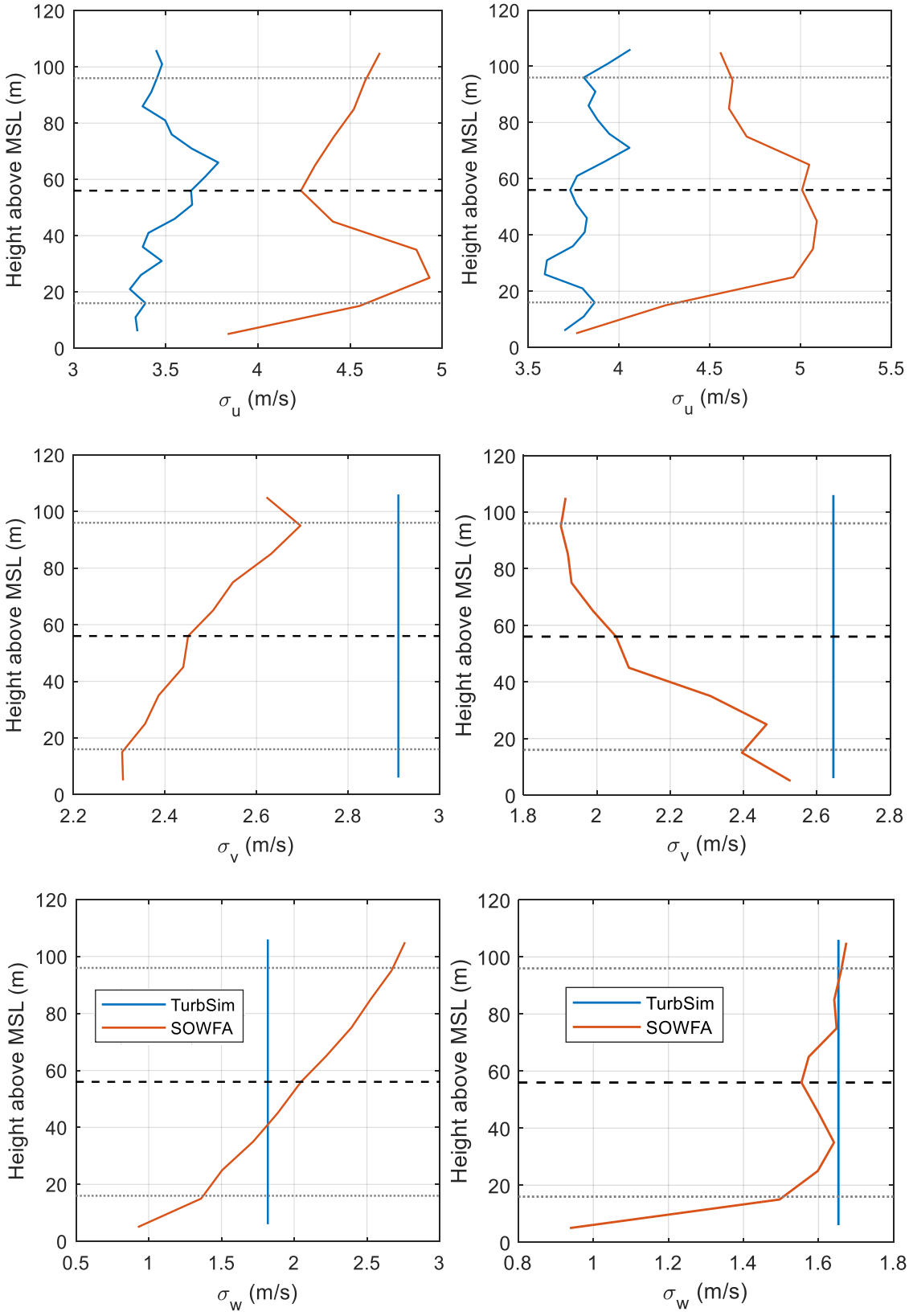

(a) 10:00 – 11:00, U_{hub} = 37.5 m/s (b) 12:13 – 10:00, U_{hub} = 38.0 m/s

Figure C.5: Standard deviations of the u-, v- and w- components of the wind speed for case 4, U_{hub} = 37.5 m/s, and case 6, U_{hub} = 38.0 m/s

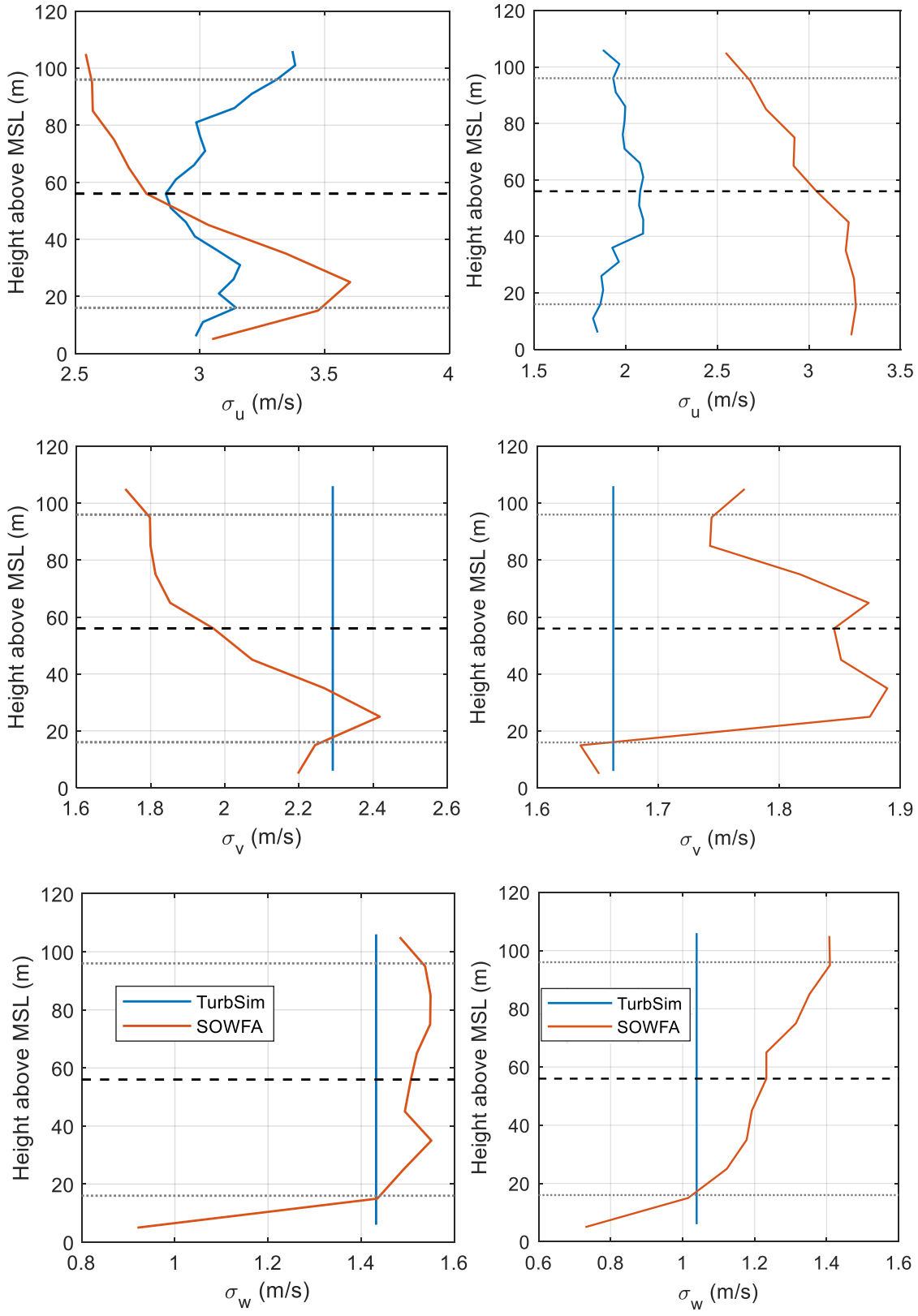

(a) 13:00 – 14:00, U_{hub} = 34.5 m/s

(b) 14:00 – 15:00, U_{hub} = 31.5 m/s

Figure C.6: Standard deviations of the u-, v- and w- components of the wind speed for case 7, U_{hub} = 34.5 m/s, and case 8, U_{hub} = 31.5 m/s

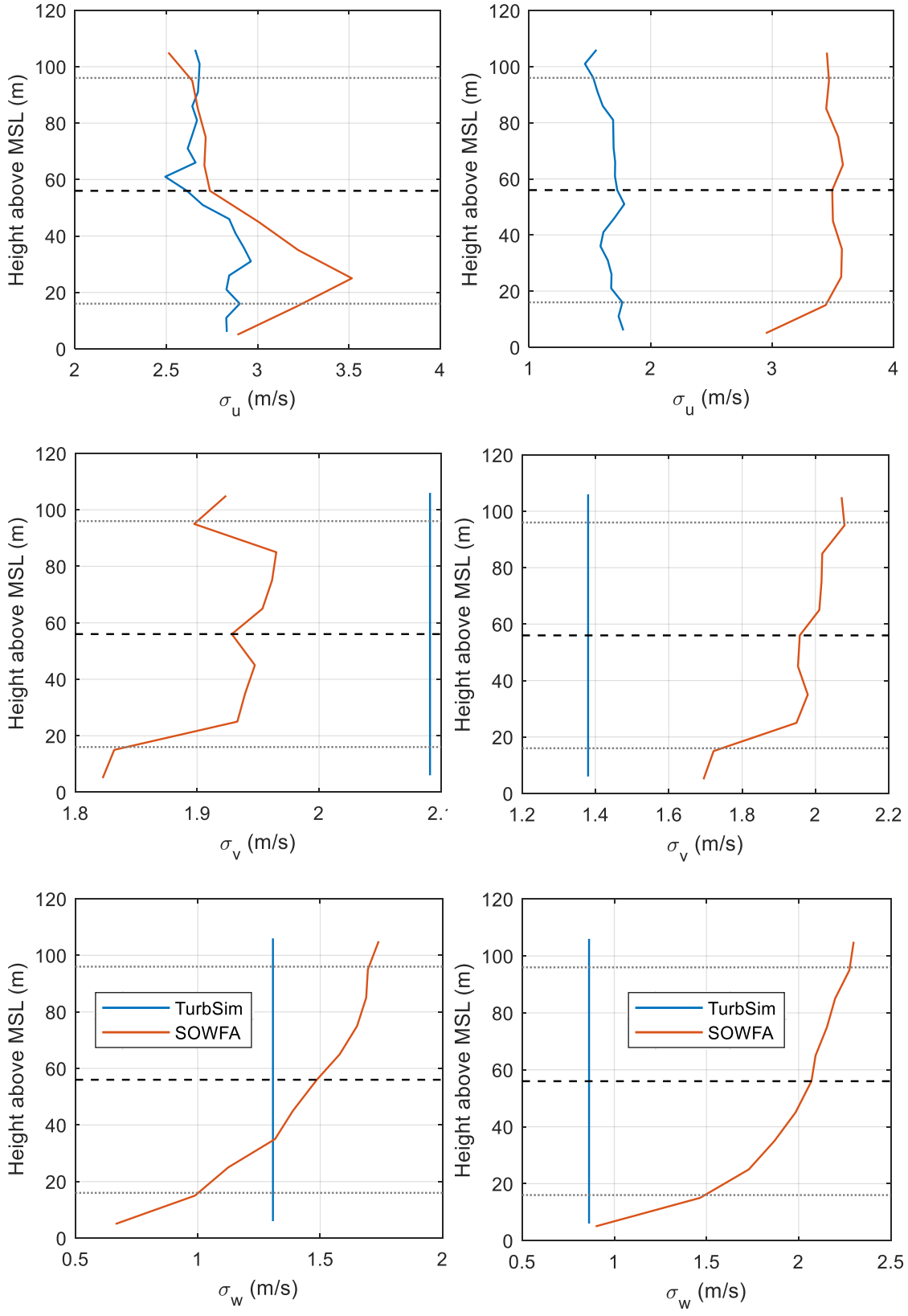

(a) 15:00 – 16:00, U_{hub} = 27.5 m/s (b) 16:00 – 17:00, U_{hub} = 22.7 m/s

Figure C.7: Standard deviations of the u-, v- and w- components of the wind speed for case 9, U_{hub} = 27.5 m/s, and case 10, U_{hub} = 22.7 m/s

D Structural Properties of Model Blade

Table D.1: Sectional structural properties along the blade. Inertia is calculated about the section centre of gravity, and offset is given with respect to the pitch axis

Normalized location along blade	Structural twist	Twist inertia	Mass density	Flap inertia	Edge inertia	Flap stiffness	Edge stiffness	Torsional stiffness	Axial stiffness	CoG offset	Shear centre offset	Tension centre offset
(-)	(deg)	(deg)	(kg/m)	(kg-m)	(kg-m)	(Nm^2)	(Nm^2)	(Nm^2)	(N)	(m)	(m)	(m)
0	14.49	15.3	945.7	3320	3298	5.69E+10	5.65E+10	4.36E+10	1.62E+10	0.002	0.002	0.002
0.02316	14.42	15.23	953.3	3401	3379	5.83E+10	5.79E+10	4.46E+10	1.63E+10	0.002	0.002	0.002
0.07319	14.26	16.53	802.1	1269	2524	2.18E+10	4.32E+10	2.03E+10	1.38E+10	-0.202	-0.202	-0.202
0.08662	14.04	16.12	784.7	955	2439	1.64E+10	4.18E+10	1.51E+10	1.35E+10	-0.195	-0.195	-0.195
0.10261	13.58	16.1	781.8	908.2	2446	1.56E+10	4.19E+10	1.45E+10	1.34E+10	-0.159	-0.159	-0.159
0.12113	12.91	15.2	786	819.3	2530	1.41E+10	4.33E+10	1.30E+10	1.35E+10	-0.149	-0.149	-0.149
0.1421	11.91	14.01	797.8	777.5	2687	1.34E+10	4.60E+10	1.23E+10	1.37E+10	-0.015	-0.015	-0.015
0.16526	10.68	12.47	806.2	710.5	2833	1.22E+10	4.85E+10	1.13E+10	1.38E+10	0.102	0.102	0.102
0.19074	9.48	10.99	792.8	551.6	2808	9.48E+09	4.81E+10	9.12E+09	1.36E+10	0.243	0.243	0.243
0.21807	8.39	9.634	778.1	405	2764	6.96E+09	4.74E+10	7.00E+09	1.33E+10	0.425	0.425	0.425
0.24725	7.61	8.824	762.3	335.8	2638	5.77E+09	4.52E+10	5.88E+09	1.31E+10	0.514	0.514	0.514
0.27817	6.96	8.244	746.7	285.5	2501	4.91E+09	4.29E+10	5.04E+09	1.28E+10	0.6	0.6	0.6
0.3106	6.37	7.78	730.2	240.4	2359	4.14E+09	4.04E+10	4.27E+09	1.25E+10	0.687	0.687	0.687
0.34418	5.81	7.161	706.6	193.2	2155	3.33E+09	3.69E+10	3.46E+09	1.21E+10	0.701	0.701	0.701
0.37892	5.25	6.502	677	149.7	1910	2.58E+09	3.27E+10	2.69E+09	1.16E+10	0.707	0.707	0.707
0.41448	4.69	5.8	644.4	114.5	1657	1.97E+09	2.84E+10	2.07E+09	1.11E+10	0.725	0.725	0.725
0.45072	4.09	5.035	613.2	89.72	1434	1.54E+09	2.46E+10	1.64E+09	1.05E+10	0.698	0.698	0.698
0.48743	3.45	4.387	580.9	75.71	1219	1.30E+09	2.09E+10	1.38E+09	9.96E+09	0.662	0.662	0.662
0.52426	2.79	3.727	548.8	63.2	1027	1.09E+09	1.76E+10	1.15E+09	9.41E+09	0.625	0.625	0.625
0.5612	2.13	3.067	516.6	52.15	856	8.98E+08	1.47E+10	9.51E+08	8.86E+09	0.589	0.589	0.589
0.5978	1.48	2.417	484.8	42.54	706.5	7.32E+08	1.21E+10	7.76E+08	8.31E+09	0.552	0.552	0.552
0.63405	0.87	1.807	453.2	34.28	576.8	5.90E+08	9.89E+09	6.25E+08	7.77E+09	0.516	0.516	0.516
0.6696	0.29	1.228	422.2	27.27	465.6	4.69E+08	7.98E+09	4.96E+08	7.24E+09	0.481	0.481	0.481
0.70434	-0.22	0.718	391.9	21.43	372.1	3.69E+08	6.38E+09	3.90E+08	6.72E+09	0.447	0.447	0.447
0.73793	-0.7	0.238	362.7	16.64	294.3	2.87E+08	5.05E+09	3.02E+08	6.22E+09	0.413	0.413	0.413
0.77024	-1.12	-0.18	334.6	12.77	230.7	2.20E+08	3.95E+09	2.32E+08	5.74E+09	0.381	0.381	0.381
0.80104	-1.52	-0.58	307.7	9.689	179.2	1.67E+08	3.07E+09	1.76E+08	5.28E+09	0.351	0.351	0.351
0.83023	-1.88	-0.94	282.4	7.275	138.1	1.25E+08	2.37E+09	1.32E+08	4.84E+09	0.322	0.322	0.322
0.85756	-2.21	-1.27	258.5	5.41	105.8	9.32E+07	1.81E+09	9.78E+07	4.43E+09	0.295	0.295	0.295
0.8828	-2.52	-1.58	236.4	4	80.7	6.89E+07	1.38E+09	7.21E+07	4.05E+09	0.269	0.269	0.269
0.90596	-2.8	-1.86	216.2	2.949	61.56	5.08E+07	1.06E+09	5.29E+07	3.71E+09	0.246	0.246	0.246
0.92693	-3.03	-2.09	198	2.18	47.16	3.76E+07	8.08E+08	3.90E+07	3.40E+09	0.226	0.226	0.226
0.94545	-3.22	-2.27	182	1.626	36.47	2.80E+07	6.25E+08	2.90E+07	3.12E+09	0.207	0.207	0.207
0.96132	-3.37	-2.42	168	1.231	28.63	2.12E+07	4.91E+08	2.18E+07	2.88E+09	0.191	0.191	0.191
0.97464	-3.43	-2.48	156.5	0.9587	23.04	1.65E+07	3.95E+08	1.69E+07	2.68E+09	0.178	0.178	0.178
1	-3.43	-2.47	134.4	0.5609	14.51	9.68E+06	2.49E+08	9.63E+06	2.31E+09	0.153	0.153	0.153

E Publications

Smith, R.E., Pillai, A.C., Tabor, G., Thies, P.R., Johanning, L., 2019, “Impact of Rotor Misalignment Due to Platform Motions on Floating Offshore Wind Turbine Blade Loads,” *Proceedings of the ASME 2019 38th International Conference on Ocean, Offshore and Arctic Engineering*, Glasgow, U.K.

References

[1] "Offshore Wind - Great.Gov.Uk International" [Online]. Available: https://www.great.gov.uk/international/content/investment/sectors/offshore-wind/. [Accessed: 02-Mar-2022].

[2] Eatough, L., 2021, *Floating Offshore Wind Technology and Operations Review*, 7523, ORE Catapult.

[3] Lamei, A., and Hayatdavoodi, M., 2020, "On Motion Analysis and Elastic Response of Floating Offshore Wind Turbines," J. Ocean Eng. Mar. Energy, **6**(1), pp. 71–90.

[4] Soares-Ramos, E. P. P., de Oliveira-Assis, L., Sarrias-Mena, R., and Fernández-Ramírez, L. M., 2020, "Current Status and Future Trends of Offshore Wind Power in Europe," Energy, **202**, p. 117787.

[5] Katsouris, G., and Marina, A., 2016, *Cost Modelling of Floating Wind Farms*, ECN-E--15-078, ECN.

[6] Butterfield, S., Musial, W., and Jonkman, J., 2005, "Engineering Challenges for Floating Offshore Wind Turbines," *Proceedings of the 2005 Copenhagen Offshore Wind Conference*, Copenhagen, Denmark.

[7] McMorland, J., Collu, M., McMillan, D., and Carroll, J., 2022, "Operation and Maintenance for Floating Wind Turbines: A Review," Renew. Sustain. Energy Rev., **163**, p. 112499.

[8] The Carbon Trust, 2021, *Floating Wind Joint Industry Project – Phase III Summary Report*.

[9] Matha, D., Schlipf, M., Cordle, A., Pereira, R., and Jonkman, J., 2011, "Challenges in Simulation of Aerodynamics, Hydrodynamics, and Mooring-Line Dynamics of Floating Offshore Wind Turbines," *Proceedings of the 21st Offshore and Polar Engineering Conference*, Maui, Hawaii.

[10] Henderson, A., Collu, M., and Masciola, M., 2016, "Overview of Floating Offshore Wind Technologies," *Floating Offshore Wind Energy: The Next Generation of Wind Energy*, J. Cruz, and M. Atcheson, eds., Springer International Publishing, Cham, pp. 87–132.

[11] Matha, D., Cruz, J., Masciola, M., Bachynski, E. E., Atcheson, M., Goupee, A. J., Gueydon, S. M. H., and Robertson, A. N., 2016, "Modelling of Floating Offshore Wind Technologies," *Floating Offshore Wind Energy: The Next Generation of Wind Energy*, J. Cruz, and M. Atcheson, eds., Springer International Publishing, Cham, pp. 133–240.

[12] Ashuri, T., Zaaijer, M. B., Martins, J. R. R. A., van Bussel, G. J. W., and van Kuik, G. A. M., 2014, "Multidisciplinary Design Optimization of Offshore Wind Turbines for Minimum Levelized Cost of Energy," Renew. Energy, **68**, pp. 893–905.

[13] Chehouri, A., Younes, R., Ilinca, A., and Perron, J., 2015, "Review of Performance Optimization Techniques Applied to Wind Turbines," Appl. Energy, **142**, pp. 361–388.

[14] "South West – Offshore Floating Wind – Design and Installation – REGISTRATIONS NOW CLOSED | SUT | Society for Underwater Technology"

[Online]. Available: https://sut.org/event/south-west-offshore-floating-wind-design-and-installation/. [Accessed: 08-May-2022].

[15] Leimeister, M., Kolios, A., and Collu, M., 2018, "Critical Review of Floating Support Structures for Offshore Wind Farm Deployment," J. Phys. Conf. Ser., **1104**.

[16] Thiagarajan, K. P., and Dagher, H. J., 2014, "A Review of Floating Platform Concepts for Offshore Wind Energy Generation," J. Offshore Mech. Arct. Eng., **136**.

[17] Kolios, A. j., Rodriguez-Tsouroukdissian, A., and Salonitis, K., 2016, "Multi-Criteria Decision Analysis of Offshore Wind Turbines Support Structures under Stochastic Inputs," Ships Offshore Struct., **11**(1), pp. 38–49.

[18] Nilsson, D., and Westin, A., 2014, "Floating Wind Power in Norway: Analysis of Future Opportunities and Challenges," Lund University.

[19] Bachynski, E. E., 2014, "Design and Dynamic Analysis of Tension Leg Platform Wind Turbines," PhD, Norwegian University of Science and Technology.

[20] Taboada, J., 2015, "Comparative Analysis Review on Floating Offshore Wind Foundations (FOWF).," *Trabajo Presentado En El 54º Congreso de Ingeniería Naval e Industrial Marítima En Ferrol*, Ferrol, Spain.

[21] Larsen, T. J., and Hanson, T. D., 2007, "A Method to Avoid Negative Damped Low Frequent Tower Vibrations for a Floating, Pitch Controlled Wind Turbine," J. Phys. Conf. Ser., **75**(1), p. 012073.

[22] Skaare, B., Hanson, T. D., Nielsen, F., Yttervik, R., Hansen, A., Thomsen, K., and Larsen, T. J., 2007, "Integrated Dynamic Analysis of Floating Offshore Wind Turbines," *Proceedings of the 2007 European Wind Energy Conference and Exhibition*, Milan, Italy.

[23] Jonkman, J. M., 2009, "Dynamics of Offshore Floating Wind Turbines—Model Development and Verification," Wind Energy, **12**(5), pp. 459–492.

[24] Davidson, J., and Ringwood, J. V., 2017, "Mathematical Modelling of Mooring Systems for Wave Energy Converters—A Review," Energies, **10**(5).

[25] Sebastian, T., 2012, "The Aerodynamics and Near Wake of an Offshore Floating Horizontal Axis Wind Turbine," PhD, University of Massachusetts - Amherst.

[26] Sebastian, T., and Lackner, M., 2012, "Analysis of the Induction and Wake Evolution of an Offshore Floating Wind Turbine," Energies, **5**(4), pp. 968–1000.

[27] Micallef, D., and Sant, T., 2016, "A Review of Wind Turbine Yaw Aerodynamics," *Wind Turbines - Design, Control and Applications*, Intech.

[28] Díaz, H., and Guedes Soares, C., 2020, "Review of the Current Status, Technology and Future Trends of Offshore Wind Farms," Ocean Eng., **209**, p. 107381.

[29] Bilgili, M., and Alphan, H., 2022, "Global Growth in Offshore Wind Turbine Technology," Clean Technol. Environ. Policy.

[30] Wang, L., Liu, X., and Kolios, A., 2016, "State of the Art in the Aeroelasticity of Wind Turbine Blades: Aeroelastic Modelling," Renew. Sustain. Energy Rev., **64**, pp. 195–210.

[31] Garratt, J. R., 1994, "Review: The Atmospheric Boundary Layer," Earth-Sci. Rev., **37**, pp. 89–134.

[32] Sathe, A., Mann, J., Barlas, T., Bierbooms, W. a. a. m., and van Bussel, G. j. w., 2013, "Influence of Atmospheric Stability on Wind Turbine Loads," Wind Energy, **16**(7), pp. 1013–1032.

[33] Cheynet, E., Jakobsen, J. B., and Reuder, J., 2018, "Velocity Spectra and Coherence Estimates in the Marine Atmospheric Boundary Layer," Bound.-Layer Meteorol., **169**(3), pp. 429–460.

[34] Micallef, D., and Rezaeiha, A., 2021, "Floating Offshore Wind Turbine Aerodynamics: Trends and Future Challenges," Renew. Sustain. Energy Rev., **152**, p. 111696.

[35] 2005, *Wind Turbines – Part 1: Design Requirements*, IEC 61400-1, International Electrotechnical Commission.

[36] Kaimal, J. C., Wyngaard, J. C., Izumi, Y., and Coté, O. R., 1972, "Spectral Characteristics of Surface-Layer Turbulence," Q. J. R. Meteorol. Soc., **98**(417), pp. 563–589.

[37] Mann, J., 1994, "The Spatial Structure of Neutral Atmospheric Surface-Layer Turbulence," J. Fluid Mech., **273**, pp. 141–168.

[38] Putri, R. M., Obhrai, C., Jakobsen, J. B., and Ong, M. C., 2020, "Numerical Analysis of the Effect of Offshore Turbulent Wind Inflow on the Response of a Spar Wind Turbine," Energies, **13**(10), p. 2506.

[39] Doubrawa, P., Churchfield, M. J., Godvik, M., and Sirnivas, S., 2019, "Load Response of a Floating Wind Turbine to Turbulent Atmospheric Flow," Appl. Energy, **242**, pp. 1588–1599.

[40] Ke, S., Yu, W., Cao, J., and Wang, T., 2018, "Aerodynamic Force and Comprehensive Mechanical Performance of a Large Wind Turbine during a Typhoon Based on WRF/CFD Nesting," Appl. Sci., **8**(10).

[41] Xu, Y., He, H., Song, J., Hou, Y., and Li, F., 2017, "Observations and Modeling of Typhoon Waves in the South China Sea," J. Phys. Oceanogr., **47**(6), pp. 1307–1324.

[42] Haghroosta, T., and Ismail, W. R., 2017, "Typhoon Activity and Some Important Parameters in the South China Sea," Weather Clim. Extrem., **17**, pp. 29–35.

[43] 2009, "Wind Turbines - Part 3: Design Requirements for Offshore Wind Turbines."

[44] Nematbakhsh, A., Olinger, D. J., and Tryggvason, G., 2014, "Nonlinear Simulation of a Spar Buoy Floating Wind Turbine under Extreme Ocean Conditions," J. Renew. Sustain. Energy, **6**(3), p. 033121.

[45] Ma, Z., Li, W., Ren, N., and Ou, J., 2017, "The Typhoon Effect on the Aerodynamic Performance of a Floating Offshore Wind Turbine," J. Ocean Eng. Sci., **2**(4), pp. 279–287.

[46] Li, J., Bian, J., Ma, Y., and Jiang, Y., 2021, "Impact of Typhoons on Floating Offshore Wind Turbines: A Case Study of Typhoon Mangkhut," J. Mar. Sci. Eng., **9**(5), p. 543.

[47] Tanaka, K., Sato, I., Utsunomiya, T., and Kakuya, H., 2020, "Validation of Dynamic Response of a 2-MW Hybrid-Spar Floating Wind Turbine during Typhoon Using Full-Scale Field Data," Ocean Eng., **218**, p. 108262.

[48] Hansen, M. O. L., and Madsen, H. A., 2011, "Review Paper on Wind Turbine Aerodynamics," J. Fluids Eng., **133**(11), pp. 114001-114001–12.

[49] Moriarty, P. J., and Hansen, A. C., 2005, *AeroDyn Theory Manual*, NREL/TP-500-36881, National Renewable Energy Lab. (NREL), Golden, CO (United States).

[50] Burton, T., Jenkins, N., Sharpe, D., and Bossanyi, E., 2011, *Wind Energy Handbook*, John Wiley & Sons, Ltd.

[51] Snel, H., 2003, "Review of Aerodynamics for Wind Turbines," Wind Energy, **6**(3), pp. 203–211.

[52] Pitt, D. M., and Peters, D. A., 1981, "Theoretical Prediction of Dynamic-Inflow Derivatives," Vertica, **5**(1), pp. 21–34.

[53] Shen, W. Z., Sørensen, J. N., and Mikkelsen, R., 2005, "Tip Loss Correction for Actuator/Navier–Stokes Computations," J. Sol. Energy Eng., **127**(2), pp. 209–213.

[54] Leishman, J. G., and Beddoes, T. S., 1989, "A Semi-Empirical Model for Dynamic Stall," J. Am. Helicopter Soc., **34**(3), pp. 3–17.

[55] Tran, T.-T., and Kim, D.-H., 2015, "The Platform Pitching Motion of floating Offshore Wind Turbine: A Preliminary Unsteady Aerodynamic Analysis," J. Wind Eng. Ind. Aerodyn., **142**, pp. 65–81.

[56] Shaler, K., Branlard, E., Platt, A., and Jonkman, J., 2020, "Preliminary Introduction of a Free Vortex Wake Method Into OpenFAST," J. Phys. Conf. Ser., **1452**(1), p. 012064.

[57] Hansen, M. O. L., Sørensen, J. N., Voutsinas, S., Sørensen, N., and Madsen, H. A., 2006, "State of the Art in Wind Turbine Aerodynamics and Aeroelasticity," Prog. Aerosp. Sci., **42**(4), pp. 285–330.

[58] Phillips, W. F., and Snyder, D. O., 2000, "Modern Adaptation of Prandtl's Classic Lifting-Line Theory," J. Aircr., **37**(4), pp. 662–670.

[59] Katz, J., and Plotkin, A., 2001, *Low-Speed Aerodynamics*, Cambridge University Press.

[60] Sebastian, T., and Lackner, M. A., 2012, "Development of a Free Vortex Wake Method Code for Offshore Floating Wind Turbines," Renew. Energy, **46**, pp. 269–275.

[61] Currin, H. D., Coton, F. N., and Wood, B., 2008, "Dynamic Prescribed Vortex Wake Model for AERODYN/FAST," J. Sol. Energy Eng., **130**(031007).

[62] Sant, T., 2007, "Improving BEM-Based Aerodynamic Models in Wind Turbine Design Codes."

[63] Corniglion, R., Harris, J., Peyrard, C., and Capaldo, M., 2020, "Comparison of the Free Vortex Wake and Actuator Line Methods to Study the Loads of a Wind Turbine in Imposed Surge Motion," J. Phys. Conf. Ser., **1618**.

[64] Kim, H., Lee, S., and Lee, S., 2010, "Numerical Analysis on the Aerodynamics of HAWTs Using Nonlinear Vortex Strength Correction," Curr. Appl. Phys., **10**(2, Supplement), pp. S311–S315.

[65] Gaertner, E., 2014, "Modeling Dynamic Stall for a Free Vortex Wake Model of a Floating Offshore Wind Turbine," Master of Science, University of Massachusetts - Amherst.

[66] Versteeg, H. K., and Malalasekera, W., 2007, *An Introduction to Computational Fluid Dynamics - The Finite Volume Method*, Pearson Education Limited.

[67] Martinez-Tossas, L. A., and Leonardi, S., 2013, *Wind Turbine Modeling for Computational Fluid Dynamics*, NREL.

[68] Wu, Y.-T., and Porté-Agel, F., 2011, "Large-Eddy Simulation of Wind-Turbine Wakes: Evaluation of Turbine Parametrisations," Bound.-Layer Meteorol., **138**(3), pp. 345–366.

[69] Sørensen, J. N., and Shen, W. Z., 2002, "Numerical Modelling of Wind Turbine Wakes," J. Fluids Eng., **124**, pp. 393–399.

[70] Stevens, R. J. A. M., Martínez-Tossas, L. A., and Meneveau, C., 2018, "Comparison of Wind Farm Large Eddy Simulations Using Actuator Disk and Actuator Line Models with Wind Tunnel Experiments," Renew. Energy, **116**, pp. 470–478.

[71] Sanderse, B., van der Pijl, S. p., and Koren, B., 2011, "Review of Computational Fluid Dynamics for Wind Turbine Wake Aerodynamics," Wind Energy, **14**(7), pp. 799–819.

[72] Shen, W. Z., Zhang, J. H., and Sørensen, J. N., 2009, "The Actuator Surface Model: A New Navier–Stokes Based Model for Rotor Computations," J. Sol. Energy Eng., **131**(1).

[73] Storey, R. C., Norris, S. E., and Cater, J. E., 2015, "An Actuator Sector Method for Efficient Transient Wind Turbine Simulation," Wind Energy, **18**(4), pp. 699–711.

[74] Sarmast, S., Shen, W. Z., Zhu, W. J., Mikkelsen, R. F., and Breton, S. P., 2016, "Validation of the Actuator Line and Disc Techniques Using the New MEXICO Measurements," J. Phys. Conf. Ser., **753**.

[75] Shen, W. Z., Zhu, W. J., and Yang, H., 2015, "Validation of the Actuator Line Model for Simulating Flows Past Yawed Wind Turbine Rotors," J. Power Energy Eng., **3**, pp. 7–13.

[76] Arabgolarcheh, A., Jannesarahmadi, S., and Benini, E., 2022, "Modeling of near Wake Characteristics in Floating Offshore Wind Turbines Using an Actuator Line Method," Renew. Energy, **185**, pp. 871–887.

[77] Micallef, D., and Sant, T., 2015, "Loading Effects on Floating Offshore Horizontal Axis Wind Turbines in Surge Motion," Renew. Energy, **83**, pp. 737–748.

[78] Li, Y., Paik, K.-J., Xing, T., and Carrica, P. M., 2012, "Dynamic Overset CFD Simulations of Wind Turbine Aerodynamics," Renew. Energy, **37**(1), pp. 285–298.

[79] Johansen, J., Sørensen, N. N., Michelsen, J. A., and Schreck, S., 2002, "Detached-Eddy Simulation of Flow around the NREL Phase VI Blade," Wind Energy, **5**(2–3), pp. 185–197.

[80] Sedaghatizadeh, N., Arjomandi, M., Kelso, R., Cazzolato, B., and Ghayesh, M. H., 2018, "Modelling of Wind Turbine Wake Using Large Eddy Simulation," Renew. Energy, **115**, pp. 1166–1176.

[81] Make, M., Vaz, G., Fernandes, G., Burmester, S., and Gueydon, S., 2015, "Analysis of Aerodynamic Performance of Floating Wind Turbines Using CFD and BEMT Methods," *OMAE2015*, St John's, Newfoundland, Canada.

[82] Reissner, E., 1973, "On One-Dimensional Large-Displacement Finite-Strain Beam Theory," Stud. Appl. Math., **52**(2), pp. 87–95.

[83] Guntur, S., Jonkman, J., Sievers, R., Sprague, M. A., Schreck, S., and Wang, Q., 2017, "A Validation and Code-to-Code Verification of FAST for a Megawatt-

Scale Wind Turbine with Aeroelastically Tailored Blades," Wind Energy Sci., **2**(2), pp. 443–468.

[84] Jonkman, J., 2013, "Overview of the ElastoDyn Structural-Dynamics Module."

[85] Mo, W., Li, D., Wang, X., and Zhong, C., 2015, "Aeroelastic Coupling Analysis of the Flexible Blade of a Wind Turbine," Energy, **89**, pp. 1001–1009.

[86] Wang, L., Quant, R., and Kolios, A., 2016, "Fluid Structure Interaction Modelling of Horizontal-Axis Wind Turbine Blades Based on CFD and FEA," J. Wind Eng. Ind. Aerodyn., **158**, pp. 11–25.

[87] Payne, G. S., Stallard, T., and Martinez, R., 2017, "Design and Manufacture of a Bed Supported Tidal Turbine Model for Blade and Shaft Load Measurement in Turbulent Flow and Waves," Renew. Energy, **107**, pp. 312–326.

[88] Faccio Júnior, C. J., Cardozo, A. C. P., Monteiro Júnior, V., and Gay Neto, A., 2019, "Modeling Wind Turbine Blades by Geometrically-Exact Beam and Shell Elements: A Comparative Approach," Eng. Struct., **180**, pp. 357–378.

[89] Tran, T. T., and Kim, D.-H., 2016, "A CFD Study into the Influence of Unsteady Aerodynamic Interference on Wind Turbine Surge Motion," Renew. Energy, **90**, pp. 204–228.

[90] Tran, T. T., and Kim, D. H., 2015, "The Aerodynamic Interference Effects of a Floating Offshore Wind Turbine Experiencing Platform Pitching and Yawing Motions," J. Mech. Sci. Technol., **29**(2), pp. 549–561.

[91] LIU, Y., XIAO, Q., INCECIK, A., and WAN, D., 2016, "Investigation of the Effects of Platform Motion on the Aerodynamics of a Floating Offshore Wind Turbine," J. Hydrodyn. Ser B, **28**(1), pp. 95–101.

[92] Li, P., Cheng, P., Wan, D., and Xiao, Q., 2015, "Numerical Simulations of Wake Flows of Floating Offshore Wind Turbines by Unsteady Actuator Line Model," *9th International Workshop on Ship and Marine Hydrodynamics*, Glasgow, U.K.

[93] Liu, Y., Xiao, Q., Incecik, A., Peyrard, C., and Wan, D., 2017, "Establishing a Fully Coupled CFD Analysis Tool for Floating Offshore Wind Turbines," Renew. Energy, **112**, pp. 280–301.

[94] "HydroDyn User Guide and Theory Manual — OpenFAST v3.0.0 Documentation" [Online]. Available: https://openfast.readthedocs.io/en/latest/source/user/hydrodyn/index.html. [Accessed: 15-Nov-2021].

[95] Cordle, A., and Jonkman, J., 2011, "State of the Art In Floating Wind Turbine Design Tools," *Proceedings of the 21st Offshore and Polar Engineering Conference*.

[96] Kreuzer, E., and Wilke, U., 2003, "Dynamics of Mooring Systems in Ocean Engineering," Arch. Appl. Mech., **73**(3), pp. 270–281.

[97] Anderson, M. T., Wendt, F. F., Robertson, A. N., Jonkman, J. M., and Hall, M., 2016, "Verification and Validation of Multisegmented Mooring Capabilities in FAST V8," *Presented at the Twenty-Sixth (2016) International Ocean and Polar Engineering Conference*, Rhodes, Greece.

[98] "OpenFAST Documentation — OpenFAST v2.3.0 Documentation" [Online]. Available: https://raf-openfast.readthedocs.io/en/docs-hydrodyn_manual/index.html. [Accessed: 12-Jan-2021].

[99] 2015, "MAP++ — MAP++ 1.15 Documentation" [Online]. Available: https://map-plus-plus.readthedocs.io/en/latest/index.html. [Accessed: 15-Nov-2021].

[100] "MoorDyn - Lumped-Mass Mooring Dynamics — MoorDyn 1.01.01 Documentation" [Online]. Available: https://moordyn.readthedocs.io/en/latest/. [Accessed: 15-Nov-2021].

[101] Quiggin, P. P., 2015, *OrcaFlex QA, Testing and Validation Document 99/005:7*, Orcina Ltd, Cumbria, United Kingdom.

[102] Hall, M., and Goupee, A., 2015, "Validation of a Lumped-Mass Mooring Line Model with DeepCwind Semisubmersible Model Test Data," Ocean Eng., **104**, pp. 590–603.

[103] Hall, M., Sirnivas, S., and Yu, Y.-H., 2021, "Implementation and Verification of Cable Bending Stiffness in MoorDyn," *ASME 2021 3rd International Offshore Wind Technical Conference*, American Society of Mechanical Engineers, Virtual, Online, p. V001T01A011.

[104] Shourangiz-Haghighi, A., Amin, H., Mohamid, Wang, L., Mussetta, M., Kolios, A., and Lander, M., 2019, "State of the Art in the Optimisation of Wind Turbine Performance Using CFD," Arch. Comput. Methods Eng., **27**, pp. 413–431.

[105] "OpenFAST" [Online]. Available: https://github.com/OpenFAST. [Accessed: 07-Aug-2020].

[106] Wang, Q., Sprague, M. A., Jonkman, J., Johnson, N., and Jonkman, B., 2017, "BeamDyn: A High-fidelity Wind Turbine Blade Solver in the FAST Modular Framework," Wind Energy, **20**(8), pp. 1439–1462.

[107] Utsunomiya, T., Sato, I., Kobayashi, O., Shiraishi, T., and Harada, T., 2019, "Numerical Modeling and Analysis of a Hybrid-Spar Floating Wind Turbine," J. Offshore Mech. Arct. Eng., **141**(3).

[108] "Adams - The Multibody Dynamics Simulation Solution" [Online]. Available: https://www.mscsoftware.com/product/adams. [Accessed: 31-May-2022].

[109] Oh, Y., Kim, K., Kim, H., and Paek, I., 2015, "Control Algorithm of a Floating Wind Turbine for Reduction of Tower Loads and Power Fluctuation," Int. J. Precis. Eng. Manuf., **16**(9), pp. 2041–2048.

[110] Yoshimoto, H., and Kamizawa, K., 2019, "Validation of the Motion Analysis Method of Floating Offshore Wind Turbines Using Observation Data Acquired by Full Scale Demonstration Project," *Proceedings of the ASME 2019 38th International Conference on Ocean, Offshore and Arctic Engineering*, American Society of Mechanical Engineers Digital Collection.

[111] "Sesam for Marine Systems Software Modules," DNV [Online]. Available: https://www.dnv.com/services/sesam-for-marine-systems-modules-2323. [Accessed: 16-Jun-2022].

[112] "OrcaFlex - Dynamic Analysis Software for Offshore Marine Systems," Orcina [Online]. Available: https://www.orcina.com/orcaflex/. [Accessed: 16-Jun-2022].

[113] 2018, "News - OrcaFlex 10.3 Released," Orcina [Online]. Available: https://www.orcina.com/news/orcaflex-103-released/. [Accessed: 16-Jun-2022].

[114] Masciola, M., Robertson, A., Jonkman, J., and Driscoll, F., 2011, *Investigation of a FAST-OrcaFlex Coupling Module for Integrating Turbine and Mooring*

Dynamics of Offshore Floating Wind Turbines: Preprint, NREL/CP-5000-52896, National Renewable Energy Lab. (NREL), Golden, CO (United States).

[115] Cermelli, C., Leroux, C., Díaz Domínguez, S., and Peiffer, A., 2018, "Experimental Measurements of WindFloat 1 Prototype Responses and Comparison With Numerical Model," *Proceedings of the ASME 2018 37th International Conference on Ocean, Offshore and Arctic Engineering*, American Society of Mechanical Engineers Digital Collection.

[116] Cheng, P., Huang, Y., and Wan, D., 2019, "A Numerical Model for Fully Coupled Aero-Hydrodynamic Analysis of Floating Offshore Wind Turbine," Ocean Eng., **173**, pp. 183–196.

[117] Liu, Y., 2018, "A CFD Study of Fluid Structure Interaction Problems for Floating Offshore Wind Turbines," PhD, University of Strathclyde.

[118] Churchfield, M. J., Lee, S., Moriarty, P. J., Martinez, L. A., Leonardi, S., Vijayakumar, G., and Brasseur, J. G., 2012, "A Large-Eddy Simulation of Wind-Plant Aerodynamics," *50th AIAA Aerospace Sciences Meeting Nashville, Tennessee*, National Renewable Energy Lab. (NREL), Golden, CO (United States), Nashville, Tennessee.

[119] Lee, S., Churchfield, M., Driscoll, F., Sirnivas, S., Jonkman, J., Moriarty, P., Skaare, B., Nielsen, F., and Byklum, E., 2018, "Load Estimation of Offshore Wind Turbines," Energies, **11**(7), p. 1895.

[120] Johlas, H. M., Martínez-Tossas, L. A., Lackner, M. A., Schmidt, D. P., and Churchfield, M. J., 2020, "Large Eddy Simulations of Offshore Wind Turbine Wakes for Two Floating Platform Types," J. Phys. Conf. Ser., **1452**, p. 012034.

[121] Stewart, G., and Muskulus, M., 2016, "A Review and Comparison of Floating Offshore Wind Turbine Model Experiments," *13th Deep Sea Offshore Wind R&D Conference*, Trondheim, Norway, pp. 227–231.

[122] Koo, B. J., Goupee, A. J., Kimball, R. W., and Lambrakos, K. F., 2014, "Model Tests for a Floating Wind Turbine on Three Different Floaters," J. Offshore Mech. Arct. Eng., **136**(020907).

[123] Robertson, A. N., Wendt, F., Jonkman, J. M., Popko, W., Dagher, H., Gueydon, S., Qvist, J., Vittori, F., Azcona, J., Uzunoglu, E., Soares, C. G., Harries, R., Yde, A., Galinos, C., Hermans, K., de Vaal, J. B., Bozonnet, P., Bouy, L., Bayati, I., Bergua, R., Galvan, J., Mendikoa, I., Sanchez, C. B., Shin, H., Oh, S., Molins, C., and Debruyne, Y., 2017, "OC5 Project Phase II: Validation of Global Loads of the DeepCwind Floating Semisubmersible Wind Turbine," Energy Procedia, **137**, pp. 38–57.

[124] Hall, M., and Goupee, A., 2015, "Validation of a Lumped-Mass Mooring Line Model with DeepCwind Semisubmersible Model Test Data," Ocean Eng., **104**, pp. 590–603.

[125] Cruz, J., and Atcheson, M., 2016, *Floating Offshore Wind Energy: The Next Generation of Wind Energy*, Springer, Cham, SWITZERLAND.

[126] Goupee, A. J., Fowler, M. J., Kimball, R. W., Helder, J., and de Ridder, E.-J., 2014, "Additional Wind/Wave Basin Testing of the DeepCwind Semi-Submersible With a Performance-Matched Wind Turbine," *Proceedings of the ASME 2014 33rd International Conference on Ocean, Offshore and Arctic Engineering*, American Society of Mechanical Engineers Digital Collection.

[127] Bayati, I., Belloli, M., Bernini, L., Boldrin, D. M., Boorsma, K., Caboni, M., Cormier, M., Mikkelsen, R., Lutz, T., and Zasso, A., 2018, "UNAFLOW Project: UNsteady Aerodynamics of FLOating Wind Turbines," J. Phys. Conf. Ser., **1037**(7), p. 072037.

[128] Bak, C., 2013, "The DTU 10-MW Reference Wind Turbine."

[129] Jonkman, J., and Musial, W., 2010, *Offshore Code Comparison Collaboration (OC3) for IEA Task 23 Offshore Wind Technology and Deployment*, NREL/TP-5000-48191, NREL.

[130] Popko, W., Vorpahl, F., Zuga, A., Kohlmeier, M., Jonkman, J., Robertson, A., Larsen, T. J., Yde, A., Sætertrø, K., Okstad, K. M., Nichols, J., Nygaard, T. A., Gao, Z., Manolas, D., Kim, K., Yu, Q., Shi, W., Park, H., Vásquez-Rojas, A., Dubois, J., Kaufer, D., Thomassen, P., de Ruiter, M. J., Peeringa, J., Zhiwen, H., and von Waaden, H., 2012, "Offshore Code Comparison Collaboration Continuation (OC4), Phase I - Results of Coupled Simulations of an Offshore Wind Turbine with Jacket Support Structure: Preprint," *Proceedings of the 22nd International Society of Offshore and Polar Engineers Conference*, Rhodes, Greece, p. 12.

[131] Robertson, A., Jonkman, J., Musial, W., Vorpahl, F., and Popko, W., 2013, *Offshore Code Comparison Collaboration, Continuation: Phase II Results of a Floating Semisubmersible Wind System: Preprint*, NREL/CP-5000-60600, National Renewable Energy Lab. (NREL), Golden, CO (United States).

[132] Robertson, A. N., Gueydon, S., Bachynski, E., Wang, L., Jonkman, J., Alarcón, D., Amet, E., Beardsell, A., Bonnet, P., Boudet, B., Brun, C., Chen, Z., Féron, M., Forbush, D., Galinos, C., Galvan, J., Gilbert, P., Gómez, J., Harnois, V., Haudin, F., Hu, Z., Dreff, J. L., Leimeister, M., Lemmer, F., Li, H., Mckinnon, G., Mendikoa, I., Moghtadaei, A., Netzband, S., Oh, S., Pegalajar-Jurado, A., Nguyen, M. Q., Ruehl, K., Schünemann, P., Shi, W., Shin, H., Si, Y., Surmont, F., Trubat, P., Qwist, J., and Wohlfahrt-Laymann, S., 2020, "OC6 Phase I: Investigating the Underprediction of Low-Frequency Hydrodynamic Loads and Responses of a Floating Wind Turbine," J. Phys. Conf. Ser., **1618**(3), p. 032033.

[133] "A2e: OC6" [Online]. Available: https://a2e.energy.gov/projects/oc6. [Accessed: 17-Dec-2020].

[134] Moukalled, F., Mangani, L., and Darwish, M., 2016, *The Finite Volume Method in Computational Fluid Dynamics*, Springer.

[135] Launder, B. E., and Sharma, B. I., 1974, "Application of the Energy-Dissipation Model of Turbulence to the Calculation of Flow near a Spinning Disc," Lett. Heat Mass Transf., **1**, pp. 131–137.

[136] Spalart, P., and Allmaras, R., 1992, "A One-Equation Turbulence Model for Aerodynamic Flows."

[137] Kolmogorov, A. N., 1991, "The Local Structure of Turbulence in Incompressible Viscous Fluid for Very Large Reynolds Numbers," Proc. R. Soc. Lond. Ser. Math. Phys. Sci., **434**(1890), pp. 9–13.

[138] Pope, S. B., 2000, *Turbulent Flows*, Cambridge University Press.

[139] Rodi, W., 1997, "Comparison of LES and RANS Calculations of the Flow around Bluff Bodies," J. Wind Eng. Ind. Aerodyn., **69**–**71**, pp. 55–75.

[140] “SOWFA” [Online]. Available: https://github.com/NREL/SOWFA. [Accessed: 15-Sep-2020].

[141] Stevens, R. J. A. M., and Meneveau, C., 2017, “Flow Structure and Turbulence in Wind Farms,” Annu. Rev. Fluid Mech., **49**(1), pp. 311–339.

[142] Spiegel, E. A., and Veronis, G., 1960, “On the Boussinesq Approximation for a Compressible Fluid.,” Astrophys. J., **131**, pp. 442–447.

[143] Issa, R. I., 1986, “Solution of the Implicitly Discretised Fluid Flow Equations by Operator-Splitting,” J. Comput. Phys., **62**(1), pp. 40–65.

[144] Rhie, C. M., and Chow, W. L., 1983, “Numerical Study of the Turbulent Flow Past an Airfoil with Trailing Edge Separation,” AIAA J., **21**(11), pp. 1525–1532.

[145] Schumann, U., 1975, “Subgrid Scale Model for Finite Difference Simulations of Turbulent Flows in Plane Channels and Annuli,” J. Comput. Phys., **18**, pp. 376–404.

[146] Deardorff, J. W., 1980, “Stratocumulus-Capped Mixed Layers Derived from a Three-Dimensional Model,” Bound.-Layer Meteorol., **18**(4), pp. 495–527.

[147] Moeng, C.-H., 1984, “A Large-Eddy-Simulation Model for the Study of Planetary Boundary-Layer Turbulence,” J. Atmospheric Sci., **41**(13), pp. 2052–2062.

[148] Türk, M., and Emeis, S., 2010, “The Dependence of Offshore Turbulence Intensity on Wind Speed,” J. Wind Eng. Ind. Aerodyn., **98**(8), pp. 466–471.

[149] Stull, R. B., 1988, *An Introduction to Boundary Layer Meteorology*, Springer Science & Business Media.

[150] Charnock, H., 1955, “Wind stress on a water surface,” Q. J. R. Meteorol. Soc., **81**(350), pp. 639–640.

[151] Weber, R. O., 1999, “Remarks on the Definition and Estimation of Friction Velocity,” Bound.-Layer Meteorol., **93**(2), pp. 197–209.

[152] Jonkman, B. J., 2009, *Turbsim User’s Guide: Version 1.50*, NREL/TP-500-46198, National Renewable Energy Lab. (NREL), Golden, CO (United States).

[153] Nieuwstadt, F. T. M., and Duynkerke, P. G., 1996, “Turbulence in the Atmospheric Boundary Layer,” Atmospheric Res., **40**(2), pp. 111–142.

[154] Glauert, H., 1935, “Airplane Propellers,” *Aerodynamic Theory*, W.F. Durand, ed., Springer Berlin Heidelberg, Berlin, Heidelberg, pp. 169–360.

[155] Ning, S. A., Hayman, G., Damiani, R., and Jonkman, J., 2015, “Development and Validation of a New Blade Element Momentum Skewed-Wake Model within AeroDyn,” *AIAA Science and Technology Forum and Exposition 2015*, Kissimmee, Florida.

[156] Snel, H., and Schepers, J. G., 1995, “Joint Investigation of Dynamic Inflow Effects and Implementation of an Engineering Method.”

[157] Minnema, J. E., 1998, “Pitching Moment Predictions on Wind Turbine Blades Using the Beddoes- Leishman Model for Unsteady Aerodynamics and Dynamic Stall.,” Master of Science Thesis, University of Utah.

[158] Pierce, K. G., 1996, “Wind Turbine Load Prediction Using The BeddoesLeishman Model For Unsteady Aerodynamics And Dynamic Stall,” Master of Science Thesis, University of Utah.

[159] Damiani, R. R., and Hayman, G., 2019, *The Unsteady Aerodynamics Module For FAST8*, NREL/TP-5000-66347, National Renewable Energy Lab. (NREL), Golden, CO (United States).

[160] Driscoll, F., Jonkman, J., Robertson, A., Sirnivas, S., Skaare, B., and Nielsen, F. G., 2016, "Validation of a FAST Model of the Statoil-Hywind Demo Floating Wind Turbine," Energy Procedia, **94**, pp. 3–19.

[161] Coulling, A. J., Goupee, A. J., Robertson, A. N., Jonkman, J. M., and Dagher, H. J., 2013, "Validation of a FAST Semi-Submersible Floating Wind Turbine Numerical Model with DeepCwind Test Data," J. Renew. Sustain. Energy, **5**(2), p. 023116.

[162] Jonkman, J., 2017, "FAST: An Open-Source Platform for Wind Turbine Multi-Physics Engineering Modeling."

[163] "Hywind Scotland" [Online]. Available: https://www.equinor.com/energy/hywind-scotland. [Accessed: 26-Apr-2022].

[164] Nichols, J., Ronold, K. O., and Hopstad, A. L., 2016, "Key Design Considerations," *Floating Offshore Wind Energy: The Next Generation of Wind Energy*, J. Cruz, and M. Atcheson, eds., Springer International Publishing, Cham, pp. 241–269.

[165] "Wamit, Inc. - The State of the Art in Wave Interaction Analysis" [Online]. Available: https://www.wamit.com/. [Accessed: 18-Feb-2022].

[166] Hasselmann, K., Barnett, T. P., Bouws, E., Carlson, H., Cartwright, D. E., Enke, K., Ewing, J. A., Gienapp, A., Hasselmann, D. E., Kruseman, P., Meerburg, A., Müller, P., Olbers, D. J., Richter, K., Sell, W., and Walden, H., 1973, "Measurements of Wind-Wave Growth and Swell Decay during the Joint North Sea Wave Project (JONSWAP).," Ergänzungsheft Zur Dtsch. Hydrogr. Z. Reihe A, **Nr. 12**.

[167] Borisade, F., Koch, C., Lemmer, F., Cheng, P. W., Campagnolo, F., and Matha, D., 2018, "Validation of INNWIND.EU Scaled Model Tests of a Semisubmersible Floating Wind Turbine," Int. J. Offshore Polar Eng., **28**(01), pp. 54–64.

[168] Wendt, F., Robertson, A., Jonkman, J., and Hayman, G., 2015, "Verification of New Floating Capabilities in FAST V8," *33rd Wind Energy Symposium*, Kissimmee, Florida.

[169] Churchfield, M., 2017, "Simulator fOr Wind Farm Applications (SOWFA)."

[170] Dhondt, G., 2019, "CalculiX CrunchiX User's Manual Version 2.16."

[171] Dhondt, G., 2004, *The Finite Element Method for Three-Dimensional Thermomechanical Applications*, John Wiley & Sons.

[172] Bungartz, H.-J., Lindner, F., Gatzhammer, B., Mehl, M., Scheufele, K., Shukaev, A., and Uekermann, B., 2016, "PreCICE – A Fully Parallel Library for Multi-Physics Surface Coupling," Comput. Fluids, **141**, pp. 250–258.

[173] "Precice.Github.Io/Material/Overview at Master · Precice/Precice.Github.Io," GitHub [Online]. Available: https://github.com/precice/precice.github.io. [Accessed: 11-May-2022].

[174] Uekermann, B., Bungartz, H.-J., Yau, L. C., Chourdakis, G., and Rusch, A., 2017, "Official PreCICE Adapters for Standard Open-Source Solvers," *Proceedings of*

the 7th GACM Colloquium on Computational Mechanics for Young Scientists from Academia and Industry, Stuttgart, Germany.

[175] Cheung Yau, L., 2016, "Conjugate Heat Transfer with the Multiphysics Coupling Library PreCICE," Master's thesis, Technical University of Munich.

[176] Chourdakis, G., 2017, "A General OpenFOAM Adapter for the Coupling Library PreCICE," Master's thesis, Technical University of Munich.

[177] Jha, P., Churchfield, M. J., Moriarty, P. J., and Schmitz, S., 2014, "Guidelines for Volume Force Distributions Within Actuator Line Modeling of Wind Turbines on Large-Eddy Simulation-Type Grids," J. Sol. Energy Eng., **136**(3).

[178] Martinez, L. A., Leonardi, S., Churchfield, M. J., and Moriarty, P. J., 2012, "A Comparison of Actuator Disk and Actuator Line Wind Turbine Models and Best Practices for Their Use," *50th AIAA Aerospace Sciences Meeting Including the New Horizons Forum and Aerospace Exposition*, Nashville, Tennessee.

[179] Troldborg, N., 2009, *Actuator Line Modeling of Wind Turbine Wakes*.

[180] Shives, M., and Crawford, C., 2013, "Mesh and Load Distribution Requirements for Actuator Line CFD Simulations," Wind Energy, **16**(8), pp. 1183–1196.

[181] Jha, P., Churchfield, M., Moriarty, P., and Schmitz, S., 2013, "Accuracy of State-of-the-Art Actuator-Line Modeling for Wind Turbine Wakes," *51st AIAA Aerospace Sciences Meeting Including the New Horizons Forum and Aerospace Exposition*, American Institute of Aeronautics and Astronautics, Texas.

[182] Simms, D., Schreck, S., Hand, M., and Fingersh, L. J., 2001, *NREL Unsteady Aerodynamics Experiment in the NASA-Ames Wind Tunnel: A Comparison of Predictions to Measurements*, NREL/TP-500-29494, 783409.

[183] Hand, M. M., Simms, D. A., Fingersh, L. J., Jager, D. W., Cotrell, J. R., Schreck, S., and Larwood, S. M., 2001, *Unsteady Aerodynamics Experiment Phase VI: Wind Tunnel Test Configurations and Available Data Campaigns*, NREL/TP-500-29955, National Renewable Energy Lab. (NREL).

[184] Jonkman, J., Butterfield, S., Musial, W., and Scott, G., 2009, *Definition of a 5-MW Reference Wind Turbine for Offshore System Development*, NREL.

[185] "REpower 5MW Wind Turbine," Renugen [Online]. Available: https://www.renugen.co.uk/repower-5mw-wind-turbine/. [Accessed: 04-Apr-2022].

[186] Jonkman, J., 2010, *Definition of the Floating System for Phase IV of OC3*, NREL/TP-500-47535, National Renewable Energy Lab. (NREL), Golden, CO (United States).

[187] Lienard, C., Boisard, R., and Daudin, C., 2020, "Aerodynamic Behavior of a Floating Offshore Wind Turbine," AIAA J., **58**(9), pp. 3835–3847.

[188] Tomasicchio, G. R., D'Alessandro, F., Musci, E., Fonseca, N., Mavrakos, S. A., Kirkegaard, J., Katsaounis, G. M., Penchev, V., Schüttrumpf, H., Wolbring, J., and Armenio, E., 2014, "Physical Model Experiments on Floating Off-Shore Wind Turbines," *Proceedings of the HYDRALAB IV Joint User Meeting*, Lisbon.

[189] Ramachandran, G. K. V., Robertson, A., Jonkman, J. M., and Masciola, M. D., 2013, "Investigation of Response Amplitude Operators for Floating Offshore Wind Turbines," *Proceedings of the 23rd International Ocean, Offshore and Polar Engineering Conference*, Anchorage, Alaska.

[190] Liu, L., Franceschini, L., Oliveira, D. F., Galeazzo, F. C. C., Carmo, B. S., and Stevens, R. J. A. M., 2022, "Evaluating the Accuracy of the Actuator Line Model against Blade Element Momentum Theory in Uniform Inflow," Wind Energy, **25**(6), pp. 1046–1059.

[191] Shen, X., Chen, J., Hu, P., Zhu, X., and Du, Z., 2018, "Study of the Unsteady Aerodynamics of Floating Wind Turbines," Energy, **145**, pp. 793–809.

[192] Farrugia, R., Sant, T., and Micallef, D., 2014, "Investigating the Aerodynamic Performance of a Model Offshore Floating Wind Turbine," Renew. Energy, **70**, pp. 24–30.

[193] Fleming, P. A., Gebraad, P. M. O., Lee, S., van Wingerden, J.-W., Johnson, K., Churchfield, M., Michalakes, J., Spalart, P., and Moriarty, P., 2014, "Evaluating Techniques for Redirecting Turbine Wakes Using SOWFA," Renew. Energy, **70**, pp. 211–218.

[194] Gebraad, P. M. O., Teeuwisse, F. W., van Wingerden, J.-W., Fleming, P. A., Ruben, S. D., Marden, J. R., and Pao, L. Y., 2016, "Wind Plant Power Optimization through Yaw Control Using a Parametric Model for Wake Effects—a CFD Simulation Study," Wind Energy, **19**, pp. 95–114.

[195] Jeong, M.-S., Kim, S.-W., Lee, I., Yoo, S.-J., and Park, K. C., 2013, "The Impact of Yaw Error on Aeroelastic Characteristics of a Horizontal Axis Wind Turbine Blade," Renew. Energy, **60**, pp. 256–268.

[196] Schepers, J. G., and Schreck, S., 2013, "The Importance of Aerodynamics and the Role of Aerodynamic Measurements."

[197] Simley, E., Fleming, P., Girard, N., Alloin, L., Godefroy, E., and Duc, T., 2021, "Results from a Wake-Steering Experiment at a Commercial Wind Plant: Investigating the Wind Speed Dependence of Wake-Steering Performance," Wind Energy Sci., **6**(6), pp. 1427–1453.

[198] 2019, *Wind Energy Generation Systems – Part 3-2: Design Requirements for Floating Offshore Wind Turbines*, IEC TS 61400-3-2, International Electrotechnical Commision.

[199] Barj, L., Jonkman, J. M., Robertson, A., Stewart, G. M., Lackner, M. A., Haid, L., Matha, D., and Stewart, S. W., 2014, "Wind/Wave Misalignment in the Loads Analysis of a Floating Offshore Wind Turbine," *32nd ASME Wind Energy Symposium*, American Institute of Aeronautics and Astronautics, National Harbor, Maryland.

[200] Bachynski, E. E., Kvittem, M. I., Luan, C., and Moan, T., 2014, "Wind-Wave Misalignment Effects on Floating Wind Turbines: Motions and Tower Load Effects," J. Offshore Mech. Arct. Eng., **136**(4).

[201] "UK Wind - Equinor.Com" [Online]. Available: https://www.equinor.com/en/what-we-do/uk-wind.html. [Accessed: 01-Feb-2022].

[202] "Equinor and ORE Catapult Collaborating to Share Hywind Scotland Operational Data - Equinor.Com" [Online]. Available: https://www.equinor.com/en/news/2019-11-28-hywind-scotland-data.html. [Accessed: 01-Feb-2022].

[203] Resor, B. R., 2013, *Definition of a 5MW/61.5m Wind Turbine Blade Reference Model.*, SAND2013-2569, Sandia National Lab. (SNL-NM), Albuquerque, NM (United States).

[204] "BModes" [Online]. Available: https://www.nrel.gov/wind/nwtc/bmodes.html. [Accessed: 11-Feb-2022].

[205] Arya, S. P. S., 1981, "Parameterizing the Height of the Stable Atmospheric Boundary Layer," J. Appl. Meteorol. Climatol., **20**(10), pp. 1192–1202.

[206] Wu, J., 1980, "Wind-Stress Coefficients over Sea Surface near Neutral Conditions—A Revisit," J. Phys. Oceanogr., **10**(5), pp. 727–740.

[207] Catapult ORE, "Floating Turbine Design Cases" [Online]. Available: https://pod.ore.catapult.org.uk/data-collection/floating-turbine-design-cases.

[208] Zhang, S., and Ishihara, T., 2016, "Effects of Multidirectional Sea States and Flexible Foundation on Dynamic Response of Floating Offshore Wind Turbine System," *Proceedings of the First International Symposium on Flutter and Its Application*, Tokyo, Japan, pp. 729–738.

[209] Ishida, S., Kokubun, K., Nimura, T., Utsunomiya, T., Sato, I., and Yoshida, S., 2013, "At-Sea Experiment of a Hybrid Spar Type Offshore Wind Turbine," *Proceedings of the ASME 2013 32nd International Conference on Ocean, Offshore and Arctic Engineering*, Nantes, France.

[210] Utsunomiya, T., Sato, I., Yoshida, S., Ishida, S., and Ookubo, H., 2013, "Dynamic Response Analysis of a Floating Offshore Wind Turbine during Severe Typhoon Event," *Proceedings of the ASME 2013 32nd International Conference on Ocean, Offshore and Arctic Engineering*, Nantes, France.

[211] Tanaka, K., Sato, I., Utsunomiya, T., and Kakuya, H., 2019, "Comparison of Dynamic Response in a 2MW Floating Offshore Wind Turbine During Typhoon Approaches," *Proceedings of the ASME 2019 38th International Conference on Ocean, Offshore and Arctic Engineering*, Glasgow, U.K.

[212] Utsunomiya, T., Sato, I., and Shiraishi, T., 2020, "Floating Offshore Wind Turbines in Goto Islands, Nagasaki, Japan," *WCFS2019*, C.M. Wang, S.H. Lim, and Z.Y. Tay, eds., Springer, Singapore, pp. 359–372.

[213] The University of Tokyo, and Hitachi Ltd, 2019, "2MW Baseline Wind Turbine Model Development (WP1-1)."

[214] Zhang, J. A., Drennan, W. M., Black, P. G., and French, J. R., 2009, "Turbulence Structure of the Hurricane Boundary Layer between the Outer Rainbands," J. Atmospheric Sci., **66**(8), pp. 2455–2467.

[215] Liu, Y., Li, S., Yi, Q., and Chen, D., 2017, "Wind Profiles and Wave Spectra for Potential Wind Farms in South China Sea. Part II: Wave Spectrum Model," Energies, **10**(1), p. 127.

[216] Doong, D.-J., Tsai, C.-H., Chen, Y.-C., Peng, J.-P., and Huang, C.-J., 2015, "Statistical Analysis on the Long-Term Observations of Typhoon Waves in the Taiwan Sea," J. Mar. Sci. Technol., **Vol. 23**, pp. 893–900.

[217] Karimirad, M., 2013, "Modeling Aspects of a Floating Wind Turbine for Coupled Wave–Wind-Induced Dynamic Analyses," Renew. Energy, **53**, pp. 299–305.

[218] Rahimi, H., Martinez Garcia, A., Stoevesandt, B., Peinke, J., and Schepers, G., 2018, "An Engineering Model for Wind Turbines under Yawed Conditions Derived from High Fidelity Models," Wind Energy, **21**(8), pp. 618–633.

[219] Schepers, J. G., 2012, "Engineering Models in Wind Energy Aerodynamics: Development, Implementation and Analysis Using Dedicated Aerodynamic Measurements," PhD, TU Delft.

[220] Luhar, M., and Nepf, H. M., 2011, "Flow-Induced Reconfiguration of Buoyant and Flexible Aquatic Vegetation," Limnol. Oceanogr., **56**(6), pp. 2003–2017.

[221] Tian, F.-B., Dai, H., Luo, H., Doyle, J. F., and Rousseau, B., 2014, "Fluid–Structure Interaction Involving Large Deformations: 3D Simulations and Applications to Biological Systems," J. Comput. Phys., **258**, pp. 451–469.

[222] Miranda, I., Ferencz, R. M., and Hughes, T. J. R., 1989, "An Improved Implicit-Explicit Time Integration Method for Structural Dynamics," Earthq. Eng. Struct. Dyn., **18**(5), pp. 643–653.

[223] Bak, C., Zahle, F., Robert Bitsche, Taeseong Kim, Anders Yde, Lars C. Henriksen, Anand Natarajan, and Morten Hansen, 2013, *Description of the DTU 10 MW Reference Wind Turbine*, DTU Wind Energy Report-I-0092, DTU Wind Energy, Technical University of Denmark.

[224] Riziotis, V., Voutsinas, S., Manolas, D., Politis, E., and Chaviaropoulos, P. K., 2010, "Aeroelastic Analysis of Pre-Curved Rotor Blades," *EWEC 2010 Scientific Proceedings*, Warsaw, Poland.

[225] Österlund, J. M., Johansson, A. V., Nagib, H. M., and Hites, M. H., 2000, "A Note on the Overlap Region in Turbulent Boundary Layers," Phys. Fluids, **12**(1), pp. 1–4.

[226] George, W. K., and Castillo, L., 1997, "Zero-Pressure-Gradient Turbulent Boundary Layer," Appl. Mech. Rev., **50**(12), pp. 689–729.

[227] Marusic, I., Monty, J. P., Hultmark, M., and Smits, A. J., 2013, "On the Logarithmic Region in Wall Turbulence," J. Fluid Mech., **716**, p. R3.

[228] Bir, G. S., 2006, *User's Guide to PreComp (Pre-Processor for Computing Composite Blade Properties)*, NREL/TP-500-38929, National Renewable Energy Lab. (NREL), Golden, CO (United States).

[229] Lindner, F., 2019, "Data Transfer in Partitioned Multi-Physics Simulations: Interpolation & Communication," Dissertation, University of Stuttgart.

[230] "Mapping Configuration | PreCICE - The Coupling Library" [Online]. Available: https://precice.org/configuration-mapping.html. [Accessed: 07-Feb-2022].

[231] Lindner, F., Mehl, M., Scheufele, K., and Uekérmann, B., 2015, "A Comparison of Various Quasi-Newton Schemes for Partitioned Fluid-Structure Interaction," *Proceedings of the VI International Conference on Computational Methods for Coupled Problems in Science and Engineering*, CIMNE, pp. 477–488.

[232] Churchfield, M. J., Lee, S., Schmitz, S., and Wang, Z., 2015, "Modeling Wind Turbine Tower and Nacelle Effects within an Actuator Line Model," *33rd Wind Energy Symposium*, American Institute of Aeronautics and Astronautics, Kissimmee, Florida.

[233] "Floatgen" [Online]. Available: https://www.bw-ideol.com/en/floatgen-demonstrator. [Accessed: 05-Jul-2022].

[234] Højstrup, J., 1982, “Velocity Spectra in the Unstable Planetary Boundary Layer,” J. Atmospheric Sci., **39**(10), pp. 2239–2248.

[235] Olesen, H. R., Larsen, S. E., and Højstrup, J., 1984, “Modelling Velocity Spectra in the Lower Part of the Planetary Boundary Layer,” Bound.-Layer Meteorol., **29**, pp. 285–312.

[236] Jonkman, J., and Shaler, K., 2021, *FAST.Farm User’s Guide and Theory Manual*, NREL/TP-5000-78485, National Renewable Energy Laboratory, Golden, CO (United States).

[237] Shaler, K., Jonkman, J., Doubrawa Moreira, P., and Hamilton, N., 2019, *FAST.Farm Response to Varying Wind Inflow Techniques: Preprint*, NREL/CP-5000-72893, National Renewable Energy Lab. (NREL), Golden, CO (United States).

[238] Roald, L., Jonkman, J., Robertson, A., and Chokani, N., 2013, “The Effect of Second-Order Hydrodynamics on Floating Offshore Wind Turbines,” Energy Procedia, **35**, pp. 253–264.

[239] Duarte, T., and Jonkman, J., 2014, *Effects of Second-Order Hydrodynamic Forces on Floating Offshore Wind Turbines*, NREL/CP-5000-60966, National Renewable Energy Lab. (NREL), Golden, CO (United States), National Harbor, Maryland.